Universidade de Aveiro Departamento de Engenharia Mecânica
2013

**PAULO JORGE
RORIZ DE OLIVEIRA**

SENSORES EM FIBRA ÓTICA PARA O ESTUDO BIOMECÂNICO DO DISCO INTERVERTEBRAL

FIBER OPTIC SENSORS FOR THE BIOMECHANICAL STUDY OF THE INTERVERTEBRAL DISC

Universidade de Aveiro Departamento de Engenharia Mecânica
2013

PAULO JORGE RORIZ DE OLIVEIRA

SENSORES EM FIBRA ÓTICA PARA O ESTUDO BIOMECÂNICO DO DISCO INTERVERTEBRAL

FIBER OPTIC SENSORS FOR THE BIOMECHANICAL STUDY OF THE INTERVERTEBRAL DISC

Tese apresentada à Universidade de Aveiro para cumprimento dos requisitos necessários à obtenção do grau de Doutor em Engenharia Mecânica, realizada sob a orientação científica do Doutor José António Oliveira Simões, Professor Associado com Agregação do Departamento de Engenharia Mecânica da Universidade de Aveiro e coorientada pelo Doutor José Luís Santos, Professor Catedrático da Faculdade de Ciências da Universidade do Porto.

A thesis presented to the University of Aveiro in fulfillment of the requirement for the degree of Doctor of Philosophy in Mechanical Engineering, under the supervision of José António Oliveira Simões, Ph.D., Associate Professor of the Department of Mechanical Engineering of the University of Aveiro and the co-supervision of José Luís Santos, Ph.D., Full Professor of the Faculty of Science of the University of Porto.

Apoio financeiro da FCT e do FSE no âmbito do III Quadro Comunitário de Apoio - SFRH/BD/45130/2008

Grant supported by the Portuguese Foundation for Science and Technology (FCT) - SFRH/BD/45130/2008

Dedico este trabalho aos meus pais, à minha esposa e aos meus filhos.

o júri

presidente	Doutor Helmuth Robert Malonek Professor Catedrático da Universidade de Aveiro
vogais	Doutor António Torres Marques Professor Catedrático da Faculdade de Engenharia da Universidade do Porto
	Doutor José Luís Campos de Oliveira Santos Professor Catedrático da Faculdade de Ciências da Universidade do Porto
	Doutor José António de Oliveira Simões Professor Associado com Agregação da Universidade de Aveiro
	Doutor José Alberto Caeiro Potes Professor Associado com Agregação da Universidade de Évora
	Doutor Jorge Augusto Fernandes Ferreira Professor Auxiliar da Universidade de Aveiro
	Doutor Orlando José Reis Frazão Professor Auxiliar Convidado da Faculdade de Ciências da Universidade do Porto

acknowledgments

Looking back I notice I have never been alone. Science is profoundly humanistic and in it, as in my family, I have found the best examples of solidarity, abnegation, ethics and human capacity. I must therefore highlight those who have accompanied me in the last four years and attribute all the virtues of this study to them. And, if it has not been possible to go beyond, on account of my exclusive limitation, to promise them that I will carry on working…

My deepest gratitude goes to my advisor, Professor José António Oliveira Simões, for having given me the honor and privilege of attending a PhD in Mechanical Engineering, accepting all my limitations. If in geniality and wisdom I cannot equal him, I find in his nature and determination, kindness, courage and abnegation, all the qualities of the good man I try to be.

I also thank Professor José Luís Santos for having accepted to be my co-advisor and offered me all the conditions to the discovery of the exciting and new world of fiber optic sensors. To him I have always been a good old PhD student, which shows his profound generosity and chivalry. To me Professor José Luís embodies the true master, in knowledge and human nature, which leads one to understand how he became such a reference in his field.

My gratitude also goes to Professor Ilda Abe, who was my first year co-advisor and offered me the opportunity to fabricate fiber Bragg gratings sensors at the Laboratory of Coherent Optical Systems at the Physics Department of the University of Aveiro.

My deepest gratitude to Professor António Lobo-Ribeiro. He has been, since the beginning, a source of knowledge and inspiration.

My heartfelt gratitude to Professor José Caeiro Potes, for receiving us at the Veterinary Hospital of the University of Évora and for his help conducting the surgery for implantation of a fiber optic sensor in the disc of an anaesthetized sheep.

Many thanks to Francisco Araújo, Product Development Director of FiberSensing, for his contribution to the design and discussion of some sensor configurations.

Many thanks to my colleagues and friends at INESC-Porto. Among them, special thanks to Orlando Frazão who indefatigably supported me every day. As a mentor and a friend, he continuously instilled the spirit of creative research and the willingness to “bring light to the unknown” into me. My deepest gratitude to Doctor João Ferreira, without his help it would be impossible to design and construct the interrogation unit and software that have been used to interrogate the Samba preclin sensor. Dear Marta Ferreira, I will need more than a hug to express my gratitude for your support and friendship. It is an honor to share the place of work and the optical table with you and our mutual “genius” friend Ricardo André. Many thanks to my friend Carlos Gaspar, namely for his ability to find what is needed when it is needed. I also would like to thank Luis Coelho, Katalin Balogh and Paula Tafulo for helping me conducting several exploratory experiences. I hope I never forget all the contributions, at the monthly meetings of the team, inside and outside the

cabinets, at the corridors, travels and lunches… Thus, many thanks to Paulo Marques, Manuel Marques, Pedro Jorge, Ariel Guerreiro, Serge Mendonça, Mikel Bravo, Ivo Leite, Paulo Caldas, Joel Carvalho, Carlos Gouveia, Susana Silva, Raquel Queirós, Ivo Nascimento, Manuel Marques (Jr.) and Luiz Rodriguez. Special thanks to Luísa Mendonça and Ireneu Dias, particularly for their efforts to make INESC-Porto and UOSE a place where one works with great pleasure and where administrative tasks are a light weight to carry.

I also would like to thank all teachers of the curricular units of the doctoral program of Mechanical Engineering, namely for giving me the opportunity to focus on academic work according to the needs of my PhD project. Special thanks to Professor António Ramos, Professor José Relvas and Professor Jorge Ferreira, namely for their involvement in many tasks performed at the Biomechanics Laboratory of the University of Aveiro and their contribution to the process of writing reports and papers.

My special thanks to my PhD fellows at the Biomechanics Laboratory, namely to Susana Meireles and Marco Santos. It was a pleasure to share the same concerns and expectations with them and, most of all, to benefit from their friendship.

I also would like to thank José Miguel Monteiro, technician of FiberSensing, for his help performing some pressure tests.

Words cannot express the thanks I owe to my parents, my brothers and their families, my wife and my children. Without their endless love and constant encouragement I would certainly not have had the boldness to begin this adventure and the strength to finish it.

I would also like to take this opportunity to express my gratitude to the institutions and companies that have provided financial and logistic support to my PhD.

I am thankful to ISMAI, in particular to its Board President, Professor Domingos Oliveira Silva, and the Board of Maiêutica, Doctor José Manuel Matias de Azevedo. The authorized leave they have granted me for a period of four years has been decisive to the accomplishment of this study.

I also thank University of Aveiro, and its Department of Mechanical Engineering, for having accepted me as a PhD student and provided good working conditions in its investigation unit, the Centre for Mechanical Technology and Automation (TEMA). I must as well acknowledge all the support provided by the Department of Physics of University of Aveiro and its Laboratory of Coherent Optical Systems, for allowing the use of the interferometric system to the inscribing of Bragg gratings.

My gratitude to INESC-Porto and particularly to its unit of Optoelectronics and Electronic Systems (UOSE) is immense. I appreciate them the opportunity of working in emerging areas of this field, making part of an exceptional work team in a very pleasant place of work. Furthermore, in a period of deep economic crisis, I must emphasize the financing for equipment acquisition, travels and participation in conferences.

I thank FiberSensing, Sistemas Avançados de Monitorização, SA, a spin-off from INESC-Porto based in Maia, Portugal, for having made the mechanical testing machine available and also the human resources to carry out the pressure tests with several configurations of optic fiber sensors.

I also thank the collaboration of the Department of Veterinarian Medicine of Science and Technology School of University of Évora. Without its support the making of studies *in vivo* would not have been possible.

I finally appreciate the financial support of the Portuguese Foundation of Science and Technology (FCT) in the last four years.

palavras-chave

Sensores em fibra ótica, biomecânica, biomédica, coluna vertebral, disco intervertebral, *ex vivo*, *in vivo*

resumo

O presente trabalho teve como objetivo principal estudar o comportamento mecânico do disco intervertebral recorrendo a sensores em fibra ótica.
Na expetativa de efetuar o melhor enquadramento do tema foi efetuada uma revisão exaustiva das várias configurações de sensores em fibra ótica que têm vindo a ser utilizadas em aplicações biomédicas e biomecânicas, nomeadamente para medição de temperatura, deformação, força e pressão. Nesse âmbito, procurou-se destacar as potencialidades dos sensores em fibra ótica e apresentá-los como uma tecnologia alternativa ou até de substituição das tecnologias associadas a sensores convencionais. Tendo em vista a aplicação de sensores em fibra ótica no estudo do comportamento do disco intervertebral efetuou-se também uma revisão exaustiva da coluna vertebral e, particularmente, do conceito de unidade funcional. A par de uma descrição anatómica e funcional centrada no disco intervertebral, vértebras adjacentes e ligamentos espinais foram ainda destacadas as suas propriedades mecânicas e descritos os procedimentos mais usuais no estudo dessas propriedades. A componente experimental do presente trabalho descreve um conjunto de experiências efetuadas com unidades funcionais cadavéricas utilizando sensores convencionais e sensores em fibra ótica com vista à medição da deformação do disco intervertebral sob cargas compressivas uniaxiais. Inclui ainda a medição *in vivo* da pressão intradiscal num disco lombar de uma ovelha sob efeito de anestesia. Para esse efeito utilizou-se um sensor comercial em fibra ótica e desenvolveu-se a respetiva unidade de interrogação. Finalmente apresenta-se os resultados da investigação em curso que tem como objetivo propor e desenvolver protótipos de sensores em fibra ótica para aplicações biomédicas e biomecânicas. Nesse sentido, são apresentadas duas soluções de sensores interferométricos para medição da pressão em fluídos corporais.

keywords

Fiber optic sensors, biomechanics, biomedical, spine, intervertebral disc, *ex vivo*, *in vivo*

abstract

The present work aimed to study the mechanical behavior of the intervertebral disc using fiber optic sensors. To address the theme an exhaustive review of the various configurations of fiber optic sensors that have been used in biomechanical and biomedical applications, in particular for measuring temperature, strain, force and pressure, was conducted. In this context, an effort was made to highlight the advantages of fiber optic sensors and present them as an alternative or even a substitution technology to conventional sensors. In view of the application of fiber optic sensors to study intervertebral disc behavior an exhaustive review of the spine and, particularly, of the spinal motion segment was made. Along with an anatomical and functional description of the intervertebral disc, the adjacent vertebrae and spinal ligaments, their mechanical properties were also highlighted as well as the most common procedures and guidelines followed in the study of these properties. The experimental section of the present work describes a set of tests performed with cadaveric spinal motion segments using conventional and fiber optic sensors to assess strain of the intervertebral disc under uniaxial compressive loads. This section also includes an experience reporting *in vivo* pressures measured in the lumbar disc of a sheep under general anesthesia. In this case, a commercial fiber optic sensor and a purpose-built interrogation unit were used. Finally, the results of ongoing research aiming to develop fiber optic sensors prototypes for biomedical and biomechanical applications are presented. Thus, the proof of concept of two possible interferometric configurations intended for pressure measurement in body fluids was presented.

Table of Contents

List of Acronyms, Abbreviations and Symbols

ν	Poisson's ratio
2D	two dimensional
3D	three dimensional
AAMI	American Association for Medical Instrumentation
ABS	acrylonitrile butadiene styrene
AF	annulus fibrosus
AIDS	acquired immunodeficiency syndrome
ALL	anterior longitudinal ligament
ANSI	American National Standards Institute
AP	Anterior/posterior
APCVD	atmospheric pressure chemical vapor deposition
AR	Axial rotation
ASTM	American Society for Testing and Materials
bpm	beats per minute
BW	body weight
C1-C7	cervical vertebrae
CA	California
CCD	charge-coupled device
CE	conformity marking
CFRP	carbon fiber reinforced plastic
CL	capsular ligament
Co	cobalt
CPM	continuous passive motion
Cr	chromium
CSF	cerebrospinal fluid
CT	computed tomography (tomogram)
d	distance
DIN	Deutsches Institut für Normung
DNA	deoxyribonucleic acid
DOF	degrees of freedom
DVRT	differential variable reluctance transducer
E	Elasticity modulus or Young’s modulus (Pa)
e.g.	Latin: *exempli gratia* (for example)
EDTA	ethylenediaminetetraacetic acid
EM	Electromagnetic
EPROM	erasable programmable read only memory
et al.	Latin: et alii (and others)
ETFE	ethylene-tetrafluoroethylene
FBG	fiber Bragg grating
FDA	US Food and Drug Administration
FDIS	Final Draft International Standard
FE	Flexion/extension
Fe	Iron
FEA	finite element analysis
FEM	finite element method
FL	Florida
fMRI	functional MRI
FOP	fiber optic plethysmography
FOS	fiber optic sensor
F-P	Fabry-Pérot
FSO	full-scale output
FSU	functional spinal unit
FWHM	full width at half maximum
G	shear modulus (Pa)
GA	Georgia
GaA	gallium arsenide
GAG	glicosaminoglycans
HEST	Hall effect strain transducer
HF	hydrofluoric acid
HiBi	high-birefringence
i.e.	Latin: *id est* (that is)
IAB	intra-aortic balloon
IAP	intra-articular pressure
IASIS	Intelligent Adaptable Surface with Optical Fiber Sensing for Pressure-Tension Relief
ICP	intracranial pressure
ICS	International Classification for Standards
IFT	implantable force transducer
IMP	intramuscular pressure
ISL	interspinous ligament
ISO	International Organization for Standardization
ITL	intertransverse ligament
IVD	intervertebral disc
K	bulk modulus (Pa)
L1-L5	lumbar vertebrae
LB	Lateral bending
LCD	liquid crystal display
LED	light emitting diode
LF	ligamentum flavum
LMSG	liquid metal strain gauge
LPG	long period gratings
LVAD	left ventricular assist devices
MA	Massachusetts
MEMS	microelectromechanical systems
MI	Michigan
MMF	multimode fiber
MN	Minnesota
Mo	molybdenum
MOMS	micro-optical mechanical system
MPT	modified pressure transducer
MRI	magnetic resonance imaging
MW	microwave
NC	North Carolina
NJ	New Jersey
NJ	New Jersey
NP	nucleus pulposus
OD	outer diameter
OEM	original equipment manufacturer
OF	optical fiber
OSA	optical spectrum analyzer
PC	personal computer
PC	portable computer
PCF	photonic crystal fibers
PDMS	polydimethylsiloxane
PE	polyethylene
PECVS	plasma-enhanced chemical vapor deposition
PEEK	polyetheretherketone
PFBG	polymer coated FBG
PLL	posterior longitudinal ligament
PMMA	polymethyl-methacrylate
PTFE	polytetrafluoroethylene
PU	polyurethane
PVC	polyvinyl chloride
r	correlation coefficient
r^2	coefficient of determination
RF	radio frequency
RIE	reactive-ion etching
RMS	root-mean-square
ROM	range of motion
RSM	regional spine models
SC	subcommittees
SD	standard deviation
SG	strain gauge
SLD	superluminescent diode
SMF	single mode fiber
SMS	spinal motion segment
SSL	supraspinous ligament
T1-T12	thoracic vertebrae
TC	Technical Committee
TDM	time division multiplexing
TEMPs	Tissue engineered medical products
Ti	titanium
TLS	tunable laser source
TX	Texas
UK	United Kingdom
USA	United States of America

USP	United States Pharmacopeia
UV	Ultraviolet
VA	Virginia
VT	Vermont
WA	Washington
WDM	wavelength division multiplexing
WG	working groups
WSM	whole spine models

List of Figures

List of Tables

List of Equations

Part I - Introduction

Motivação / Motivation

O homem é talvez o único ser vivo capaz de se interrogar. E nessa busca interior, das razões da sua existência, do seu comportamento e da sua relação, sustentada pela intrincada rede do instinto e do pensamento, pela matéria e pelo corpo, pela cultura e pela técnica, tem sido capaz de conquistar, ainda que reconhecendo retrocessos, desvios e limites.

Assiste-o nessa conquista a dúvida e por isso é inesgotável o que há para saber. A dúvida é o limite do conhecimento e por essa razão o conhecimento não tem início nem fim, somente a expectativa de se alargar. A dúvida é a motivação para a construção de um intervalo do saber maior, a voz da consciência, apelando ao que há para saber sobre o passado, no presente e para o futuro.

E é comungando dessa inquietação pelo saber, fecundada pela dúvida, que o autor do presente trabalho, com vestes de explorador e "equipamento limitado", se precipita sobre as fronteiras do desconhecido. Interessa-o o corpo, matéria por excelência, manifestação palpável da existência. Interessa-o, sobretudo, o estudo das forças que nele atuam e que determinam o seu estado de repouso ou de movimento. E nessa ascese newtoniana, que o conduz à compreensão mais elementar das leis que regem a partícula, o corpo rígido ou deformável, tem encontrado novas questões e a motivação para explorar um pouco mais.

Surgiu assim este programa doutoral, da voz da consciência.

Alguns anos depois de ter tido aulas de Biomecânica com o Professor José António Oliveira Simões, num curso de pós-graduação em Engenharia Biomédica na Faculdade de Engenharia da Universidade do Porto, quis o destino que o voltasse a procurar. Preocupava-me o estudo da coluna vertebral, particularmente o das cargas a que está submetido o disco intervertebral. E se lhe soube expor o problema devo-o a quem me ensinou quase tudo, o Professor José Luís de Castro Gonçalves, meu professor de Biomecânica no Instituto Superior de Educação Física (atual Faculdade de Desporto da Universidade do Porto). Assim, e na condição de submeter e ver aprovado um projeto de investigação pela Fundação para a Ciência e Tecnologia pude contar com a supervisão do Professor José Simões no programa doutoral em Engenharia Mecânica da Universidade de Aveiro. Quis ainda o destino que os esforços para compreender o comportamento do disco intervertebral se centrassem na utilização de sensores minimamente invasivos apontando-se os sensores em fibra ótica como um recurso incontornável. Desse modo, e após uma primeira incursão pelo Laboratório de Sistemas Óticos Coerentes do Departamento de Física da Universidade de Aveiro, foi no INESC-Porto, e contando com a coorientação do Professor José Luís Santos, que encontrei as melhores condições para desenvolver e testar algumas configurações de sensores em fibra ótica com vista a aplicações biomecânicas e biomédicas. O processo culminou com a medição da pressão intradiscal *in vivo* num disco lombar de uma ovelha sob anestesia geral e a oportunidade de desenvolver sensores em fibra ótica para aplicações biomédicas e biomecânicas.

Man is perhaps the only living being capable of questioning himself. And in this inner search for the reasons for his existence, his behavior and his relationship, underpinned by the intricate network of instinct and thought, by matter and body, by culture and technology, he has been able to conquer, though acknowledging setbacks, detours and limits.

In that quest doubt is always present and therefore what there is to know is inexhaustible. Doubt is the limit of knowledge and that is why knowledge has no beginning and no end, only the expectation of extending itself. Doubt is the motivation for building a greater range of knowledge, the voice of consciousness appealing to what there is to know about the past, present and future.

Sharing this restlessness for knowledge, fertilized by doubt, the author of present work, with robes of explorer and "limited equipment", rushes on the borders of the unknown. Interested in the body, subject matter par excellence, tangible manifestation of existence. Interested especially in the study of forces that act on it and that determine its state of rest or motion. And in that Newtonian asceticism, which leads to the most basic understanding of the laws governing the particle, rigid or deformable body, he finds new issues and motivation to explore a little more.

Thus emerged this doctoral program, from the voice of consciousness.

Some years after having Biomechanics classes with Professor José António Oliveira Simões, in a postgraduate course in Biomedical Engineering in the Faculty of Engineering of University of Porto, Fate determined to contact him once more. I was worried about the study of the spine, particularly the loads to which the intervertebral disc is subjected. And if I knew how to present him the problem, I owe it to the one who taught me almost everything, Professor José Luís Gonçalves de Castro, my professor at the Institute of Biomechanics of Physical Education (now the Faculty of Sport, University of Porto). Thus, on condition of submitting and see a research project approved by the Foundation for Science and Technology, I could rely on the supervision of Professor José Simões, from the University of Aveiro, in the doctoral program in Mechanical Engineering. Fate still wanted that efforts to understand the behavior of the intervertebral disc should be focused on the use of minimally invasive sensors, mainly the optical fiber sensors, as an indispensable resource. Thus, after an initial foray by Coherent Optical Systems Laboratory, Department of Physics, University of Aveiro, it was at INESC-Porto, and relying on the co-supervision by Professor José Luis Santos, that I found the best conditions to develop and test some configurations of fiber optic sensors bearing in mind biomechanics and biomedical applications. The process resulted in the measurement of *in vivo* intradiscal pressure in the lumbar disc of a sheep under general anesthesia and the opportunity to develop optical fiber sensors for biomedical and biomechanical applications.

1. Objective and Thesis Organization

The present thesis aimed to study the mechanical behavior of the intervertebral disc using fiber optic sensors.

It is organized in four main parts. In Part I the author describes the motivation that led him to start the doctoral process and how he found the partners that supported his journey. Author main contributions are also described in Part I, namely those focusing on main academic contributions, in full fulfillment of the requirements of the doctoral syllabus in Mechanical Engineering at the University of Aveiro, and a list of posters, oral presentations and published papers.

Part II is devoted to the review of literature and was organized in two chapters. In chapter 1 an extensive review of fiber optic sensors that have been used in biomedical and biomechanical applications, in particular those measuring temperature, strain, force and pressure, was conducted. In chapter 2 a review focused on the spinal motion segment was made. This chapter seeks to describe the anatomical structures that have been the object of study during experimental work: the spinal motion segment and, particularly, the intervertebral disc.

Part III represents author main contributions in terms of experimental work. Four studies were described. The purpose of study 1 is to demonstrate that strain gauges can be successfully glued to the outer surface of the intervertebral disc (IVD) and provide readings of circumferential and axial strain under compressive load. In study 2 a fiber Bragg grating is used to measure radial strain. In study 3, *in vivo* intradiscal pressures were measured using a fiber optic sensor implanted in the lumbar disc of an anesthetized sheep. Finally, in study 4 the results of ongoing research aiming to develop fiber optic sensors prototypes for biomedical and biomechanical applications are presented.

In Part IV some conclusions are drawn regarding the work that was done, its limitations, potentialities and, particularly the need for future work that could enhance the contribution of fiber optic sensors in biomedical and biomechanical applications.

2. Author Main Contributions

2.1 Academic Work

The doctoral program in Mechanical Engineering of the University of Aveiro presumes an individual syllabus with specific curricular units directed to the training for investigation. The author took this opportunity to get a more profound knowledge on the research methods used in mechanical engineering to conduct biomechanical studies (*e.g.*, finite element analysis and mechanical testing of materials) and the techniques used on optoelectronics to fabricate and test fiber optics sensors. This work was accomplished at the facilities of the Biomechanics Laboratory of the Department of Mechanical Engineering of the University of Aveiro, the Laboratory of Coherent Optical Systems of the Physics Department of the University of Aveiro and at the Optoelectronics and Electronic Systems Unit (UOSE) of the Institute for Systems and Computer Engineering of Porto (INESC Porto). Along with the previous learning process and having in mind to create future lines of research, the state of the art about specific topics on spine biomechanics and about fiber optic sensors that are being used in biomechanical and biomedical applications was described. The most relevant reports that resulted from this process were[1]:

- Finite element analysis of a lumbar vertebra under compression;
- Intelligent and bio-inspired products: Spinal implants and prostheses;
- Fiber Bragg grating sensors: A product and market overview;
- Fiber Bragg grating sensor for intradiscal pressure measurement *in vivo*: A technological surveillance study;
- Using MATLAB to visualize, filter and build neural networks with experimental data obtained from disc bulging under compression;
- Fiber optic sensors for biomechanical and biomedical applications.

2.2 Posters

Roriz P, Abe I, Schiller M, Simões J Bulging of the intervertebral disc under compressive loading. In: Research Day, Aveiro, June 8 2011. University of Aveiro.

Roriz P, Frazão O, Simões J, Santos J Sensores de pressão baseados em fibra ótica para aplicações biomédicas e biomecânicas. In: Física 2012: Comunicação e Informação em Ciência, Aveiro, September, 6-8 2012.

---

[1] Full access to these reports can be obtained from the thesis CD ROM or under request (paulororiz@ua.pt)

2.3 Conference Papers and Oral Presentations

Roriz P, Abe I, Schiller M, Simões JA Intervertebral disc bulging measurement using a Fibre Bragg Grating sensor. In: Santos JL (ed) EWOFS 2010, Porto, September, 8-10 2010. SPIE, p 131.

Roriz P, Ramos A, Frazão O, Santos J, Simões J Não linearidade e anisotropia do anel fibroso do disco intervertebral submetido a compressão. In: I Simpósio de Biomecânica e Performance Humana, Universidade Fernando Pessoa, Porto, March, 25-6 2011.

Roriz P, Frazão O, Santos JL, Simões J Fiber optic sensors for biomechanical and biomedical applications. In: Natal-Jorge R, Tavares JS, Belinha J, Parente ML, Martins PS (eds) 5th Portuguese Congress on Biomechanics, Espinho, Portugal, Feb. 8-9 2013. Sociedade Portuguesa de Biomecânica, pp 503-8.

Roriz P, Frazão O, Santos JL, Simões J Fiber optic sensors for physiological pressure measurements. In: VIII RIAO/XI OPTILAS 2013, Porto, Portugal, July 22-26 2013, paper 100-692

2.4 Papers in Journals

Roriz P, Abe I, Schiller M, Gabriel J, Simões JA (2011) Intervertebral disc bulging measurement using a fibre Bragg grating sensor. Exp Mech 51:1573-7.

Roriz P, Ramos A, Santos J, Simões J (2012) Fiber optic intensity-modulated sensors: A review in biomechanics. Photonic Sensors 2 (4):315-30.

Roriz P, Frazão O, Lobo-Ribeiro A, Santos J, Simões J (2013) Review of fiber optic pressure sensors for biomedical and biomechanical applications. Journal of Biomedical Optics 18 (5):1-18.

Ferreira MS, Roriz P, Silva SO, Santos JL, Frazão O (2013) Next generation of Fabry-Pérot sensors for high-temperature. Optical Fiber Technology. Available online 17 August 2013, (Invited paper).

Part II – Review of Literature

Chapter 1 - Fiber Optic Sensors for Biomedical and Biomechanical Applications: A Review [2;3]

---

[2] Roriz P, Ramos A, Santos J, Simões J (2012) Fiber optic intensity-modulated sensors: A review in biomechanics. Photonic Sensors 2 (4): 315-30.

[3] Roriz P, Frazão O, Lobo-Ribeiro A, Santos J, Simões J (2013) Review of fiber optic pressure sensors for biomedical and biomechanical applications. Journal of Biomedical Optics 18 (5):1-18.

1. Introduction

In the coming years *in vivo* biomedical and biomechanical applications will benefit from a wide range of fiber optic sensor (FOS) turnkey systems for sensing and measuring almost any physical quantity. These systems have four basic components: the light source, the optical fiber (OF), the sensor element, and the light detector (figure 1).

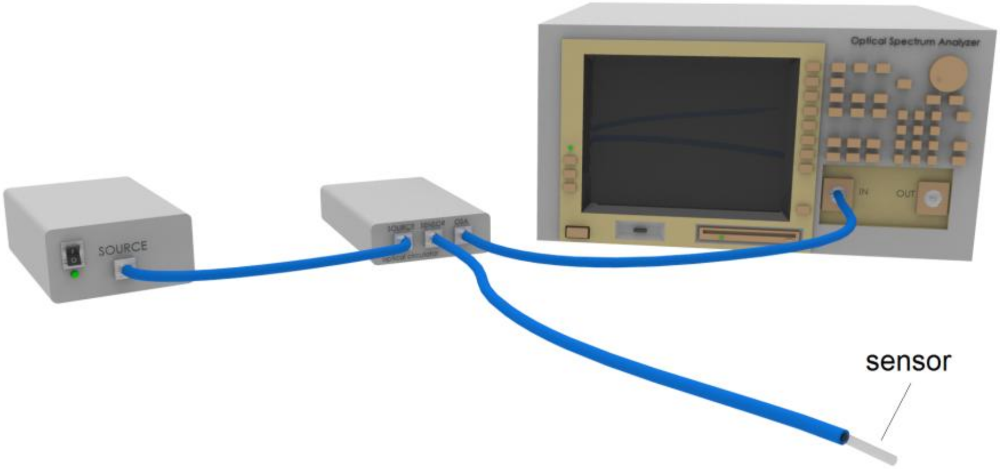

Figure 1 - Schematic drawing of a typical laboratory fiber optic system. Optical fibers provide flexible connections between the optoelectronic components of the system. In this case an optical circulator connects the source to the sensor and the sensor to the detector. Optical spectrum analyzers are commonly used as optoelectronic light detectors and analyzer devices.

The light source provides the electromagnetic (EM) radiation whose energy is transmitted through the OF to the sensor element, in general, under the principle of total internal reflection. The fiber optic sensor or transducer is the light modulator, *i.e.*, the entity that causes a light property to change (*e.g.*, amplitude or optical power, phase, polarization, and wavelength or optical frequency) under the influence of a certain physical quantity. Thus, a physical quantity (*e.g.*, temperature) can change the physical properties of the sensing element, which in turn leads to a change in the light properties. The light detector is necessary to read and analyze a light property variation. Since the four light properties can be considered in most circumstances independent parameters they offer a wide range of solutions to sense several physical quantities.

Fiber optic sensing technology is about forty years old and presents substantial advantages compared to conventional electric sensing systems. Conventional sensors applied in biomedical and biomechanical applications are based on piezoresistive, strain gauge (SG) or other solid-state sensing technologies. They represent a highly tested, mature and overspread technology, offering good sensitivity, precise measurements and competitive price. However, their miniaturization, typically requiring sensor head diameters below 0.5 mm, such as for minimally invasive procedures, presents some drawbacks. Mignani *et al.* [1] have pointed some of them, including fragility, long term instability, inconsistency and excessive drift. Additionally, their output is restricted to a small sensing area making it necessary to use more sensors to sense larger regions (*e.g.*, a temperature profile along a tissue), but only at the expense of increased dimensions and loss of flexibility [2]. These disadvantages combined with poor biocompatibility of metallic components and large sensitivity to EM interference, can compromise some *in vivo* applications and their use in clinical practice. A good example is their application in magnetic resonance imaging (MRI) environment. As pointed by Ladd *et al.* [3] ferromagnetic based sensors should not be used because they will act as an antenna and generate significant heating effects, which might cause image artifacts.

While OFs guide light, the majority of conventional sensors guide electricity through metallic wires (*e.g.*, copper-nickel alloys). This fundamental difference of carrying information, along with the following properties, makes OF the ideal tool in an increasingly number of sensing environments:

- Inertness and biocompatibility: A typical OF is made of amorphous silica glass, also known as silicon dioxide (SiO_2), fused silica or fused quartz. This compound is almost chemically inert and biocompatible [4]. Only hydrofluoric acid (HF) and some alkaline substances are capable of chemically attacking it [5-6]. Thus, an OF has the potential to neither adversely affect the physiological environment nor be adversely affected by it [7]. Under sterile conditions, OF will minimize contamination and the risk of infection associated to invasive procedures. Even so, there is a need of special care to glass debris that can be generated along with fiber breakage. Sharpened glass pieces can easily lacerate the skin, enter into the circulatory system or damage internal body cells and tissues. One should remember that some materials are biocompatible in their bulk form but wear debris can incite adverse reactions from the body cells. To avoid it the OF is usually embedded into biocompatible sterilizable protective layers, such as coatings, buffers, jackets and cables (figure 2). Materials such as polyimide, polydimethylsiloxane (PDMS), ethylene-tetrafluoroethylene (ETFE) or Tefzel®, and polytetrafluoroethylene (PTFE) or Teflon® are being used in biomedical and biomechanical applications [8-13]. The strength, fatigue and biocompatibility of silica fibers with several polymeric (*e.g.*, UV-cured acrylate, silicone, and polyimide), metallic (*e.g.*, aluminum, indium, tin, and gold) and inorganic (*e.g.*, oxides, carbides, nitrides, and carbon) coatings were also studied by Biswas [9]. The UV-curable dual acrylate coating used in standard OF may be inappropriate for biomedical and biomechanical applications requiring heating procedures, because it cannot withstand temperatures above 85 ºC [14]. Some manufacturers, like Ocean Optics (Dunedin, FL, USA; www.oceanoptics.com) and OFS (Norcross, GA, USA; www.ofsoptics.com), are producing nontoxic and biocompatible fibers, cables and assemblies, with materials used in implants and/or approved by the United States Pharmacopeia (USP Class VI Biological Test for Plastics). Some examples of these materials are polyetheretherketone (PEEK), fluoroacrylates, Poly(p-xylylene) or parylene, and polyimide. The OF can also be enclosed or encapsulated into surgical instruments, catheters, metallic tubes or needles. These objects can play several cumulative functions such as guide the FOS to the target during invasive procedures, protect the sensor or the host from direct contact, allow exposure of the sensing head only, minimize the risk of sensor breakage and the release of debris, or incorporate additional sensors and devices [10,15-21]. While almost all needles and metallic tubes are made of stainless steel, catheters can be made from a wide variety of materials, such as silicone rubber, latex, PTFE, polyethylene (PE), polyurethane (PU) and polyvinyl chloride (PVC);

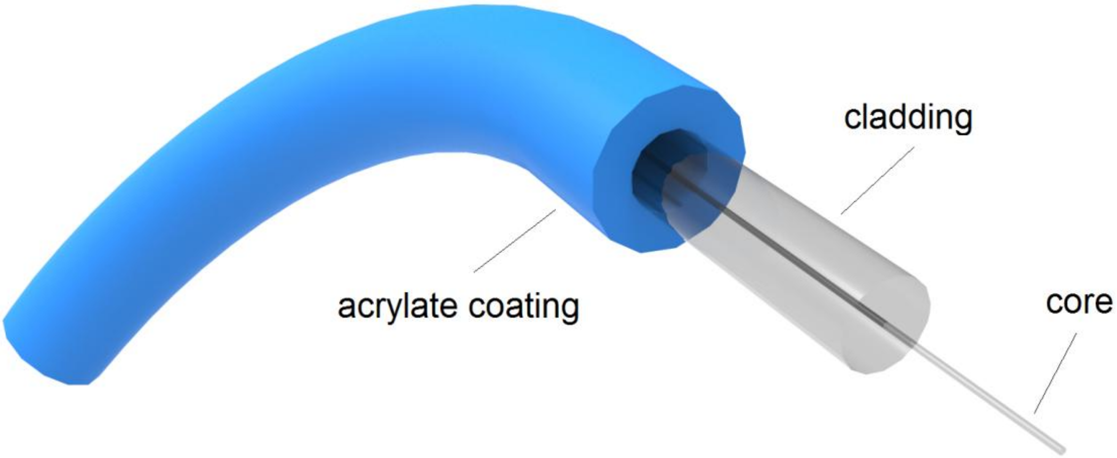

Figure 2 - Schematic drawing of a typical single mode fiber. This optical fiber has two main dielectric materials: the core and the cladding. The core is the inner and center cylinder of the fiber which transports the optical information. The clad provides an optical boundary capable of reflecting light back into the core due to a slightly lower refractive index than the core. The acrylate coating is a typical additional layer that protects the fiber from physical damage.

- Low coefficient of thermal expansion and thermal conductivity. The coefficient of thermal expansion of an OF is 1/34 of copper [22]. This low sensitivity minimizes cross sensitivity in the sensor probe. The operating temperature of a silica fiber can go up to ~ 900 °C, above which the core and the cladding material begin to migrate. Thus, an OF will not lose its integrity with body temperature monitoring, especially during hyperthermia or cryotherapy treatments. In fact, the critical issue relies on the selection of high temperature resistant layers for coating, buffering and cabling. Some recommended high temperature resistant polymers are Teflon/PTFE (230 ºC), polyimide (220 °C) and silicone rubber (200 °C) [16]. Other materials with higher melting points, such as sapphire (2040 ºC) and silicon carbide (2700 ºC), can even replace silica based OF [22];

- No electrical conductivity: An OF has excellent electrical insulation, up to approximately 1000 °C [22-24]. Thus, it is intrinsically safer to be used in animals or patients without the risk of electrical shock or explosion;
- Immunity to EM interference [23,25]: The dielectric properties offered by OF will maximize the signal-to-noise ratio and the sensitivity of any FOS system. Of particular importance is the possibility of using the OF in MRI rooms;
- Remote operation and sensing: An OF is capable of transmitting a large amount of data over long distances (several kilometers) at the speed of light without significant signal loss (typically <0.4 dB km^{-1}) [23,25];
- Small dimensions and lightweight: The OF is very thin, no thicker than a standard surgical suture [26]. A typical single mode fiber (SMF) has an outer diameter (OD) of only 125 μm. Supplementary protective layers will increase dimensions, but to no more than 500 μm OD if minimally invasive procedures are pursued. The OF is also lightweight. Silicon dioxide density (2200 kg m^{-3}) is approximately four times smaller than that of copper [22], which also facilitates miniaturization;
- Adhesion to biological tissues: An OF can easily adhere to bone by use of the US Food and Drug Administration (FDA) approved polymethyl-methacrylate (PMMA) as bonding adhesive [26]. This is of particular importance for *ex vivo* biomechanical experiments where bone strains need to be assessed;
- Geometrical versatility: An OF can bend within the host structure to radii of 10 mm [23] making it suitable to adapt to complex surfaces, such as skin, teeth, joint and bone surfaces [27];

Particularly important is that OF itself can be used as the sensor element, without the necessity of adding any other element. These intrinsic sensors are clearly a step forward into development of miniaturized and minimally invasive sensors.

An OF is only a component of FOS systems but its unique properties definitely contribute to enhance the performance of the whole system and to claim FOSs as a standard for sensing and capable of providing reliable solutions for those applications where conventional sensors are not suitable.

FOSs were introduced in the 1960s, mainly for endoscopic, intravascular and cardiac applications [28-42]. In the last years, their expansion has been benefiting from the development of telecommunications and OF communications, in particular, which are offering high quality, miniaturized and affordable optoelectronic components at competitive prices.

The most common working principles applied to FOSs for biomedical and biomechanical applications are based on intensity, phase and wavelength modulation, the latter associated with the operation of fiber Bragg gratings (FBGs).

Intensity modulated sensors were introduced in the early 1960s [29-42]. Their working principle is based on the variation of the light intensity or amplitude. Some possible configurations have been described [43]:

- An OF placed in front of a movable reflecting mirror (figure 3). The fiber guides the light to the mirror. The measurand varies the original mirror distance to the fiber tip and changes the intensity of the reflected light that is coupled by the same fiber or another fiber parallel to the first one. As will be described, initial studies made use of similar configurations. However, instead of a single OF, bundles of OF were used as waveguides due to the difficulties in light coupling [29-42,44];

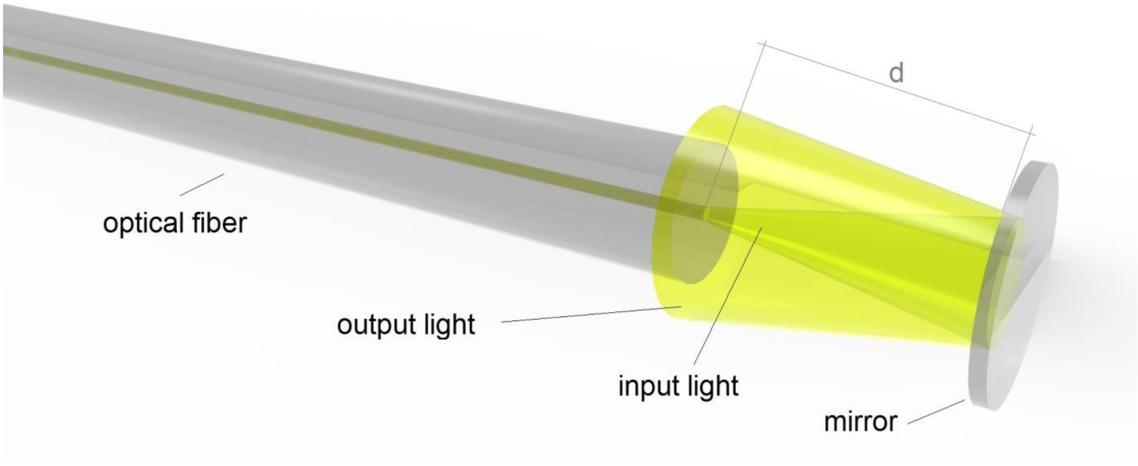

Figure 3 - Schematic drawing of an optical fiber (OF) placed in front of a movable reflecting mirror. The back-reflected intensity decreases when the distance, d, between the OF and the mirror increases.

- Two OF in front of each other at a known distance (figure 4). The measurand will change the distance between the two fibers and, consequently, the intensity transmitted. Differential configurations, with two or more fibers in front of the OF connected to the light source, can compensate changes in light source intensity or losses in the OF (figure 5);

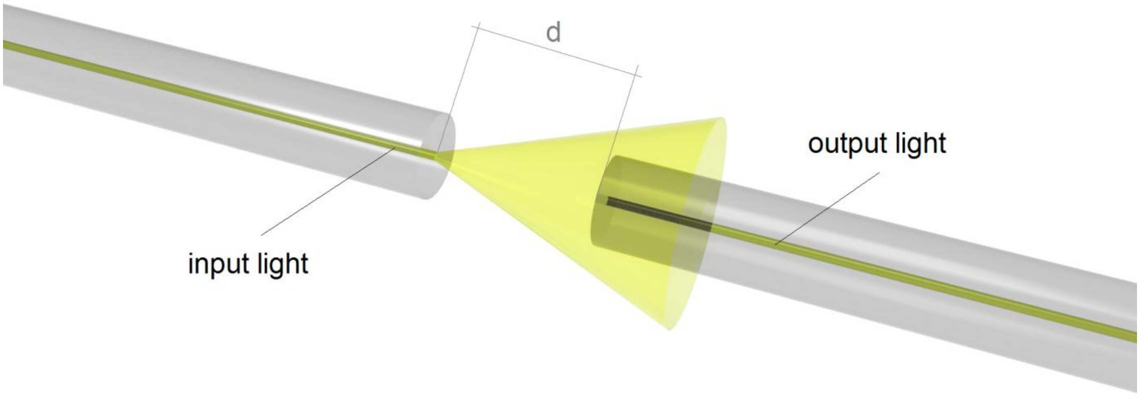

Figure 4 - Schematic drawing of two optical fibers in front of each other at a known distance (d). The intensity transmitted decreases when d increases.

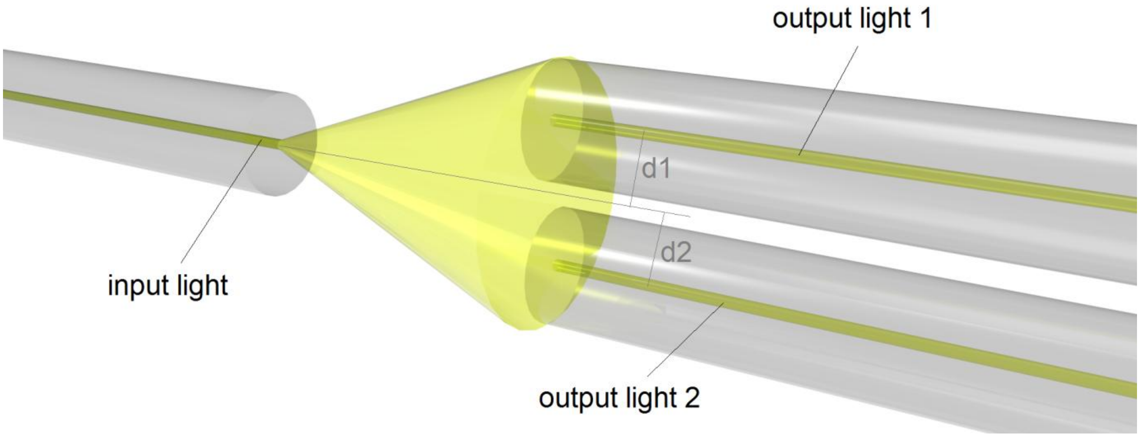

Figure 5 - Schematic drawing of a differential configuration. The input light from one optical fiber (OF) is coupled by the two OF. If the distances, d_1 and d_2, between the longitudinal axis of the input OF and the corresponding longitudinal axes of the two output OF increase the intensity transmitted decreases.

- An OF submitted to macrobending (figure 6) or microbending (figure 7). These actions will result in light loss and decrease the light intensity output [45].

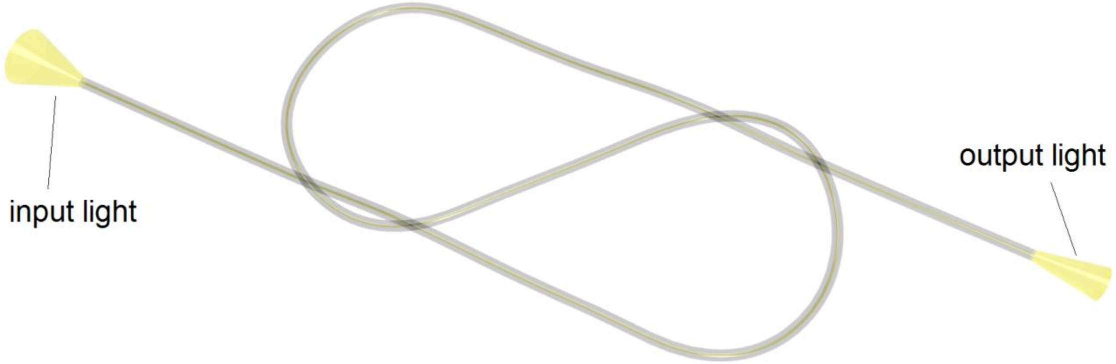

Figure 6 - Schematic drawing of a typical macrobending configuration (figure-of-eight loop). A variation of elongation applied to both fiber ends is converted into a variation of curvature radius of both loops causing the macrobending light loss effect.

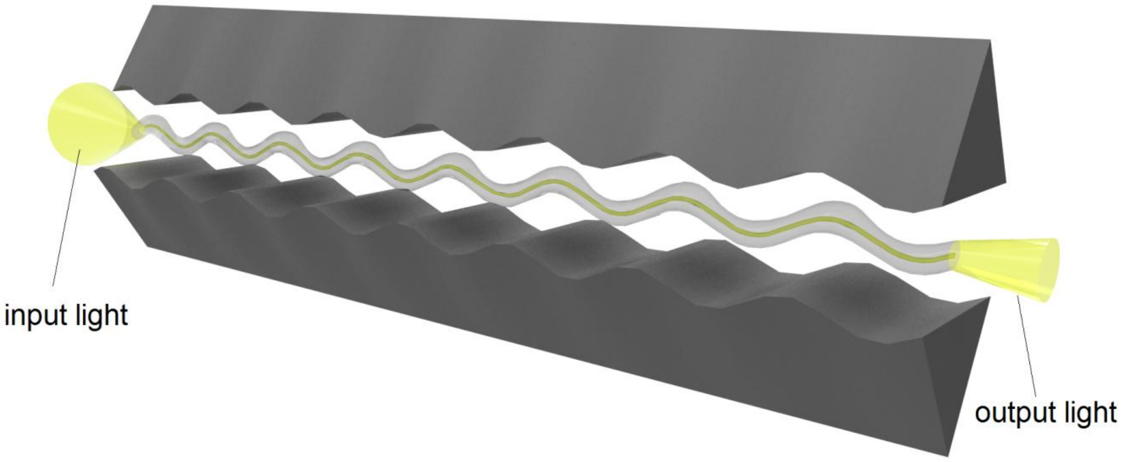

Figure 7 - Schematic drawing of a microbend configuration. The optical power leakage is a function of the microbend radio of curvature which may be induced by strain or force applied along the fiber length.

Interferometric based sensors also made several configurations possible (*e.g.*, Sagnac interferometer, Michelson interferometer, Mach-Zehnder interferometer), but the Fabry-Pérot (F-P) interferometer [46] has been the most applied in minimally invasive sensors. F-P interferometer sensors were introduced in the early 1980´s and solved many drawbacks of intensity modulated sensors. Instead of measuring a change in light intensity, these sensors aim at phase differences in the light beams. Their most common configuration includes a small-size sensing element bonded to the tip of the fiber. This element is an optical cavity formed by two parallel reflecting surfaces where multiple reflections will occur (figure 8). One of the reflecting surfaces is a diaphragm that changes the optical cavity depth (*i.e.*, the distance between the mirrors) under the action of the measurand and, consequently, the characteristics of the signal that reaches the photodetector. Compared to intensity modulated schemes and FBG sensors, F-P interferometers are capable to achieve high sensitivities and resolutions, but at the expense of relatively complex interrogation/detection techniques [47].

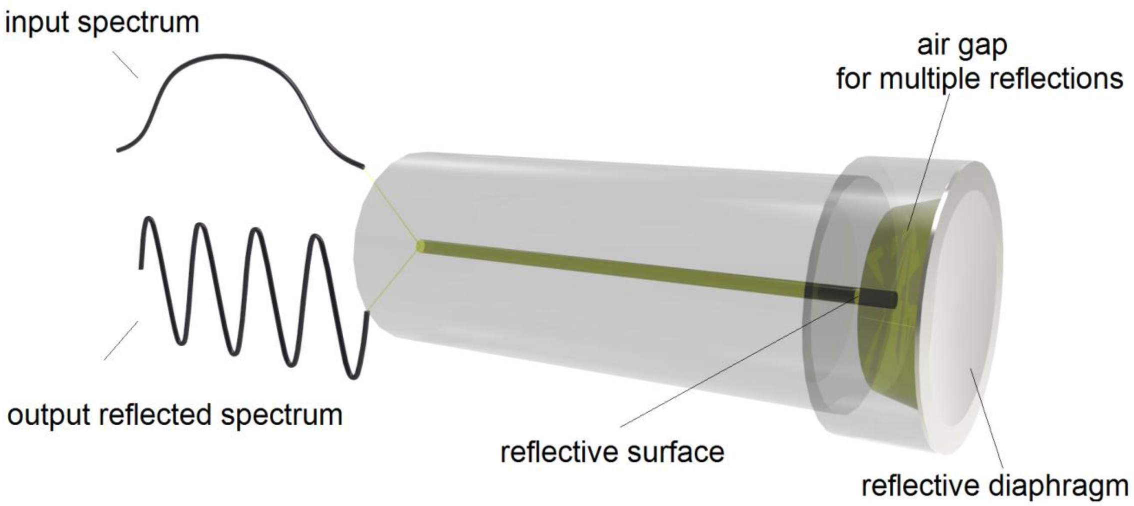

Figure 8 - Schematic drawing of a typical Fabry-Pérot (F-P) configuration that can be used for pressure measurements.

Wavelength modulation is typically achieved through use of FBG sensors which are probably the simplest and most interesting type of FOSs, particularly, for temperature and strain measurements. A Bragg grating can be defined as a periodic perturbation of the refractive index of the fiber core (figure 9). Several disruptive discoveries have to occur to make their use as sensors possible. The first one in 1978 was the discovery of photosensitivity in OF by Hill *et al.* [48-49]. In 1987 it was followed by the invention of the externally UV photowriting technique, by Meltz *et al.* [50]. In fact, it was this new transverse holographic UV photowriting technique of inscribing Bragg gratings into the core of OF with high concentration of core Ge-doping that contributed to the growth of FBG devices in the R&D telecom and sensing communities [51]. Their working principle is based on the reflection of light, at the Bragg wavelength, when the OF is illuminated by a broadband source whose center wavelength is close to the Bragg wavelength. When the fiber is stretched or compressed along its axis, the spacing between the grating lines (*i.e.* the grating period or grating pitch) will change. Because the Bragg wavelength is directly proportional to the grating period a shift in the Bragg wavelength will be observed making possible to monitor the induced strain [52]. The sensitivities for strain and temperature of a FBG recorded at 1550 nm are approximately 1.2 pm $\mu\varepsilon^{-1}$ and 13.7 pm $^{\circ}C^{-1}$, respectively [52].

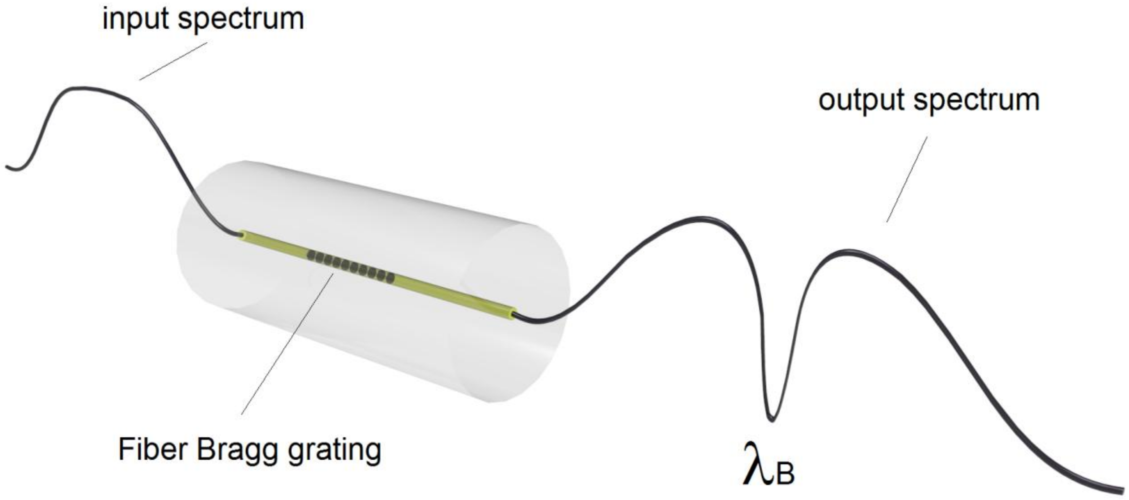

Figure 9 - Schematic drawing of a fiber Bragg grating (FBG). The grating acts as an effective optical filter. When illuminated by a broadband optical source, whose center wavelength is close to the Bragg wavelength (λB), a narrow band loss centered in the Bragg wavelength is present in the transmitted spectrum (the missing light appears in the grating reflection spectrum).

The possibility of multiplexing these structures is also revolutionizing the world of sensing. With time division multiplexing (TDM) and wavelength division multiplexing (WDM) or switching, hundreds in-line FBG sensors can be read with a single decoder unit [25,53-55]. As an example, considering strain, about 33 FBG sensors can be accommodated in a 50 nm spectrum using a Bragg wavelength spacing between 2-4 nm and taking into account each FBG is allowed an independent strain range of ±500 με and a 250 με guard band [56]. Additionally, multiplexing will also contribute to reduce the cost per sensor and of the whole system making FBG competitive with conventional sensors [57]. Compared to conventional sensors, namely the foil SG, FBG sensors are capable to provide absolute strain measurements with easier instrumentation [52]. They also offer an excellent measurand-type range and can be used as a generic sensing element to quantify other physical quantities (*e.g.*, force, acceleration, pressure, vibration, EM field, etc.) and certain chemical quantities [58-59].

Some of the ideas just presented seem to be appellative. However, FOSs remains unknown to many engineers, clinicians and researchers. Most probably, because engineering courses and research are focused on conventional sensors and nonoptical technologies. On the other hand, there is a relatively small number of turnkey solutions as well as companies and retailers commercializing these devices, which may justify their limited wide spreading. Even so, some companies are offering customer specified or plug-and-play sensing solutions specifically for biomedical and biomechanical applications (table 1).

Table 1 - Companies commercializing fiber optic sensors for biomechanical and biomedical applications.

Company	Local, Country	Website
Arrow International, Inc	Teleflex Medical, NC, USA	www.arrowintl.com
BioTechPlex	Escondido, CA, USA	www.biotechplex.com
Camino Laboratories[4]	San Diego, CA	www.integralife.com
Endosense, SA	Geneva, Switzerland	www.endosense.com
FISO Technologies, Inc.	Québec, Canada	www.fiso.com
InnerSpace Medical, Inc.	Tustin, CA, USA	www.innerspacemedical.com
InvivoSense	Trondheim, Norway;	www.invivosense.co.uk
LumaSense Technologies	Santa Clara, CA, USA	www.lumasenseinc.com
Luna Innovations	Blacksburg, VA, USA	www.lunainnovations.com
MAQUET Getinge Group	Rastatt, Germany	http://ca.maquet.com
Neoptix Inc.	Québec, Canada	www.neoptix.com
Opsens	Québec, Canada	www.opsens.com
Radi Medical Systems[5]	Uppsala, Sweden	www.radi.se
RJC Enterprises, LLC	Bothell, WA, USA	www.rjcenterprises.net
Samba Sensors[6]	Västra Frölunda, Sweden	www.sambasensors.com

Some companies will benefit from small or hand held interrogators, capable of minimizing patient discomfort during continuous day-to-day monitoring [60]. Others will require more comparative studies, particularly *in vivo* experiments and clinical trials to clearly state their potentialities. In fact, an important drawback of some FOSs is the lack of scientific information (*e.g.*, peer reviewed papers) reporting their use in clinical practice. Probably, they are being used but without the necessity of writing a paper or putting the brand name on it. The absence of detailed technical specifications (*e.g.*, pressure range, accuracy, resolution, and response time) was also detected in some published papers that report use of commercial solutions, particularly from non original equipment manufacturer (OEM) or reseller companies. Those benefiting from approvals of the American Association for Medical Instrumentation (AAMI), International Organization for Standardization (ISO), US FDA or similar regional/country organizations will probably lead the market. Cost is also a critical issue. In fact, the high cost associated to some optoelectronic (*e.g.*, integrated source and detector devices) and miniaturized solutions, developed to achieve the resolutions required for biomedical and biomechanical applications can compromise their

---

[4] acquired by FISO Technologies, Inc., a wholly owned subsidiary of Nova Metrix LLC (MA, USA).

[5] operates as a subsidiary of St. Jude Medical Systems AB

[6] FISO Technologies, Inc., a wholly owned subsidiary of Nova Metrix LLC, has acquired certain assets, including intellectual property assets, of Samba Sensors AB

acquisition. A shared problem with almost sensors is that FOSs also suffer from interference of multiple effects or cross sensitivity. A good example is that of FBG sensors, presenting dual sensitivity to strain and temperature. Nevertheless, currently used compensation techniques are capable of minimizing erroneous readings or uncertainties from non-desirable effects [61]. To enable secure readings these techniques should always be implemented instead of assuming negligible effects under apparently controlled situations.

Finally, FOSs are also competing with mature nonoptical technologies that seem capable of overcoming some of their traditional limitations. The most promising are microelectromechanical systems (MEMS) whose technology, along with examples and applications, is well described in the work of Polla *et al.* [62] and Voldman *et al.* [63]. The Neurovent microchip SG catheter (Raumedic AG, Münchberg, Germany; www.raumedic.com) is a good example of a commercially available solution offering zero drift and MRI compatibility [64-66]. Semiconductor SG, such as piezoresistive-based silicon devices, are also becoming competitive, particularly for micro-strain measurements. This powerful technology is offering linear mechanical and electrical response with negligible hysteresis and a relatively low temperature effect [67].

In the following sections, a review effort has been done to present the most relevant contributions of FOSs in biomedical and biomechanical applications. Some of the most pertinent physical parameters, such as temperature, strain, force and pressure were addressed. Other interesting chemical or physiological parameters, such as glucose, PH, gases or vapors, and deoxyribonucleic acid (DNA) were not and can be found elsewhere [60,68-75]. Our approach to FOSs has been carried out after a brief mention to conventional sensors and their limitations. Emphasis was given to description of *in vivo* experiments and clinical applications. Thus, we hope to have contributed for a better framework of FOSs, pointing their advantages and triggering new ideas for those engaged in their development and application in the biomedical and biomechanical fields.

2. Sensing Temperature

In clinical practice, patient temperature is a basic diagnostic procedure and often a critical control parameter as in hyperthermia therapy [76]. Almost all chemical processes and reactions are temperature dependent justifying temperature sensors as the largest class of commercially available FOSs. Nevertheless, they are quite few compared to the large amount of schemes that have been proposed but never reached commercialization [77].

Thermocouple and thermistor devices have been extensively used for temperature measurements in clinical practice. However, due to the presence of metallic conductors, they are inappropriate for clinical procedures involving incident radio frequency (RF), EM or microwave (MW) fields [57,78-79]. To overcome these limitations fiber optic fluorescent techniques have been proposed.

The fluoroptic technology uses fluorescent materials, such as the rare-earth phosphors or the gallium arsenide (GaAs), and an adequate light source to excite them. Temperature can be determined by measuring fluorescence emission decay times in the fluoroptic probes [80-83]. Solid state materials can also be used for fluorescence thermometry and some schemes have been presented for biomedical purposes, using the ruby [80,84] and the trivalent-chromium ion doped material [85]. An excellent review of fluorescent intensity, the first technique being proposed, and fluorescence lifetime based systems was published by Grattan and Zhang [77].

The Luxtron m3300 is a current available fluoroptic system that can be used in biomechanical and biomedical laboratory setting (LumaSense Technologies, Santa Clara, CA, USA). Its non-metallic probe has a phosphorescent sensor localized at the probe tip and is capable of providing real-time temperature measurements, ranging from 0 ºC to 120 ºC, with an accuracy of ±0.2 °C and 2 °C, respectively [86]. The probe has 0.5 mm OD and is protected with a Tefzel® ETFE fluoropolymer jacket allowing its use in MRI, RF, or MW environments and during ablation procedures [11,87]. A reported limitation of the Luxtron fluoroptic probe is its propensity to record higher temperatures than reference thermocouples sensors [88]. This was observed under localized heating at distances less than 4 mm from the laser source [88].

The T1™ Fiber Optic Temperature Sensor (Neoptix Inc., Québec, Canada) is also a commercial available FOS based on a GaAs semiconductor crystal located in the tip of the sensor. Sensor specifications include a temperature range from -272 ºC to +250 ºC, an accuracy of ±0.2 ºC, a resolution of 0.1 ºC and a response time of 500 ms [89]. The outer protective jacket is made out of PTFE Teflon™ with 1.15 mm OD. It has been used to monitor temperature during cryogenic [90] and laser ablation procedures [13,91] as well as in non-incineration methods for sterilizing hospital infectious wastes [92]. Unfortunately, fluorescent materials are relatively bulky and expensive, which rises the cost of these systems [78].

The interferometric technology was explored by Wolthuis *et al.* [78] who presented a F-P temperature sensor based on a LED-microshift method (figure 10). It consisted of a light emitting diode (LED) light source, used to interrogate changes in the optical cavity depth occurring between two reflectance peaks, and of a dichroic ratio technique used to analyze the returned signal [93]. Authors argued that the method was more sophisticated than others involving F-P sensors, such as incremental, intensity, white-light and LED-deep cavity. The optical cavity consisted of a thin layer of silicon packed between two pieces of glass. Temperature variations cause the silicon refractive index to change and, consequently, the light being reflected. Sensor performance fulfilled AAMI specifications presenting a span linearity of 1% and sensitivity of 0.1% ratio change per ºC. Temperature resolution and accuracy were 0.2 ºC (0.02 ºC with averaging) and 0.1 ºC, respectively, for a measurement range from ~15 ºC to ~55 ºC. Sensor was able to reach 90% of its final value for a temperature change from ice to boiling water in about 200 ms [78]. RJC Enterprises, LLC (Bothell, WA, USA) is commercializing this type of sensor with some possibilities of customization (*e.g.*, total assembly length and capillary pedestal length).

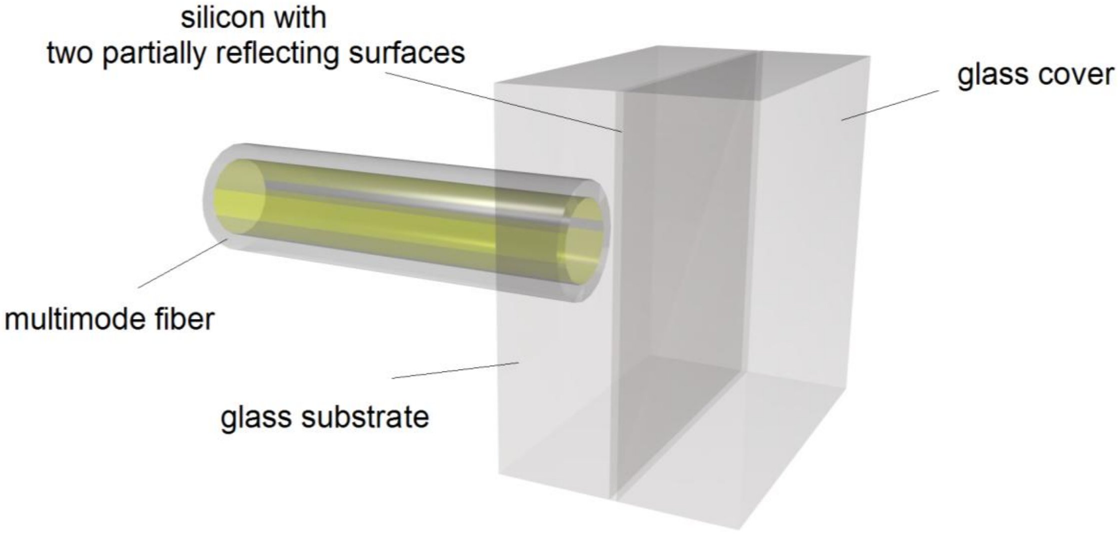

Figure 10 - Schematic drawing of the temperature sensor proposed by Wolthuis *et al.* [78].

An interferometric configuration was also applied by Rao and Jackson [94] to propose a high resolution temperature sensor (figure 11). It consisted of a miniature extrinsic fiber optic based Fizeau temperature sensor, with a cavity length of several hundred microns and a dual-wavelength pseudo-heterodyne phase detection scheme. A measurement resolution of 0.006 ºC, a 1% span linearity over a temperature range of 27.3 ºC to 62.5 ºC and a bandwidth of 30 Hz were achieved. To get temperature independent measurements, two FBG sensors located in a bimetallic beam were monitored interferometrically. Sensor performance meets or exceeds medical requirements but, to our best knowledge, it is not being marketed.

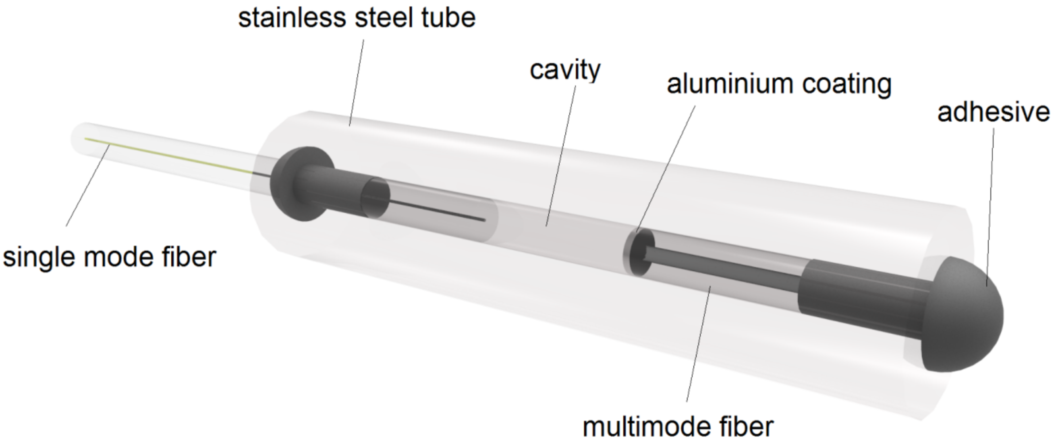

Figure 11 - Schematic drawing of the temperature sensor proposed by Rao and Jackson [94]. Stainless steel tube was made transparent to allow components visualization.

Previously mentioned sensors are point sensors, *i.e.*, they provide information only at the site they are placed, and may be insufficient for a more complete clinical assessment. Multiplexing techniques using FBG sensors can contribute to overcome this spatial constraint. First configurations for medical use were proposed by Rao *et al.* [57] and Rao [95], consisting of an array of four in-line FBG (4mm length each and 10 mm spaced) and a simple monochromator for demultiplexing the wavelength encoded signals (figure 12). Wavelength-shifts induced by temperature variations were measured using a high-resolution drift-compensated interferometric detection scheme, based on a bulk unbalanced Michelson interferometer. To minimize strain effects the probe end was sealed with a nylon sleeve of 1mm OD. A resolution of 0.1 ºC and an accuracy of ±0.2 ºC over a temperature range of 30 ºC to 60 ºC were achieved in bench tests [96].

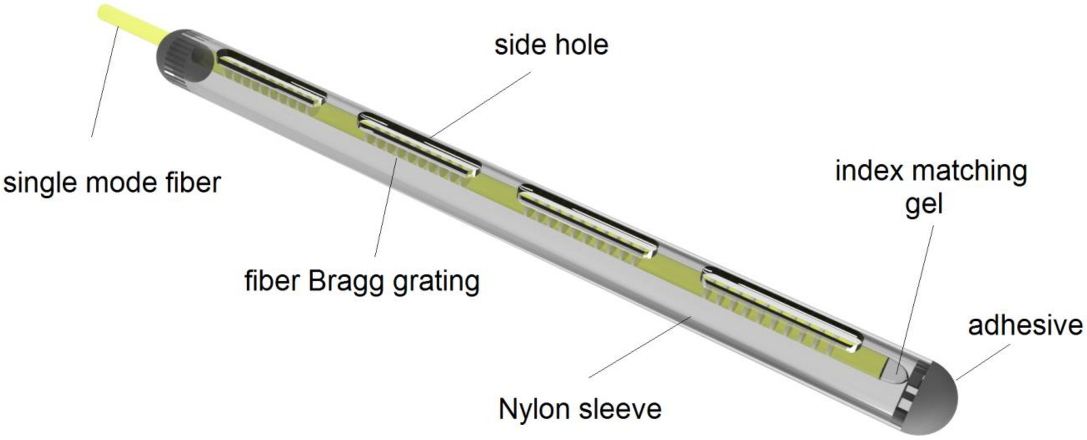

Figure 12 - Schematic drawing of the temperature sensor proposed by Rao *et al.* [57]. Nylon sleeve was made transparent to allow components visualization.

The above sensor was proposed for *in vivo* temperature monitoring during tumor therapy and *in vivo* trials occurred later using a similar configuration, that was proposed by the same research group (Applied Optics Group, The University Canterbury, Kent, United Kingdom) [15]. A portable sensing unit with five in-line FBG was used. The source was a super luminescent diode (SLD) and the detector a miniature charge-coupled device (CCD) based spectrometer. Sensor resolution was 0.2 °C. This type of sensor was used to monitor hyperthermia treatments of the kidney and liver on rabbits [15,97]. Nevertheless, it was not applied in clinical setting because a nonlinear response of some FBG sensors and an initial system calibration drift exceeding 10 °C was reported [98]. To overcome these limitations a polymer coated FBG (PFBG) probe was proposed [98]. It consisted of a 0.5 mm OD prototype with ten FBG sensors at 5 mm intervals and 50 mm length. The PFBG sensor closely followed the behavior of well-established commercial hyperthermia thermometry probes. A swept wavelength laser based readout system was capable to achieve 0.1 °C precision while maintaining a better than 0.5 °C stability over ten hours and an absolute measurement accuracy of ±0.25 °C [98]. The sensor was tested only under simulated MW hyperthermia treatment to a tissue equivalent phantom.

The potentialities of other coating materials were explored in both MRI environment and cryoablation procedures. Samset *et al.* [10] were capable of observing the dynamics of the freezing process during *in vivo* cryoablation of a porcine liver in a MRI room. Two multiplexed FBG array probes were used, one coated with polyimide (1.25 OD), the other with titanium (1.40 mm OD). Materials were considered biocompatible, sterilizable and immune to EM interference. Probes exhibited an excellent mechanical stability under cooling (-195.8 °C), hitting over a sharp edge, and bending to a radius of 20 mm at body temperature. The sensor, with ten in-line FBG, was calibrated for temperature through immersion into liquid nitrogen (-195.8 °C), ice slush (0 °C) and boiling water (100 °C). A reference platinum thermoresistance (Pt-100) was used to obtain the wavelength to temperature conversion parameters.

Temperature measurements performed during prostate cancer cryosurgery confirmed FBG sensor thermometry potentialities for clinical applications [99-100]. A commercial reusable multiplexed FBG temperature monitor system was used (TMS, MultitempTM 1601, InvivoSense, Trondheim, Norway). Ultrafine 17 gauge needles were used to guide the sensor to the target tissue and temperatures were measured in four and eight FBG sensors with 10 mm and 5 mm distance intervals, respectively. Temperatures of about -40 ºC or -60 ºC are attained during cryosurgery treatments, which are in the range (-100 ºC and +130 ºC) of these FBG multiplexed sensors.

Use of FBG sensors and spatially distributed sensing techniques (*e.g.*, modal modulation techniques) is also assuming particular relevance for non-intrusive monitoring of temperature and other clinically relevant parameters (*e.g.*, pressure, heart rate, and respiration rate). These sensors are being developed for in bed-ridden and wheelchair patients, seeming to provide more automation and safety in patient care [101-102].

FBG sensors also prove to be useful in the field of prosthesis design and testing, namely, to measure polymerization temperature profiles of cemented hip mantles [103]. Peak temperatures of 110 °C reached within 300 s and stabilized to room temperature after 3600 s were measured with a resolution of 1 $\mu\varepsilon$ and a precision of ±5 $\mu\varepsilon$.

3. Sensing Strain

At least three categories of sensors can be identified for strain measurements of body tissues. Those with variation of electrical resistance, such as the liquid metal strain gauge (LMSG) or other electrical output SG sensors. Those measuring a variation of magnetic field, such as the Hall effect strain transducer (HEST) and the differential variable reluctance transducer (DVRT), and those based on light modulation, such as FOSs.

The LMSG transducer, introduced by Whitney in 1953 [104], also known as the implanted mercury-in-silastic SG, has been extensively used to assess strain in soft tissues. The sensor is well described in the work of Ravary *et al.* [105]. It was widely applied for *ex vivo* studies of knee ligaments [104,106-111]. To the best of our knowledge, *in vivo* studies were performed with animal specimens only, namely in soft tissues [112-115] and bone [116]. The possibility of disruption of the silastic tube and release of toxic liquid, such as mercury, suggests caution for human *in vivo* procedures [105]. Mercury is also classified as a hazardous substance by the European Union Directive 2002/95/EC and shall not be used in electrical and electronic equipment. Other important limitations include a relatively small service life due to the porosity of the silastic tube, failure of wire connections [105,112], and inflammatory reactions [112,115].

Besides the LMSG a wide variety of electrical SG sensors were used to assess strain in body tissues, mainly in bone [117-124]. In fact, the SG was considered to be the gold standard for measuring deformation in bone [26]. Some of them have been used parallel to FOSs to study their correlation and will be mentioned later in this section. A large number, such as buckle transducers, have been applied to measure ligament and tendon forces and will be mentioned in the next section. For the moment, two *in vivo* studies making use of SG will be highlighted. The first one is the original study of Barnes and Pinder [117], carried out in 1974. Strain was measured in the metacarpal bone of the horse and results related to tendon action, weight bearing and locomotion. From comparison of large and small foil resistance SG sensors, valid results were possible to obtain with those covering 1 mm^2 of bone surface [117]. The second study is a human *in vivo* application. Following earlier *in vivo* studies [118,125], tibial strains were measured with micro SG (Measurements Group Inc, Raleigh, NC, USA; www.vishaypg.com/micro-measurements) [122,126]. No pre or post-surgery complications were reported, but the implantation technique seems too complicated to be applied on a routine basis. It included a 20-30 mm skin incision under local anesthesia. Moreover, one subject reported a deep sensation of pain due to drilling through the cortical bone into the bone marrow [126]. Others had to be excluded due to problems in the attachment of the transducer [126]. In fact, these evidences are sufficient enough to justify improvements in developing new minimally invasive sensors and techniques to assess *in vivo* data.

Looking to the category of magnetic field based sensors, the HEST (MicroStrain Inc., Burlington, VT, USA; www.microstrain.com) and the DVRT (MicroStrain Inc., Burlington, VT, USA) have been used to assess strain on ligaments and tendons either *ex vivo* [127-128] and *in vivo*

[129-133]. More recent than HEST, the DVRT exhibits a better performance [131]. Their implantation requires intra-articular anesthesia [130,134]. No significant patient adverse reactions due to surgical or experimental procedures have been reported [130,134]. Providing only localized measurements of strain they make it difficult to correlate strain with the total force in the ligament or tendon [135]. Theoretically, it is possible to map strain distribution in soft tissues using multiple DVRT but it requires further miniaturization [134]. Additionally, in the specific case of the DVRT and despite being classified as a miniature displacement sensor, it shall not be used in activities where the knee joint is near full extension, such as gait and jumping, due to impinging against the roof of the intercondylar notch [134].

FOSs, namely FBG sensors, seem to be in good position to substitute the above strain sensors. Compared to them, they are smaller, easier to implement, minimally invasive, with lower risk of infection, highly accurate, well correlated, inexpensive and multiplexable [57,136]. Moreover, FBG sensors have a linear response to axial strain and provide direct and absolute measurements [26,52]. Nevertheless, few applications with FBG sensors are known to assess strain in soft tissues. Ren *et al.* [137] proposed a displacement sensor based on a FBG and shape memory alloy technology to monitor cadaveric tendon and ligament strains. Recently, Roriz *et al.* [138] embedded a FBG sensor into the intervertebral disc (IVD) of a cadaveric porcine spine and measured disc bulging under axial compression (figure 13).

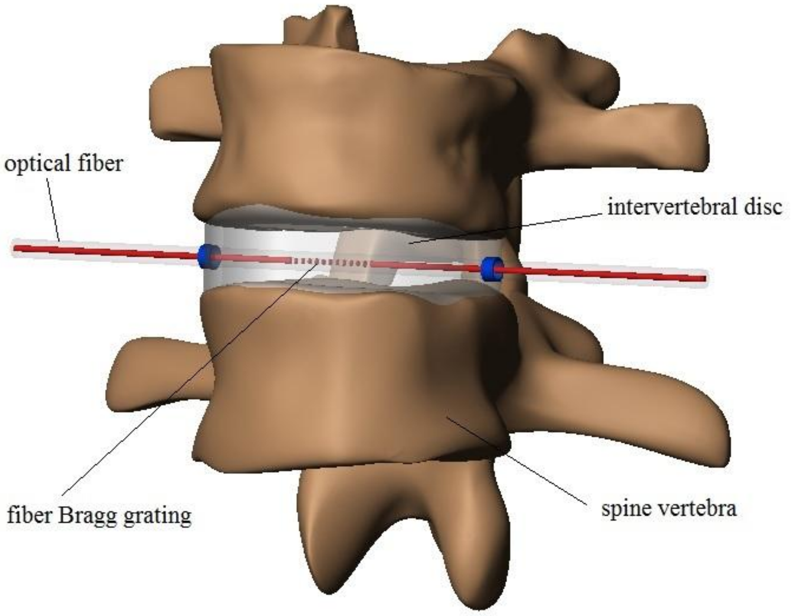

Figure 13 - Schematic representation of the fiber Bragg grating sensor used to measure intervertebral disc bulging under compression [138].

FBG sensors can also contribute to map strain along the entire tissue using multiplexing techniques. This work still has to be done, but it will ensure more reliable comparisons. In fact, conventional sensors are only capable of providing an average strain output between the ligament insertion sites or between known points within the ligament mid-substance [134]. Results from both techniques cannot be compared because strain varies along the ligament [139]. Because FBG can be multiplexed, strain can be mapped along the entire length or throughout the cross section of tendons or ligaments, giving a more complete picture of the whole structure.

While few applications for soft tissues are known, many can be found for hard tissues and materials, such as skeletal bone, cartilages and dental implants. The study of Fresvig *et al.* [26], was an important contribution to appreciate the agreement between FBG sensors and SG sensors. An acrylic and bone sample were instrumented with eight sensors each (four FBG sensors and four SG) and loaded. Both type of sensors exhibited similar behavior without significant differences. The standard deviation (SD) of the measurements varied the same for both types of sensors ranging from 1.0 to 5.2%, in the acrylic sample, and from 3.1 to 31.5% in the bone sample evidencing the effect of its anisotropy. The Pearson correlation coefficient, *r*, between the sensors was significant at the 0.01 level (two-tailed) ranging from 0.986 to 1.0 in the acrylic sample, and from 0.629 to 0.999 in the bone sample. Strain-load linearity in the acrylic was excellent for both types of sensors because the lowest linearity was 0.996 as expressed by the coefficient of determination (r^2). In the bone sample linearity was better than 0.998 for five of the eight sensors. Two SG sensors showed less linearity (r^2 = 0.75 and 0.97) and the value for the FBG sensors was r^2 = 0.98. It was argued that this lack of linearity could reflect a genuine bone nonlinearity [26].

Study of dental implants and supporting tissues is a major topic in biomechanics and clinical dentistry. Carvalho *et al.* [140] tried to understand how the mandible behaves under static and impact loads acting on dental implants. Uncoated FBG sensors and standard SG were glued directly to the surface of a human cadaveric mandible (figure 14). Besides an excellent correlation between both types of sensors, the FBG sensor was considered to be more precise in predicting load transfer from the implant to the bone [140].

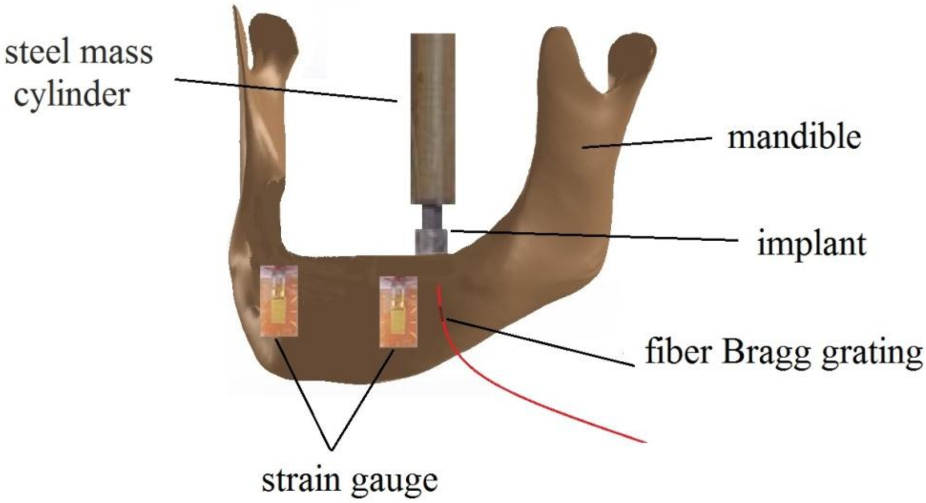

Figure 14 - Schematic representation of the FBG and SG sensors used to measure bone strain at the surface of an implanted cadaveric mandible [140].

The loading effect of several dental implant materials, such as steel alloy, acrylonitrile butadiene styrene (ABS) and a combination of both, on the stress-strain patterns of different supporting structures (bovine cancellous bone and silicone) was also studied by the same research groups [141]. A good agreement was obtained for experimental and numerical results and contributed to a better comprehension of bone physiological response to load.

A potential advantage of FOSs over conventional sensors is the possibility to embed the sensor in the material taking advantage of its small dimensions (typically 125 μm OD). Several studies have reported use of FBG sensors to monitor the curing process of dental resin cements [142-144]. To compensate temperature effects and get precise strain measurements, read-outs from two FBG sensors are usually necessary [61,137]. One of the sensors needs to be placed on a location of the specimen with zero mechanical strain in order to sense temperature only whereas the active FBG will sense both quantities. Strain can be obtained by subtracting the signal of the compensation FBG from the active one. This technique was applied to measure polymerization contraction and setting expansion of several dental materials [144-145]. The compensation FBG was placed freely inside a needle to isolate it from strain and the other was placed directly in contact with the dental material (figure 15).

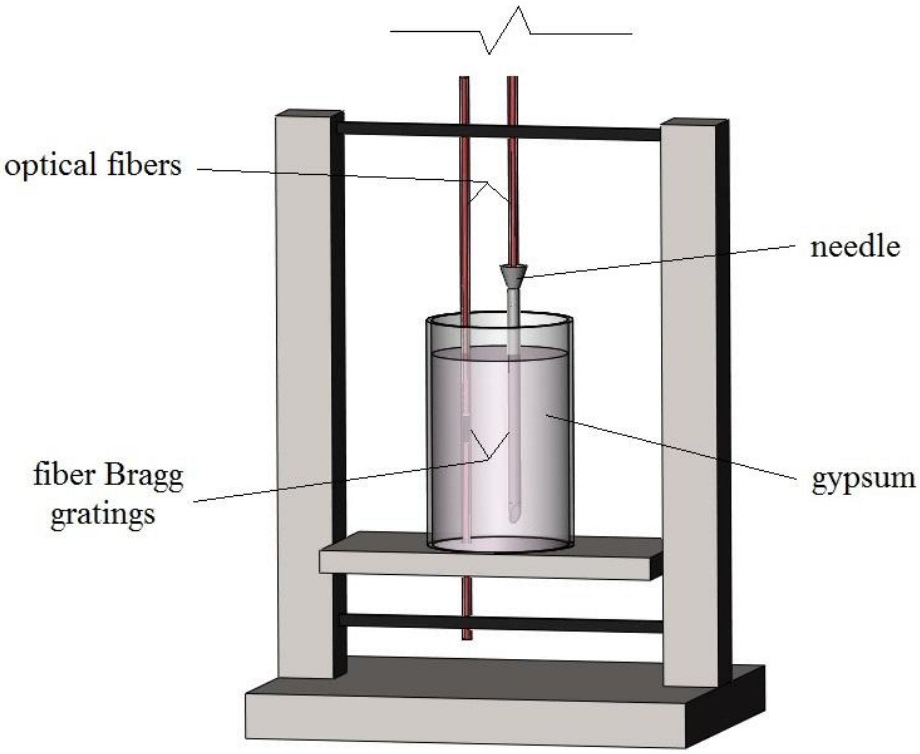

Figure 15 - Schematic representation of the setup used to measure the setting expansion and temperature variation which occurred during the setting reaction of dental gypsum. The compensation FBG was placed freely inside a needle to isolate it from strain. The other was placed directly in contact with the dental material [144-145].

Bone cements play an important role in the fixation of implants or prostheses and their long-term stability is a critical issue in joint biomechanics. *In vitro* strain and temperature characterization of PMMA based bone cements of femoral prostheses was studied by Frias *et al.* [146] at different temperatures and load conditions, namely, those expected to occur inside the human body during locomotion. FBG sensors prove to be an interesting *in situ* measuring tool for characterization of these biomaterials. A similar study has contributed to confirm that FBG sensors are easier to implement and are less time consuming than standard SG, making them suitable for use in pre-clinical tests of prostheses and implants [103].

A large number of implants and prostheses are metallic or incorporate metallic components, such as iron (Fe), titanium (Ti), cobalt (Co), chromium (Cr), molybdenum (Mo) or their alloys. As non-conductive devices, FBG sensors can offer new possibilities of measurement because it is technically complex to use SG in conductive metals. In the original work of Talaia *et al.* [147] seven FBG sensors were glued to stainless steel bone plates making it possible to study the effect of these fracture fixation plates in synthetic femurs (figure 16).

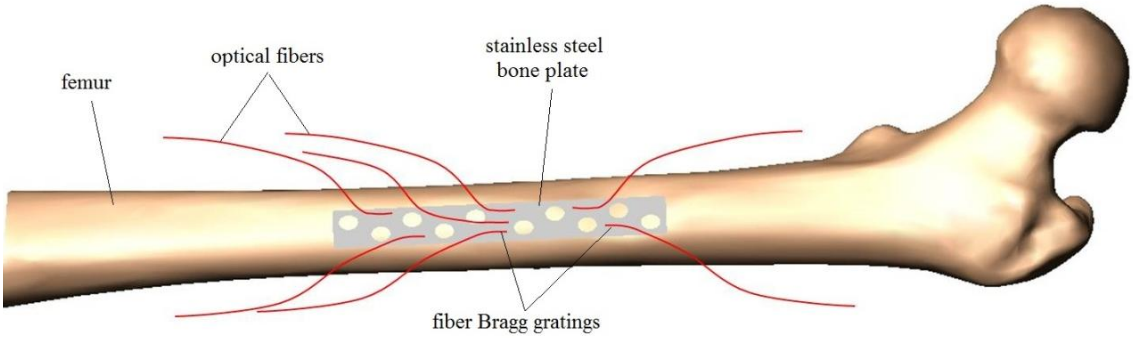

Figure 16 - Schematic drawing of fiber Bragg gratings glued to a stainless steel bone plate

Fractures may be caused by traumatic injuries or metabolic diseases, such as osteoporosis. This silent disease is the most common type of bone illness affecting two hundred million individuals worldwide [148]. FBG sensors can contribute to classify the stage of bone decalcification. First steps were taken in the *in vitro* experiment of Mishra *et al.* [149]. The strain response of bone under loading at a particular site gave a direct indication of the degree of calcium present in the bone. Further studies are needed to characterize the global response of bone and to apply the technique *in vivo*.

Other interesting studies made use of FBG sensors to quantify the ventilatory movements of the chest. Wehrle *et al.* [24] used a fixed optical filter reference scheme with full width at half maximum (FWHM) of 1.5 nm to detect respiratory movements with frequencies up to 10 Hz. Besides FBG sensors, intensity modulated schemes were also applied to monitor the respiratory and cardiac function. That was the case of the fiber optic plethysmography (FOP) technique. Based on macrobending losses it consists of an expandable belt encircling the chest and a fiber optic loop that changes its radius of curvature as a function of the chest perimeter [150-153]. Other FOP configurations may include long period gratings (LPG) arrays, which are more sensitive to bending [154-155]. Ensuring that LPG high sensitivity to the ambient refractive index is compensated, namely using multilayered fibers embedded into a flexible platform, the technique can be applied to obtain a three dimensional geometric profile of the chest and abdomen during respiratory movements [155].

Of particular interest is the possibility of embedding FOSs into technical textiles to create smart wearable clothes and monitor some vital functions such as the respiratory rate (figure 17) [156]. A €2.3million European Project (*Optical Fiber Sensors Embedded into Technical Textile for Healthcare* - OFSETH) gave the first contributions in this promising field [157]. Commercial available products are still to apply.

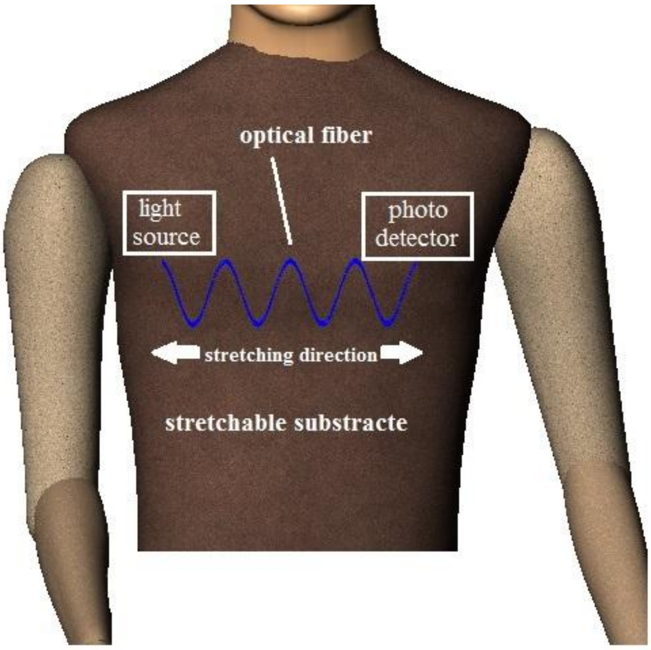

Figure 17 - Schematic drawing of macrobending sensor in optical fiber embedded into textile fabrics for the monitoring of respiratory movements [156].

FBG sensors were also embedded into MRI compatible needles to study their deflection [158]. Assuring temperature compensation, these preliminary investigations can contribute to improve MRI-guided percutaneous needle biopsy and brachytherapy procedures. The applications described to measure the heartbeat sound [159] and blood pressure [160] from non-invasive strain measurements are also interesting examples of the FBG technology versatility.

Finally, we would like to highlight a recent application in sports and clinical biomechanics. Traumatic head and dental injuries can be avoided trough the use of protective devices, such as helmets and mouthguards. Mouthguards are particularly useful for athletes because they reduce the risk of injury caused by impacts resulting from many sports activities (*e.g.*, boxing). Studying their absorption capability like in the experiment of Tiwari *et al.* [161] can contribute for new designs and material improvements. In this study, pairs of FBG sensors were bonded parallel on the mouthguard and jaw model. The mouthguard was submitted to several impact loads and the corresponding absorbed impact energy was calculated by subtracting the strain in the mouthguard from that of the jaw. Results encourage use of mouthguards as effective protective devices.

4. Sensing Force

The study of ligament or tendon/muscle forces is a main topic in medicine and sports. Ligaments connect bone to bone. They resist stretch (tension) to assure the stability and congruency of a joint or a group of joints. Ligaments act like joint controllers of the range of motion (ROM). Tendons connect muscle to bone transferring to them the force generated during muscle contraction. Thus, studying the forces acting in these soft tissues will contribute to understand some of their main functions. Usually, *in situ* forces are measured with SG based transducers. They can be inserted in the ends of insertion sites or within the mid-substance. Most of them have been designed to measure strain as the result of a compressive action on the ligament or tendon when it is stretched. Therefore, to obtain force, strain has to be converted, meaning that the calibration protocol requires special attention. There is no single or universal calibration protocol for this type of studies. Those applied before implantation of the transducer should be avoided because re-implantation leads to different results [162]. Those applied after the experiment are restricted to animal experiments because they have to be sacrificed [163]. There is general agreement on the fact that calibration has to be made after implantation and the sensor must not be removed from the site where it was calibrated [134,164-165]. In addition, results comparison is possible only between similar implantation sites because it has been demonstrated the force varies along the tendon or ligament [134]. Even so, it should be taken into account that there is considerable variability between specimens making it difficult to compare results [166]. The calibration procedure also depends on the specific characteristics of the study. In fact, only this justifies a wide variety of technical resources that are being applied such as mechanical loading machines, analytical equations from cadavers, ergometer devices, equilibrium conditions from mechanics and use of pre-calibrated transducers [163-164,167-170].

Looking to conventional sensors used to measure ligament or tendon forces, the buckle transducer, introduced in 1969 by Salmons [171], has been the most used. The frame (*i.e.*, buckle) where the SG is attached may present several different forms, such as a rectangular or oval form [117,164,172-177], a C-form [178-179], an E-form [180-182], an I-form [166,183], or an S-form [184]. Some of the previous frames and the corresponding working principles were described in the paper of Ravary *et al.* [105]. Despite wide spreading, these transducers have large dimensions compromising minimally invasive procedures. As an example, the size (length x width) of the implantable E-form buckle transducer for animal studies is about 9×5 mm [180] and about 34×20 mm for human studies [105]. Hence, far from being minimally invasive their use is typically restricted to large tissues, such as the Achilles tendon, the anterior cruciate ligament or the patellar tendon [105,134]. Long recovery times (two to three weeks) seem to be necessary for complete healing of the implantation wound [175,177,182,185]. They can also modify the natural biomechanical behavior of the tissue because the frame usually diminishes its length [135]. *In vivo* studies require surgery under local intra-articular anesthesia [164]. Their sensitivity can vary with joint angle, sensor placement and orientation [134,174].

Besides buckle transducers, two other types of SG based transducers can be used to sense force in ligaments and tendons, namely the implantable force transducer (IFT) [127,162,167,169-170,186-192] and the modified pressure transducer (MPT) [163,165]. The IFT was introduced in 1992 by Xu *et al.* [187]. Some IFT configurations (*e.g.*, two point, three point) and the corresponding working principles were described in the paper of Ravary *et al.* [105]. The IFT is smaller than buckle transducers but the MPT is the smallest. Typical dimensions of the MPT are 3.5-4 mm OD and 0.5-1.5 mm thick [105]. Even so, all of them are much larger than FOSs. Like buckle transducers IFT sensitivity may vary with joint angle, sensor placement and orientation [165,167,169,187]. Depending on the calibration protocol results can vary significantly [167]. More repeatable results can be obtained using the *in situ* calibration method proposed by Herzog *et al.* [167]. Another important constraint is a nonlinear relationship between the compressive load acting on the sensor and the tensile load applied to the tissue [162,165,169,188].

The first contribution of FOSs in measuring the force of ligaments and tendons was an attempt to reduce the errors associated to the large geometry of conventional sensors and to minimize subject’s complaints. This was pursued in the *ex vivo* experiment of Komi *et al.* [185] through the use of an intensity modulated sensor. A guiding needle was used to insert the OF (Toray Industries Inc., PG-series, 265μm or 500μm OD) in the rabbit common calcaneal tendon mid-substance. It was expected that the tensile load applied to the tendon would produce a compressive load on tendon fibers and bend the OF. The fiber was illuminated by an infrared LED with central wavelength at 820 nm and the detector was an integrated IC photodiode. Strain to force calibration was done using the moment equilibrium condition of a rigid body. Under static conditions a good linear fit (r = 0.999) was registered between the sensor output and the applied loads. Hysteresis was considered negligible. Under dynamic loading conditions (using load drops) the OF followed the response of a reference SG transducer, despite a time delay of 6.5 + 2.6 ms that was measured for the OF response [185].

In vivo studies followed that of Komi *et al.* [185]. The first, was probably that of Finni *et al.* [193] who used the same optical system, with telemetry incorporated, to measure the Achilles tendon force during locomotion. Instead of intra-articular anesthesia, an anesthetic cream was applied to the skin surrounding the tendon. Sensor calibration was made in situ, after implantation (figure 18), using an ankle ergometer to perform isometric plantar flexions (from 10 to 40% of maximum voluntary muscle contraction) [185]. Similar intensity modulated FOSs were used to carry out more *in vivo* experiments, namely to study the individual muscle contributions to the Achilles tendon force [168], leg muscles contributions to perform standardized jumps [194], muscle behavior during jump skills [195], the interaction between the lower leg muscles and the Achilles tendon in walking [196] and the influence of tendon’s creep in sensor behavior [197].

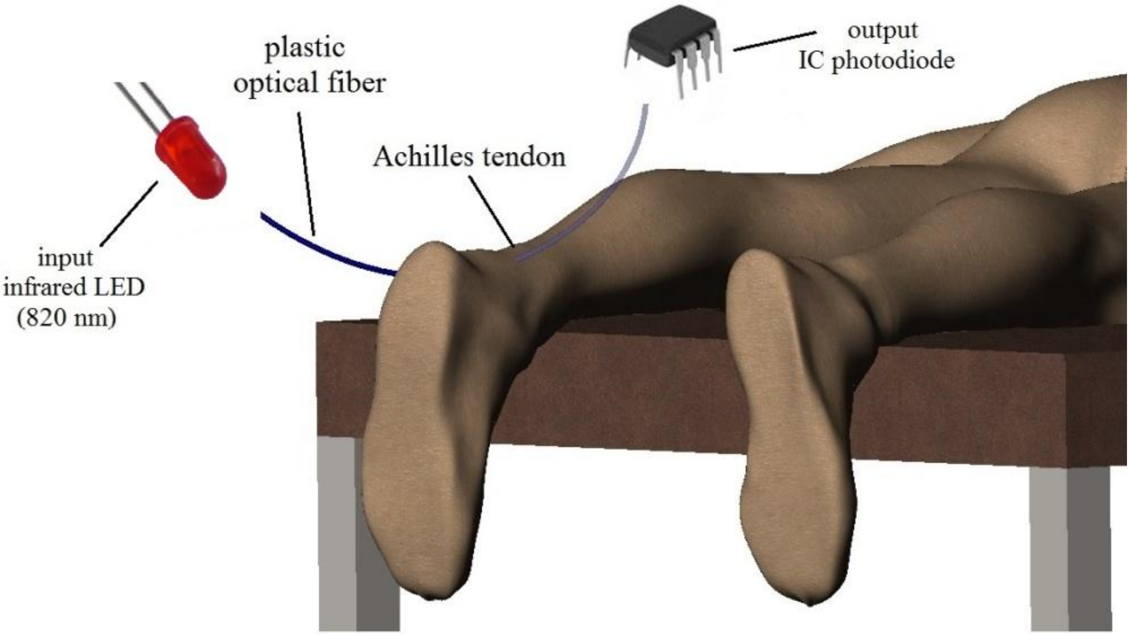

Figure 18 - Schematic representation of the intensity modulated force sensor proposed by Komi *et al.*, [185] to be implanted into the human Achilles tendon [168,193,196].

The validity of previous studies can be questioned in the absence of efforts to identify possible sources of error in estimating tendon forces. In fact and contradicting the original findings of Komi *et al.* [185] a nonlinear relationship was observed between the OF output and the tendon force, requiring use of 3rd order polynomials for adequate curve fitting [136]. Hysteresis, cable migration, loading rate, joint angle and skin movement were also pointed as possible sources of error in force prediction. Root-mean-square (RMS) errors due to hysteresis were estimated to be less than 5% of maximum load [136]. RMS errors due to migration of the OF were less than 27% [136]. Differences in the loading rate led to RMS errors less than 17% [198]. RMS errors due to the combined effects of loading rate and cable migration were less than 32% [198]. Compared to the C-form transducer the FOS previously described by Komi *et al.* [185] seems to exhibit lower errors in force prediction but larger errors in hysteresis and loading rate [136,191]. Tendon creep [197] and skin movement artifacts [198] can also affect the output of the optical signal. In particular, *ex vivo* experiments should be conducted without skin, because RMS errors in estimating tendon force decreased from 24-81% of maximum force to 10-33% after skin removal [198]. Finally, the applied calibration procedures required assumptions concerning the location of joint axes and the length of moment arms, another possible source of error [134]. Trying to diminish these sources of error is, in fact, a challenge because soft tissues are complex structures with nonlinear, visco or poroelastic properties requiring the most accurate sensors and techniques to get precise measurements.

FBG sensors could represent a step forward in the way of sensing these soft tissue forces. We have found three *ex vivo* studies using them, meaning there is much to be done [199-201]. In the study of Vilimek [199] the force of porcine leg tendons was successfully estimated under loads applied by a tensile machine. It has been argued that FBG measurements are more accurate than those obtained with intensity modulated sensors. Even so, accurate measurements will require a technique capable of avoiding migration of the OF and give the exact location of the grating within the tendon. FBG sensors were also used in the original study of Goh *et al.* [200] with the purpose of measuring the axial load within the menisci of porcine knee joints. A transverse load was applied and to relate it better with the measured axial load, the FBG sensor was placed between uneven layers of carbon-epoxy composites using a buckle configuration [56,200]. A tunable laser source (TLS) and an optical spectrum analyzer (OSA) were used. Calibration was accomplished with a mechanical testing machine and suggested a wavelength/load linear relationship. However, the overall dimensions of the probe (5×5 mm) compromise its use as a minimally invasive device [200]. A novel sensor was also proposed by Behrmann *et al.* [201] for tendon force measurements. The sensor incorporates FBG and microfabricated stainless steel housings that were used to convert radial forces applied to the housing into axial forces that could be sensed by the FBG. The housings were fabricated by several methods including laser micromachining, swaging, and hydroforming. Several designs allowing simultaneous temperature and force measurements and simultaneous resolution of multi-axis forces were presented. *In vitro* experiments were performed with success in excised tendon and in a dynamic gait simulator [201].

Dental biomechanics seems to be a promising field for FOSs. One of the first applications was a mouthpiece system capable of measuring the biting forces [202]. The mouthpiece, made of two stainless steel plates, had a microbending sensor placed between them. The sensor was able to measure forces ranging from 0 to 1000 N with a resolution of 10 N [202]. Force magnitude was also quantified in dental splints, which are orthodontic devices designed to address dental problems such as loose teeth and bruxism in addition to problems with snoring and apnea. In the original study of Tjin *et al.* [203] FBG sensors were applied to measure strain and temperature during positioning of a splint within the mouth and after its placement. The strain sensor was calibrated to measure force using a previously described protocol [56]. Temperature effects were compensated and the accuracy for force and temperature measurement was 0.5 N and 0.1 ºC, respectively [56,203]. More applications in dentistry biomechanics include use of high-birefringence (HiBi) FBG sensors to measure *in vitro* orthodontic forces [204], and use of bracket polymer photonic crystal fibers (PCF) sensors to measure the forces applied in the tooth during realistic orthodontic treatments [205-206].

Specific applications for sports and robotic surgery have been also proposed, such as in the case of handgrip devices that were used to measure strength and to evaluate fitness condition. An alternative to conventional dynamometric devices was presented by Paul *et al.* [207], incorporating the advantage of assessing individual finger participation in force production. Five FBG sensors were sandwiched between rubber bushings in a cylindrical grip holder. Wavelength shifts were related to the pressure applied by fingers onto the rubber bushing [207].

Park *et al.* [208] took first steps in the creation of force sensing robot fingers to be used in the presence of large magnetic fields. Fingers were made of urethane polymer with embedded FBG sensors and a copper mesh has been applied to reduce creep and provide thermal shielding. Controlled grasp force during manipulation tasks of small weights (0.1 kgf) was possible to obtain.

Efforts are being made to develop sensors capable of providing force feedback during robotic assisted minimally invasive surgeries and catheter based operations, such as cardiac catheterization and ablation procedures. Intensity modulated sensors [209-210] and FBG sensors have already been proposed [211-214]. A good example of a novel application of light intensity-modulated sensors supported by reflective membranes is the RF ablation catheter with force feedback, presented by Polygerinos *et al.* [209-210]. Three plastic OFs were aligned inside a plastic catheter in a circular pattern to provide a three axes force sensing system (figure 19). The sensor was tested in an artificial blood artery showing a working range of 0 to 1.1 N, a resolution of 0.04 N and good dynamic response.

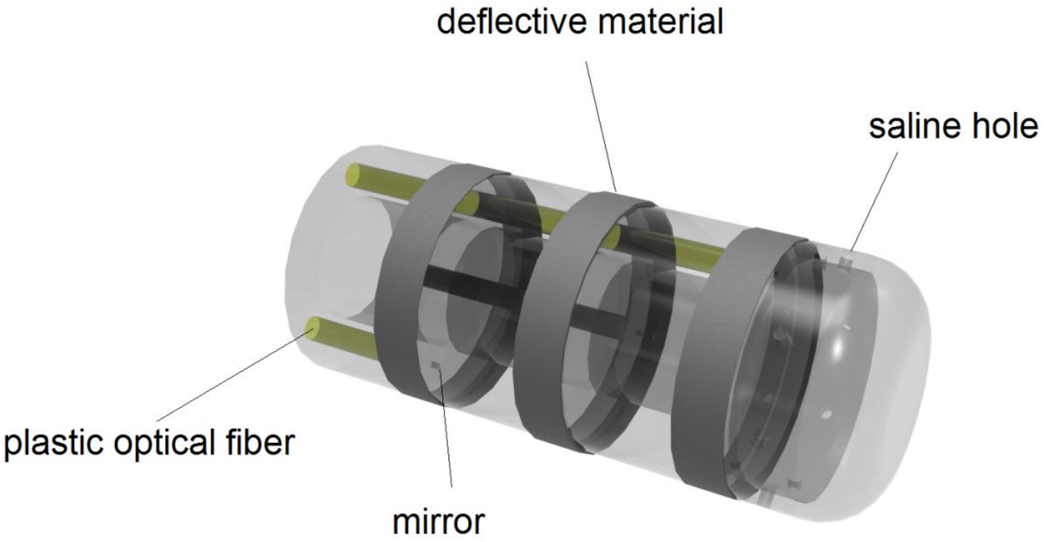

Figure 19 - Schematic drawing of the force sensor proposed by Polygerinos *et al.* [209-210].

TactiCathTM is a commercially available solution from Endosense SA (Geneva, Switzerland). This sensor is one of few sensors that have been submitted to prospective, randomized, multi-center interventional studies [214]. It is composed of three FBG capable of measuring strain of the catheter tip (3.5 mm OD) in contact with tissue [211,215-216]. Contact forces along three different directions can be measured with a 10 Hz frequency and a resolution better than 0.001 kgf. Monitoring these forces during catheter based ablation procedures is an important task because it was demonstrated that the incidence of lesions increases with the catheter force applied to the tissue [211,215-216]. This is of particular importance in robotic surgery because it contributes to minimize the lack of haptic feeling from the surgeon [212,217]. Also for surgery procedures requiring extremely subtle maneuvers and forces, usually lower than human perception [213].

Some advanced clinical procedures requiring MRI environment will benefit from the immunity of FOS systems to MW interference. As in the case of brain function, studied trough functional MRI (fMRI), FOSs can be implemented to assess other related functions such as the motor function [218-220]. Additionally, the possibility of combining haptic sensing and optical trackers, developed to trace curves of pertinent anatomical structures [221], seems a promising field in medicine.

5. Sensing Pressure

Following some original works in the first half of the last century [222-225], it was in the 1960s that interstitial fluid pressure monitoring became a relevant procedure in biomedical and biomechanical applications [32,39,226-229]. In the early 1970s Millar Instruments Inc. (Houston, TX, USA; www.millarinstruments.com) made significant efforts to develop miniaturized piezoresistive pressure sensors and to integrate them into catheters for clinical practice [230]. These are currently known as the Millar Mikro-Tip® pressure transducer catheters. Their accuracy is ~0.2% but they are also fragile, expensive and affected by EM interference [78,231].

Fluid-filled catheters attached to external pressure transducers can be used as an alternative to the previous solid-state sensors [78,224,232]. Early configurations, such as a simple needle connected to a mercury pressure manometer [225], gave place to more advanced configurations, such as the wick catheter [229,233], the slit catheter [234] or the side-ported needle [235]. Nevertheless, besides low-cost, their performance seems to be lower than that of Millar catheters. According to the review of Kaufman *et al.* [236] the accuracy of fluid-filled systems ranges between 1% and 18% and their linearity between 2% and 15%. They also suffer from hydrostatic artifacts caused by body movements, limiting their use to static positions or movements in the horizontal plane [232,237]. Furthermore, they require flushing or infusion to maintain accuracy, particularly during long-term measurements (*i.e.*, more than one hour) [238]. Meanwhile, other fluid-filled catheter-transducers, such as the Spiegelberg intracranial pressure monitoring system (Spiegelberg KG, Hamburg, Germany; www.spiegelberg.de) and the AirPulse™ Air Management System (InnerSpace, Tustin, CA), have been developed to overcome the previous problems [239].

FOSs are intrinsically free from hydrostatic artifacts and flushing, making them attractive for interstitial fluid pressure measurements. Intensity modulated schemes were initially proposed, namely for *in vivo* blood pressure measurement, such as in the original work of Lekholm and Lindström [40,44] and other similar configurations [39,240-241]. The previous work was also the basis for development of Camino pressure sensors (Camino Laboratories, San Diego, CA, USA; acquired by Integra LifeSciences; Plainsboro, NJ, USA), probably the most widespread dual-beam referencing intensity-modulated based sensors [242]. Camino sensors became popular in the 1980s, and since that time they have been extensively used for pressure measurement in different sites of the body, as in the brain, muscles and joints. In 1996, Keck reported that the company was producing around 60000 devices/year [51]. These sensors also underwent extensive scrutiny leading to identification of several drawbacks and questioning their routine use, particularly in clinical practice [64,243-255].

To overcome some of the drawbacks of intensity modulated sensors alternative configurations have been presented. In the early 1980s, F-P interferometer based sensors were introduced. An earlier configuration of a F-P sensor was presented in 1983 by Cox and Jones [256], but large size and complex signal analysis limited further applications [78]. MetriCor Inc. (acquired by

Photonetics, Inc.; at present part of GN Nettest, Copenhagen, Denmark; www.gnnettest.com) developed a compact version, based on anodic bonding of a silicon membrane to the fiber tip and use of two wavelengths to monitor the interferometer [51,257]. The same technology was adapted by Sira, Ltd. (Kent, UK; www.siraeo.co.uk) to measure temperature and the refractive index [51]. Innovation also came from miniaturized forms, namely those using all-fused-silica designs and clean room microfabrication techniques [78,236,258].

Recently, FBG sensors have also been proposed to assess pressure, namely in the nucleus pulposus (NP) of the IVD of the spine [19-20,59,259]. However, these apply only to *ex vivo* experiments. Thus, innovative solutions are mandatory for *in vivo* and clinical studies, namely to be integrated into specific diagnostic procedures of the spine (*e.g.*, discometry) and surgical procedures (*e.g.*, arthrodesis and arthroplasty).

Considering the wide variety of pressure FOSs and their applications, a better framework can be obtained by looking at the specific pressure applications that have been developed. We expect to contribute to them in the following subsections.

5.1 Intravascular and Intracardiac Pressure

Among several experiments that started in the mid 1960s [32,39-40,44] the original work of Lekholm *et al.* [40] and Lindström [44] deserves to be highlighted. A sensor intended for *in vivo* blood pressure measurement with sensor heads of only 0.85 mm (unshielded) and 1.5 mm OD was proposed (figure 20). It consisted of an air-filled chamber covered by a 6 μm pressure sensitive beryllium-copper membrane. As in similar works of that period [29,39], the guiding system was made of two independent OF bundles due to problems in light coupling. One bundle was used to guide the light from a gallium-arsenide LED source to the sensor head, the other to guide the reflected light into a photodetector [44]. First fabricated probes had a flat frequency response from static pressure to about 200 Hz [40], but it increased to 15 kHz in the following experiments [44]. Zero drift was observed under temperature variation from 20 °C to 37 °C, recovering the baseline after ~40s [44]. The above sensor was also extensively described, covering the theoretical topics of fiber optics properties, membrane reflection, operation modes, number of fibers and their distribution, membrane mechanics, volume displacement, frequency dependence and limitations [44]. Error sources, sensitivity and miniaturization, failure and redundancy were also addressed [44]. Another interesting feature of the sensor was its low sensitivity to mechanical vibrations, shocks, and movements due to a light and stiff membrane. After successful tests on one dog and one human [40], clinical tests have followed [44].

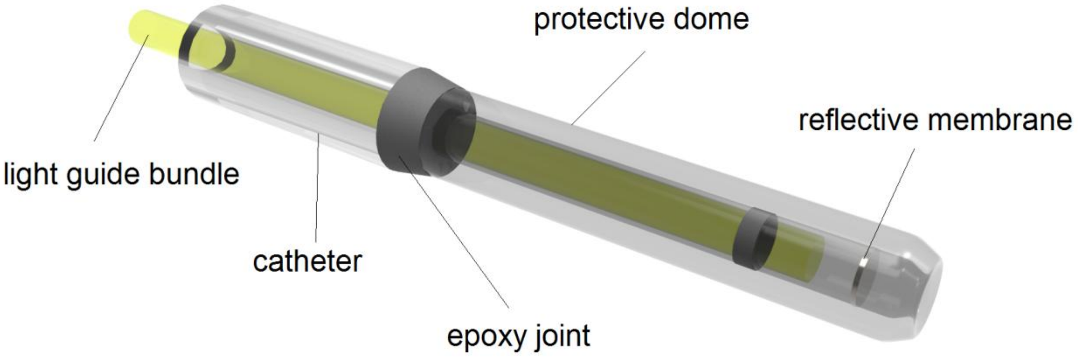

Figure 20 - Schematic drawing of the pressure sensor proposed by Lekholm and Lindströn [40] and Lindströn [44].

In the following years, similar sensors with vibrating membranes located at the tip [39,240-241] or at the side of a catheter have been proposed [260-261]. Side membranes contribute to reduce pressure artifacts due to tip collisions with the blood vessels or the ventricular walls (the so-called wall or piston effect) [210,261-262] and to avoid clot formation occurring for long periods of monitoring [260-261]. An earlier application of a pressure sensor incorporating a side membrane was proposed by Matsumoto *et al.* [261] (figure 21). Nevertheless, tip and side-hole configurations have been adopted up to today. In fact, the most important achievement in the following years was implementation of microfabrication techniques [263-267].

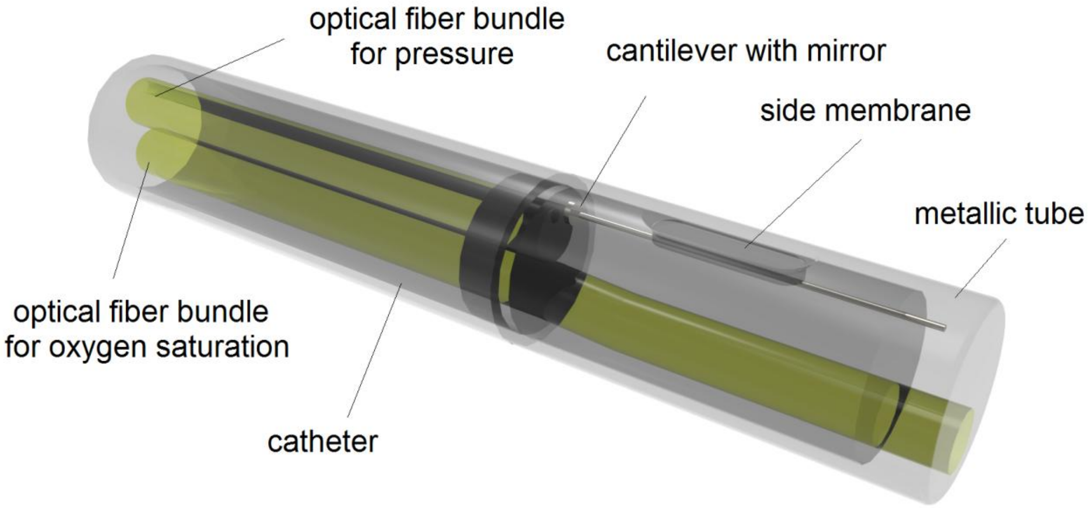

Figure 21 - Schematic drawing of the pressure and oxygen saturation sensor proposed by Matsumoto *et al.* [261]. A side membrane was used to sense pressure and a tip configuration for measurement of oxygen saturation.

The configuration proposed by Lekholm *et al.* [40] and Lindström [44] was also the basis for the development of Camino pressure sensors (San Diego, CA, USA). This transducer-tipped catheter consisted of a 1.35 mm OD tip enclosed in a saline-filled sheath (2.1 mm OD) with side holes (figure 22). A pressure sensitive diaphragm caused the mirror distance from the fiber tip to vary, changing the intensity of the reflected light. As will be seen, identical designs were also applied to measure intramuscular [232], intraarticular [268-271] and intracranial pressures [272]. These transducers are interrogated by the intensity modulation technique with dual-beam referencing, recommended for single use and should not be resterilized or reused [242]. They are also relatively large (1.35 mm OD) and require special handling because of potential for fiber breakage [243,245].

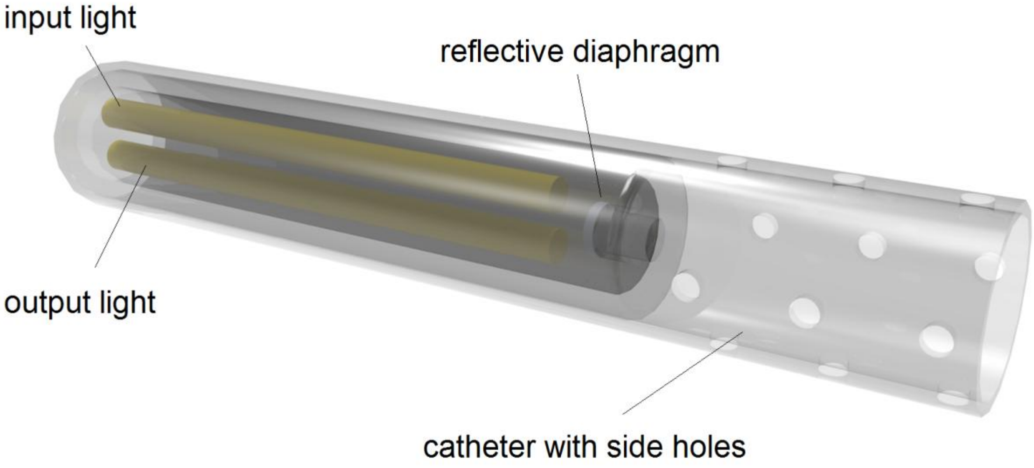

Figure 22 - Schematic drawing of earlier Camino sensors [232].

Several alternative configurations to the above sensors were presented, namely those based on the photo-elastic effect [273]. It was, however, the introduction of F-P sensors that made it possible to incorporate important features [256]. The LED-microshift sensor proposed by Saaski *et al.* [93] and Wolthuis *et al.* [78] is a good example (figure 23). It consisted of a glass cube (300×300×275 μm) containing a thin F-P cavity (1.4-1.7 μm depth; 200 μm OD) covered by a pressure sensitive single crystal silicon diaphragm anodically bonded to the glass cube. A LED, with emission bandwidth of ~60 nm, was used to interrogate the cavity operating within a single reflectance cycle. A dichroic ratio technique was applied to analyze the reflected light. A linear pressure working range from ~250 to ~1250 mmHg was achieved. Sensor's resolution (1 mmHg) and accuracy (±1 mmHg) fulfilled AAMI medical standards. It was validated using a Millar micro-tip catheter and proposed for absolute pressure measurements of the left heart chamber and systemic arterial pressures. The system was also low cost and easy to fabricate [78]. Wolthuis *et al.* [274] also have proposed a dual function sensor system for simultaneous measurement of pressure and temperature. RJC Enterprises, LLC (Bothell, WA, USA) is commercializing these type of sensors, namely for resellers. For example, the pressure sensor has been integrated in the intra-aortic balloon (IAB) catheter of Arrow International, Inc. (Teleflex Medical, Research Triangle Park, NC, USA) [275].

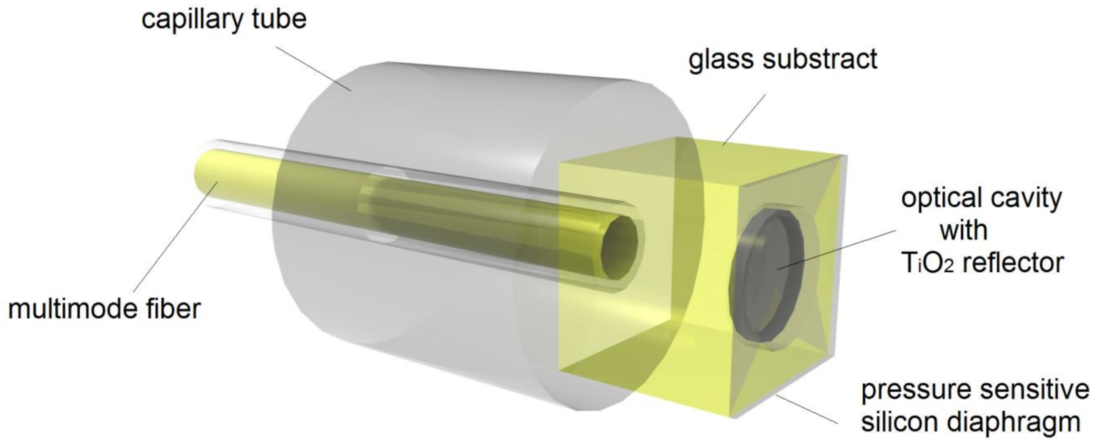

Figure 23 - Schematic drawing of the pressure sensor proposed by Saaski *et al.* [93] and Wolthuis *et al.* [78].

Recently, another F-P sensor was successfully tested *in vitro* and proposed for continuous flow left ventricular assist devices (LVAD) [276]. The F-P cavity consisted of a biocompatible parylene diaphragm and a silicon mirror fabricated directly on the inlet shell of the LVAD device. Sensor sensitivity (1 mmHg achieved by fringe counting; less than 0.1 mmHg with interpolation), linear range (up to 100 mmHg) and response time (1 ms; limited by the response time of the optical detector and the self-resonance frequency of the parylene-C membrane) meet the requirements of LVAD pressure sensing systems [277]. Nevertheless, as mentioned, further improvements are mandatory for animal and human testing. In this case, however, authors have pointed the necessary steps to accomplish it [277].

Several companies, like FISO Technologies (Québec, Canada), Arrow International, Inc. and MAQUET Getinge Group (Rastatt, Germany), are providing F-P based sensors to monitor the arterial pressure during IAB pump therapy. FISO Technologies is recommending the FOP-MIV sensor (550 μm OD) [278]. According to manufacturers' specifications, it has a measurement range from -300 to 300 mmHg, an accuracy of 1.5 % (or ±1 mmHg) of full-scale output (FSO), a resolution better than 0.3 mmHg, a thermal effect sensitivity of −0.05% $°C^{-1}$ and a zero drift thermal effect of -0.4 mmHg $°C^{-1}$ [21]. It was also demonstrated that *in situ* pressure monitoring with these sensors is more accurate and safer than external pressure monitoring through fluid-filled catheters [79]. Yet, to our best knowledge, FOP-MIV has been used to measure the left ventricular pressure uniquely in animals [279]. Other applications of the same sensor, still with animals, included measurement of intracranial [280-281], intraocular [282] and intramedullary pressures [283]. An human *in vivo* application was reported for deglutition analysis assessed by measurement of pharyngeal pressure [284]. Arrow international, Inc. commercializes the FiberOptix™ IAB Catheter, used in clinical practice to monitor arterial pressure [275,285]. MAQUET Getinge Group is commercializing two IAB catheters (Sensation Plus™ 8Fr. 50cc IAB Catheter and Sensation® 7Fr. IAB Catheter), both allowing *in vivo* calibration and recalibration [286]. Unfortunately, we were unable to found further scientific or technical data (*e.g.*, pressure range, accuracy, resolution, and response time) for the above sensors.

Frequently, the F-P cavity is bonded to the OF tip [284,287]. Typically, with this type of extrinsic configuration the tip diameter is larger than that of the OF which may represent a limitation concerning further miniaturization. Yet, new approaches are contributing to enhance the potential of miniaturization offered by FOSs [258,288-291]. Totsu *et al.* [258,288] have presented a sensor of only 127 μm OD to monitor pressure in the heart and aorta of a goat. The F-P cavity (≅ 2 μm depth) was composed of two mirrors, a chromium half-mirror located at the tip of a multimode fiber (MMF) and an aluminum mirror in the head of the sensor. The head of the sensor was made of a thin silicon dioxide diaphragm with a mesa (to support the mirror) and a polyimide spacer that was bonded to the MMF. Cleanroom microfabrication techniques were applied to produce the probe, in particular plasma-enhanced chemical vapor deposition (PECVS), atmospheric pressure chemical vapor deposition (APCVD), evaporation in vacuum, spin-coating, and deep reactive-ion etching (RIE). The all system included a white light source, a fiber coupler and a spectrometer. White light interferometry was used to avoid error and noise caused by bending of the OF and fluctuation of the light source. Sensor exhibited a pressure working range from -100 to 400 mmHg and a resolution of 4 mmHg [258,288]. A slightly different vacuum sealed F-P cavity technique was proposed for temperature compensation [288].

Cibula *et al.* [290-291] were also capable of presenting a similar but slightly smaller sensor (125 μm OD). In this case the diaphragm was designed to be a part of the OF, because the bonding process used in the work of Totsu *et al.* [258,288] limited the temperature range and sensor long-term stability [291]. The F-P cavity was created at the tip of the fiber by chemical etching. The diaphragm, made of polymer, was laid over the tip cavity by a “dip and evaporate” technique [290]. Several prototypes were presented with resolution of 10 Pa and pressures ranging from 0 to 40 kPa and from 0 to 1200 kPa. An all-fused-silica design, based on the replacement of the polymer diaphragm by a silica one, was also proposed [289]. This approach changed resolution to 300 Pa.

The advantage of all-fused-silica fabrication techniques (*e.g.*, splicing, cleaving, and wet etching) is their low-cost. However, mass production may be compromised due to a large number of production steps, including fusion splices, precision cleaves, and micrometer length adjustments of the spliced fiber segments [291]. Significant efforts are being made to reduce some of these critical and time-consuming steps. That is the case of time-controlled chemical etching which eliminates precision length adjustments of critical sensor constituents and improves sensor sensitivity [291]. Future applications will certainly include biomechanical and biomedical applications. Meanwhile, FISO Technologies (Québec, Canada) has already claimed the smallest (125 μm OD) all-glass commercially available sensor (FOP-F125) for human body fluid pressure measurements [292-293]. Depending on the pressure range, the accuracy of the sensor varies from ±5 mmHg [−25 to +125 mmHg] to ±8 mmHg [−300 to +300 mmHg]. Its resolution is better than 0.4 mmHg. The sensitivity thermal effect is of 0.1% $°C^{-1}$ and the zero thermal effect of 0.4 mmHg $°C^{-1}$. Proof pressure is of 600 mmHg and the operating temperature is between 10 ºC and 50°C [293].

5.2 Intramuscular or Intracompartmental Pressure

Intramuscular pressure (IMP) is defined as the hydrostatic fluid pressure within a muscle [294]. Its measurement is of particularly importance for diagnosis of acute and chronic (muscle) compartment syndromes [232,237-238]. IMP is directly correlated with the force output of the muscle [294-295]. Therefore, by measuring IMP, the contribution of an individual muscle group to the force measured over a joint can be assessed.

Crenshaw *et al.* [232,238] were the first to use fiber optic transducer-tipped catheters (Camino Laboratories, San Diego, CA, USA) to measure IMP. The accuracy and reliability of the system were validated trough a comparison with a slit catheter [238]. Preliminary tests also indicated their ability to continuously measure pressures ranging from 0 to 250 mmHg for a three day period. Experiments were made in animal and human volunteers [238]. These sensors prove to be insensitive to hydrostatic artifacts caused by body movements and capable of long-term measurements (≅ 2.5h) without the necessity of flushing to maintain accuracy. Conversely, long-term measurements were also associated with patient discomfort, probably due to the size and rigidity of the polyethylene sheath enclosing the sensor [238]. Even so, these sensors were extensively used for IMP measurements, such as for isometric and concentric exercises [238], to demonstrate that IMP varies with muscle depth [296], to study compartment syndrome following prolonged pelvic surgery [297], and to analyze muscles contribution during gait [237].

To accomplish the requirements of miniaturization for minimally invasive procedures Kaufman *et al.* [236] proposed a new fiber optical microsensor with 360 μm OD (Luna Innovations, Blacksburg, VA, USA). Previous diameter represents about 5 to 6 times the diameter of muscle fibers diameters (ranging from 57 to 73 μm) [298]. The sensor consisted of an extrinsic F-P air cavity in-between a polished end fiber and a reflective membrane [236,299]. It was calibrated inside an air pressure chamber under slowly dynamic pressures ranging from 0 to 250 mmHg back to 0 mmHg, over a period of 120s. The output was compared with that of a reference sensor (Model PX5500, Omega Engineering Inc., Stanford, CT, USA; www.omega.com). Sensor's accuracy, repeatability and linearity were better than 2% FSO, hysteresis of 4.5% FSO and sampling frequency of 66 Hz (~10 Hz with 8 channels). Its accuracy was better than most of the fluid-filled systems (between 1 and 18%), but smaller than electronic transducer-tipped catheters

(0.2% accuracy) [300]. Despite that, the small diameter and immunity to EM fields prevailed [236]. Following functional characterization, sensor was evaluated for biocompatibility using ISO standard 10993-6:2007 (Tests for Local Effects After Implantation) [301]. *In vivo* experiments took place to measure swine intra-myocardial pressure under calibration procedures resembling body physiological conditions [302]. In this case, a fluid pressure chamber was used to calibrate the sensor under sinusoidal pressure variation around a static pressure of ~60 mmHg. Reproducibility was possible only with degassed water but unpredictable results were obtained with tap water. Calibration frequencies varied from 0.5 to 10 Hz and the output was compared with that of a reference sensor (Millar Instruments, Inc., Houston, TX, USA). Hysteresis was not significant. Sensor sensitivity was 8.78 mV mmHg^{-1} remaining flat at 6 Hz and presenting a slightly decrease from 6 to 10 Hz. A slightly lower sensitivity was registered at 23 ºC than at 37 ºC suggesting a possible, but smaller, temperature effect. A constant time delay of 0.13 s was also registered probably due to post-processing electronics. Phase delay was independent of temperature and increased linearly with frequency. Sensor also demonstrated excellent reproducibility during tests of two consecutive days [302].

A second generation sensor (Luna Innovations, Blacksburg, Virginia) with smaller OD (250 to 280 μm), similar accuracy (1.45 ± 0.32%) and repeatability (1.5 ± 0.81%), but lower hysteresis (0.60% FSO) and higher sampling frequency (960 Hz, ~240 Hz with four channels), was used to study IMP in anesthetized rabbits [303-304]. Fatigue effects have also been studied contributing to 0.25% FSO after over 10,000 pressure cycles [287]. It was used to study IMP in anesthetized rabbits [304].

5.3 **Intra-articular Pressure**

Intra-articular pressure (IAP) is associated with joint and capsule loading [305]. It is a complex function of volume, time, joint angle, joint history, pathology, fluid distribution, and muscle action [306]. In the first study using FOSs, IAP was monitored during continuous passive motion (CPM) of the knee joint, a common post-surgery therapeutic procedure [268]. The FOS system consisted of a pressure transducer-tipped catheter (Camino Laboratories, San Diego, CA, USA) similar to those intended for intravascular and IMP measurements. Similar sensors were used to measure IAP in cadaveric glenohumeral joints [269] and during *in vivo* studies of the elbow joint in patients suffering from cubital tunnel syndrome [270-271].

The potentialities of FBG for joint pressure mapping were explored by Mohanty e*t al.* [27]. A FBG array was developed to map stresses across the tibio-femoral interface during total knee arthroplasty. The array was embedded into a stack of unidirectional fiber-reinforced composite (PMMA) and molded to adapt to the femur condyles surface. Embedding is important to enhance FBG sensitivity to transverse loading [27,56,200]. Each OF was composed of sampled chirped FBG sensors capable of detecting force magnitude and its application point. *Ex vivo* experiments were carried out to sense prosthetic misalignments trough the analysis of contact stress distribution during knee flexion/extension [27].

Dennison *et al.* [19-20,259] used minimally invasive FBG sensors to assess the pressure in the NP of the IVD. It was recognized that large diameters of previously used nonoptical sensors (*e.g.*, 1.5 mm OD) [307] could interfere with the normal behavior of the joint and induce degenerative effects [307-309]. Dennison's first proposal consisted of a bare FBG sensor (125 μm OD, 10 mm length, Bragg wavelength 1550 nm) that was left directly in contact with the NP [259]. After that, a configuration with increased spatial resolution and less affected by the inhomogeneity of the nucleus material was presented [19-20]. This new sensor was housed within a stainless steel hypodermic tube allowing only just the tip to sense the external pressure. The sensing area, with 0.4 mm OD, consisted of exposed surfaces of silicone sealant (Dow Corning 3140 RTV, Midland, MI) and of the OF. Under pressure, the area was compressed inducing a shift in the Bragg wavelength. Sensor's mean sensitivity to pressure was -2.7 ± 1.5 E^{-5} mV MPa^{-1}. Data from *ex vivo* porcine compression tests suggested a linear relation between intradiscal pressure and compressive load ($r^2 = 0.97$). A good agreement was obtained with SG sensors. Yet, the mean relative difference in disc response to load between the FBG sensors and the SG sensor was 9.39% and ranged from 0.424 to 33.2% [20]. Dennison *et al.* [19] compared the sensor's sensitivity obtained from strain-optic relationships used in finite element analysis (FEA) with that obtained from experimental results. FEA sensitivity was −23.9 pm MPa^{-1} ($r^2 = 1$) and experimental sensitivity was −21.5 ± 0.07 pm MPa^{-1} ($r^2 = 0.99$). Using experimental sensitivity as reference the relative difference between these sensitivities was 11.1% [19].

The above FBG sensors have not been tested *in vivo* and will require further efforts to be available as commercial plug-and-play devices. Meanwhile, F-P sensors from Samba Sensors (Västra Frölunda, Sweden) and Radi Medical Systems (Uppsala, Sweden) are already available to measure intradiscal pressure. Samba Preclin 360 transducer is a micromachined silicon sensor (photolithographic and wet etching techniques were applied) with 0.36 mm OD and a pressure range from -0.1 to 17 bar [310]. Depending on the pressure range its accuracy is of ±20 mbar and ±2.5% of reading (from -0.1 to 10 bar) or ±20 mbar and ±3% of reading (from 10 to 17 bar) [310]. Temperature coefficient is less than 14 mbar $^{\circ}C^{-1}$ for a temperature range between 20 ºC and 45 ºC [310]. Additionally, it can be coated with radiopaque material to be used in X-ray studies [310]. Some studies reported the use of a similar version (420 μm OD) in pigs [311-312], rabbits [313] and human cadaveric spines [314]. In the case of the Radi Medical Systems sensor, it was used to monitor intradiscal pressure in sedated pigs [315] and patients suffering from lumbar back pain [316]. With 0.55 mm OD this sensor exhibits a pressure range from 0 to 800 kPa, a combined nonlinearity and hysteresis of <0.5% FSO and a time response of less than 0.2 s [316]. Despite their small size, these sensors can still damage the IVD, namely those from small animals (*e.g.*, rats). Meanwhile, Hsieh *et al.* [317] and Nesson *et al.* [18,318] were encouraged to overcome this limitation. They presented a low-coherence interferometric-based optical interrogation system with a sensor probe of 366 μm OD. The glass tube F-P cavity (15.2 μm length) was composed of two mirrors, a biocompatible polymer-metal composite diaphragm and a well-cleaved end face of a SMF. It was fabricated by simple batch-fabrication methods without necessity of a cleanroom environment. The sensor exhibited a linear response to the applied pressure over the range of 0 to 70 kPa, a sensitivity of 0.0206 μm kPa^{-1} and a resolution of 0.17 kPa. Despite being attractive for *in vivo* and clinical practice, due to its biocompatible diaphragm and small size, it was used only for *in vitro* measurements of rodent tail discs [18,317-319].

5.4 **Intracranial Pressure**

Intracranial pressure (ICP) is the pressure inside the skull, namely in the brain tissue and the cerebrospinal fluid (CSF). Following the original works of Adson and Lillie [222], Guillaume and Janny [223] and Lundberg [226], continuous monitoring of ICP became a routine method in neurosurgery. Depending on the location of the sensor inside the skull the techniques to measure ICP may be classified as intraventricular, subdural/subarachnoid, or epidural technique [320]. The intraventricular catheter is placed directly at the ventricle and allows the most accurate ICP measurements [320]. However, this deep location in the brain also presents the highest risk of infection [249,321]. The subarachnoid catheter projects through the Dura into the subarachnoid space [320,322]. The epidural technique is the less invasive as it avoids introduction of the catheter through the brain parenchyma restricting the risk of infection to the extradural space [321]. Unfortunately, with this technique ICP results are usually overestimated making it not recommended for neurocritical care patients [323-324]. The technique is useful in patients requiring ICP monitoring for long periods (> 5 days) because in these patients the most important information is provided by analysis of the frequency and amplitude of slow ICP waves [324].

First ICP measurements [272,325-326] resulted from the adaptation of the intravascular Camino sensor (Camino Laboratories, San Diego, CA, USA) originally proposed by Lekholm and Lindström [40] and Lindström [44]. Camino model 110-4B was considered to be accurate and reliable for ICP monitoring, presenting high-quality readings under laboratory and clinical conditions, a good correlation with SG sensors and fluid-filled systems, less drift and improved waveform resolution, insensitivity to hydrostatic artifacts and no flushing or infusion requirements [244-245,247,255,327-328]. On the other hand, they also underwent extensive scrutiny leading to identification of several drawbacks and questioning their routine use, particularly in clinical practice. Transducer failures (*e.g.*, breakage, cable kinking, probe dislocation, abnormal readings, etc) may range from 10% to 25% [250]. In the study of Yablon *et al.* [245], 12% of sensors failures were caused by breakage of its components. Moreover, contamination of the probes is frequent and long term monitoring seems to be associated with higher rates of infection [249]. Yet, clinically significant infections were considered to be rare [249]. To minimize infections and zero drift of the transducer the manufacturer recommends placement of a new system under sterile conditions if monitoring is continued for more than five days [242]. Several studies have addressed the drift characteristics of the transducer either in laboratory [247] and clinical practice [244,249-250]. Zero drift is an important feature because this type of transducers cannot be re-zeroed after implantation, meaning that cumulative significant errors may occur in long term monitoring [244,249]. Electrical calibration of external monitors is possible but it cannot correct for inherent zero drift of the catheter once it is implanted [250]. Manufacturers' specifications for model 110-4B indicate a maximum zero drift during the first 24 hours from 0 to ±2 mmHg and less than ±1 mmHg per day on subsequent days [242]. Thus, a continuous five-day monitoring can introduce a maximum error of 6 mmHg. This is not satisfactory because normal values for ICP usually range from 7 to 15 mmHg in adults and from 3 to 7 mmHg in children [252]. Furthermore, values exceeding 20 mmHg require immediate treatment [329]. Laboratory tests have indicated the transducer complied with manufacturers' zero drift specifications, while results from clinical practice have suggested zero drift can be greater than reference values. As an example, Crutchfield *et al.* [244] found a larger maximum daily drift of ±2.5 mmHg, a lesser average daily drift of ±0.6 mmHg and an average drift over a 5-day period of ±2.1 mmHg. Münch *et al.* [248] reported an average daily drift within reference values but after being removed from the patient it was 3.2 ± 17.2 mmHg for 50% of the probes. This value was normalized to the number of days of monitoring and decreased to only 6% [248]. Martinez-Manas *et al.* [249] reported only six of 56 implanted probes exhibited no zero drift while the other readings ranged from a minimum of -24 mmHg and a maximum of +35 mmHg. After comparing their results with manufacturer's specifications, they conclude that 61% of the probes performed according to the expected values. It is interesting to note that no correlation was found between zero drift and the duration of monitoring [249-250]. Sensitivity to temperature remains a problem. A maximum of 3 mmHg over a temperature range of 22 °C to 38 °C is reported by the manufacturer [242]. However, in the study of Czosnyka *et al.* [247] temperature drift was ~0.3 mmHg $°C^{-1}$ leading to a maximum of 4.8 mmHg for the same temperature range.

The insertion method of 110-4B Camino transducer requires a drill hole through the skull of 2.71 mm OD [242]. Thus, innovation with FOSs may arrive from smaller sensors and less invasive procedures. Some recommendations were provided to those interested in developing new sensors for this purpose. According to Mignani and Baldini [70], new sensors should meet a working range from -50 to 300 mmHg, a sensitivity of at least 0.1 mmHg, an accuracy of at least 1% and a flat frequency response up to 1 KHz. The American National Standards Institute (ANSI) for ICP monitoring, published by the AAMI [330-331], includes minimum performance requirements that are clearly less demanding than those of Mignano and Baldini [70]. In fact, AAMI requisites are a pressure range between 1 and 100 mmHg, an accuracy of ±2 mmHg in the range of 0 to 20 mmHg, and a maximum error of 10% in the range of 20 to 100 mmHg [330].

A good example of innovation effort was accomplished by Dennison and Wild [59]. They developed an FBG sensor with 200 μm OD, a sensitivity of 58.7 pm MPa^{-1} and a sensing area of only 0.02 mm^2. Calibration results have demonstrated its ability to measure pressure with ±2.7 mmHg repeatability over a range of 105 mmHg. This FBG sensor was proposed for ICP and blood-pressure measurements but is far away from clinical applications because *ex vivo* and *in vivo* tests remain undone.

It is interesting to note that commercially available FOSs are becoming competitive with each other. The Ventrix® ICP monitoring catheter (Integra LifeSciences, Plainsboro, NJ, USA), the OPX100 transducer (InnerSpace, Tustin, CA, USA), the FOP-MIV (FISO Technologies, Québec, Canada) and the OPP-M series (OPP-M250 and OPP-M400; Opsens, Québec, Canada) pressure sensors are some possible candidates to compete with the most popular ICP Camino 110-4B transducer. The Ventrix® ICP monitoring catheter and the Camino 110-4B are from the same company, but the F-P OPX100 transducer is not and claims for new features, such as *in situ* re-zeroing and multimodal monitoring. In a comparative study the OPX-100 transducer presented a lower 24-hour zero drift and temperature drift than the Camino 110-4B transducer [247]. On the other hand, the OPX-100 exhibited a static error (<8 mmHg) higher than that of 110-4B (<0.3 mm Hg). Furthermore, its bandwidth is lower (20Hz) than that of 110-4B (33-120 Hz) [247] and it presents a high incidence (17%) of hematoma formation [332]. Few clinical data is available about this sensor and, to our best knowledge, it is no longer available. The FOP-MIV sensor is a versatile micro-optical mechanical system (MOMS) that can be used for many physiologic pressure measurements. It consists of a F-P vacuum cavity made of a micromachined silicon diaphragm membrane that is bonded on a cup-shaped glass base (550 μm OD). The F-P cavity is connected to a MMF and interrogated with white light [79,280]. According to manufacturers' specifications, FOP-MIV exhibits a measurement range from -300 to 300 mmHg, an accuracy equal to 1.5 % FSO (or ±1 mmHg), a resolution better than 0.3 mmHg, a thermal effect sensitivity of −0.05% $°C^{-1}$ and a zero drift thermal effect of -0.4 mmHg $°C^{-1}$ [21]. The sensor allows for absolute external pressure measurements because vacuum inside cavity prevents pressure errors caused by gas thermal expansion [79]. Manufacturing technologies derived from the semiconductor industry (*e.g.*, photolithography processes and automated assembly) allow their production in large quantities for a competitive price [79]. For ICP measurements the FOP-MIV can be introduced into catheters with diameters smaller than 1.2 mm [79]. However, to our best knowledge, ICP measurements with the FOP-MIV were made only in rats [280-281]. Both OPP-M250 (0.25 mm OD) and OPP-M400 (0.40 mm OD) have similar specifications (-50 to +300 mmHg pressure range; ±1 mmHg precision; 0.2 mmHg accuracy; 4000 mmHg proof pressure; 10 to 50 °C operating temperature; 0% to 100% operating humidity range). They were specifically designed for physiological pressure measurements in preclinical environment and for OEM integration [333]. Besides ICP other possible applications of these F-P sensors include intra vascular blood pressure, urodynamic pressure, intra uterine pressure, intraocular pressure and IAB pump therapy [333]. Nevertheless, almost all applications need to be supported by scientific publications.

5.5 Other Pressure Applications

Previously mentioned applications are probably the most common. Nevertheless, more contributions can be found concerning the use of FOSs to sense pressure in other sites of the human body, such as the trachea [334-335], the gastrointestinal tract [2,55,336], and the intravaginal [17], intraocular [282] and intramedullary spaces [283]. We will explore some of them in the following lines.

Respiratory monitoring in pediatric or neonatal intensive care requires minimally invasive sensors for direct measurements of tracheal pressure. This was achieved for the first time using the Samba Resp. 420 transducer (Samba Sensors, Västra Frölunda, Sweden) [334-335]. This F-P sensor has an OD of 420 μm contrasting with larger FOSs, such as the Camino XP400 (1mm OD) (Camino Laboratories, San Diego, CA, USA), that have been used only in adults patients [337]. Samba Resp. 420 transducer is also a certified CE class IIb Medical Device approved for use in human patients within the European Union [338]. It exhibits a measurement range from -50 to +350 cmH_2O, an accuracy of ±2.5 % of reading (between -50 cmH_2O and +250 cmH_2O) or ±4 % of reading (between +250 to +350 cmH_2O), a temperature drift less than 0.2 $cmH_2O\ °C^{-1}$ (between 20ºC and 45ºC) and a response time of 1.3 ms [334,338].

The possibility of measuring peristalsis, *i.e.*, the rhythmic contraction of smooth muscles through the digestive tract, can help diagnosis of several gastrointestinal motility disorders. While this is possible using manometric techniques, particularly high resolution solid-state and water-perfusion pressure sensors, the ability to present smaller, flexible and higher spatial resolution sensors remains a challenge. To give an example, an increase in the number of solid-state or water perfusion sensors into the same catheter is followed by increased complexity in signal processing, less flexibility and larger catheter diameter [2]. For that reason the number of sensors per catheter is limited to ~36 for the solid-state technology and ~20 for the water perfused technology [2]. Such limitations can be overcome by exploring the potentialities of real time WDM to interrogate several in-line FBG. In fact, this feature was accomplished by Arkwright *et al.* [55] using 32 in-line FBG sensors (written between 815 and 850 nm; 3 mm length; 10 mm spaced) to measure the pressure along the esophagus of a subject [2]. To sense pressure each FBG was fixed to a rigid metallic substrate and a flexible diaphragm. Afterwards, the multiplexed FBG array was inserted into a catheter of silicone rubber (3mm OD) which was sealed at one of the extremities and the other connected to the data acquisition system. The excellent and significant correlation ($r \geq 0.992$) between the FBG based catheter and a reference solid-state catheter (Gaeltec, Dunvegan, Scotland; www.gaeltec.com) suggested one could substitute the other. Meanwhile, further studies have been published confirming FBG potentialities as multipoint or multiparameter sensors [336,339] and their ability to incorporate new features, such as the measurement of longitudinal and circumferential muscular activity in the gastrointestinal tract [336].

An interesting example of the versatility and applicability of FBG sensors was given by Ferreira *et al.* [17] who proposed a complete system for dynamic evaluation of the women pelvic floor muscle strength. The lack of muscle action seems to play an important role in development of several pelvic dysfunctions, such as urinary incontinence and genital prolapses. The system consisted of a silicone ergonomic intravaginal probe (100 mm length and 25 mm OD) with two in-line FBG sensors and an autonomous optoelectronic measurement unit. One FBG transduced radial muscle pressure into axial load, the other used for temperature referentiation. A mean sensitivity of ~120 pm N^{-1} was calculated for a measurement range of ~20 N. With temperature compensation, maximum estimated error (0.0075 N $^{o}C^{-1}$) was considered negligible. Additionally, clinical trials were conducted in patients with pelvic floor disorders. Further improvements will include the substitution of silicone to eliminate some hysteretic behavior due to material's viscoelasticity and reduction of cross-sensitivity to axial induced load, torsion and bending [17].

The possibility of using FOSs to construct pressure-mapping devices to be placed in-between the body parts and supporting surfaces (*e.g.*, floor, seat, mattress, cushion and backrest) is an exciting opportunity to enlarge the spectrum of FOSs applications, namely in the fields of medicine and rehabilitation, sports, ergonomics, automotive industry, etc. However, to accomplish it FOS systems must compete with many recognized companies, such as Tekscan Inc. (South Boston, MA, USA; www.tekscan.com) and Novel GmbH (Munich, Germany; http://novel.de) that are offering powerful accurate electronic based systems at relatively low cost. Nevertheless, some limitations can be pointed to the technology mentioned above. Tekscan sensors are based in conductive elastomers, which may exhibit nonlinear response, hysteresis, and gradual voltage drift [340]. Novel uses capacitive-based transducers, which can be affected by electrical interference and suffer from low spatial resolution, drift, and high sensitivity to temperature [340]. Moreover, with both technologies only normal loads and pressures can be measured. Thus, a window of opportunity is open to FOSs capable of overcoming these limitations and introducing new features, namely the ability to measure normal and shear loads. A possible configuration was explored by Pleros *et al.* [12] by embedding multiplexed FBG arrays into PDMS silicon-polymer to built a pressure mat made of smaller scale blocks, each block consisting of four FBG sensors distributed to form a 2×2 matrix array with a square sensing area of 400 mm^2 and 25 mm thickness. Authors were also engaged in the FP7 project IASIS (*Intelligent Adaptable Surface with Optical Fiber Sensing for Pressure-Tension Relief*) that finished in 2011 [341]. IASIS project aimed at presenting intelligent rehabilitation systems based on multiplexed FBG arrays capable of sensing pressure in therapy beds or wheelchair seats and provide feedback information to prevent onset and evolution of pressure ulcers [342]. Same concept was extended to knee-socket interfaces to sense pressure in amputees [343-344].

The possibility of using FOSs to create smart systems and provide feedback about patient condition was also explored by Hao *et al.* [345]. Bed surface mounted FBG arrays were proposed to monitor several clinical signals, namely body pressure, respiratory rate, heart rate and body temperature. Security alerts to prevent patients from maintaining prolonged static positions or falling out of the bed were also addressed. Sensor consisted of twelve in-line FBG sensors (5 mm length each) organized to form a 3×4 matrix array that was mounted beneath the mattress surface of the bed. To sense pressure, each FBG was previously embedded into an arc-shaped elastic bending beam (40 mm length, 0.625 mm thick and 2.2mm height) using uneven layers of carbon fiber reinforced plastic (CFRP). Calibration results suggested an excellent coefficient of determination (r^2=0.9985) between the wavelength shift and the applied load. Sensitivity obtained from the linear regression equation of calibrated data was equal to 0.1121 nm N^{-1}. Authors failed to present the algorithms used for pressure calculation. Vital signs, such as the respiratory rate and hearth rate, were assessed by signal processing techniques. Temperature sensor consisted of a FBG (10 mm length) isolated from strain by insertion into a glass/copper tube, which ends were encapsulated with a resin/epoxy system [345].

Pressure mats are often used in biomechanical studies, namely to analyze foot pressure distribution in static postures or dynamic activities, such as gait, jumping, running or load carrying. This assessment has particular importance in diabetic insensitive feet because excessive pressure can lead to their ulceration, necrosis and subsequent amputation [346]. The pedobarograph was probably the first device using optical techniques applied in clinical practice to study foot condition. The upper glass surface of a pedobarograph is covered with a thin opaque material, usually a plastic sheet, which in contact with the feet changes the refractive index [347-348]. This action leads to light attenuation in the glass plate, making possible to obtain a footprint and to calculate the applied pressure by means of light intensity variation [349]. More recently, OF and FBG sensors were also introduced to sense foot pressure [56,350]. Multiplexed FBG arrays were positioned accordingly to the foot anatomy, embedded into uneven layers of carbon/epoxy laminates and cut into a shape of a footpad [350]. Calibration results suggested an excellent linear relationship (r=0.99927) between the applied perpendicular load and wavelength shift. Wavelength sensitivity to load and pressure was ~5.44 pm N^{-1} and ~700 pm MPa^{-1}, respectively. A clinical experiment was conducted to evaluate pressure distribution under normal and abnormal standing [350].

The study of Wang *et al.* [351] is of particular interest because it represents the first attempt to create in-shoe shear sensors. Instead of using a wavelength modulation design, sensor development was based on bend-loss technique. A 2×2 array of MMF, embedded into high-compliance material and forming four orthogonal intersection points (each with a sensing area of 100 mm^2), was used as a basic sensing sheet. Under compressive loading, light attenuation caused by physical deformation of the fibers at the intersection points was used to calculate the x and y coordinates of the pressure point and the corresponding normal stress. To obtain shear stress two layers of the basic sensing sheet, placed between gel/polymeric shoe insole pads, were used. This way, the relative difference between the corresponding pressure points could be used to calculate the amount of shear. The entire system consisted of a LED source, an eight-element photodetector array and a data-acquisition system (National Instrument 16-input, 500 kb s^{-1}, 12-bit multifunction input/output data-acquisition card; Lab-VIEW software; and a laptop computer). Repeatable results were obtained under bench mechanical loading tests consisting of vertical forces up to 6.5 N and displacements of 6 mm, and shear forces up to 13.8N. The minimum detectable vertical and shear forces were 0.4 N and 2.2 N (at 60 pitch angle), respectively. To address some limitations of the previous configuration (*e.g.*, low spatial resolution, consistent and accurate manufacturing of the sensor, cost and noise) a batch process to fabricate PDMS-based waveguide sensor, and a neural network technique to provide an accurate description of the force distribution, were proposed in further studies [340,352-353]. After successful bench tests, the same group has recently presented a full-scale foot pressure/shear sensor, capable of measuring normal forces ranging from 19.09 to 1000 kPa [354].

6. Final Remarks

The state of the art of FOSs intended for biomedical and biomechanics applications has been reviewed. Our approach to FOSs was made after introducing conventional sensors and pointing some of their limitations. FOSs seem particularly suitable for use in minimally invasive procedures, allowing precise and accurate point, multipoint or distributed measurements without necessity of increasing sensor's dimensions and with easier instrumentation. Minimum dimensions are achieved when the OF itself is used as the sensing element, such as with FBG sensors and all-fused-silica designs. Nevertheless, small dimensions are also related to mechanical fragility. FOSs without protective layers require special handling. They can be suitable for *in vitro* or *ex vivo* biomechanical experiments, but will fail during *in vivo* trials and clinical practice. Thus, use of biocompatible and sterilizable layers, both capable of maintaining the minimally invasive function and providing mechanical stability, is mandatory.

FOS technology has about forty years of history and most underlying working principles are sufficiently mature to provide accurate solutions for sensing almost any physical and chemical quantity. Despite that, few companies are exploring FOSs potential and offering turnkey solutions for biomedical and biomechanical sensing. Even fewer, have supported their products with peer reviewed papers, standardized testing protocols or approvals from regulatory/standardization entities. These are, indeed, the greatest challenges for those wishing to develop FOSs for biomechanical and biomedical applications, especially for the medical market.

Chapter 2 - The Spinal Motion Segment: A Review

1. Introduction

The process of developing or applying fiber optic sensors (FOSs) to measure a physical quantity of an object requires an extensive knowledge of both the sensor and the object. In the previous chapter a review effort was made to describe FOSs potentialities, configurations and applications in biomechanical and biomedical fields. This chapter seeks to describe the anatomical structures that have been the object of study during experimental work: the spinal motion segment (SMS) or the functional spinal unit (FSU) and, particularly, the intervertebral disc (IVD).

The SMS consists of two adjacent vertebrae with the intervening IVD and ligaments intact. The most important reason to consider the SMS in the study of the IVD mechanical behavior is that it is defined as the functional unit of the spine. In other words, the whole spine is like a composition of several SMS, each of them with its own singularities, but all of them with the same anatomical and functional components. Thus, in a certain way, studying the biomechanics of the SMS is equivalent to study the whole spine. As an example, if a compressive load is applied to a single SMS the IVD will bulge, a typical behavior that will be observed in all SMS. Naturally, the validity of the extrapolation depends on the observed phenomenon or quantity under analysis. Therefore, if the range of motion (ROM) is studied for each SMS the differences will be noticeable, particularly between those belonging to distinct regions of the spine. For example, a SMS of the lumbar region has a limited axial rotation whereas a SMS of the cervical region does not.

To better understand the SMS behavior, its limitations and potentialities, a generic description of the whole spine and of its main regions was included in the manuscript. Spine kinematics was also addressed because the main biomechanical differences between SMS are related to the degrees of freedom (DOF) and ROM each SMS is capable of offering.

Along with the anatomical description of the main components of the SMS, some histological, physical and mechanical properties were also addressed. The guidelines for spinal testing have been described in order to contribute for a better framework of the experimental work and, particularly, to point out its limitations and contribute to further and improved approaches. All issues were addressed bearing in mind the human spines although experiments have been conducted with animal specimens. Considerations concerning comparison between animal and human specimens have been attended in the experimental part.

2. The Spine or Vertebral Column

The spine or vertebral column (Columna Vertebralis, Spinal Columnis) is located at the center and posterior region of the trunk (figure 24). It is a complex multi-segment functional structure with an average length of 75 cm [355], made up of rigid (the vertebrae) and elastic elements (the IVD and the ligaments), that extends from the skull to the pelvis. The skull, the vertebral column and the thoracic cage form the axial skeleton.

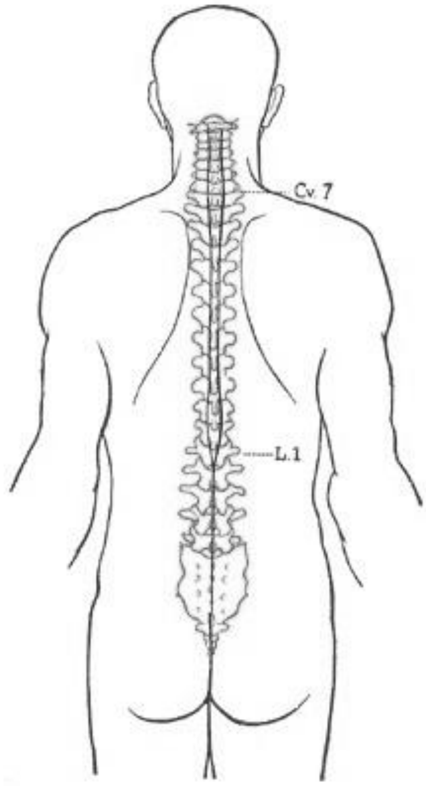

Figure 24 - Location of the spine in the human body [Adap.356].

The spine accomplishes several functions. The foremost is the protection of the spinal cord, the spinal nerves roots and meninges [355]. It also acts as a support structure of the upper body, being capable of transferring its weight and forces to the lower extremities trough the sacroiliac joints [355,357-358]. If the mass of both the upper arms, forearms and hands is calculated, the lumbar structures of spine have to support about 67.8% of body weight [359]. The trunk along with the neck and head accounts for about 57.8% of the total body weight [359]. The lower body also interacts with the spine trough the same sacroiliac joints. Therefore the ground reaction forces acting at the feet along with muscle forces, acting during standing or locomotion activities (*e.g.*, walking, running and jumping), will also be transmitted to the spine trough the sacroiliac joints [307,360].

Each subject has a unique spine which is modeled by genetic and environmental factors [361]. That is why normal spines can differ, particularly in dimension and shape, in the number of elements, composition, physical and mechanical properties [362-365]. There is however several common attributes that can be described.

Spine vertebrae are stacked on top of each other forming four main regions: the cervical, thoracic, lumbar, and sacral-coccygeal regions (figure 25).

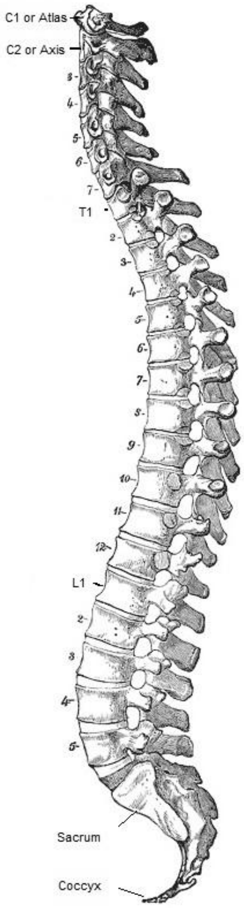

Figure 25 – Vertebrae organization in the spine [Adap.356].

The first three regions of the spine (cervical, thoracic and lumbar) are movable and comprise a total of 24 vertebrae [356]. Cervical spine is located at the neck and consists of seven vertebrae (Vertebrae Cervicales), which are abbreviated C1 through C7 (figure 25). Thoracic spine is located beneath the cervical region, at chest level, and consists of twelve vertebrae (Vertebrae Thoracales), abbreviated T1 through T12 (figure 25). Lumbar spine is located at the low back region of the trunk and is made up of five vertebrae (Vertebrae Lumbales), abbreviated L1 through L5 (figure 25).

In general vertebrae increase in size from above downward and the lumbar vertebrae are the largest segments of the movable part of the spine [356]. Thus, cervical vertebrae are smaller when compared with thoracic vertebrae, and these are smaller than lumbar vertebrae. This geometry seems to be a structural adaptation to the increase of body weight from the head to the pelvis [366].

The last lumbar vertebra (L5) articulates with the sacral-coccygeal region which is located behind the pelvis (figure 25). The sacrum connects the spine to the pelvis and consists of five fused bones abbreviated S1 through S5 (figure 25). Immediately below the sacrum four fused additional bones represent the coccyx (figure 25). Vertebrae of the sacrum and coccyx are termed false or fixed and do not contribute for the movement of the spine [356].

The total number of vertebrae is sometimes increased by an additional vertebra in one region, or it may be diminished. This congenital malformation is rarely observed in cervical vertebrae [356,367]. However it is often related to the lumbosacral region where the 1st sacral vertebra can develop as a lumbar vertebra (lumbarization), or the 5th lumbar vertebra can be bilaterally fused with the sacrum (sacralization) [362,368-370]. These lumbosacral transitional vertebrae have a prevalence in the general population of 4% to 30% [370]. Lumbarization seems to be more frequent in males than females [362].

Ligaments are responsible for stabilizing the spine and are capable of limiting and controlling the movements produced by muscle contraction [371]. The IVD is a fibrocartilaginous structure found between each adjacent vertebra of the spine [372]. As it occurs for ligaments the IVD also participates in the control of the spine movement. However, whereas the main function of most ligaments is to resist tensile forces generated during joint movement, the IVD function is to resist compressive loads acting as a load bearing element. As described for vertebrae they also seem to increase in size from above downward [373]. Both, the ligaments and the IVD will be described more deeply in a later section (see p.68).

Spine curvatures have great importance on the maintenance of the upright posture and the efficacy of bipedal walking [374-377]. From behind, the normal spine appears to be straight (figure 25). However, viewed from the side the spine presents four normal curvatures either kyphotic or lordotic (figure 25). The kyphotic curve is concave anteriorly and convex posteriorly, while the lordotic curve is convex anteriorly and concave posteriorly. Cervical and lumbar regions present a lordotic curve, while thoracic and sacral-coccygeal exhibit a kyphotic one (figure 25).

The IVD play an important role in the formation of the spinal curves. In the cervical and lumbar regions the discs, apart from the disc at the L4/L5 level, are slightly wedge-shaped and thicker ventrally, exhibiting an elliptical cross-sectional shape [367,373,378]. Cervical discs are entirely responsible for the formation of the cervical lordosis [367]. Lumbar discs are responsible for the lumbar lordosis in the upper part of the lumbar spine and for the formation of the lumbosacral angle [367]. In the thoracic region the discs are dorsally thicker but less wedge-shaped than those in the cervical and lumbar regions [373]. They present a more circular cross-sectional shape and seem to slightly contribute to the kyphotic curve [367,373].

The degree of curvature of the regions of the spine is an important topic in postural evaluation. It can be measured using X-ray images and the standard Cobb method [379-381] or other alternative techniques [382-386]. For its assessment the subject should adopt a position similar to the anatomical position *i.e.*, the body erect with feet slightly apart and palms facing forward. Observing the subject from the sagital plane the curvatures of the spine contribute to a normal standing posture in such a way that the line of gravity should pass through the mastoid process, just in front of the shoulder joint, through or just behind the hip joint, through the knee joint and just in front of the ankle joint [381,387].

It should be mentioned that precise measurements from radiographic images are difficult to obtain, particularly due to image distortion in central projection, off-center position, deviations from true sagital projection (introduced by axial rotation and lateral tilt of the spine) and lack of information such as the factor of radiographic magnification and the subject's stature [388]. On the other hand the ideal conditions are difficult to accomplish in clinical context.

In the sagital plane several Cobb angles can be measured, such as the cervical, thoracic, lumbar, sacral, lumbosacral and pelvic tilt [387]. The guidelines for their correct measurement are provided in table 2 [387].

Table 2 – Cobb angles measured in the sagital plane

Angle	Description
Cervical	Intersection between lines drawn parallel to the superior endplate of C1 and inferior endplate of C7
Thoracic	Intersection between lines drawn parallel to the superior endplate of T1 and inferior endplate of T12
Lumbar	Intersection between lines drawn parallel to the superior endplate of L1 and inferior endplate of L5.
Sacral	Intersection between lines drawn parallel to the superior endplate of S1 and horizontal
Lumbosacral	Intersection between lines drawn trough the geometric centers of the endplates of L5 and S1
Pelvic tilt	Intersection between lines drawn trough the promontory of the sacrum and the anterior superior border of the pubic symphysis

In the frontal plane the angle of scoliosis, which is an abnormal curvature of the spine, can also be measured using the classical Cobb method (table 3) or several other alternative methods [381,386,389-391]. These alternative methods represent an effort to measure the degree of scoliosis more accurately than the Cobb method, which cannot account for the influenced of vertebrae rotations. For that reason the Scoliosis Research Society has defined scoliosis as a lateral curvature of the spine greater than 10º as measured using the Cobb method (table 3) on a standing radiograph [392]. A Cobb angle of less than 10º is considered to be within the normal range [387]. Meanwhile, new techniques based on photogrammetry are being developed to avoid repeated exposure to radiation [393]. Scoliosis prevalence seems to be higher and more severe in adolescent females than males [394].

Table 3 – Cobb angle measured in the frontal plane [392]

Angle	Description
Scoliotic	The apical vertebra is first identified (the most likely displaced and rotated vertebra with the least tilted endplate). Then end vertebrae above and below the curve are identified. The end vertebrae are the least displaced and rotated and have the maximally tilted endplate. A line is drawn along the superior endplate of the superior end vertebra and a second line drawn along the inferior endplate of the inferior end vertebra. If the endplates are indistinct the line may be drawn through the pedicles. The angle between these two lines (or the lines drawn perpendicular to them) is the Cobb angle. In S-shaped scoliosis where there are two contiguous curves the lower end vertebra of the upper curve will represent the upper end vertebra of the lower curve.

The relationship among spine angles and the correct upright posture has not been clearly established [395-396]. It seems a broad range of combinations is possible to ensure a normal posture [377,387].

Spine kinematics is the geometric description of spinal movements. In such a view, the spine is considered flexible and capable of all kinds of anatomical and combined movements. In fact, each SMS has six DOF, three for translation and three for rotation. Thus, the spatial movement of the spine can be defined as the expression, or contribution of twenty-three synchronized SMS, each of them offering six DOF. Translation movements are in the order of the millimeter and more difficult to measure than rotational movements.

Three anatomical planes are used to describe the major anatomical angular displacements, such as flexion/extension (the angular displacement parallel to the median/sagital plane), lateral bending (parallel to frontal plane), and axial internal/external rotation (parallel to transverse plane) [397]. Knowing the ROM for each angular displacement is critical for many activities. In fact, many studies and techniques have been published trying to report ROM normal values of the spine and of the SMS [398-406]. As an example, normal ROM for trunk flexion is between 110º and 140º, for lateral bending ROM between 75º and 85º and for axial rotation is about 90º [406]. However, in the case of trunk flexion it seems the ROM is not exclusively produced by the spine elements. For a certain degree of flexion (between 50 to 60º) the increase of flexion is produced by an anterior pelvic tilt [407-408].

The most critical anatomical constraint that seems to affect the DOF and ROM of each SMS is the spatial orientation of the articular processes at different spinal levels [409-412]. The cervical spine is the most movable region of the spine. In this region (C3-C7), the facets angle of 45º to the transverse plane and 0º (parallel) to the frontal plane allows all three DOF for rotation (flexion/extension; lateral bending and axial rotation). The orientation of the thoracic facets (60° to the transverse plane and 20° to the frontal plane) gives no axial rotational restriction for each SMS. However the presence of the ribs prevents rotation making this region the least mobile of the spine. In the lumbar region (facets oriented 90° to the transverse plane and 45° to the frontal plane), flexion is the freest movement and lateral flexion, as well as axial rotation, is quite limited. While the previous results are the most cited more recent studies have indicated they seem to present some inconsistencies [412].

The role of spinal complications is large. They can be caused by congenital malformations, trauma, degenerative disorders, inflammatory disorders, tumors, vascular disorders, postoperative disorders and metabolic disorders [369].

3. The Spinal Motion Segment: Its Anatomical, Histological and Mechanical Properties

The SMS is considered the smallest functional unit representing the general mechanical behavior of a given region of the spine [413-414] (figure 26). It consists of two adjacent vertebrae with the intervening disc and ligaments intact [414-423]. Nevertheless, depending on the purpose of the study, the ligaments may not be included, the IVD may be replaced by an artificial disc or the vertebrae may be fused [424-426].

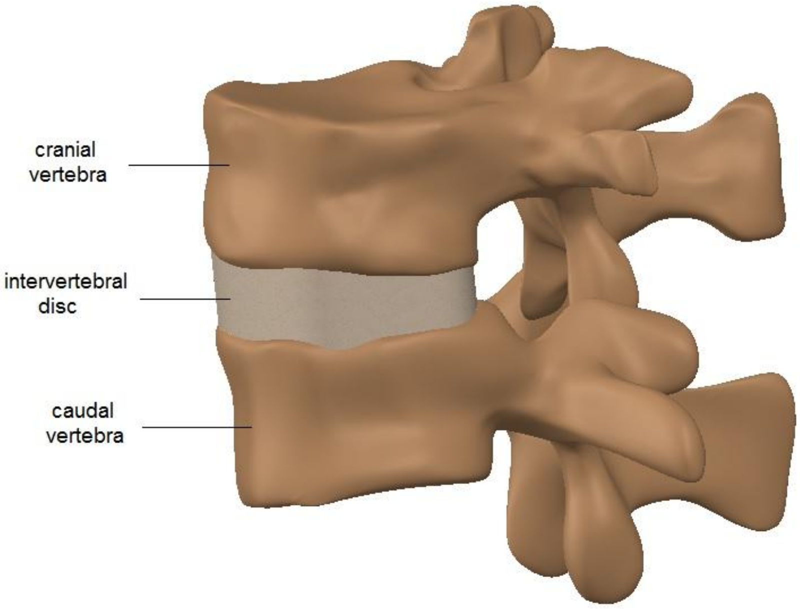

Figure 26 - A 3D view of a spinal motion segment (SMS) and of the intervertebral disc (IVD). Ligaments are not represented.

There are usually twenty-three complete SMS segments along the spine [371]. Details about the components of the SMS (vertebrae, IVD, the facet joints and the ligaments) will be provided in the following subsections. Emphasis will be given to their gross anatomy, some histological findings and biomechanical behavior.

3.1 The Vertebrae

Typical or true vertebrae have the same general structure, despite slight modifications due to their position and function [356]. With exception to the first two cervical vertebrae (C1 and C2) all other movable vertebrae share some common features that will be described. Slight but important characteristics in the vertebrae structure, responsible for their arrangement into the three movable regions, will not be attended. Moreover, the description of special attributes of some vertebrae (*e.g.*, C6, C7, T1, T10, T11, T12 and L5) as well as the structure of highly modified vertebrae (*e.g.*, C1 and C2) is also beyond the scope of this study.

All vertebrae comprise an anterior region and a posterior region. The first one is the vertebral body and the second one the vertebral or neural arch. These two regions enclose the vertebral foramen (figure 27).

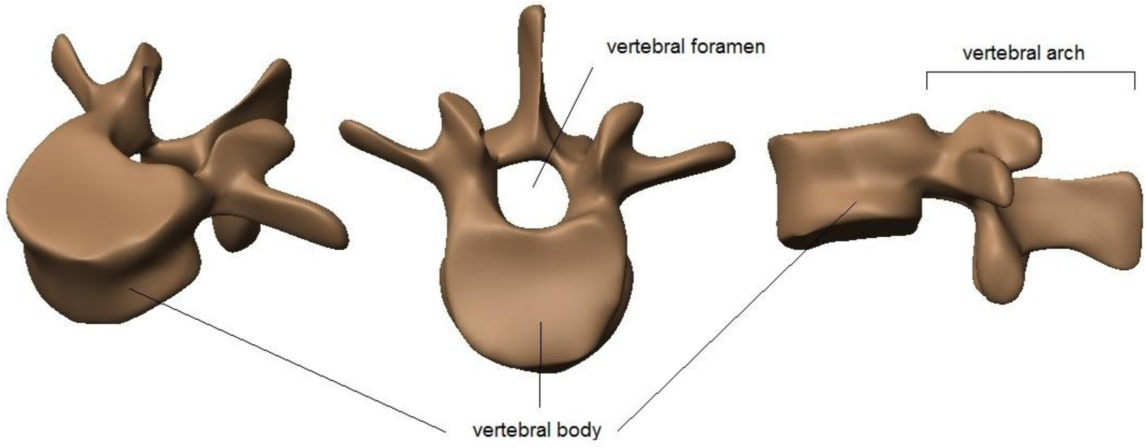

Figure 27 - A typical vertebra observed from different views. Left: perspective. Center: transversal view; right: sagital view.

The human vertebra is made of bone. Bone has unique structural and mechanical properties. It is one of hardest structures of the body, it is highly vascularised and has an excellent self repair capacity being able to change its properties in response to mechanical demands [427].

Bone consists of cells (osteocytes) and an organic extracellular matrix. The matrix is composed of mineralized collagen fibers (≈95%) surrounded by gelatinous ground substance (≈5%) that works as a cementing substance between the layers of collagen fibers [407]. The high content of inorganic or mineral material is embedded in the collagen fibers. The composition of the inorganic material is an amorphous form of hydroxyapatite [427].

Due to the previous configuration bone tissue can be modeled as a two-phase or biphasic composite material, made of collagen and hydroxyapatite [407,427]. The collagen and ground substance represents one phase, the mineral and inorganic component the other [427]. A non biologic example of this kind of composite is fiberglass. The collagen fibers are capable to resist stretch but have little extensibility [407]. The minerals, mainly calcium and phosphate, give bone its consistency, hardness and rigidity [407]. In fact, the Young modulus of single-crystals of hydroxyapatite ranges between 54 and 79 GPa, a very stiff and strong material [428-429]. The Young modulus of bone may range between 16 and 22 GPa [430] which represents about 30% of that of single-crystals of hydroxyapatite.

Water represents about 25% of the bone total weight: about 85% in the bone’s ground substance and the remaining 15% in canals and cavities that house bone cells [407].

At the microscopic level the fundamental structure of cortical bone is the osteon (figure 28). The osteon is composed of a bone matrix organized in concentric series of layers surrounding a central canal (osteonic or Haversian canal) [407]. These layers, called lamellae, present small cavities (lacunae) at their boundaries, each containing one bone cell or osteocyte.

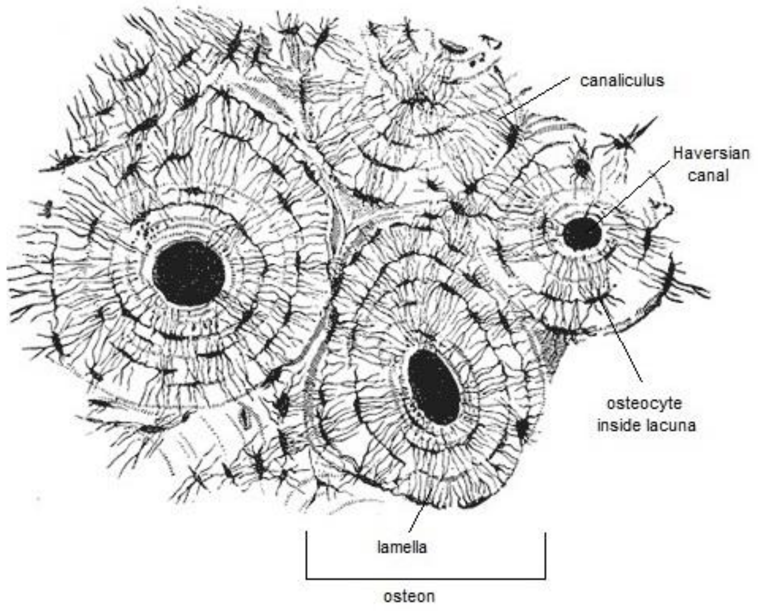

Figure 28 – Schematic representation of the osteon, the bone matrix and the Haversian system [Adapt.356].

At the macroscopic level bone is composed of two types of osseous tissue: the cortical or compact tissue, and the cancellous, trabecular or spongy tissue (figure 29).

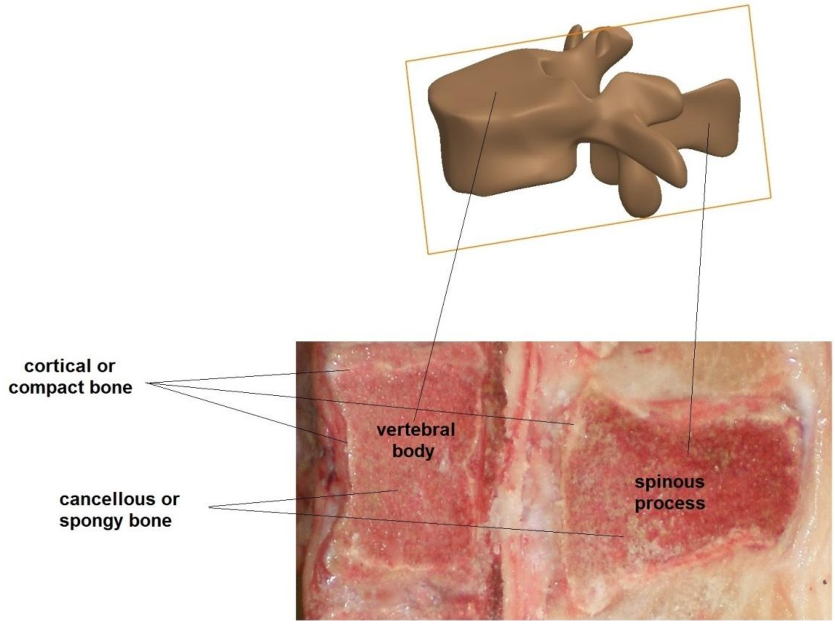

Figure 29 – Midsagital cut view of a porcine vertebra.

Cortical tissue forms the cortex or the outer shell of the vertebra and has a supportive and protective function [431]. Cancellous bone is located inside the vertebra and is composed of thin plates, or trabeculae, in a loose mesh structure filled by red marrow [431]. Its function is mainly related to mineral homeostasis, but also supportive [431]. As mentioned, both tissues are arranged in concentric layers called lamellae (figure 28). However the main anatomic difference between cortical and cancellous tissues is that the last does not contain the haversian canals [427].

The distribution of cortical and cancellous bone varies greatly between individual bones [431]. For example, a typical vertebra consists of 62% cortical and 38% of cancellous bone while the ulna is 92% cortical and 8% cancellous [431].

Cortical bone is denser than cancellous bone. At the macroscopic level, cortical bone porosity, or apparent density, varies from 5% to 30% and in cancellous bone from 30% to more than 90% [407]. The porosity of cancellous bone gives it a large capacity of storing energy and resisting strain before failure [407]. Both cortical and cancellous bone densities may vary substantially, from 1000 to 2000 kgm^{-3} [431-432] and from 300 to 1300 kgm^{-3} [431,433-434], respectively. In fact, cancellous bone can even be classified as a high density tissue if its density is equal or higher than 1180 kgm^{-3} [434]. The higher density of cortical bone makes it stiffer than cancellous bone. Its stiffness is more than ten times greater than that of cancellous bone [435]. The yield strength of cortical bone is about 140 MPa, while for cancellous bone is approximately 5 MPa [431]. Nevertheless, while it is capable of withstanding greater stress its strain tolerance is lower [427]. Its plastic deformation for ultimate strength is about 1% while for cancellous bone it is about 22% [431]. In fact, cortical bone will fail if strain exceeds 2% and cancellous only after 75% [436].

The mechanical properties of bone depend not only on bone density or composition, but also on bone structure (*e.g.*, geometric shape, bond between fibers and matrix, and bonds at points of contact of the collagen fibers), sex, age, location of bone, load orientation, strain rate and specimen condition (*e.g.*, wet or dry bone) [427].

The Young’s modulus is useful to quantify bone stiffness. While it should be measured in the linear portion of a stress/strain curve it was suggested that the elastic portion of the previous curve is not a straight line for cortical bone but it is slightly curved yielding somewhat during loading in the elastic region [437]. This is probably due to the collagen component of the bone, which has a tangent modulus of about 1.24 GPa [427].

Due to its macro and microstructure bone exhibits an anisotropic behavior, with mechanical properties that vary according to load direction [427,437-439]. Its strength and stiffness seems to be higher in the longitudinal direction than the transverse direction and, particularly, in the directions of the applied loads [438]. It was sustained that bone yields under tension due to the failure (debonding) of osteons at the cement lines (the boundary of an osteon) [407].

To consider the extent of deformation of bone before failure it is important to classify it as a brittle or a ductile material. However, bone tissue seems to exhibit both properties depending on its age and load rate. Mature bone is less ductile and higher loading speeds make the bone more brittle [407]. Dry bone also seems also to be more brittle than wet bone. It fails at a strain of 0.4% while wet bone fails at 1.2% [440]. The effect of strain rate seems to be especially significant [427]. Higher ultimate strength was obtained at higher strain rate [427]. In table 4 and table 5 the Young modulus along with other mechanical properties of vertebrae bones and of the endplates are presented. These values have been implemented in several FEA studies.

Table 4 – Mechanical properties of vertebrae bones

Material	Properties	References
Cortical bone	Exx = Eyy = 11.3 GPa ; Ezz = 22,0 GPa Gxy = 3.8 GPa ; Gyz = Gxz = 5.4 GPa νxy = 0.484 ; νyz = νxz =0.203	[439,441]
	E = 12 GPa ; ν = 0.3	[415,418,426,442-444]
Cancellous bone	Exx = Eyy = 0.14 GPa ; Ezz = 0.2 GPa Gxy = Gyz = Gxz = 0.0483 GPa νxy = 0.450 ; νyz = νxz = 0.315	[439,441]
	E = 0.1 GPa ; ν = 0.2	[415,424,426,443,445-447]
Posterior bony elements	E = 3.5 GPa; ν = 0.25	[439,448]
	E = 3.0 GPa ; ν = 0.3	[329,426]

E: Young’s modulus; G: Shear modulus; ν: Poisson’s ratio

Table 5 - Mechanical properties of the endplates

Material	Properties	References
Bony endplates	E = 4.0 to 12.0 GPa ; ν = 0.3	[439]
	Outer portion: E = 12.0 GPa ; ν = 0.3 Intermediate portion: E = 6.0 GPa ; ν = 0.3 Center (inner) portion: E = 2.0 GPa ; ν = 0.3	[426,449]
Cartilaginous endplates	Isotropic: E=23.8 MPa; ν=0.4	[421,439,441]
Endplates	E=2.5 GPa; ν=0.3 (≈PMMA)	[450]

E: Young’s modulus; G: Shear modulus; ν: Poisson’s ratio; PMMA: Polymethylmethacrylate

3.1.1 The Vertebral Body

The vertebral body (corpus vertebrae) or centrum is the largest part of a vertebra and is located anteriorly (figure 30).

The upper and lower surfaces of the body are approximately cylindrical in shape and present a cortical rim (epiphyseal ring) around their external contour (figure 30) [356].

The anterior surface of the vertebral body is convex viewed from the transverse plane and concave in the sagital plane (figure 30). The posterior surface is moderately concave from the transverse plane and approximately flat in the sagital plane (figure 30).

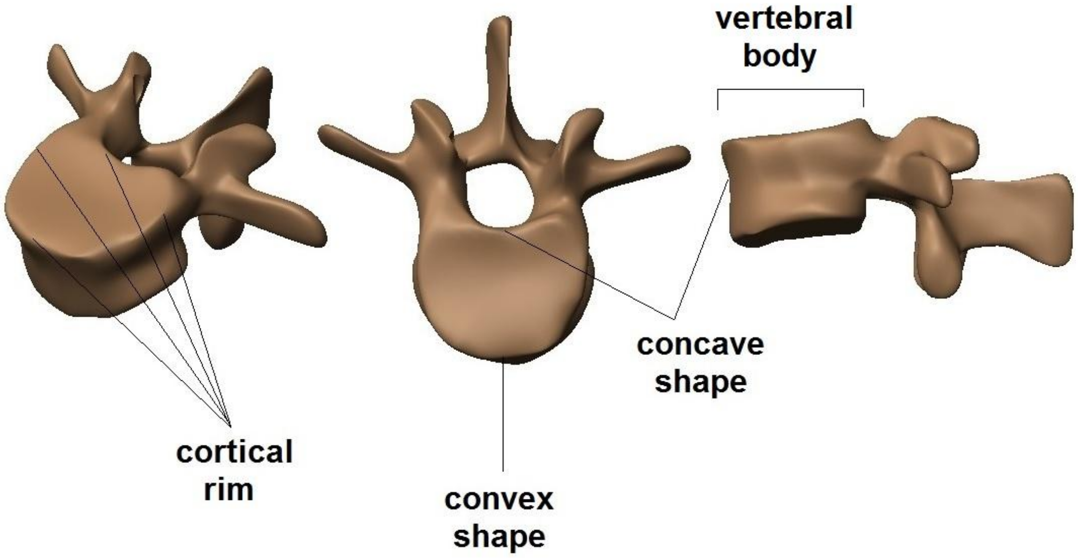

Figure 30 – The vertebral body of a vertebra is located anteriorly.

The vertebral body is composed of cortical bone on the outside and cancellous bone on the inside (figure 29). Based on direct and CT observations it was suggested that the thickness of the cortical bone of the vertebral endplates (≈0.5 mm) is greater than that of the vertebral wall (≈0.35 mm) [451].

3.1.2 The Vertebral Arch

The vertebral arch is made up of paired pedicles, paired laminae and seven spinal processes (the spinous process, two pairs of articular processes, and two transverse processes) (figure 31).

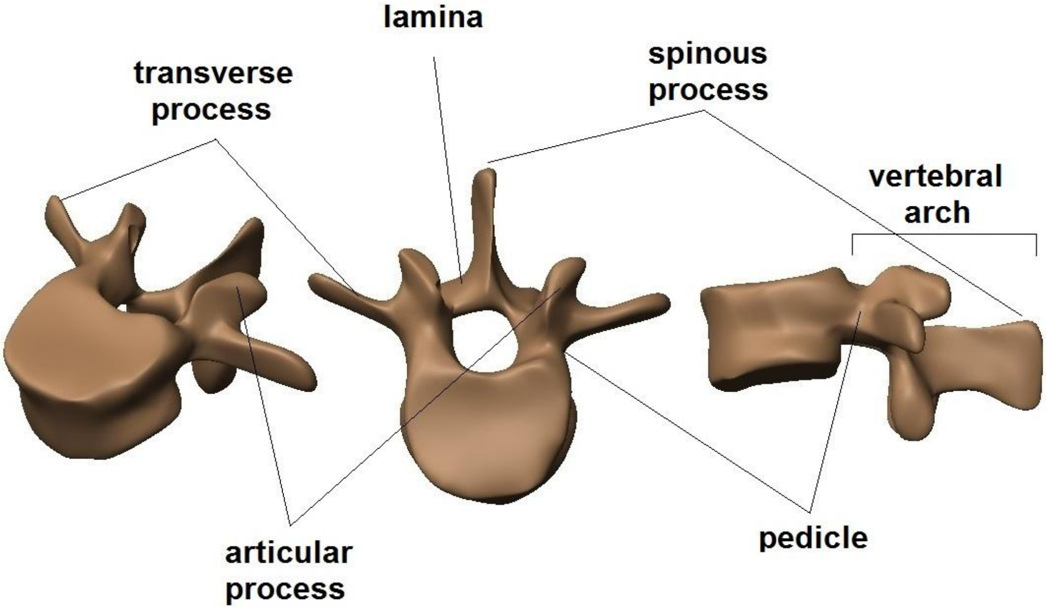

Figure 31 – Components of the vertebral arch.

The previous anatomical components can be described as follows [356]:

- Pedicles (radices arci vertebrae) are two short and thick processes projected backward, one on either side, from the upper part of the body, at the junction of its posterior and lateral surfaces (figure 31). The concavities above and below the pedicles are named the vertebral notches forming the intervertebral foramina in the SMS. The intervertebral foramina gives passage to the spinal nerves and vessels (figure 32);

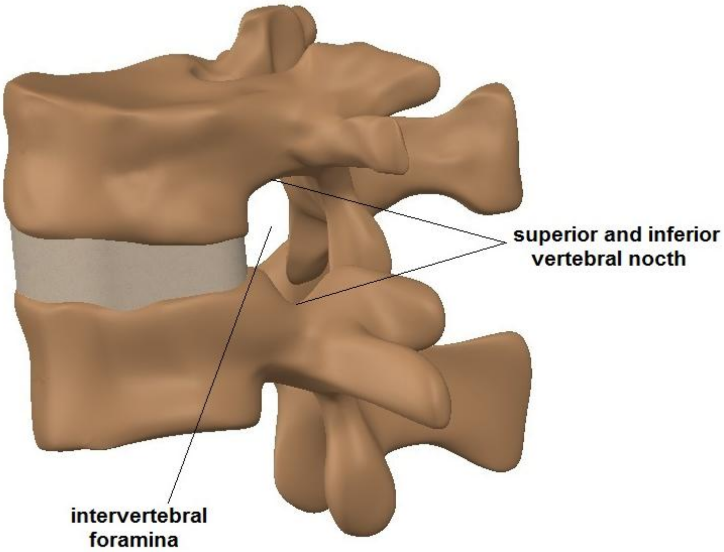

Figure 32 – The intervertebral foramina is formed by the superior and inferior vertebral notches.

- Laminae are two large plates directed backward and medially from the pedicles to complete the vertebral arch and fuse at the spinous process (figure 31);
- The four articular processes, two superior and two inferior, on either side of the vertebra, are also formed at the junction of the pedicles and laminae and possess articular surfaces (articular facets) that participate in the facet joints (zygapophyseal or apophyseal joints). The two superior articular processes project upward and face dorsally. The two inferior articular processes project downward and face ventrally (figure 31). Their spatial orientation defines the DOF and ROM of each SMS and of the entire spine;
- The two transverse processes (processus transversi) are formed at the junction of the pedicles and laminae, one on either side, between the superior and inferior articular processes and project laterally (figure 31);
- The spinous process (processus spinosus) is the most posterior part of the vertebra having a central location and being directed backward and downward from the junction of the laminae (figure 31).

3.1.3 The Endplates

At the top and bottom of each vertebral body there is a thin cartilaginous plate, the endplates, sometimes regarded as part of the body sometimes as part of the IVD [367]. The endplates form the junction between the vertebral body and the IVD and are made of two distinct components: the hyaline cartilage and the osseous component [452-453]. The endplates are responsible for the nutrition of the disc trough diffusion of fluids and nutrients since the blood vessels surrounding the disc disappear during the early phases of development [454]. Their thickness is about 0.35 mm in lumbar elements [451].

3.2 The Intervertebral Disc

The IVD is a fibrocartilaginous structure found between adjacent vertebrae of the spine [372] (figure 33). It represents the anterior joint of the SMS, a symphysis cartilaginous joint [455]. It is the largest avascular and aneural structure in the body [456].

There are twenty-three IVD in the normal spine and they represent approximately 20 to 33% of the spine length above the sacrum [367,457-458]. On average IVD thickness is about 3.5 mm in the cervical region, 5 mm in the thoracic region, and 9 mm in the lumbar region [355,459]. In the lumbar region the discs are thicker than elsewhere and they account for 30 to 36 % of the height of the lumbar spine [367].

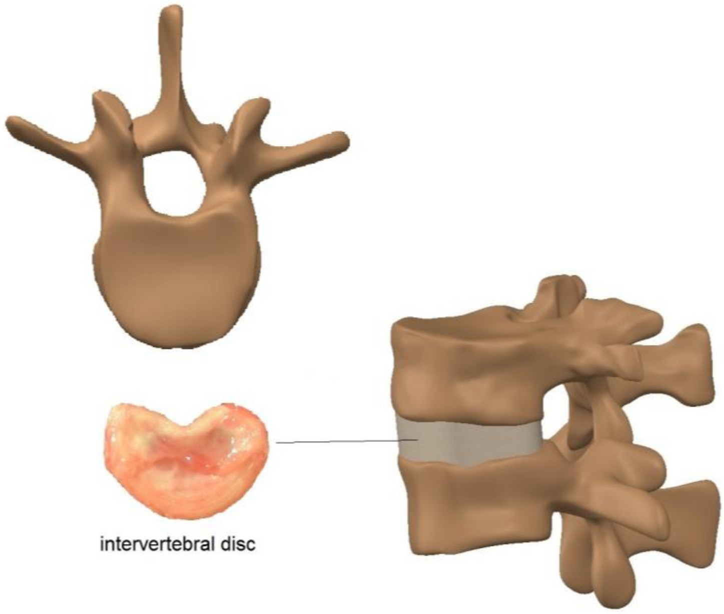

Figure 33 – Schematic representation of the location of the intervertebral disc in the spinal motion segment. A picture of an *ex vivo* porcine intervertebral disc specimen is presented.

Despite variations in geometry the structure of the IVD is almost the same for all discs of the spine. Basically, it has two main components, the nucleus pulposus (NP) and the annulus fibrosus (AF) (figure 34). Yet, at the top and bottom of each vertebral body there is a thin cartilaginous plate, the endplates, sometimes regarded as part of the vertebral body sometimes of the IVD [367].

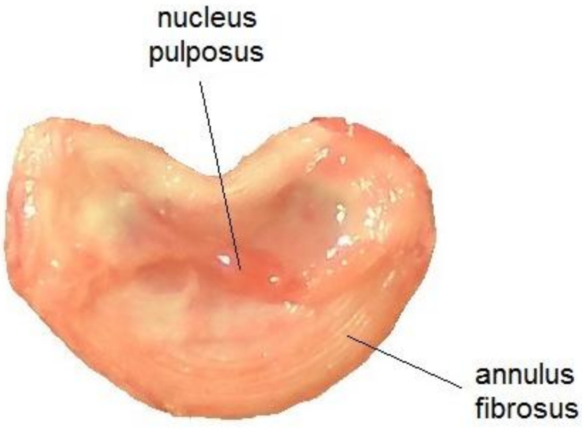

Figure 34 – The intervertebral disc of a porcine specimen (transverse plane view). The annulus lamellae surrounding the softer nucleus pulposus are visible in the anterior portion of the disc.

3.2.1 The Nucleus Pulposus

The NP is defined as a semi-fluid, amorphous, highly hydrated and proteoglycan-rich region located in the center of the IVD and surrounded by the AF [19,452,460-461] (figure 34). It can also be located in a somewhat eccentric position, slightly posterior, as it seems to occur for cervical and lumbar discs [462-464].

The NP occupies a significant volume of the IVD. In the case of lumbar specimens, on average, it represents 43% of the disc volume [462] and 60% of the cross-sectional area of lumbar discs [465]. In cervical IVD the NP seems to occupy a smaller area since its diameter represents on average about 38% of the disc diameter [463].

The NP consists of a dense and random three dimensional (3D) network of collagen fibers enmeshed in an extracellular matrix rich in proteoglycans and water [466-469]. Thus, the main components of the NP are water, proteoglycans and collagen.

Between 80% of the NP weight is due to water molecules [467]. Water content varies with age [467,470], health state [471] and the loads applied to the spine [472-473]. It also suffers diurnal changes loosing water during the active day and recovering it during the resting night. Lumbar discs, for example, lose and regain approximately 20% of water every day [474] and most of the loss occurs during the first hour of the morning [475]. Interestingly a permanent loss of 20% of water seems to occur with aging [467]. Water loss can be simulated *in vitro* submitting the IVD to a compressive load of 150N during a period of two to six hours [463,476]. It was confirmed that a reduction of about 0.50 mm in the height of a cervical SMS under a compressive load of 150N corresponds to a loss of 10% in the height of the IVD [463].

Proteoglycans contribute to about 50% of the NP dry weight [456]. They present a core protein to which glicosaminoglycans (GAG), or mucopolysaccharides, are linked [452,454,466]. These GAG are heteropolysaccharides with highly negatively charged molecules that are capable of absorbing sodium and water (the NP hydrophilic property) [454]. This protein polysaccharide complex is often called a mucoprotein gel [466] and is responsible for the hydrostatic and viscous nature of the IVD [469].

Collagen accounts for about 15 to 20% of the dry weight of the NP [456]. Predominant collagen is of type II while type I collagen seems to be absent [372]. Spherical chondrocyte-like cells that synthesize the type II collagen and similar to those seen in articular cartilage are also present in the NP [477-480]. Collagen type II is thought to resist compressive load [478].

In the mechanical view the NP is considered to be incompressible [421,426,439,481-482] or a pure Newtonian fluid with a bulk modulus [443]. It seems to exhibit an isotropic and hydrostatic behavior [421,439,463], well designed to act as a cushion, increasing the intradiscal pressure linearly under compressive load [259,465,478,483].

In the anatomic position the IVD is already submitted to a continuous pressure caused by the weight of the body above the disc level and the residual muscle tension or tonus. This pressure is measured in the NP and seems to depend on the applied load relative to disc area. Both parameters increase in the cephalocaudal direction, particularly from one region to another, suggesting the increase in disc area compensates the increase in load. Moreover, IVD stresses seem to be inversely proportional to disc size [463] suggesting the increase in area is the most relevant factor and contributes effectively to a reduction of pressure. In fact, the pressures in the cervical discs seem to be higher than those in lumbar discs [483]. In the cervical region of cadaveric specimens, the corresponding average pressure (from C2-C3 to C7-T1) in neutral position was about 1.09 MPa for a load of 200N representing the combined effects of head weight and muscle tension [463]. Higher loads lead to higher pressures as observed in the study of Cripton *et al.* [483]. In this study pressure increased linearly with compressive loading up to 800N, while depending on the disc level. At the maximum load of 800N disc pressure was about 2.4 MPa for C4-C5 level and 3.5 MPa for C3-C4 level [483]. In the lumbar discs, *in vivo* studies reported a disc pressure of 0.5 MPa at the level L4-L5, with the subject in the anatomical reference position [307,484]. The same pressure was observed for a compressive load of 500N [485]. For compressive loads of 800N lumbar disc pressures did not exceeded 1 MPa [486]. In FEA lumbar pressures usually do not exceed 2 MP [421,482]. As a "gross" rule it was proposed that a load of 1 kN leads to a pressure of 1.0 MPa in lumbar IVD and 3.75 MPa in cervical IVD [483]. Finally, in the thoracic region the *in vivo* average pressures found in upright standing for the upper region (T6-T7 and T7-T10) and lower region (T9-T10 and T10-T11) were of 1.01 and 0.86 MPa, respectively [487].

In table 6 some physical and mechanical properties of the NP that have been implemented in FEA studies of lumbar discs are presented.

Table 6 – Mechanical properties of the nucleus pulposus

Properties	Reference
Isotropic, incompressible, hyperelastic Mooney-Rivlin formulation. $C_1 = 0.12$; $C_2 = 0.03$; $\nu = 0.4999$	[439]
Incompressible, fluid-filled cavity $\rho = 1.0\ E^{-6}$ kg/mm^3	[421]
E = 0.1 MPa ; $\nu = 0.499$	[329,418,426,442,446-447]
K = 2.5 MPa	[443]

E: Young's modulus; C1 and C2: material constants; K: bulk modulus; ν: Poisson's ratio; ρ: density

3.2.2 The Annulus Fibrosus

The AF is a solid elastic ring that forms the main mass of the disc and encloses the NP [452]. It attaches above and below to the central portions of the endplates, to the cortical ring and to the sides of the vertebral bodies [460]. Its peripheral portion also fuses to the anterior and posterior longitudinal ligaments, making them inseparable [460].

Water is the main component of the AF and represents on average 70% of the AF weight [467,488]. Collagen fibers represent about 65 to 70% of the dry weight of the AF [456]. Proteoglycans account for about 10 to 20% of the dry weight of the AF [456].

For mechanical and modeling purposes the AF can be considered as a composite material with a homogeneous ground substance (matrix) reinforced by a collagen fiber network.

The homogeneous ground substance or matrix (mesenchyme) fills the space between the collagen fibers and is described as an amorphous proteoglycan-rich gel [461].

The collagen fiber network was observed for the first time in 1932 by Beedle [489] and it is made of lamellae, a series of discontinuous concentric layers [460,490] that may range between 10 to 25 [372,490-491]. Some layers can merge into each other [492-493]. The posterior AF seems to present fewer distinct lamellae, and subsequently a greater number of incomplete lamellae as compared to the anterior AF [493].

Intra and inter-lamellar matrices of ground substance can be distinguished [469]. The intra-lamellar matrix is the connective tissue found between parallel collagen fibers. It functions to keep collagen fibers tightly bound together. The inter-lamellar matrix is comprised of similar components but is located between adjacent layers of the annulus, and helps to prevent delamination between these layers.

The relative volume content of the collagen fibers with respect to the surrounding ground substance may vary. An average value of 19% was proposed [415,426,446]. However it may vary accordingly to the fibers location, for example, from 23% at the outer layer to 5% at the inner fiber layer [441].

Within each lamella the collagen fibers are arranged parallel to each other, making approximately a 30º angle to the transverse plane [461,490-491,494]. In consecutive lamellae slope orientation alternates from positive (counterclockwise) to negative (clockwise) [490]. Nevertheless, this slope seems to vary according to the region of interest as it was observed for the outer AF fibers, varying from 23º anteriorly to 47º posteriorly [495-496].

The highly orientated and layered structure of the collagen fibers of the AF suggests that its behavior is nonlinear and anisotropic [443]. Thus, for FEA purposes it is usually modeled as an anisotropic material with hyper elastic properties [421,443,497]. These hyper elastic properties are probably due to the elastic fibers that run parallel to type I collagen fibers in the intralamellar space and have a less isotropic arrangement in the interlamellar space [461]. These fibers are responsible for the resilience and low strain stiffness of the AF, complementing the role of collagen fibers [461]. Their density in lumbar disc is significantly higher in the posterolateral region than the anterolateral one as well as in the outer regions, rather than the inner regions of the AF [461].

Equally, the morphology of the collagen fibers seems to vary according to the region of interest. The inner AF is more similar to the NP in its composition, presenting more type II collagen than type I [372,477-478,480]. At the extreme portions of the outer AF only type I collagen seems to exist [461]. The thickness of each lamella in the inner annulus is approximately 300 µm while it is of approximately 130 µm in the outer [490-491].

The outer AF is composed primarily of collagen type I, which is more elastic than type II [372,467,491] and gives the AF the ability to deform and restrain the NP content when the IVD is loaded. These loads can occur parallel, perpendicular or circumferentially to the collagen fibers [498-499] affecting the mechanical properties of single or multiple layers of the AF. Collagen type I is considered to resist tensile rather than compressive forces [478]. Type I collagen is synthesized by the fibrochondrocyte-like disc cells. These cells are elongated and fusiform, with long processes radiating from the cell bodies and parallel to the collagen fibers, and are thought to act as mechanoreceptors [477,480].

Maximal physiologic circumferential strains observed along the outer AF are about 4% in compression or torsion, and about 6% when in flexion or extension [500]. A FEA study suggested the maximal strains of the AF are about 10 and 20% during symmetric and non-symmetric lifting activities, respectively [501]. They seem to be higher in the innermost AF layer at the posterolateral location [501].

The Young's modulus and tensile strength seem to be higher in the direction parallel to the collagen fibers [502]. In the case of single lamella specimens the Young's modulus ranged from 28 to 78 MPa [495]. It was of 0.22 MPa when load was applied perpendicular to the collagen fibers [495]. Failure stress was also calculated for single lamella of lumbar discs and results suggested a dependence on their location on the AF [498]. In the AF anterior outer portion the results were of 10.3 ± 8.4 MPa and higher than those observed for the anterior inner portion (3.6 ± 2.0 MPa) [498]. Those of the posterior outer portion (5.6 ± 3.2 MPa) were slightly lower than the observed for the posterior inner portion (5.8 ± 2.9 MPa). Nevertheless, adjacent single lamellae seem to have similar tensile strength, suggesting local uniformity in the AF mechanical behavior [498].

The collagen fibers are also capable of changing their orientation with tension forces [469]. During axial compression and circumferential tension the fibers become closer to horizontal [503-504]. During flexion the anterior fibers also become closer to the horizontal but the posterior fibers become closer to vertical [503-504]. Under torsion the fibers in every second layer become slack and their angle closer to the vertical, while the fibers in the alternating layers become more tense and horizontal [503].

The contribution of inter-lamellar cohesion to the strength of the outer lamellae seems to be low [505-506]. In fact if stretched perpendicularly to the direction of the fibers, the adjacent lamellae are easily pulled apart [505-506]. This delamination phenomenon was proposed to explain the mechanism of herniation progression [507] in which the NP squeezes through the AF pushing through weak inter-lamellar bonds rather than rupturing the AF fibers [469].

Shear mechanical properties of human lumbar annulus were also analyzed. Results suggested that, in thin transverse slices of the anterior AF, shear modulus increase with strain rates and decreases with strain magnitude [508]. It was also observed that shear modulus was higher in the axial than in the circumferential direction; the outer higher than the inner [506].

In table 7 some mechanical properties of the AF that have been implemented in FEA studies are presented.

Table 7 – Mechanical properties of the annulus fibrosus

Material	Properties	References
Ground substance (ground matrix)	isotropic, incompressible, hyperelastic Mooney-Rivlin formulation. C1 = 0.18 ; C2 = 0.045 ; ν= 0.45	[439]
	Isotropic. E = 4.0 MPa ; ν = 0.4	[421]
	E = 4.2 MPa ; ν = 0.45	[329,415,418,426,442,446-447]
Collagen fibers	nonlinear function obtained from stress strain curve	[439,448]
	Isotropic, no compression E = 45 MPa	[421]
	nonlinear behavior Outermost fiber layers E = 550 MPa ; ν = 0.3 Intermediate fiber layers E = 485 MPa ; ν = 0.3 Intermediate fiber layers E = 420 MPa ; ν = 0.3 Innermost fiber layers E = 360 MPa ; ν = 0.3	[329,426,442,509]

E: Young's modulus; C1 and C2: material constants; ν: Poisson's ratio

3.3 The Facet Joints

The articular processes of adjacent vertebrae create a joint which is called the facet joint (zygapophyseal or apophyseal joints) (figure 35). There is a facet joint on each side of the SMS, typically behind the spinal nerves as they emerge from the central spinal canal. The surfaces of the facet joint are capped with cartilage and the joint is contained in a capsule lined by synovium.

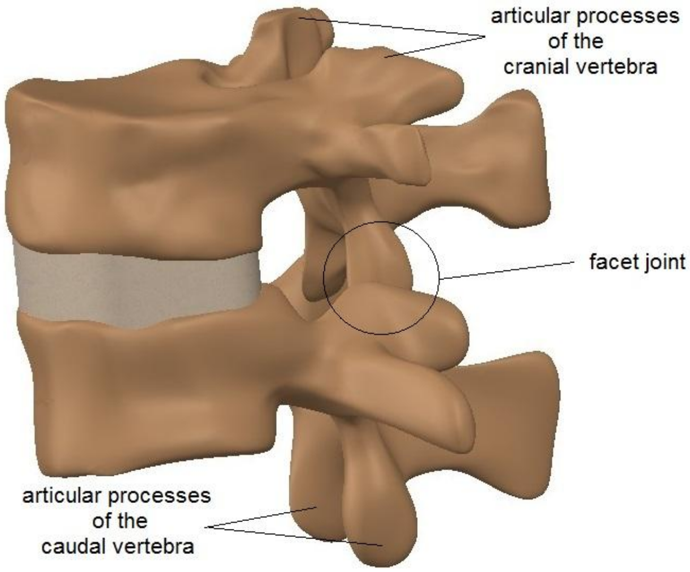

Figure 35 – Location of the facet joints.

The facet joints are gliding synovial joints and contribute to support the weight above them and to control movement between individual vertebrae of the spine [455]. In fact, these joints are capable of accomplishing two important functions: give kinematic constraints to the movement of the SMS and to withstand the loads applied to the SMS [409].

The two facet joints together with the IVD form the SMS joint complex. Usually, abnormalities of any one of the three affects the other two [510]. However, it is also possible that degenerative changes in the disc may reach a marked degree without severe changes in the facet joints or vice-versa [510].

In several studies the facet cartilage was assumed to be multilinear elastic in compression [439,446]. The facet joints can be modeled as planar surfaces interacting with a frictionless exponential pressure-over-closure relationship reflecting frictionless nonlinear contact properties [417,426,446,511-512]. In the case of compressive forces, the facet joints seem to be capable of sustaining up to approximately 30% of the load, particularly when the spine is in hyperextension [513].

3.4 The Ligaments

The ligaments of the spine can be classified as multisegmental or intersegmental. Multisegmental ligaments run along the entire spine and intersegmental are attached between the spinal processes of adjacent vertebrae. The major ligaments of the spine are distinguished as follows [460] (figure 36):

- The anterior longitudinal ligament (ALL): a multisegmental vertical band of fibrous tissue. It has uniform width and is very strong, being firmly attached to the whole anterior and medial surface of each vertebral body;
- The posterior longitudinal ligament (PLL): a multisegmental vertical band of fibrous tissue, which is attached to the IVD and to the superior and inferior margins of the vertebral bodies;
- Supraspinous ligament (SSL): a multisegmental ligament that runs on top of spinous process from the cervical region to the sacrum;
- Interspinous ligament (ISL): an intersegmental ligament connecting the spinous processes of adjacent vertebrae, namely, the inferior edge of the superior spinous process to the superior edge of the inferior spinous process;
- Ligamentum flavum (LF): an intersegmental ligament connecting the laminae of adjacent vertebrae;
- Intertransverse ligament (ITL): an intersegmental ligament connecting the transverse processes of adjacent vertebrae;
- Capsular ligament (CL): an intersegmental ligament which is part of the articular capsule of the facets joint.

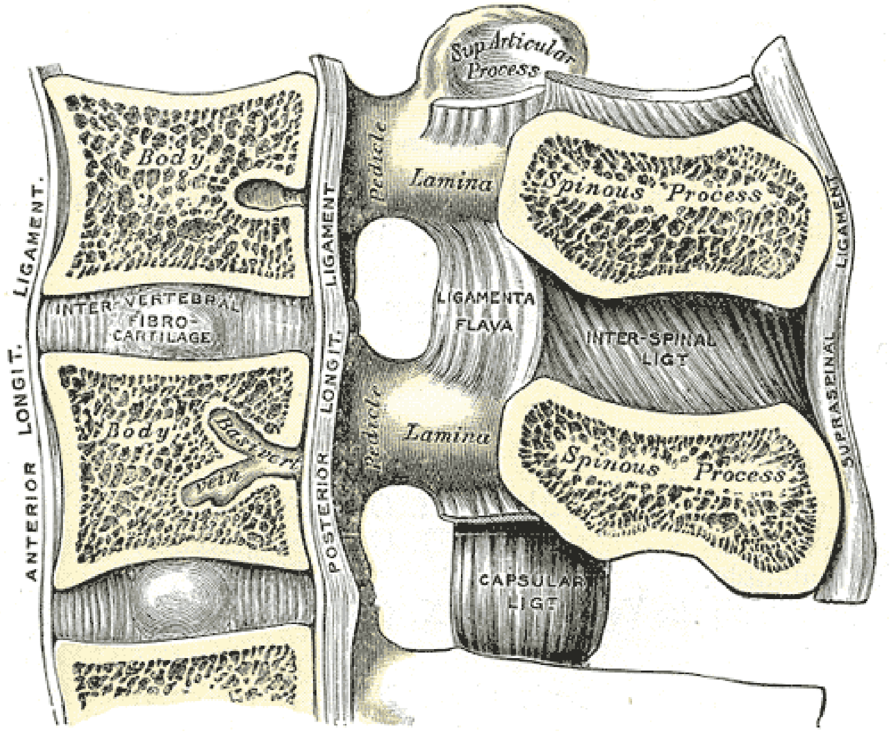

Figure 36 – Partial mid-sagital cut view of multisegmental and intersegmental ligaments of the spine [356].

In table 8 some geometric properties of the spinal ligaments of a lumbar SMS are presented.

Table 8 – Geometric properties of spinal ligaments at the spinal motion segment level

	ALL	PLL	LF	ISL	SSL	CL	ITL	References
Length (mm)	10	10	16.5	14.25	13	4.8	4.8	[426]
Cross-sectional area (mm2)	63.7	20	40	30	40	30	30	[418,442,447]

ALL: anterior longitudinal ligament; PLL: posterior longitudinal ligament; LF: ligamentum flavum; ISL: interspinous ligament; SSL: Supraspinous ligament; ITL: intertransverse ligament; CL: capsular ligament.

A natural ligament exhibits strong nonlinear load/deformation behavior [481].

In table 9 some mechanical properties of the spinal ligaments that have been implemented in FEA studies are presented

Table 9 – Mechanical properties of spinal ligaments

Ligament properties	ALL	PLL	LF	ITL	CL	ISL	SSL	References
Small strain Young's modulus (MPa)	7.8	10	15	10	7.5	8	10	[418,442,447]
Young Modulus (MPa)	Isotropic E = 6 to12							[418,421,442,514]
Transition strain (%)	12	11	6.2	25	25	20	14	
Large strain Young's modulus (MPa)	20	50	19	33	33	15	12	[418,442,447]
Max. failure load (N)	510	384	340	284	284	130	200	[481]

ALL: anterior longitudinal ligament; PLL: posterior longitudinal ligament; LF: ligament flavum; ISL: inter spinous ligament; SSL: supra spinous ligament ITL: intertransverse ligament; CL: Capsular Ligament;

4. Guidelines for Testing

Some standardization exists concerning the study of the spine. The majority of standards have been published by ISO and the American Society for Testing and Materials (ASTM International) to regulate the design and implantation of spinal implants or prostheses and ensure good implantation results. Spinal implants are foreign bodies which are used to replace degenerated spinal components functioning below an acceptable level, for example a degenerated and painful IVD. Nevertheless, whenever applicable or possible, the same standards can be followed or adapted to perform experimental studies with other purposes. In fact, the best and effective way to compare results from different sources is to apply the same standardized test protocols.

The ISO category that regulates spinal implants has the International Classification for Standards (ICS) number 11.040.40. These standards have been published by the ISO Technical Committee (TC) 150, named “Implants for surgery”, which was created in 1971. The Deutsches Institut für Normung (DIN) is the TC150 secretariat. Presently, ISO TC150 is formed by seven subcommittees (SC) and three working groups (WG). The complete reference where spinal implants standards can be found is the ISO TC150/SC5. This reference can be found in the ISO catalogue along with other important standards related with the process of testing medical devices. Among them, emphasis should be given to those published by ISO TC 108/SC 4 (Mechanical vibration, shock and condition monitoring: Human exposure to mechanical vibration and shock), TC76 (Transfusion, infusion and injection equipment for medical and pharmaceutical use), TC84 (Devices for administration of medicinal products and intravascular catheters), TC121 (Anaesthetic and respiratory equipment), TC135 (Non-destructive testing), TC159 (Ergonomics), TC168 (Prosthetics and orthotics), TC170 (Surgical instruments), TC194 (Biological evaluation of medical devices), TC209 (Cleanrooms and associated controlled environments), TC210 (Quality management and corresponding general aspects of medical devices), and TC212 (Clinical laboratory testing and *in vitro* diagnostic testing systems).

The ASTM Committee F04 (Medical and surgical materials and devices), particularly the subcommittee 025 are the appropriate ones to find standards concerning spinal implants and prostheses. Besides F04.025 subcommittee, significant information can be also found in standards published by subcommittees, F04.11 (Polymeric materials), F04.12 (Metallurgical materials), F04.13 (Ceramic materials), F04.15 (Material test methods), F04.16 (Biocompatibility test methods), F04.21 (Osteosynthesis), F04.22 (Arthroplasty), F04.41 [Classification and terminology for tissue engineered medical products (TEMPs)], F04.42 (Biomaterials and biomolecules for TEMPs), F04.43 (Cells and tissue engineered constructs for TEMPs) F04.44 (Assessment for TEMPs), and F04.97 (Editorial and terminology).

The papers published by Panjabi *et al.* [515-517], Ashman *et al.* [518], Adams [519-520], Wilke *et al.* [414,521-524], and Goel *et al.* [525] are also among the most valuable resources addressing spinal testing protocols.

Usually, a complete set of standards for testing implantable spinal devices includes the topics of biocompatibility, materials requirements, mechanical testing, FEA, *in vivo* animal testing, and clinical trials [525]. For the purpose of the present work the topics of mechanical testing and *in vivo* animal testing are the most relevant and will be addressed[7].

The mechanical testing of SMS requires *ex vivo* specimens and loading machines. These experiments are of major important in the case of spinal implants since they represent the step before *in vivo* animal testing and clinical trials. They are also important to test new sensors and surgical techniques, or to validate the results obtained from FEA studies.

4.1 *Ex Vivo* and *In Vivo* Specimen

Ideally, healthy human cadaveric and fresh specimens are preferred. In the fresh state specimens should be tested few hours after death and dissection [526-527]. Formalin-fixed specimens have their biomechanical properties affected and are not recommended for biomechanical and clinical testing [521,528-529]. Degenerated and osteoporotic spines as well as those with significant injury or tumors should not be used as well, particularly for testing spinal implants [414]. Nevertheless, several recommendations exist to implant spinal devices in osteoporotic spines [530-532]. The quality of the IVD and bone should be assessed from quantitative measures obtained with CT, MRI or other methods [414,533]. Several factors can affect the vertebral bone density such as race, age, sex, menopause, nutrition and physical exercise [534-538].

More than one specimen has to be tested to allow statistical analysis, particularly for repeatability and reproducibility. In the case of spinal implants six specimens are recommended [414], and groups should be formed accordingly to sex, age, cause of death, bone mineral density and length [414,525].

Specimens should be sealed in double or triple plastic bags. If it is not possible to test them fresh, they have to be stored frozen at -20 to -30 °C and thawed out several hours before testing [259,414,539-540]. Freezing and thawing out at room temperature seems to have little effect on the biomechanical behavior of the bone and soft tissues [515,541-543]. Even so, the time spent in the thawed condition at room temperature should be reported, because the properties of the specimens after twenty hours will begin to change [414,419]. Moreover, freezing seems to modify the ultimate compressive load of the SMS and its creep behavior [544-545]. Tests should be performed between 20° and 30 °C [414]. Higher temperatures can accelerate the cellular autolytic process and compromise the biomechanical properties of the specimen [414].

Mechanical tests on soft tissues are usually performed with the specimen immersed in a physiological solution at constant temperature. In some studies the SMS specimen was kept in a

---

[7] A more complete description of spinal implants, standards and testing protocols can be obtained from the report of Intelligent and Bio-inspired Products: Spinal implants and Prostheses (see Academic Work, p.7).

Ringer's solution[8] before and during the tests [546]. Nevertheless full immersion of the specimen can introduce artifacts during mechanical testing [419,547-549]. Swelling can either be reversed or prevented by axial compression in the physiologic range or with iso-osmotic solutions [547-548].

Specimens also need to be protected against drying. A 100% humidity chamber should be used for that purpose [414]. Alternatively, dehydration can also be prevented wrapping the specimens loosely in plastic, a food-packaging wrap or in gauze tissue moistened with saline [414,540]. Spraying the specimen intermittently with 0.9% saline further assures its moist condition [414] and has a negligible effect on the mechanical behavior of the specimen [419]. Hydrophilic samples should be pre-soaked prior to testing and then the initial weights should be recorded accordingly.

Extrapolations from experiments with *ex vivo* or even *in vivo* animal specimens to human purposes may be controversial [414,516,525]. In fact, there are substantial anatomical differences between humans and animal specimens that may compromise the validity of the results [550]. Most reliable data is obtained when tests are performed directly on living subjects or on human cadaveric specimens [414,551]. Even so, a cadaveric model will not accurately represent the response of the spine or the SMS to loading *in vivo* [551]. For example, the muscle forces are usually neglected because muscles are dissected from the specimen. Nevertheless, animal specimens must not be underestimated. In the case of spinal implants, for example, *ex vivo* and *in vivo* animal experiments are mandatory before clinical trials. Some animal specimens such as the calf and sheep are considered to be valid for specific purposes, such as for ROM measurements, study of the stabilization capacity of spinal implants, and disc hydration [414,522,524,550,552-553]. Furthermore, in the case of spinal implants, there is a strong basis to compare the output data of new implants to those that were tested before and approved for human use [414]. The use of other animal species should also not be neglected. It has have been useful to test new approaches, methodologies and techniques with potential to be explored in veterinary or human applications [20,552]. Still, in such cases and taking the ideas just presented into account, the results should not be extrapolated to human purposes, particularly if no human data is available.

Major risk concerning use of cadaveric specimens is infection (AIDS, hepatitis and others) [414].

In vivo animal testing is performed to assess the structure, function, histology, and the biomechanics of the device *in situ,* a final and decisive step before clinical trials [525]. Use of comparable surgical techniques and approaches as in humans is strongly recommended [525].

Animal welfare requirements are standardized (ISO 10993-2:2006).

Several species have been used, from rats to rabbits, sheep [524,554], goats, dogs [555], pigs and baboons [525,556]. The sheep and the baboon are often used for the cervical and lumbar regions, respectively, and to evaluate interbody devices [525,554]. Smaller primates can be used to

---

[8] Introduced by Sidney Ringer in 1882. The solution contributes for tissue preservation and contains sodium chloride (6 g), potassium chloride (0.075 g), calcium chloride (0.1 g), and sodium bicarbonate(0.1 g), in the concentrations in which they occur in body fluids. If sodium lactate is used instead of sodium bicarbonate, the mixture is called lactated Ringer's solution.

approximate load modes, but larger primates, such as baboons, are required to simulate both load magnitude and direction [525].

Animals are particularly suitable to evaluate both implant and implant-tissue interface behavior, such as resorption (for instance with polylactic acid and/or polyglycolic acid devices), static compressive strength, wear, cracking, and deterioration [525]. The interface may be investigated for subsidence (endplate deterioration), fixation (migration of the device), ingrowth (into osteoconductive coatings), and possible wear debris effects on neural elements and surrounding tissues [525].

In most animal studies, a systemic analysis is also commonly performed, including the histopathologic response in local and systemic tissues to device material and possibly wear debris generated in non-failure and failure modes [525]. Pathologic assessment for all tissues should include but not be limited to comments on the architecture of the tissues and the presence of wear debris, as well as any signs of foreign-body giant-cell and/or granuloma inflammatory reactions, degenerative changes, or autolysis [525]. For motion preservation devices, the segmental stiffness properties through the normal ROM may be investigated [525].

Limitations of animal studies, as was already mentioned for *ex vivo* research, include dissimilarities between human and animal spines with respect to the spinal loads, spinal motions, anatomy, and the difficulties in adjusting a spinal device (or sensor) to properly fit the animal spine [525].

4.2 Spine Wear Simulators

A loading device or a spine loading simulator is a special test apparatus in which spinal specimens can be mounted and tested under defined loading conditions [414]. These simulators are mandatory to characterize the *in vitro* or *ex vivo* mechanical behavior (*e.g.*, wear) of new spinal devices and compare them with those clinically accepted [557-558]. They have been designed to replicate the static and dynamic loading conditions, motion patterns and lubrication/physiologic conditions that are observed *in vivo*. To accomplish the previous purpose, a spine loading simulator should fulfill ISO standards, namely the ISO 18192-1 (Loading and displacement parameters for wear testing and corresponding environmental conditions for tests) [414,557-558]. Some general guidelines of ISO 18192-1 include:

- Test specimens from all spine regions;
- Test single SMS, multiple SMS and entire spines;
- Allow the specimen to move freely in all six DOF;
- Apply all the six loading components separately, in both directions, and without manipulation;
- Provide all loading combinations;

- Allow application of loads in a continuously or in stepwise mode.

ISO 18192-1 also defines the loading and motion profiles for cervical and lumbar SMS as well as the lubrication requisites. In table 10 these parameters are compared to the ASTM F2423-05 (Standard guide for functional, kinematic, and wear assessment of total disc prostheses) [559].

Table 10 – Comparison between ISO 1892-1 and ASTM F2423-05

Test parameters	ISO 1892-1		ASTM F2423-05	
Loading profile	Cervical	Lumbar	Cervical	Lumbar
Load limit (N)	50-150	600-2000	100	1200
Frequency (Hz)	1.0	2.0	2.0	
Tolerance (%)	±5		±5	
Motion profile				
Flexion/extension (FE)	±7.5º	+6.0º/-3.0º	±7.5º	±7.5º
Lateral bending (LB)	±6.0º	±2.0º	±6.0º	±6.0º
Axial rotation (AR)	±4.0º	±2.0º	±6.0º	±3.0º
Phase angles	LB phased by 90° from FE; AR and LB phased by 180°		User defined	
Frequency (Hz)	1.0 ±0.1 (up to 2.0)		2.0	2.0
Tolerance	± 0.5° at the peaks		± 0.5° at the peaks	
Lubrication				
Temperature	37±2 °C		37±3 °C	
Protein additives	Sodium Azide or other anti-bacterial/antimycotic and ethylenediaminetetraacetic acid (EDTA)			
Protein concentration	30g/l		20g/l	
PH monitoring	optional		Not mentioned	
Fluid collection	0.5 million cycles		1.0 million cycles	

Regardless of the loading protocol that can be used, a “free-end model” approach is recommended in the construction of spine simulators [557]. In this approach loads are applied to the cranial vertebra, while the caudal vertebra is fixed and reacts to the forces. A six-component load cell is fixed into the base of the loading machine to measure the net reaction forces applied to the caudal vertebra [414]. Thus, fixing the specimen to the holder of the spinal loading simulator is a critical step. The caudal vertebra should also have an orientation approximating that *in situ* and matching the global coordinate system of the test apparatus [414]. If compression loads are the only to be applied, depending on the SMS that is used, it may be necessary to partially cut the cranial and caudal vertebral bodies to maintain them parallel and ensure one DOF in load application [138]. Both, the cranial and caudal segments, should be potted in a suitable polymeric or low-melting-point alloy, such as PMMA [414,557]. Anchoring the specimen in the potting medium may be improved with screws set partly into the specimen and several thread-pitches and the screw head jutting into the potting [138,414].

Wilke *et al.* [414] have also presented a set of procedures to accomplish during testing of spinal implants:

- The project title and number;
- Specimen data, including sex, age, weight, cause of death;
- Preparation methods;
- Test series order;
- Moment and distraction magnitudes for screws, clamps, and hooks;
- Test apparatus drawings and functional description;
- Preconditioning of specimens;
- Environmental conditions (temperature, humidity);
- Control parameters (loading magnitude and speed);
- Test duration.

These procedures can be followed or adapted to many other experiments and will contribute for the reproducibility of the results and better data comparison. To follow the previous guidelines seems a relatively easy task if research centers possess a well-designed spinal loading simulator. Nevertheless, those commercially available are quite expensive (their price may exceed €250,000.00) and for that reason many research centers have to customize their loading simulators and protocols, which may difficult data comparison [560-561].

Some of the current commercially available spine simulators are (figure 37):

- the PROSIM Hip & Spine Implant Wear Simulator (Simulation Solutions Ltd, UK; www.prosim.co.uk);
- the Bionix® Spine Wear Simulator (MTS, MN, USA; www.mts.com);
- the EndoLab® Spine Simulator (EndoLab® Mechanical Engineering GmbH, Thansau, Deutschland; www.endolab.org);
- AMTI simulators (AMTI, MA, USA; www.amti.biz), such as the ADL Hip Simulator, ADL Force 5, and the VIVO^{TM} simulator;
- the BioPuls^{TM} Multi-axial Spine Testing System (Instron, MA, USA; www.instron.us);

- Bose simulators (Bose Corporation ElectroForce Systems Group, MN, USA; http://worldwide.bose.com/electroforce), such as the multi-axial Kinematic Spine Simulator, the ElectroForce Spinal Disc Fatigue/Wear system, and the Multi-specimen ElectroForce® BioDynamic® test instrument.

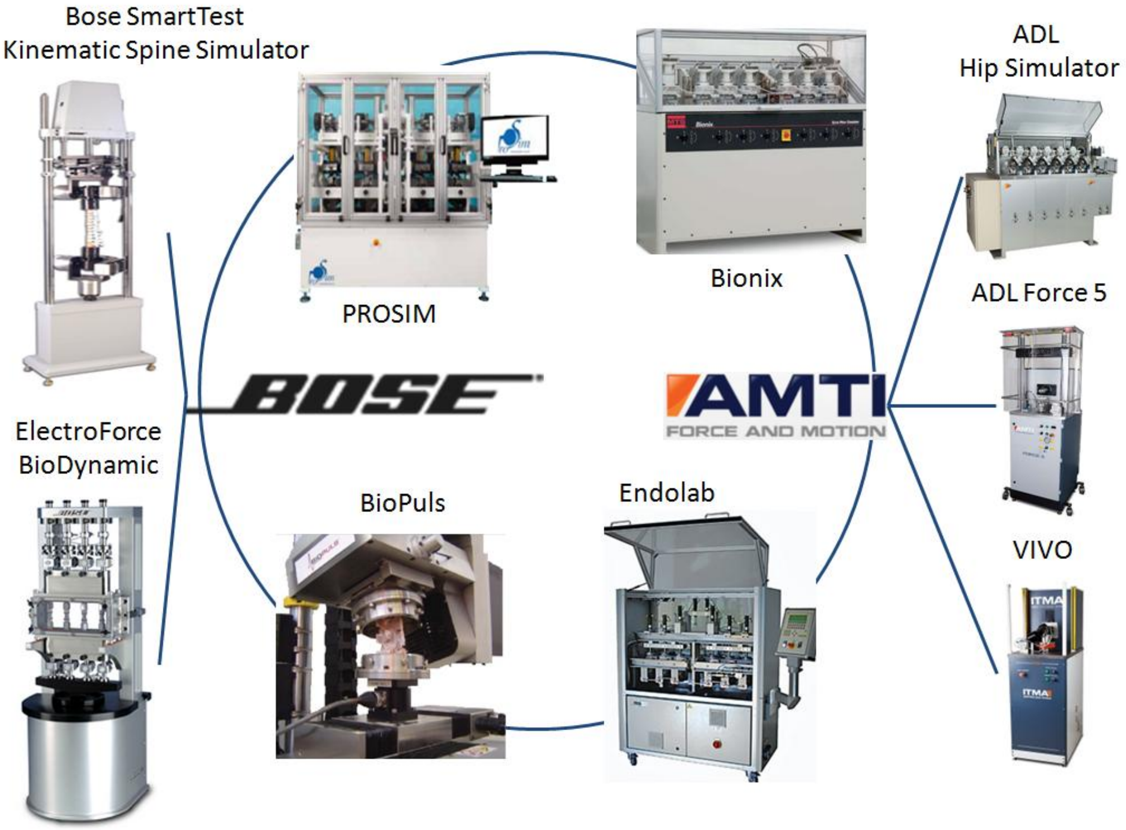

Figure 37 - Spine simulators [Adap. 562,563-569].

A comparative description of some of these simulators is listed in table 11.

Table 11 – Comparison of basic features of some loading simulators*

Features/Simulator	PROSIM	Bionix	EndoLab	ADL Hip Simulator	ADL Force5	VIVO	Bose*
Test wear/ Load-soak stations	6/2	6/2	6/2	6+6/--	1/--	1/--	
Max. axial load (kN)	Up to 5	4	5	4.5	±4.5	±4.5	±5.6
Max. axial Displacement (mm)	--	+12.7/-3.2	--	±25	±25	--	±50
Max. flexion/extension:							
ROM (º)	±60°	±10°	30°/25°	±55°	±100º	±100º	120º/-60º
Torque (Nm)	--	15	--	20	45	--	±15
Max. lateral bending:							
ROM (º)	±20°	±10°	20°/15°	±20°	--	±30º	±60º
Torque (Nm)	--	15	--	20	--	--	± 15
Max. int./ext. rotation:							
ROM (º)	±30°	±7.5°	9°/9°	±20°	±100º	±40º	±50º
Torque (Nm)	--	10	--	8	45	--	0.074
Max. ant./post							
Load (N)	--	zero to fully locked	--	--	±4500	--	±1000
Displacement (mm)	--	±4.5	±20	--	25	±25	±50
Max. left/right							
Load (N)	--	zero to fully locked	--		--	--	±1000
Displacement (mm)	--	±4.5	±20		--	±25	±50
ISO standards	18192-1	18192	18192-1	12189 18192-1	12189 18192-1	16402 18192-1	--
ASTM standards	--	F2624	--	F1717-04 F2423-05	F1717-04 F2423-05	F2790-10 F2694-07	--
References	[562,570-572]	[573-577]	[576,578-581]	[576]	[568]	[569]	[582]

* BioPuls and other Bose simulators were not described due to lack of information

4.3 Load Protocol

Precondition loads and the load protocol are among the most critical issues in spine testing since both can affect the mechanical behavior of the specimen [583-586].

Translational and rotational preloads in clinically relevant loading modes may simulate the effect of spinal muscles [525]. In the lumbar region, a preload of 400 N (about 60% of the body weight above L3-L4 disc level of an average person) with a maximum of 1000 N is recommended to test spinal implants [525]. For the cervical region the preload may range from 50 to 100 N (about one or two times the weight of the head) [525]. In both cases a progressive increase of compressive load should be used [586].

Loading precycles should also be applied in the three primary test directions, in both positive and negative directions, to minimize the viscoelastic behavior of the specimen and ensure reproducibility [414]. The first two cycles of at least three cycles shall be used as precycles [414]. In fact, the load displacement behavior of the first two cycles can be clearly distinguished, while the difference between the 2nd and 3rd cycles is considerably reduced [414]. The 3rd cycle in many cases is nearly identical to all subsequent cycles [414]. For this reason the 3rd cycle is usually recommended for analysis [414,525]. If this is not the case the cycles should be repeated until a reproducible result is achieved [414]. In any case, the rate of loading and the number of preconditioning cycles should be reported [414].

There is however some controversy considering the application of preloads. Their effect on the results seems to be dependent on its location with respect to the segment center of rotation producing satisfactory results only in flexion and extension [586]. Others have concluded that the quality of the measured data with and without preloads is similar [525]. Thus, tests without preload may also be acceptable for comparative evaluation of spinal instrumentation.

Loads can be applied using two basic protocols, the displacement control or stiffness protocol and the load control or flexibility protocol [525]. In the first a known displacement is applied at the free end of the specimen and the resulting loads and motions across various segments are quantified. In the second, motion is measured in response to a known load.

As previously mentioned the reaction loads and moments are usually measured at the caudal end of the specimen [414]. Their directions have also been normalized [414,525,587].

Spinal simulators can present several possible combinations. In the case of EndoLab simulators, for example, motions are applied in the caudal end and loads are applied in the cranial end [559]. In the case of Bionix simulators, flexion/extension and lateral bending motions are applied in the cranial end while the axial load and the axial rotation is applied in the caudal end of the station [559].

Loads should be applied within the elastic range of the specimens [414]. As a general rule the load should be at least as high as that needed to achieve the normal ROM for the given specimens [414].

Loading protocols may vary according to the region of the spine and the condition of the specimen [414]. Standard loading is defined as the three pure moments (flexion/extension, axial rotation, and lateral bending) without preload [414]. Moments of ±7.5 Nm [414] or ranging from 6 to 10 Nm [525] have been suggested for the lumbar region. For the thoracic region ±5 Nm [414]. For the cervical region of ±1 Nm at C1-2 levels and of ±2.5 Nm from C2 to C7 [414], or ranging from 1.5 to 3 Nm [525]. If osteoporotic spines are tested the magnitude of the corresponding moments should be reduced by one-half [414]. All spine simulators that have been described meet or exceed these recommendations.

Moments should be applied in a quasistatic manner with three load-unload cycles and data recorded on the 3rd load cycle [525]. Hybrid protocols (ISO/AWI 13077-1) intended to measure the effects of the spinal implant in the adjacent levels were also proposed [516,588-589]. The idea underlying hybrid approach is to produce an overall rotation of the implant model equal to the intact case [588].

Load combinations are recommended because they are capable of simulating *in vivo* condition. All combinations should be reported as well as the strategies used to apply them [414].

The loading rate seems to affect the stiffness of the specimen and should be controlled [419]. Moments of ±7.5Nm over the range of 0.6 to 5.1 $°s^{-1}$ are recommended [419]. Much slower rates may introduce creep effects and much faster rates may amplify the effect of the mechanical system inertia [414]. If loading is applied stepwise, the time between load stepping and motion measurement at each interval should be reported [414].

5. Final Remarks

The SMS is the functional unit of the spine and it usually represents the general mechanical behavior of a given region of the spine. Its comprehension requires a global understanding of the spine, its regions, major anatomical components and curvatures. In the present review, special emphasis was given to the vertebrae and the intervertebral discs, focusing on their anatomical structure, histological and biomechanical properties. The guidelines for testing the SMS were also addressed. These guidelines are usually part of ISO or ASTM standards and should be followed because they represent an effective way to compare results from different sources. They also represent a strong contribute for those research centers interested in spine research, allowing them to understand their present limitations and define future investment and research lines.

Part III – Experimental Work

Study 1 – Using Conventional Sensors to Assess Intervertebral Disc Bulging [9]

---

[9] Roriz P, Ramos A, Frazão O, Santos J, Simões J Não linearidade e anisotropia do anel fibroso do disco intervertebral submetido a compressão. In: I Simpósio de Biomecânica e Performance Humana, Universidade Fernando Pessoa, Porto, March, 25-6 2011.

1. Introduction

A wide variety of strain gauges (SG) have been used to assess strain in body tissues, mostly in bone [117-125]. In fact, they are considered the gold standard measuring bone strain [26,120,590-592].

Technically, the surface for bonding a SG should be chemically clean (*i.e.*, free of oil, greases, organic contaminants and soluble chemical residues), water proof and sufficiently rough [592]. Whereas this is relatively easy to perform with cadaveric bone [590] it seems more difficult to accomplish in soft tissues due to their high water content (between 65% to 80%) and strong elastic behavior [105,593]. Thus it may be hypothesized that in such kind of tissues the risk of debonding or faulty adhesion is increased and it can lead to underestimation or erroneous readings of strain [592]. Nevertheless, to our best knowledge, few studies have reported the use of SG glued directly to soft tissues [216]. Alternatively, SG can be fixed to special frames (buckles) which, in turn, are attached to the soft tissue [134,164-165]. Ravary *et al.* [105] provided an excellent review of these and other transducers that have been used to sense strain and force in soft tissues. The major problem of buckle transducers is their large dimensions restricting their use to large structures, such as the Achilles tendon, the anterior cruciate ligament or the patellar tendon [105,134]. For example, the dimensions of the implantable E-form buckle transducer may range between 9×5 mm and 34×20 mm, for animal [105] or human [180] applications, respectively.

The purpose of the present study was to demonstrate that SG can be successfully glued to the outer surface of the intervertebral disc (IVD) and provide readings of strain under compressive loads.

The IVD is a fibrocartilaginous structure found between adjacent movable vertebrae of the spine. It acts as a load bearing structure preventing the vertebrae from contacting each other and protecting the nerve roots that irradiate from the spinal cord.

In the mechanical view the IVD deforms under compressive load while the majority of soft tissues, such as tendons and ligaments, deform under tension loads. To accomplish this load bearing function the IVD has two main anatomical structures: the nucleus pulposus (NP) and the annulus fibrosus (AF). The NP is a semi-fluid (gelatinous) region located in the inside of the IVD. It consists of a three dimensional network of collagen fibers (mainly type II), enmeshed in a mucoprotein gel composed of water and proteoglycans [466-469]. Under compression it exhibits an incompressible [421,426,439,481-482] and isotropic [421,439] behavior. Thus, it acts as a cushion, increasing the intradiscal pressure under compression [259,465,478]. The AF encloses the NP like a solid elastic ring [452]. It is composed of a homogeneous ground substance (the matrix or mesenchyme) reinforced by a collagen fiber network. This network is arranged in a series of discontinuous concentric layers called lamellae [460,492]. The highly orientated and layered structure of the lamellae [481,491-492,494] along with the AF elastic content (mainly collagen type I) [372,467,491] suggests a nonlinear and anisotropic behavior [421,443,497,506,594-597]. In the mechanical view the AF seems particularly well adapted to resist tensile forces resulting from the loads encountered during compression and torsion of the spine [478,598].

Loads acting on the spine are usually followed by an increase in the NP pressure, a bulging action of the AF and a decrease of IVD height [496]. These actions will result in the increase of the strain, particularly in the outer portions of the AF and excessive load can contribute to disc disruption, degeneration and pain [599-600]. Thus, studying these actions seems an important topic.

2. Material and Methods

One healthy disc of an *ex vivo* male porcine (weight: 9.2 kgf; age: 1.½ months) dorsal SMS was obtained by dissection, instrumented with SG and tested under compression using a mechanical testing machine.

2.1 Specimen

The SMS consisted of two adjacent vertebrae with the intervening disc and ligaments intact (muscles removed). The anterior longitudinal ligament was partially removed to allow SG placement on the anterior (ventral) surface of the IVD. When removing soft tissues it is important not to damage the IVD, mostly during the excision of the anterior longitudinal ligament which is firmly attached to the whole anterior and medial surface of the vertebral bodies. The whole process took about two hours. After dissection the SMS was stored in a sealed polyethylene bag, frozen to approximately −20°C for less than one week, and allowed to complete thaw at laboratory room temperature (25°C) before testing. Freezing and thawing should not significantly affect specimen physical properties [515,551]. To prevent dehydration the SMS was wrapped in tissue moistened with saline. The bone and disc status were confirmed by means of X-ray, visual inspection and manipulation, before and after the experiment.

2.2 Specimen Holder Apparatus

A built-for-purpose stainless steel specimen holder, consisting of two plates with drilled metallic rings for screw attachment, was used to fix and align the SMS with the compression machine (figure 38).

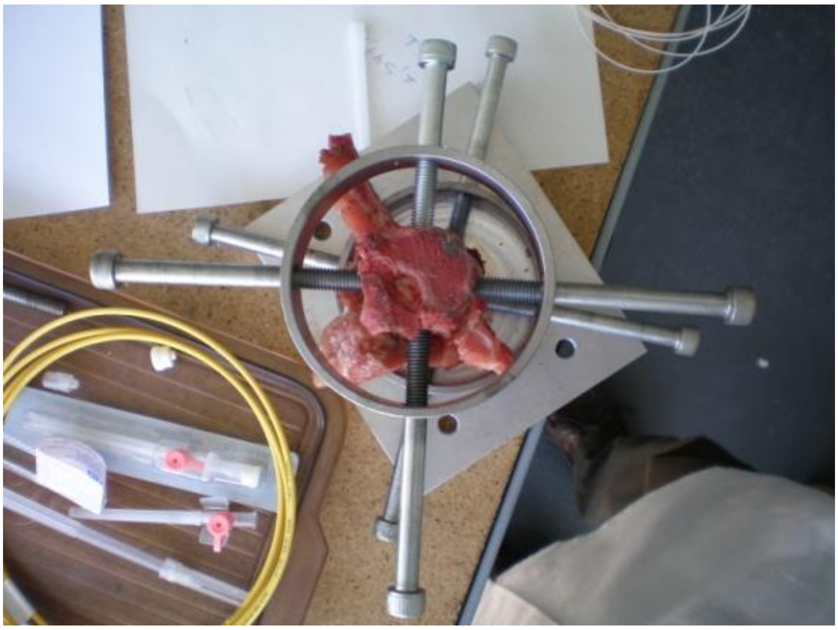

Figure 38 - Top view of the specimen holder (removed the top plate and vertical jigs).

The cranial and caudal vertebral bodies of the SMS were partially cut, attached with screws and cemented to the plates and metal rings of the specimen holder. Bone cement also contributed to fulfill gaps and to allow a better distribution of stress during compression. Additionally, four vertical jigs were used to guide vertical motion and maintain the plates parallel to each other. The most critical issue concerning this procedure is the working time of bone cement (about 5 to 8 minutes after mixing). The whole process took about one hour.

2.3 Strain Gauge Bonding

Three previously soldered linear SGs (HBM 1-LY11-3/120) with a measuring grid of 3 X 1.4 mm and a grid carrier of 8.5 X 4.5 mm were bonded directly to the AF surface with a low viscosity cyanoacrylate adhesive (HBM Z70, Darmstadt, Germany) (figure 39).

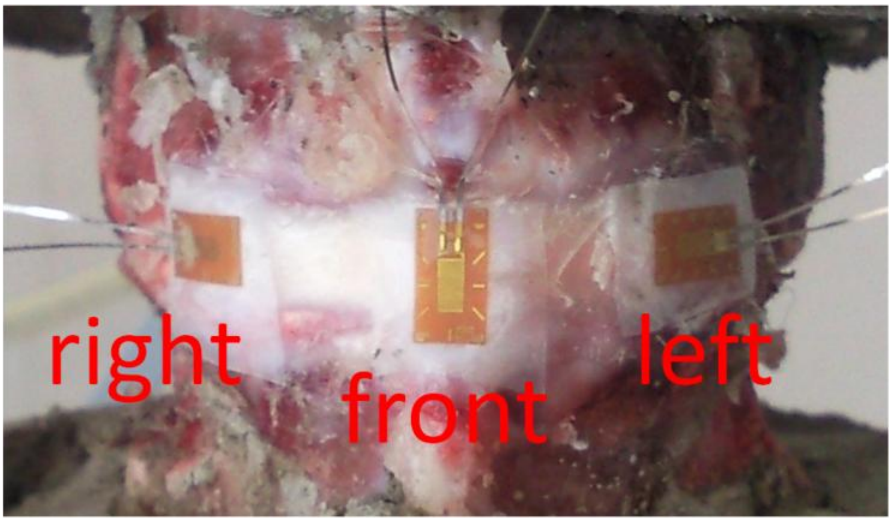

Figure 39 - Anterior view of the functional spinal unit and strain gauges bonded to the annulus fibrosus of the intervertebral disc.

Two SGs (labeled as “left” and “right”) were glued to the anterolateral wall of the AF in order to measure circumferential strain (figure 39). One SG (labeled as “front”) was glued to the anterior wall of the AF in order to measure axial strain (figure 39).

Initially the bonding area was marked, cleaned and degreased with alcohol. Then the area was slightly roughened with a dental tungsten carbide abrasive bur and cleaned again with alcohol. A polyurethane-based transparent dressing for wounds (Opsite spray, Smith & Nephew, London) was applied for waterproofing of the surface. Finally, the cyanoacrylate adhesive was applied and the SG oriented to the desired measurement position on the AF surface, and pushed using thumb pressure over a Teflon foil for 1 minute. The whole process took less than one hour.

2.4 Testing Loading Machine

A customized loading machine was used to apply a uniaxial compressive load to the specimen. It consisted of a servo-pneumatic system having a double effect pneumatic cylinder (Festo CRDNGS-80-200-PPV-A), a servo-valve (Festo MPYE-5-1/8-HF-010-B), an optical linear scale (Fagor SV- B220), and a load cell (AEP TC4) with 10 kN capacity and 0.1% resolution of that value [601] (figure 40). All the control, monitor and data acquisition software were implemented using LabVIEW 8.0. The interface and the connection between the software and instrumentation devices were made using a hardware platform (National Instruments PAC CompactRIO®). A more detailed description can be found elsewhere [601-602].

Figure 40 – A view of the complete setup. A detail of the specimen *in situ* is provided.

2.5 Load Protocol

A preload of 5N was slowly applied and maintained during testing to ensure permanent contact and alignment between the specimen holder and the loading machine. It also contributed to minimize zero shifts and allow more stable initial strain readings [26]. After this, two pre-conditioning cycles were performed before data acquisition and a set of six repeated cycles was collected for analysis.

A quasi-static compression load protocol was applied for each cycle. It consisted of a load part ranging from 0 to 200N and an unload part from 200 to 0N. Load step was of 25N. Each load was held constant for a period of 30s and load transition time was set to be linear for a period of 0.5s (figure 41).

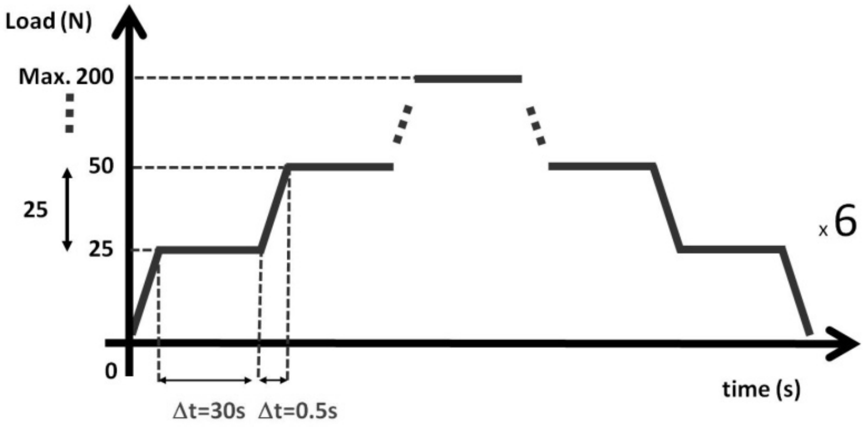

Figure 41 - Schematic representation of a load cycle.

The load protocol, including previous alignment of the sample with the loading machine and SG calibration, took less than two hours.

2.6 Statistical Procedures

Related Samples Wilcoxon Signed Rank Test was applied to evaluate significant differences between trials ($p \leq 0.05$). To express strain measurements variability under repeated conditions (multiple trials or loading cycles) the standard variation (SD) and the coefficient of variation (CV) were calculated. The SD gives an idea of the variability at each point of the loading cycle (for each applied load) and the CV is a relative variability measure that can be used to “summarize SD” information over the whole cycle [603]. It is calculated as the ratio between the average standard deviation (SD) and the average mean (X) of the loading cycle (equation 1)

$$CV(\%) = \frac{\sqrt{\frac{1}{N}\sum_{i=1}^{N} SD_i^2}}{\frac{1}{N}\sum_{i=1}^{N}\left|\overline{X}_i\right|} \times 100$$

Equation 1 – Coefficient of variation (CV). SD_i is the average standard deviation at step i of the loading cycle and $\overline{X}_i$ is the mean at step i of the loading cycle. N is the number of steps.

3. Results and Discussion

One healthy disc was submitted to compression in order to measure strain in different locations of the AF. No signs of disc failure or tears, fissures, protrusions or prolapses were observed during and after the experiment. Moreover, no signs of debonding or faulty adhesion of the SG where detected during and after the experiment.

Circumferential strain is plotted in figure 42 and figure 43 for the right and left SGs, respectively. Axial strain, measured by the frontal SG, is plotted in figure 44.

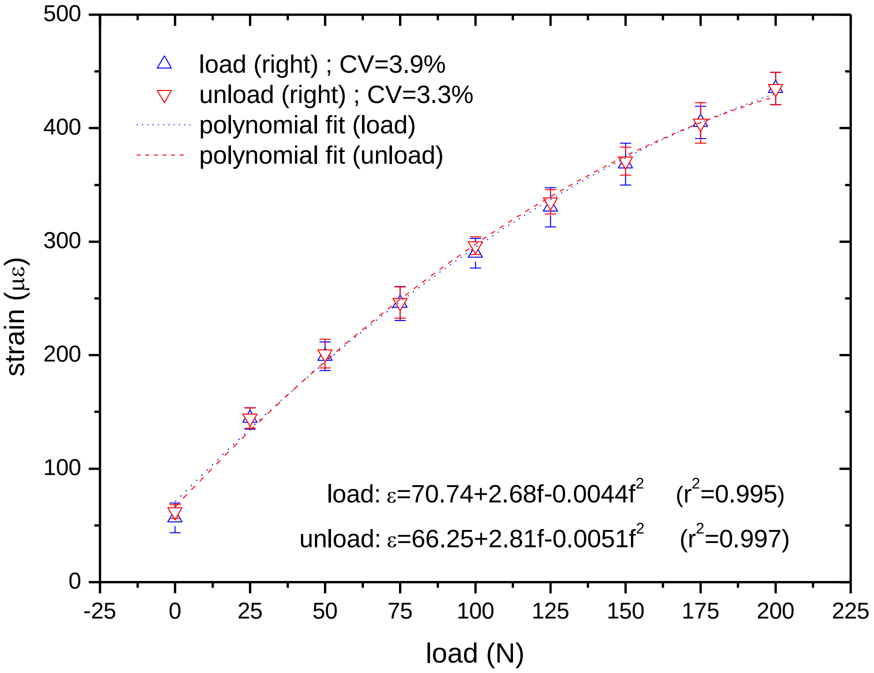

Figure 42 - Circumferential strain on the right side of the outer annulus fibrosus under compressive load. Average results of the six loading cycles are presented. Y error corresponds to one standard deviation. The adjusted coefficient of determination (r^2) was calculated

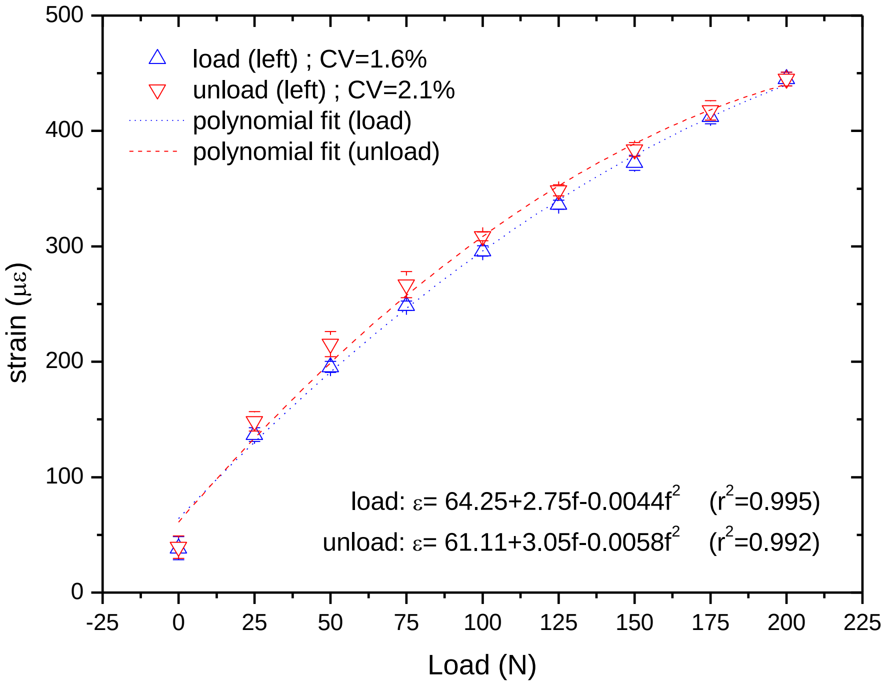

Figure 43 - Circumferential strain on the left side of the outer annulus fibrosus under compressive load. Average results of the six loading cycles are presented. Y error corresponds to one standard deviation. The adjusted coefficient of determination (r^2) was calculated

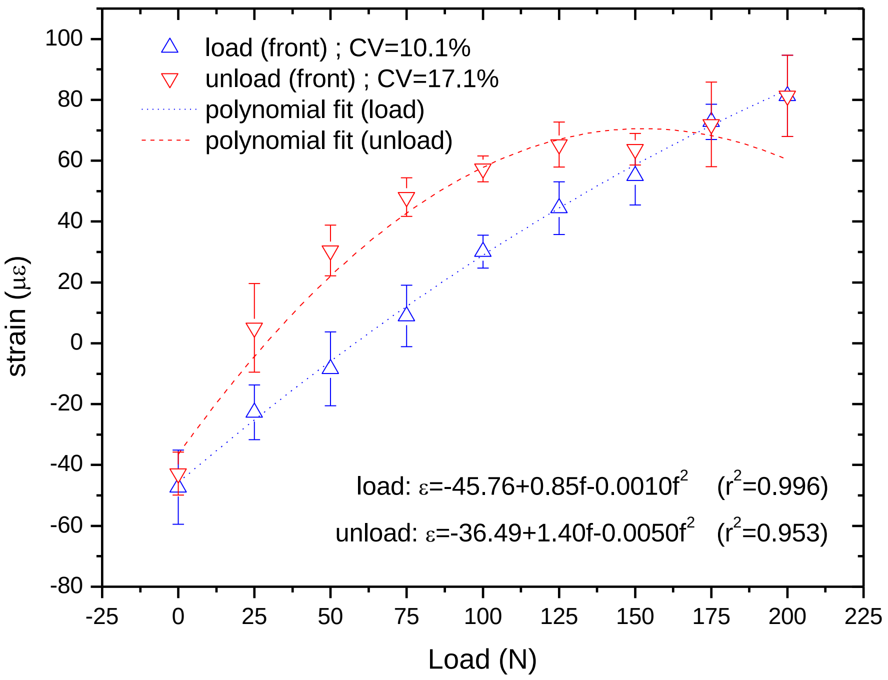

Figure 44 - Axial strain of the outer annulus fibrosus under compressive load. Average results of the six loading cycles are presented. Y error corresponds to one standard deviation. The adjusted coefficient of determination (r^2) was calculated

Circumferential and axial strain increased during loading and decreased for unloading, suggesting that the AF collagen fibers were able to resist the tensile forces induced by the bulging action of the IVD [491,496]. Nevertheless, significant differences ($p \leq 0.05$) were found between the load and unload counterparts. The average of these differences was smaller for the right SG (-2.86±2.51 $\mu\varepsilon$; p=0.017) than it was for the left one (-11.59±6.18 $\mu\varepsilon$; p=0.012) and front SGs (-20.77±15.27 $\mu\varepsilon$; p=0.017). A similar behavior was observed in other studies suggesting the presence of hysteresis [138,597,604].

Hysteresis seems to be more evident in the case of axial strain. Nevertheless, its magnitude may not represent a pure physiologic behavior of the AF. In fact, disc height (5.6 ± 0.4 mm) seemed adequate to accommodate the SG grid carrier of 3mm height. However, as can be observed in figure 45, the measuring grid and the grid carrier (8.5 mm height) of the “front” SG stayed in contact with the adjacent caudal vertebra. Thus, this incorrect positioning may have affected the results of axial strain to some extent.

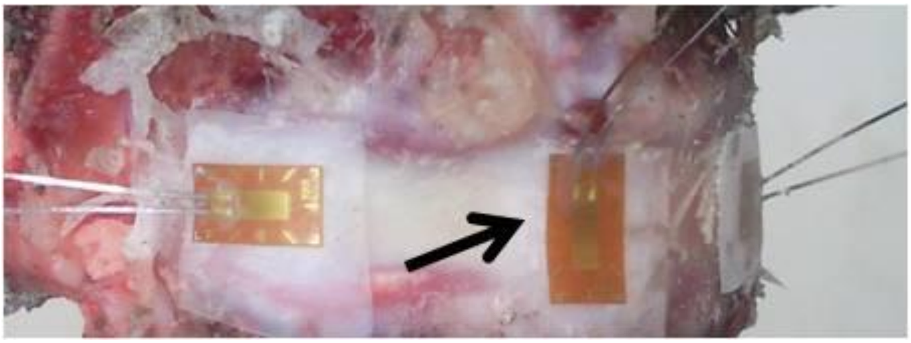

Figure 45 - The measuring grid and the grid carrier of the “front” strain gauge are contacting the caudal vertebra.

In fact, the difficulties in getting precise and reproducible SG placement in spinal structures are probably a major source of error in spinal studies [605]. Thus, future studies will benefit from smaller SG, particularly to measure axial strain. Furthermore, in the present study, the excision of the anterior longitudinal ligament should have also affected the output of axial strain. As can be seen from figure 45 it led the front SG to occupy a slight concave position, explaining the negative axial strain values that were observed for loads ranging from 0 to approximately 75N (figure 44).

Disc recovery is an important topic in spine biomechanics and SGs can contribute to study it. Strain values for unload were significantly higher ($p<0.05$) than those observed for loading (figure 42 to 44), suggesting the elastic components of the AF were not capable of completing recovery during unloading. The difference was small but it was an expected behavior because the IVD seems to need a resting period to recover to a normal pre-load state after compression [606-607].

Another interesting behavior is the nonlinearity of the AF [540] and SGs were able to detect it (figure 42 to 44). Present results suggest that the local stiffness of the outer AF increases with load, confirming the load bearing function of the IVD [540,597]. To express the nonlinear behavior of the AF, polynomial 2nd order fitting equations were presented, and peak loads as well as maximum strain values were estimated for circumferential strain. Peak loads (normalized to body weight (BW) and averaged for load and unload) for the right and left SG were of 3.25BW and 3.19BW, respectively. The corresponding mean maximum strains values were of 466 $\mu\varepsilon$ and 478 $\mu\varepsilon$ for the right and left side, respectively. These values could represent a physiologic limit beyond which plastic deformation may occur. Nevertheless, these are point values and the mechanical behavior of the entire AF depends on several other parameters, such as tensile properties of the lamellae, fibers orientation, and the regional variation of these quantities [495].

Another observed feature of the AF was a symmetrical behavior under compression. In fact, and despite regional variations of the AF and slight differences in SG placement and orientation, no significant differences ($p>0.05$) were found between the load and unload counterparts of the right and left SG. Knowing that the AF behaves asymmetrically when submitted to eccentric loads [496,540,605], the present results also confirm that the disc was submitted only to axial load.

The anisotropic behavior of the AF was assessed comparing the results of circumferential to axial strains. Despite the errors that have probably influenced axial strain results, it can be observed that the magnitude of axial strain (figure 44) was significantly lower than that of circumferential strain (figure 42 and figure 43) suggesting that the AF exhibits an anisotropic behavior (figure 46).

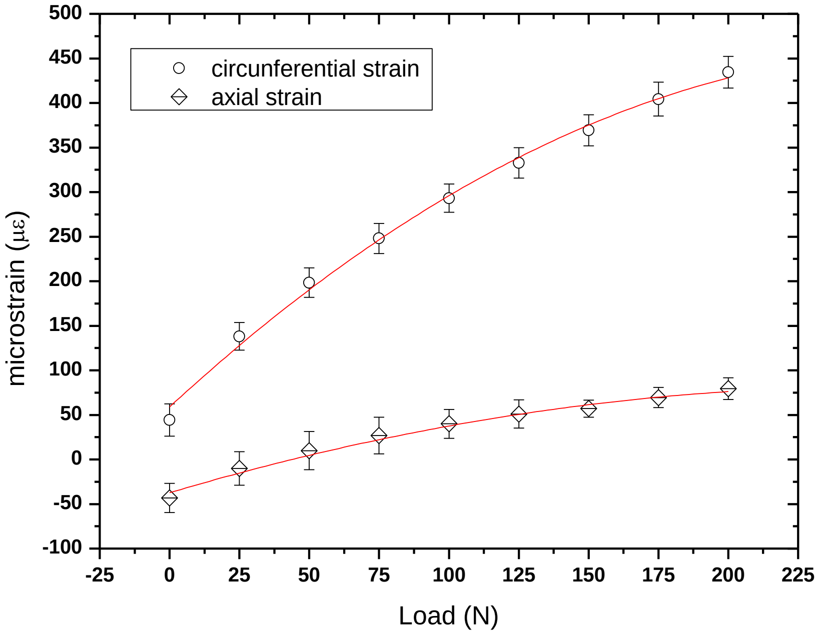

Figure 46 – Comparison between circumferential (mean of left and right) and axial strain.

The results of the present study should be compared with others with caution. In fact, the majority of studies differ in their purposes, specimens, methodologies and techniques, leading to controversial data comparison. For example, Ebara *et al.* [499] demonstrated that the tensile behavior of the AF is dependent on the compositional and structural variations in the IVD. Controversial results in the literature regarding axial and circumferential strain were detected by Heuer *et al.* [496]. In an effort to summarize them a mean maximal axial and circumferential strain of approximately 20% was proposed [496]. In the present study mean circumferential and axial strain were of 0.05% and 0.008%, respectively, both for a load of 200N. These results should not be compared to the previous ones because maximal loads were not applied and different techniques have been used. A better comparison can be made with the study of Shah *et al.* [540] where a similar technique was used. In this study strain results for a load of 200N vary between 0.1% and 0.4%. However they have been obtained for the posterolateral region of the AF which is considered to admit higher strain than the anterolateral regions. Additionally, it should take into account that strain was measured relatively to an arbitrarily defined zero strain of the tissue [593] which, in the present study, was defined after positioning the specimen holder into the mechanical testing machine and the application of the two pre-conditioning cycles.

The technique of bonding SGs directly to the tissue is interesting because it provides direct measurements of strain [105]. However it is invasive and can produce undesirable effects, such as inflammatory responses and modification of normal tissue behavior. To minimize inflammatory responses and allow *in vivo* applications SGs should be encapsulated along with use of FDA approved non-toxic bonding agents, such as PMMA [26,120]. Even so, the effect of cleaning and bonding on the histological and mechanical properties of the tissue requires further investigation. In general, adhesives should be capable of firmly attaching the SG to the tissue and compliant enough to deform along with it. The research on bone adhesives [26,120,608] is more advanced than it is for soft tissues [609]. In the present study the low viscosity cyanoacrylate worked well for loads that did not exceed 200 N. Nevertheless, it could fail for higher loads and it cannot be applied *in vivo* since its biocompatibility has not been studied. Meanwhile, other adhesives such as PMMA and topical skin closure adhesives (*e.g.,* 2-octyl cyanoacrylate) are FDA approved and can be explored in future studies. For example, PMMA and isobutyl 2-cyanoacrylate monomer have been used *in vivo* with bone [592].

Finally, SGs are point sensors meaning that only the strain at the attachment site can be measured. To get a representative strain map of the whole tissue larger sensors or more sensors need to be used. A wider transducer will be in contact with a greater portion of heterogeneous soft tissue fibers and the discriminative power in strain variation may be lost. Use of more sensors will probably lead to better outputs but at the expense of increased complexity and undesirable effects on the tissue. Micro-SGs are already available and can be explored to avoid SG contact with the vertebrae and eliminate potential sources of error. Naturally, other techniques, such as finite element analysis (FEA) [421,439,497,596,610-613], non-contacting laser or imaging techniques [500,613-615], and fiber optic sensors [26,105,138] can also be explored to map strain.

4. Final Remarks

In the present study an attempt was made to glue SGs directly to the annulus surface of the IVD and measure strain under compressive loads. The bonding area was previously marked, slightly roughened, cleaned and degreased with alcohol. A polyurethane-based transparent dressing for wounds was applied for waterproofing of the surface. Then, SGs were glued directly to the annulus surface with cyanoacrylate adhesive. A good adhesion was obtained with this procedure and SGs were able to confirm some properties of IVD behavior, such as hysteresis, nonlinearity and anisotropy. The output data seems adequate to demonstrate a potential application of SGs. Nevertheless, the technique can only be considered effective after studying the local effects of the procedures on the annulus fibers and its reproducibility using more specimens.

Study 2 – Using a Fiber Bragg Grating to Assess Intervertebral Disc Bulging [10;11;12]

---

[10] Roriz P, Abe I, Schiller M, Simões JA Intervertebral disc bulging measurement using a Fibre Bragg Grating sensor. In: Santos JL (ed) EWOFS 2010, Porto, September, 8-10 2010. SPIE, p 131.

[11] Roriz P, Abe I, Schiller M, Simões J Bulging of the intervertebral disc under compressive loading. In: Research Day, Aveiro, Portugal, June, 8 2011. University of Aveiro.

[12] Roriz P, Abe I, Schiller M, Gabriel J, Simões JA (2011) Intervertebral disc bulging measurement using a fibre Bragg grating sensor. Exp Mech 51:1573-7.

1. Introduction

There is strong evidence that immobilization, repetitive and high mechanical loading are environmental risk factors associated with IVD degeneration [616]. Preventing disc degeneration is an important issue because it represents gross structural disruption and it is irreversible [600]. Such disruption is more closely related to pain than to any other feature of ageing discs [600]. Measuring biomechanical parameters of the IVD such as displacement, strain, stress and pressure should contribute for better comprehension of its mechanical response to external applied forces.

Nachemson, in 1959, was the first to measure pressure in *ex vivo* human discs using a needle connected to an external mechano-electrical pressure transducer [465]. Nachemson *et al.* [227,617-618] also carried out, during the 1960s and 1970s, *in vivo* measurements of disc pressures for several body postures and tasks. Since that time needle-mounted SG sensors have been used to measure intradiscal pressure [307,483,619-623]. However the above sensors may interfere with the natural disc mechanics, particularly when studying small SMSs due to their rigidity and diameters over the millimeter order [20,309,483].

Advances using OFs as sensors may represent an important contribution to development of minimally invasive techniques for biomedical and biomechanical applications. Particularly, FBG sensors seem to be more appropriate for biomechanical applications than conventional resistive, piezoelectric or other solid state sensing technologies. These sensors have diameters of the order of 10^{-6} m and present considerable flexibility to adapt to complex surfaces allowing bending within the host structure to radii of 10mm [259]. FOS, in general, also present several additional advantages compared to conventional sensors such as: less weight; immunity to EM interference and RF interference making them suitable for use in magnetic resonance studies; biocompatibility, because fibers are made of silicate glass; higher temperature and pressure capability; the ability to be embedded into polymer or composite materials and used with instruments requiring sterilization; resistance to water and corrosive environments [23]. Nevertheless their relatively low strain sensitivity and signal artifacts caused by transverse loading may constitute a problem in the analysis and interpretation of tissue strain data [624].

Conventional sensors are mostly used to measure stress or strain at the body external surfaces to which they must adhere. Inner body measurements, as in the case of the IVD, require the sensor to be implanted in the needle. However, in the case of FBG sensors, as it was suggested by Dennison *et al.* [259], needles can be used for guiding the OF leaving the sensor *in situ* and making measurement less invasive.

In this study we addressed the possibility of using a needle only for guiding the sensor into the disc. The work of Nesson *et al.* [18] was the first successful demonstration of using a needle only for FOS guiding and positioning. In our study the needle was completely removed and the sensor let *in situ* to measure radial strain of the AF of a porcine disc submitted to axial compression. In fact, axial compressive loads contribute to reduce disc height, increase intradiscal pressure and make the outer annulus to expand horizontally (disc bulging) beyond the edges of the disc space. This bulging action can interfere with the surrounding tissues, assuming particular interest when normal physiologic limits are exceeded such as the case of disc herniation.

2. Material and Methods

2.1 Specimen

An ex vivo porcine dorsal SMS was tested. An SMS consists of two vertebral bodies connected by an IVD, facet joints and ligaments. In this study the surrounding soft tissues were carefully removed to guarantee preservation of disc, facet joints and spinal ligaments. After dissection the specimen was stored in a plastic sealed bag and frozen (-20 ºC). For instrumentation and testing the specimen was allowed to complete thaw inside the plastic bag to laboratory room temperature (25 ºC).

2.2 Specimen Holder Apparatus

A built-for-purpose stainless steel specimen holder, consisting of two plates with drilled metallic rings for screw attachment, was used to fix and align the SMS with the compression machine (figure 47).

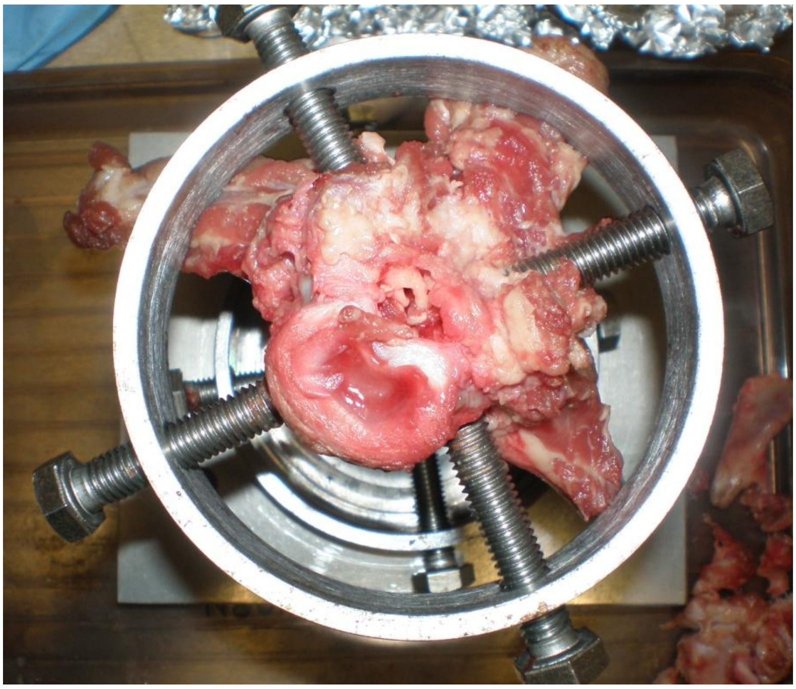

Figure 47 - Top view of the specimen holder (removed the top plate and vertical jigs).

The cranial and caudal vertebral bodies of the SMS were partially cut, attached with screws and cemented to the plates and metal rings of the specimen holder. Bone cement also contributed to fulfill gaps and to allow a better distribution of stress during compression. Additionally, four vertical jigs were used to guide vertical motion and maintain the plates parallel to each other. The most critical issue concerning this procedure is the working time of bone cement (about 5 to 8 minutes after mixing). The whole process took about an hour.

2.3 Fiber Bragg Grating Sensor

The FBG used in this study was recorded by illuminating a photosensitive fiber optic (Fibercore single mode PS1250/1500; ID 31007/B-00CK; Attenuation 1550 nm: 10 dB/km; Cut-off wavelength 1234 nm; Cladding diameter 124.2 µm; Mode field diameter 8.9 µm; Numerical aperture: 0.14; Operating wavelength 1550nm) with UV radiation from an interferometric setup (Spectra-physics LASER model: 2045-15; Serial number: 118-E20007) [625]. The estimated length of the grating was 2 mm.

The FBG sensor was implanted along the mediolateral (transverse) axis of the IVD. A 25-gauge hypodermic needle (0.5 mm OD, 87 mm length) was used to guide the sensor through the disc and removed after positioning the FBG in the center of the IVD (figure 48).

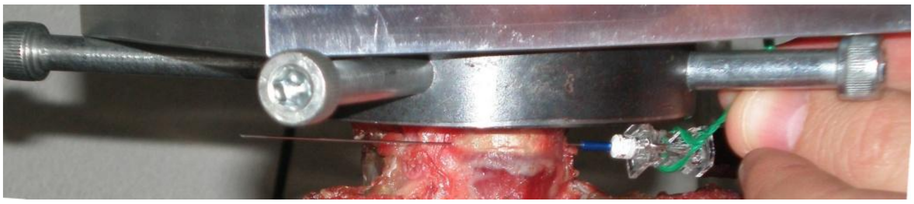

Figure 48 – Ventral view of the spinal motion segment. A needle was used to perforate the intervertebral disc from side to side and guide the sensor into the center of the disc.

For correct positioning of the sensor the mediolateral disc diameter was measured with a caliper (resolution: 1/20 mm) and marked in the OF so that the FBG would stay in the middle of the IVD, where the NP is expected to be. Then, the OF was glued with cyanoacrylate adhesive to one side of the AF, slightly pre-tensioned and bonded to the opposite side of the AF (figure 49; figure 50). Additionally, small plastic tubes were used to increase the bonding area and prevent the OF from sliding.

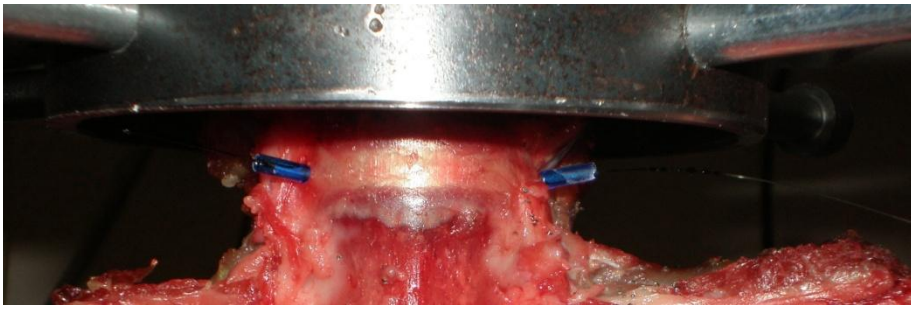

Figure 49 – Ventral view of the optical fiber inserted into the intervertebral disc. Small cylindrical plastic tubes and cyanoacrylate adhesive were used to attach the optical fiber to the disc surface.

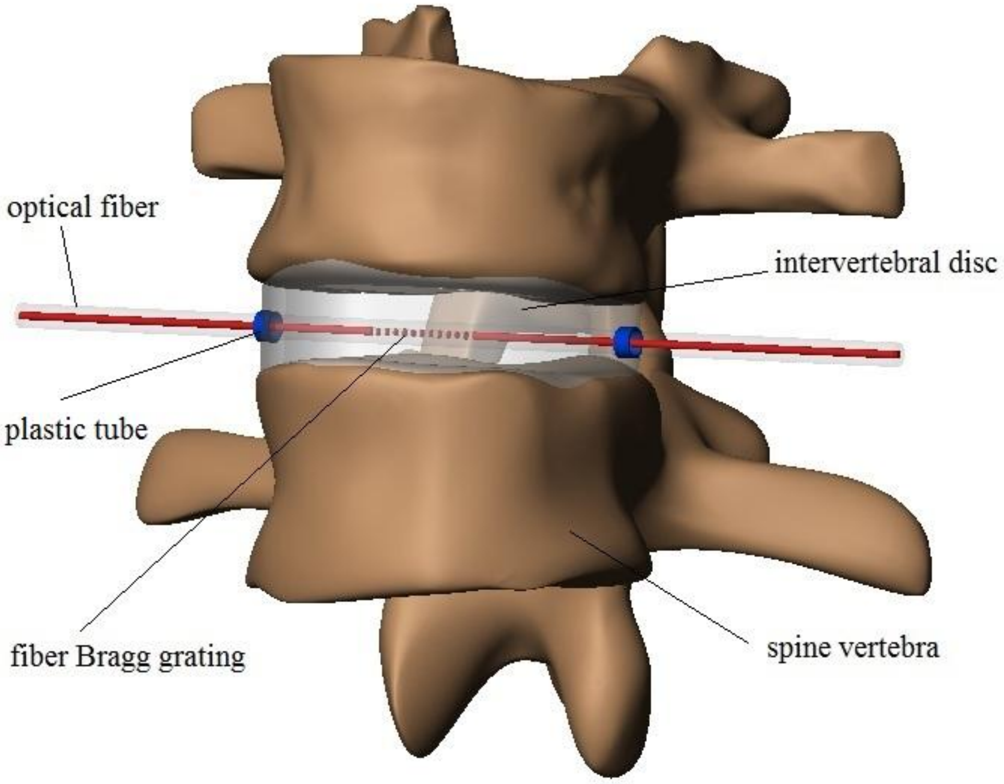

Figure 50 – Schematic representation of the fiber Bragg grating sensor inside the intervertebral disc.

This setup allowed the disc to bulge under axial compressive force and the OF elongate in the radial direction causing a shift in the Bragg wavelength. A portable FBG interrogator (Sensing Interrogator SM 125, Micron Optics, Atlanta, GA, USA; www.micronoptics.com) was used to read the wavelength variations. The resolution of the system was in the order of 10^{-12} m. Wavelength was converted to microstrain applying the conversion factor of 1.2 pm $\mu\varepsilon^{-1}$.

2.4 **Testing Loading Machine**

A customized loading machine was used to apply a uniaxial compressive load to the specimen. It consisted of a servo-pneumatic system having a double effect pneumatic cylinder (Festo CRDNGS-80-200-PPV-A), a servo-valve (Festo MPYE-5-1/8-HF-010-B), an optical linear scale (Fagor SV- B220), and a load cell (AEP TC4) with 10 kN capacity and 0.1% resolution of that value [601] (figure 40). All the control, monitor and load data acquisition software were implemented using LabVIEW 8.0. The interface and the connection between the software and instrumentation devices were made using a hardware platform (National Instruments PAC CompactRIO®). A more detailed description can be found elsewhere [601-602].

2.5 Load Protocol

A preload of 5N was slowly applied and maintained during testing to ensure permanent contact and alignment between the specimen holder and the loading machine. It also contributed to minimize zero shifts and allowed more stable initial strain readings [26]. After this, two pre-conditioning cycles were performed before data acquisition and a set of four repeated cycles was collected for analysis.

A quasi-static compression load protocol was applied for each cycle. It consisted of a load part (UP) ranging from 0 to 150N and an unload part (DW) ranging from 150 to 0N. Load step was of 25N. Each load was held constant for a period of 60s and load transition time was set to be linear for a period of 0.5 s (figure 51).

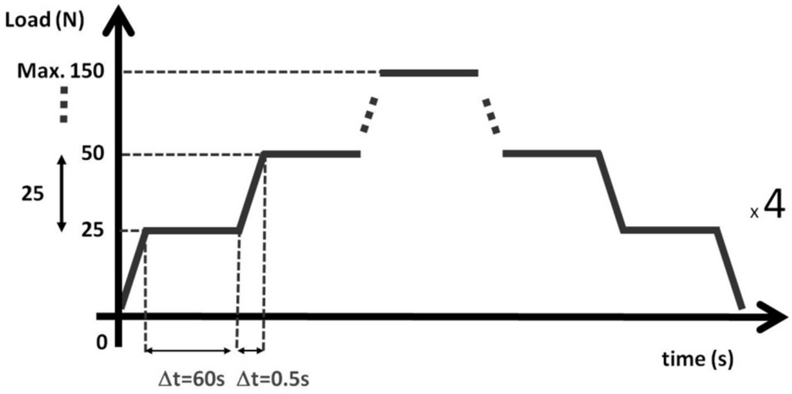

Figure 51 - Schematic representation of a load cycle.

The load protocol, including previous alignment of the sample with the loading machine and SG calibration, took less than two hours.

2.6 Statistical Procedures

Related Samples Wilcoxon Signed Rank Test was applied to evaluate significant differences between trials ($p \leq 0.05$). To express strain measurements variability under repeated conditions (multiple trials or loading cycles) the standard variation (SD) and the coefficient of variation (CV) were calculated. The SD gives an idea of the variability at each point of the loading cycle (for each applied load) and the CV is a relative variability measure that can be used to “summarize SD” information over the whole cycle [603]. It is calculated as the ratio between the average standard deviation (SD) and the average mean (X) of the loading cycle (see equation 1,p.106).

3. Results and Discussion

The IVD had an average mediolateral diameter of 33.45 ± 0.01 mm. Each load was applied for 60 seconds and data acquisition time was, on average, 24 ± 5 s.

Radial strain increased during loading and decreased during unloading, suggesting that the AF collagen fibers were able to resist the tensile forces induced by the bulging action of the IVD [491,496] (figure 52).

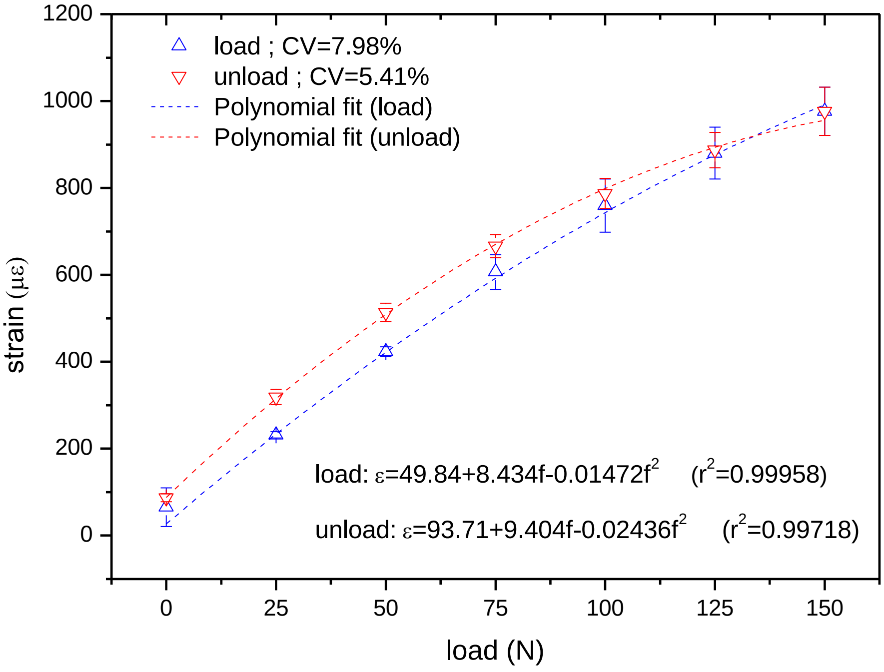

Figure 52 – Radial strain of the outer annulus fibrosus under compressive load. Average results of the four loading cycles are presented. Y error corresponds to one standard deviation. The adjusted coefficient of determination (r^2) was calculated.

Significant differences ($p \leq 0.05$) were found between the load and the unload counterparts suggesting hysteresis of the AF. The average of the differences was calculated (-48.94±35.38 με) and it seems to be higher than the differences observed for circumferential and axial strain in the previous study.

Strain values for unload were significantly higher ($p < 0.05$) than those observed for loading, suggesting that the elastic components of the AF were not capable of complete recovery during unloading. Thus, load application time as well as the recovery time may be important variables in this type of experiments. In the present study each load was maintained for about 60 seconds and there was no recovery time between load steps and between loading cycles. In fact, as suggested in the previous study, the IVD seems to need a resting period to recover to a normal pre-load state after compression [606-607].

The magnitude of radial strain was also higher than the ones observed for circumferential strain (figure 42 and figure 43) and axial strain (figure 44). Radial strain obtained for a maximal applied load of 150 N was 3.16 times greater than circumferential strain and 17.01 times greater than axial strain. These results reinforce the anisotropic behavior of the AF but more research seems mandatory to confirm the extent and the differences in strain values. Furthermore, it should be mentioned the OF is stiffer than the IVD and will resist to bulging of the disc suggesting that the radial strain force could also be measured. Thus, the technique may not be suitable for measurement of physiologic strain and more indicative of the radial force exerted by the AF.

The nonlinear behavior of the AF suggested that radial stiffness increased with load and confirmed disc ability to act as a load bearing structure [540,597]. To express the nonlinear behavior of the AF, polynomial 2nd order fitting equations were presented, and peak loads as well as maximum strain values were estimated for radial strain. Peak loads (normalized to BW) for the load and unload counterparts were of 3.25BW and 2.19BW, respectively. The corresponding mean maximum strains values were of 1258 $\mu\varepsilon$ and 1001 $\mu\varepsilon$ for the load and unload counterparts, respectively. These values could represent a physiologic limit beyond which plastic deformation may occur. Nevertheless, these are point values and the mechanical behavior of the entire AF depends on several other parameters, such as tensile properties of the lamellae, fibers orientation, and the regional variation of these quantities [495].

Similar concerns about results comparison and the bonding technique that were discussed in the previous study should be taken into account. On the other hand, compared to SGs, FBG can be easily multiplexed allowing multipoint measurements without increasing the dimensions of the sensor and the complexity of the acquisition system. In the near future these potentialities are expected to be explored.

4. Final Remarks

In the present study a FBG was used to measure radial strain of the AF under compressive loading. A needle was used only to guide the sensor into the NP. After removing the needle the FBG was pre-tensioned and the OF fixed to the outer AF surface. Under the previous configuration the FBG was able to measure radial strain resulting from the bulging action of the IVD. Results suggested that the disc exhibits some hysteresis and a nonlinear behavior. Radial strains were compared to circumferential and axial strains that were obtained with SGs and suggested that the disc also exhibits an anisotropic behavior.

Study 3 – Measurement of Intradiscal Pressure in Sheep under General Anesthesia[13]

---

[13] Roriz P, Frazão O, Santos JL, Simões J Fiber optic sensors for physiological pressure measurements. In: VIII RIAO/XI OPTILAS 2013, Porto, Portugal, July 22-26 2013.

1. Introduction

The loading conditions of the spine and particularly of the IVD are of great importance in several fields such as orthopedics, physiotherapy, biomechanics, ergonomics and sports. Explaining it is the evidence that repetitive and high mechanical loading can lead to disc degeneration [626-627]. Disc degeneration represents gross structural disruption and it is irreversible. Such disruption is more closely related to pain than to any other feature of ageing discs, and it is most common in the lower lumbar human spine [628-630]. Thus, studying the loading conditions of spine and the IVD could contribute to understand the mechanisms underlying its normal or deleterious response to load. In such a field, assessing intradiscal pressures has special relevance due to the association between high pressures and disc degeneration [600,631-634].

Intradiscal pressure data from Nachemson studies formed the basis of the current knowledge about the *in vivo* loading conditions of the spine [539]. In 1959, Nachemson was the first to measure *ex vivo* intradiscal pressure in human discs [465]. Nachemson *et al.* [227,617-618] also carried out, during the 1960s and 1970s, *in vivo* measurements of intradiscal pressures for several body postures and tasks, which became a reference in the field. Since that time few *in vivo* studies have been published [487,620,635-636]. A possible explanation for it lies on sensor geometry, particularly large diameters (over 1 mm) that could interfere with the natural disc behavior and lead to disc degeneration [20,308-309,483]. On the other hand, relatively few pressure data is available which hampers the use of numerical models predicting intradiscal pressure [307]. Even so, several models have been used [514,610,637-638], despite general agreement on further *in vivo* data that could validate them and contribute for more accurate predictions [635]. Moreover, intradiscal pressures can integrate some clinical diagnostic procedures as in the case of discography that can be used when diagnostic from MRI is inconclusive [639-642].

Using minimally invasive sensors such as FOS could represent a good alternative to conventional sensors in measuring intradiscal pressure. This possibility was explored by Dennison *et al.* [19-20,259] who proposed a needle housed FBG sensor. Sensor OD was 0.4 mm and it was used to measure intradiscal pressures in cadaveric specimens. A commercial solution was available from Samba Sensors (Västra Frölunda, Sweden). These sensors, with 430 μm OD and a protective coating of 0.7 mm diameter were used to measure intradiscal pressure in pigs [311-312], rabbits [313] and human cadaveric spines [314]. Another commercial solution is available from Radi Medical Systems (Uppsala, Sweden). This intensity modulated sensor has an OD of 0.55 mm and was used to monitor intradiscal pressure in sedated pigs [315] and patients suffering from lumbar back pain [316]. A smaller FOS was also proposed by Hsieh *et al.* [317] and Nesson *et al.* [18,318]. It consisted of a F-P sensor with a sensor probe of 366 μm OD. To our best knowledge it was used for *in vitro* measurements of rodent tail discs [18,317-319]. Meanwhile, a Samba sensor (Samba Preclin 360 HP) with only 360 μm OD was available for intradiscal pressure measurements but, to our best knowledge it was not tested *ex vivo* or *in vivo*.

The purpose of the present study was to measure intradiscal pressure in the 5th lumbar IVD of an anesthetized sheep using a Samba Preclin 360 HP sensor.

2. Material and Methods

2.1 Fiber Optic Sensor

An ultra-miniature fiber optic high pressure sensor (Samba Preclin 360 HP, Västra Frölunda, Sweden) was used to measure the pressure in the NP of a lumbar IVD of an anesthetized sheep (figure 53). The sensor consisted of a silicon sensing head with 360 μm OD mounted on an optical MMF with 400 μm OD. The sensor head and the MMF were coated with a radiopaque material (about 15 cm long) which allowed knowing the position of the sensor inside the body trough X-ray or fluoroscopic images.

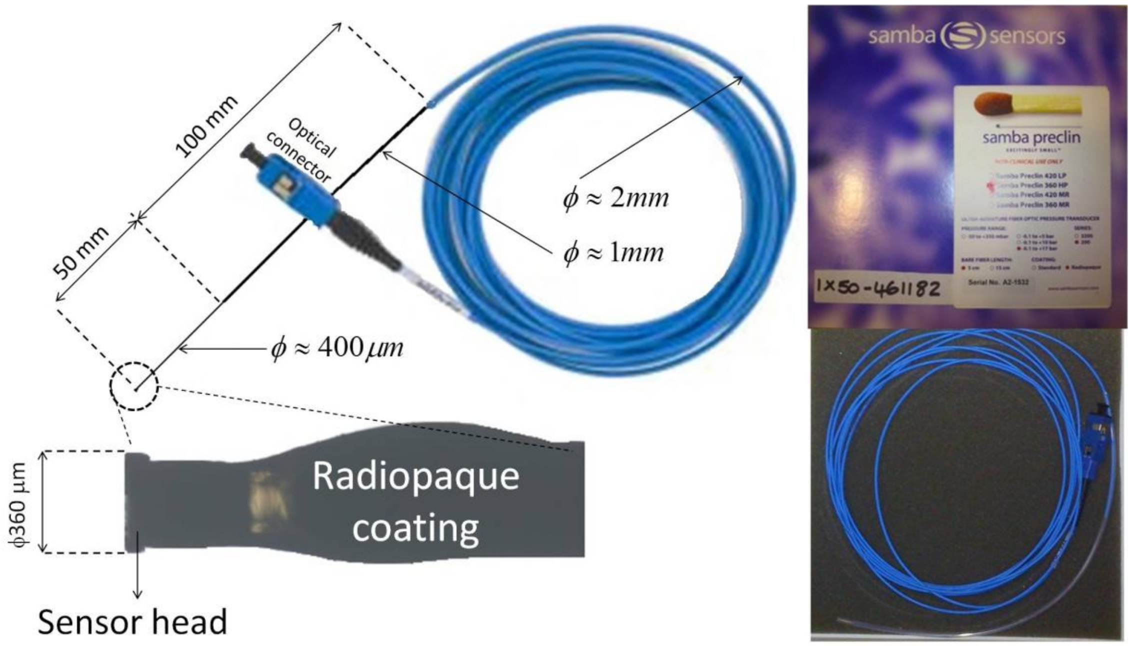

Figure 53 – The Samba Preclin 360 HP sensor (Serial nº.A2-1532). The sensor head (a Fabry-Pérot cavity) and the MMF were coated with a radiopaque material which allowed knowing the position of the sensor inside the body. A view of the sensor's packaging is presented on the right.

Samba sensor was handled in accordance to the manufacturer's instructions which are summarized in table 12 [643].

Table 12 – Handling and cleaning instructions applied to Samba sensor.

Handling instructions	Cleaning instructions
Do not touch the transducer tip. Only allow contact of the transducer tip with the measurement object.	Immediately submerge the transducer tip in cold distilled and de-ionized water after removing the transducer from the object (*in vivo* use). Keep it submerged until cleaning.
Shield the optical connectors with the protective caps when not in use.	Place the transducer tip in enzyme cleaner mixture and soak it for 10 to 20 minutes. CIDEZYME® Enzymatic Detergent Solution (Johnson & Johnson, Medical Inc, NJ, USA) was used in the present study Magnetic stirring is recommended (not followed)
Always use the protective tube to shield the transducer tip when not in use.	Rinse the transducer tip afterwards in distilled and de-ionized water.
Do not use tweezers or clamps with sharp edges.	Disinfect the transducer with 70% alcohol.
Do not use clamps with exaggerated clomp pressure.	
Do not bend the transducer more than the recommended minimum radius of 10 mm.	

Prior to *ex vivo* and *in vivo* experiments, the CIDEZYME® Enzymatic Detergent Solution (Johnson & Johnson, Medical Inc.) was used to clean the sensor. This solution is often used to clean medical instruments and endoscopes prior to sterilization or high level disinfection. The sensor was left at room temperature for about 10 minutes in a solution of 4% Cidezyme in water and rinsed afterwards in distilled and de-ionized water.

2.2 **Interrogation Unit**

Samba sensors are calibrated from factory to eliminate the need of customer's calibration. The calibration data is stored on a small erasable programmable read only memory (EPROM) positioned on the connector and is read automatically at start up. Nevertheless, to read EPROM data a manufacturers' control unit is required (figure 54). These units (Samba 201/202 control unit) are compact, portable (hand-held), battery operated and capable of temporary data storage and transmission to a computer. Nevertheless they are also expensive.

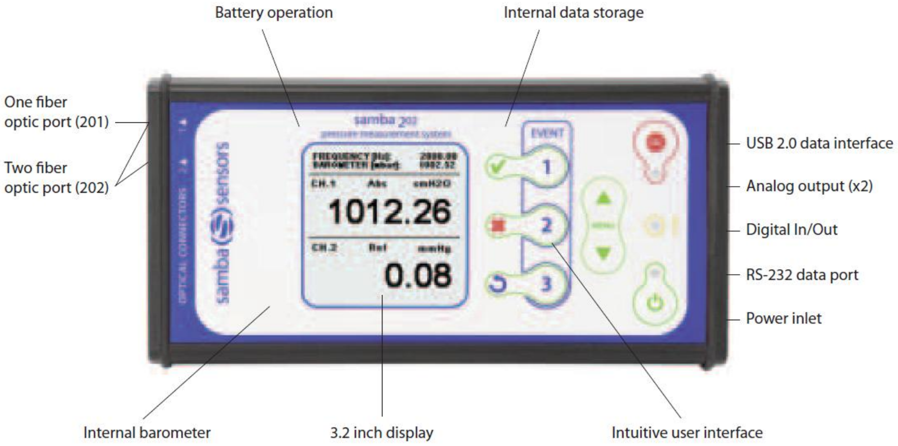

Figure 54 – Samba 201/202 control unit [310].

To overcome the previous constraint, a purpose-built control unit was used to interrogate the Samba sensor by means of available electrical and optical components at INESC-Porto facilities

The INESC-Porto interrogation unit consisted of several electrical and optical components that were housed in a stainless steel chassis; an optical power meter; and a portable computer (PC) (figure 55).

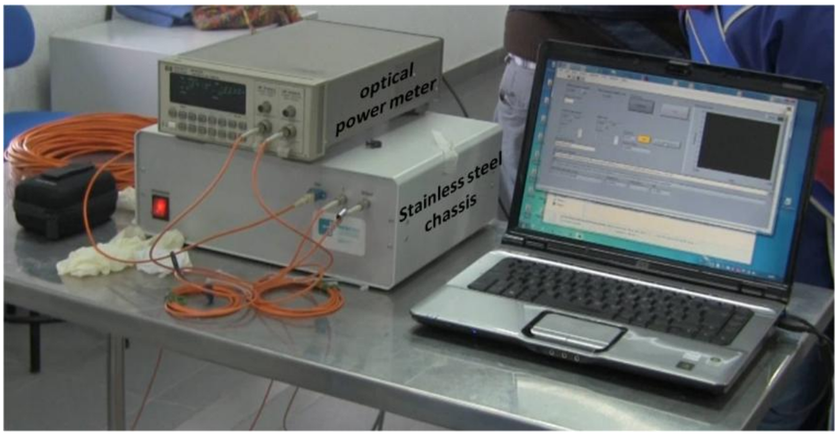

Figure 55 – The interrogation unit developed at INESC-Porto that was used for acquisition of pressure data in the nucleus pulposus of a lumbar intervertebral disc of an anesthetized sheep.

The components that were housed in the stainless steel chassis were arranged in two floors. Electrical components were housed on the 1st floor and consisted of a power supply (Traco®Power; Model: TXL 050-05S; Input: 100-240 VAC, 1.6 Amax. / 47-63 Hz; Output: 50W max., 5 VDC / 10.0 A) and a current and temperature controller (SuperLum, Ltd.; Imin. = 90mA; Imax. = 230 mA; S/N: PLT 60488) of a superluminescent diode (SLD) (figure 56). Optical components were housed on the 2nd floor and consisted of a SLD (SuperLum, Ltd.; SLD-561-DIL-3-SM; S/N: 60488) connected to an optical coupler/splitter (Newport F-CPL–M22855, 850 nm

07022509) that provided the external connections to an optical power meter (Hewlett Packard 8153A Light Wave Multimeter) and the Samba sensor (figure 56). The coupler is for 850 nm and the light source emits at 1300nm. Despite this discrepancy between the only available components it was assumed the performance is acceptable to 1300 nm.

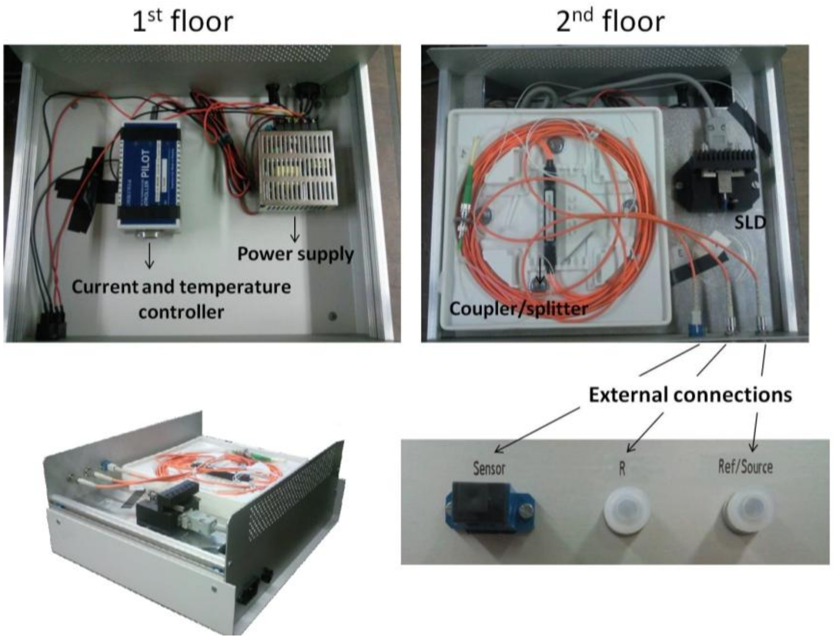

Figure 56 – Detail on the electrical and optical components of the interrogation system. The external connections to the sensor and the optical power meter were identified.

The basic functioning of the interrogation unit can be depicted in figure 57.

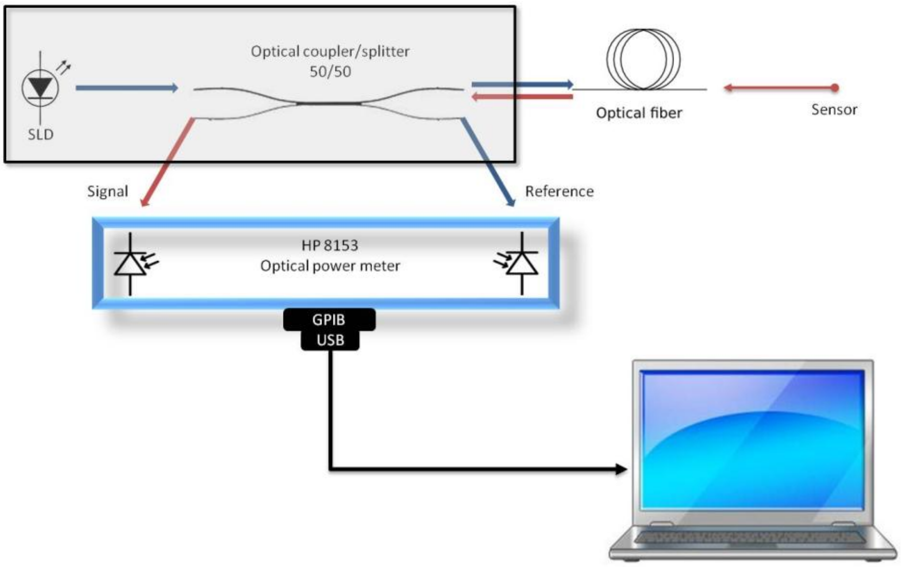

Figure 57 – Schematic representation of the connections between the optical components of INESC-Porto interrogation unit.

As can be observed from the previous figure, the power of the incoming light of the SLD was split 50/50 at the optical coupler/splitter. Splitting allowed using part of the light as the signal of reference and the remaining light to interrogate the sensor. The optical power of the light source was used as the signal of reference (at approximately 1310 nm) in order to account for source power fluctuations that could affect the readings of the sensor. The remaining light was used to interrogate the Samba sensor. At the sensor head (a F-P cavity - figure 8), part of the incoming light is back reflected to the coupler/splitter and its power measured by the optical power meter. The optical power meter allows for readings of the above individual signals (in μW or dB) and of the output signal $(sensor\ signal/reference\ signal)$ (figure 58). The sampling rate was 17 Hz.

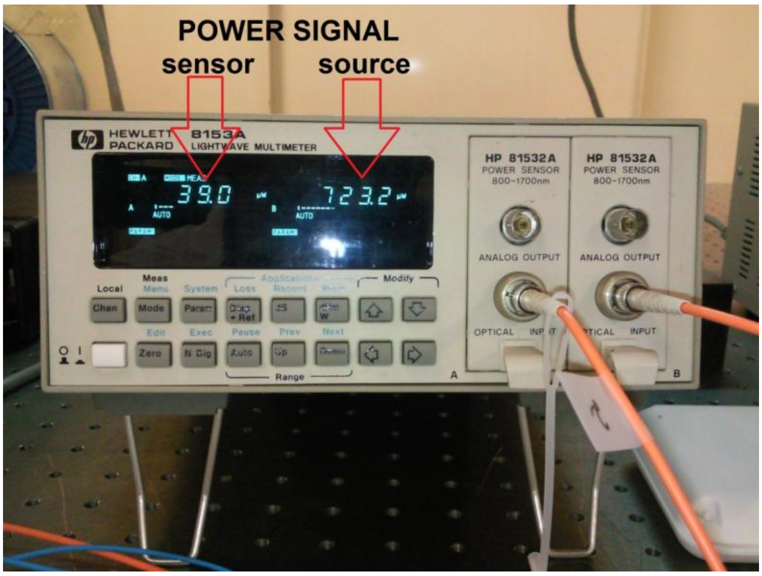

Figure 58 – The optical power meter (HP8153A) that was used for readings of the optical power of the source (reference) and sensor signals.

A GPIB-USB (Prologix, LLC, WA, USA) controller was used to allow communication between a PC and the optical power meter. Concomitantly, two LabVIEW routines were implemented to control data acquisition during calibration of the sensor and pressure experiments. These routines were described in the following sections.

2.3 Sensor Calibration and Data Acquisition

It was not possible to use the calibration data from the factory of the Samba sensor because a purpose-built interrogation unit was designed. Therefore, a new calibration protocol was implemented to express pressure as a function of the output signal.

Along with the new interrogation unit that was used to calibrate the Samba sensor, a purpose-built pressure device was also constructed (figure 59).

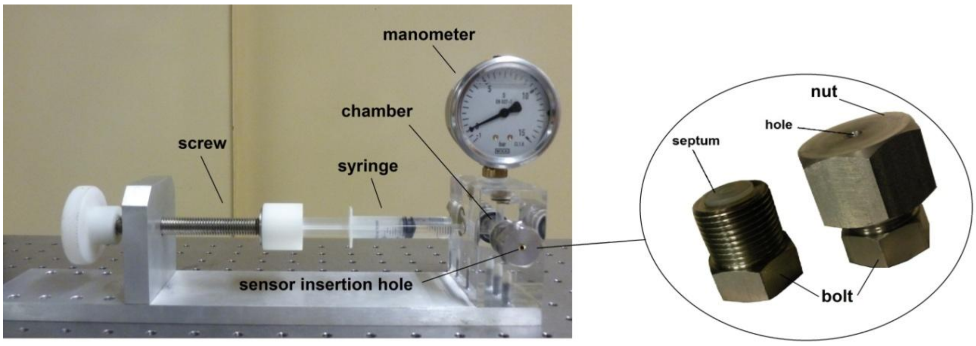

Figure 59 – The pressure device used to calibrate the Samba sensor.

The main components of the pressure device consisted of an acrylic compartment and a syringe, both filled with distilled water; a screw connected to the syringe plunger and used for pressure adjustment (figure 59). A manometer intended for medical applications (WIKA 111 series; EN 837-1, WIKA Instrument Corporation incorporated, GA, USA) with a pressure range from -1 to 15 bar and accuracy class of 1.6 was used for pressure readings (figure 59). On both sides of the acrylic piece a bolt and nut with passing holes were used to provide insertion of the sensor into the acrylic compartment where the pressure was measured (figure 59). The sensor was guided through the holes by means of a hypodermic needle that was removed after correct positioning of the sensor (see detail on figure 60). To seal the passing holes a septum of silicone (similar to those used with injectable drugs) located in between the bolt and nut was used (figure 59). The basic functioning of the pressure device was to manually rotate the screw pushing the water inside the syringe into the acrylic compartment. This action increases the pressure and the torque in the opposite direction and decreases the pressure.

The complete setup that was used in sensor calibration is presented in figure 60.

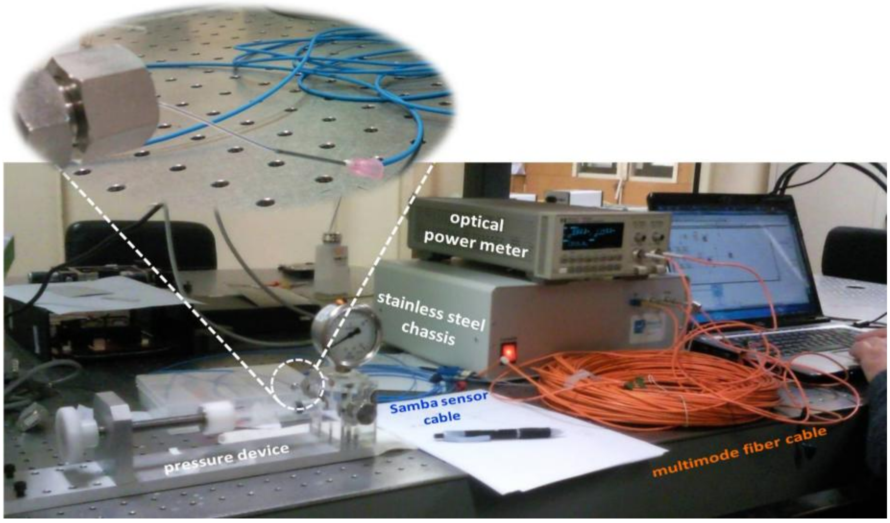

Figure 60 – The complete setup used in sensor calibration. A detail on the location of sensor insertion is presented.

In order to facilitate sensor calibration and to avoid errors in readings from the optical power meter display, a semiautomatic calibration process was implemented trough a LabVIEW routine. In figure 61, a flowchart of the routine is presented.

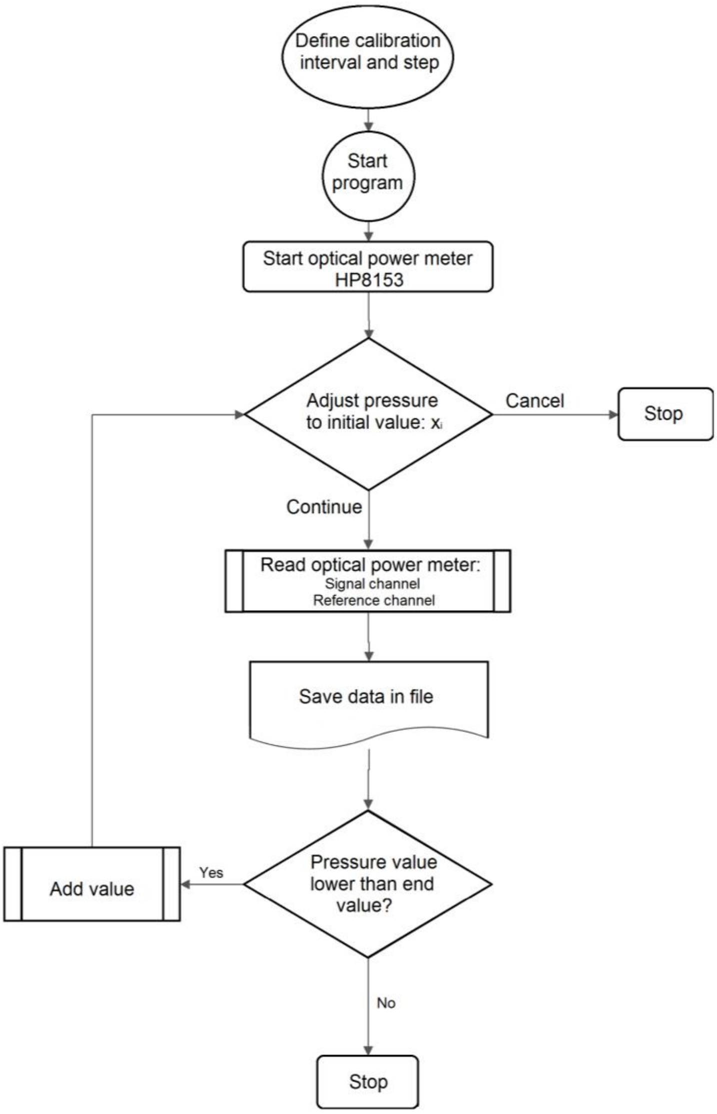

Figure 61 – Flowchart of the LabView routine used for calibration of the sensor.

The pressure interval that was used in sensor calibration varied from 0 to 14 bar (1.4 MPa) which is in the range of intradiscal pressures [307]. A calibration step of 0.5 bar (0.05 MPa), depending on the pressure gauge resolution, was defined. After initializing the LabVIEW routine it goes through the previously defined pressure values asking the user to manually adjust the pressure at each calibration step. An array of optical power values for each step was stored (n=10) allowing calculation of the optical power average and the corresponding standard deviation. In order to detect hysteresis in the measuring system three increasing and decreasing pressure cycles were performed. Values were exported to OriginPro 8.5 allowing plotting of the calibration curves, fitting the data and calculating linear and quadratic calibration coefficients. The function with the highest r^2 was selected for pressure acquisition. These coefficients were used in another LabVIEW routine to read the pressure during *in vivo* experiments (figure 62).

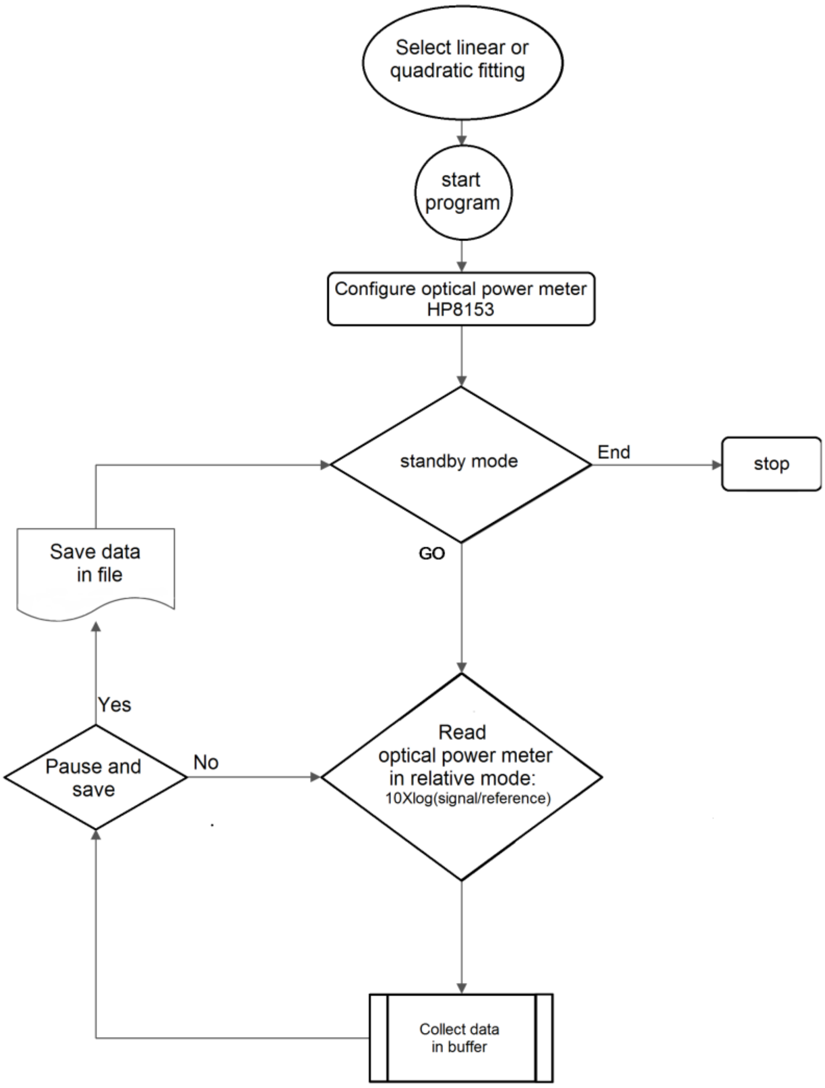

Figure 62 - Flowchart of the LabView routine used for read pressure data during *in vivo* experiments.

The user only has to control the start, pause and save acquisition buttons. During acquisition the LabVIEW routine also plots pressure values providing some feedback to the user about the acquisition process. Output data was saved in a text file and exported to OriginPro 8.5 for subsequent analysis.

The maximum error introduced by hysteresis of the sensor was calculated as a percentage of the maximum pressure used during calibration (14.0 bar). Maximum sensor drift during a measurement period of 30 minutes was also calculated for pressures of 0.0 bar, 7.0 bar and 14.0 bar.

2.4 *Ex Vivo* Experiments

Ex vivo experiments were conducted by a skilled veterinary prior to *in vivo* testing at the facilities of the Veterinary Hospital of the University of Évora. These experiments were useful to decide about the most appropriate *in vivo* surgical approach and to test the whole system and sensor performance under more harsh and realistic conditions.

After practicing several surgical approaches on an adult sheep cadaver it was decided to apply a percutaneous approach under fluoroscopic control (Digital C-Arm - ZEN 2090 Pro, Genoray America Inc., CA, USA) for measurement of *in vivo* pressures. This minimally invasive procedure requires a needle puncture on the skin instead of using an open ventral approach where inner organs and tissues have to be exposed.

A dorsolateral transforaminal approach into the center of the NP, similar to that used in discography and percutaneous nucleotomy, was followed [307,644]. After positioning a standard 11-gauge biopsy Jamshidi needle (cannula with ≈3.0 mm OD and ≈2.3 mm ID) in the intervertebral space the stylet of the needle was taken out and substituted by a 2.0 mm Kirschner-wire to make a deeper hole into the NP and prepare the disc for sensor implantation (figure 63). At this stage the Samba sensor was not used to prevent it from breaking.

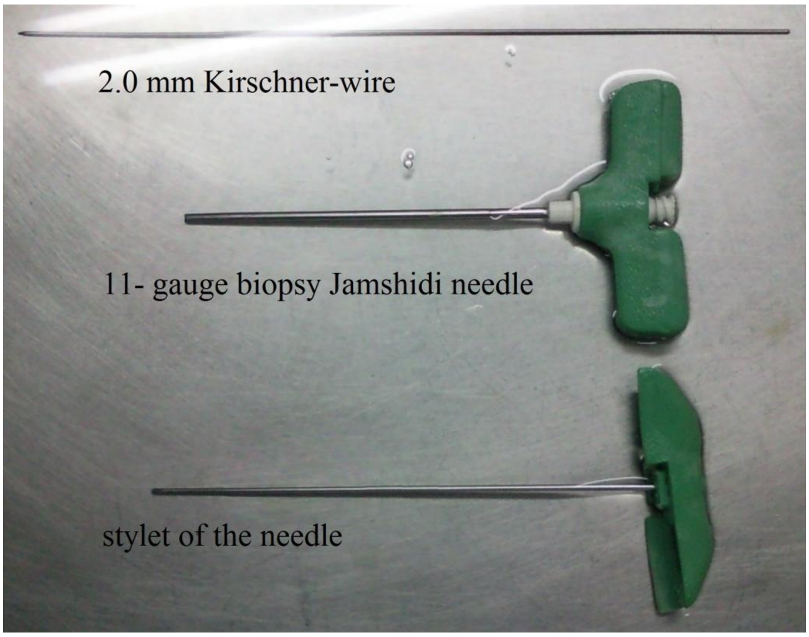

Figure 63 – The standard 11- gauge biopsy Jamshidi needle used to implant the Samba sensor into the nucleus pulposus of the intervertebral disc, the stylet and the 2.0 mm Kirschner-wire.

To test the acquisition system and sensor performance a simpler methodology was used. The IVDs of a cadaveric lumbar spine of a sheep were exposed. The AF was punctured ventrolateraly and a 20-gauge hypodermic needle was guided by haptic sensing into the NP (figure 64). Then the sensor was guided into the NP through the lumen of the needle. The needle was then removed from the fiber optic cable holding the sensor *in situ*.

Figure 64 – Insertion of the Samba sensor into the needle lumen.

To prevent sensor displacement inside the NP the cable of the sensor was sutured to the surrounding soft tissues (figure 65).

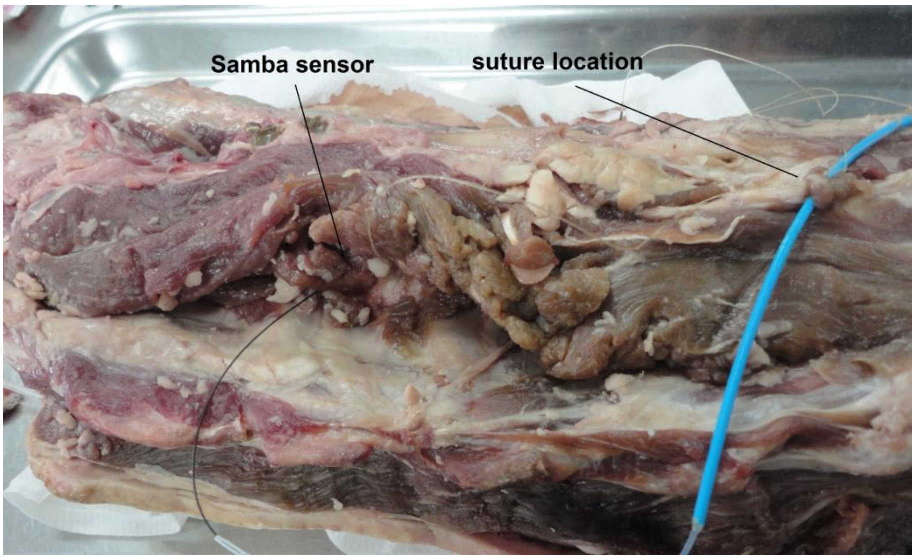

Figure 65 – Location of the suture to prevent slippage of the sensor.

In the previous conditions, several spinal maneuvers were performed by the veterinary trying to simulate the three major anatomical movements of the spine, namely flexion/extension, lateral flexion and axial rotation (figure 66). These maneuvers aimed at measuring intradiscal pressure in the position of maximum ROM, although without controlling the magnitude of the applied force and the ROM.

Figure 66 – An example of the conditions under which the spinal maneuvers were accomplished.

Sensor location in the intervertebral space was confirmed by X-ray imaging (figure 67).

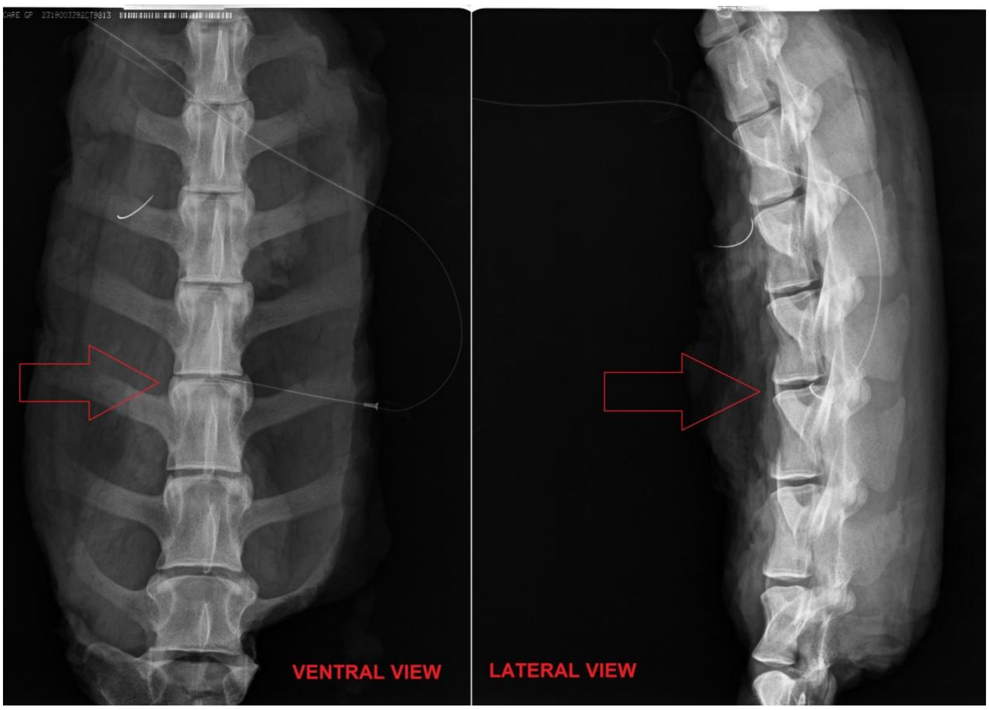

Figure 67 – An example of an X-ray used to confirm Samba sensor position into the intervertebral space. Ventral and lateral X-ray images were taken to confirm sensor location in the anterior and sagital planes. In the present example the sensor seems to occupy a central but slightly posterior position.

2.5 *In Vivo* Experiments

The study was performed at the facilities of the Veterinary Hospital of the University of Évora. It was authorized by competent national authorities and conducted according to the guidelines for animal care of the Federation of Laboratory Animal Science Association (FELASA) [645-646].

The Samba sensor was implanted in the 5th lumbar intervertebral disc (IVD) of a 4-year-old female merino ewe with 45 kgf body-weight, under general anesthesia. The following major procedures were adopted:

- The lumbar region was sheared before taking the animal to the operating room and it was pre-medicated with atropine (0.7 mg kg^{-1}), xylazine (0.1 $mgkg^{-1}$) and butorphanol (0.01mg kg^{-1});
- At the operating room, holding the animal in the standing position, anesthesia was induced with thiopental sodium 5% (5 mg kg^{-1}) by intravenous injection (figure 68). Then the animal was moved to a radiolucent table and maintained in a lateral right recumbence position (figure 68);

Figure 68 – Animal preparation at the operating room. After anesthesia the animal was moved to a radiolucent table and maintained in a lateral right recumbence position.

- Endotracheal intubation was performed and the anesthesia was maintained through isoflurane (2-3%) in oxygen with spontaneous ventilation, under control of vital parameters (heart rate and respiratory rate) (figure 69);

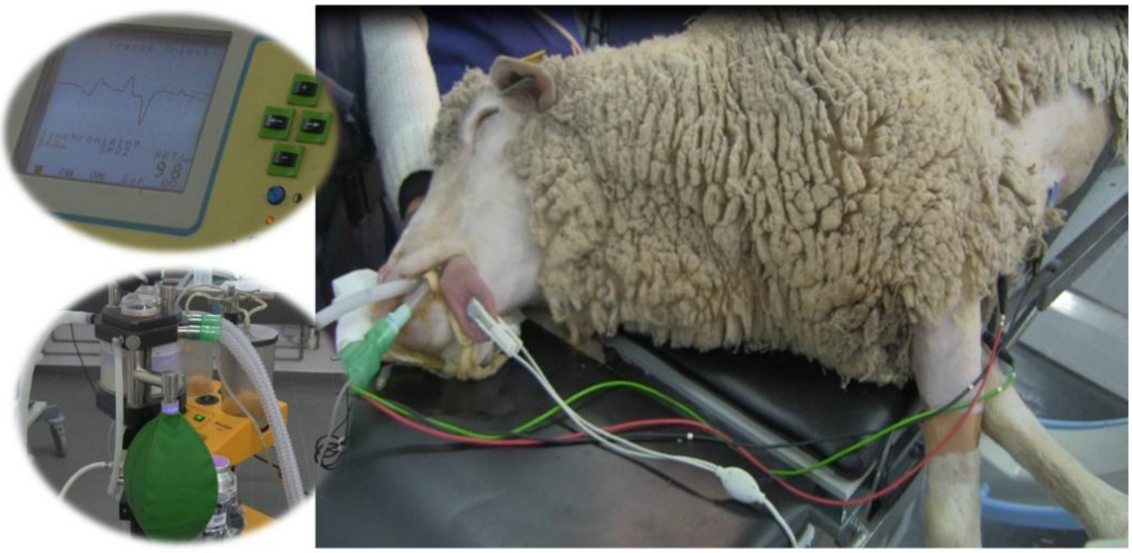

Figure 69 – The anesthesia was maintained through isoflurane (2-3%) in oxygen with spontaneous ventilation and vital parameters were controlled.

- The lumbar region was prepared for needle puncture with a povidone-iodine solution in 70% ethanol (figure 70);

Figure 70 – The lumbar region was prepared a solution of povidone-iodine in 70% ethanol.

- A standard 11- gauge biopsy Jamshidi needle (figure 63) was inserted percutaneously in the dorsolateral intervertebral disc space (figure 71) under fluoroscopic control (figure 72);

Figure 71 – Insertion of the standard 11-gauge biopsy Jamshidi needle percutaneously in the dorsolateral intervertebral disc space.

Figure 72 - Fluoroscopic control of needle position.

- Then the stylet point was taken out and substituted by a 2.0 mm Kirschner-wire to penetrate into the NP. Leaving the cannulae in that position, the K-wire was substituted by the Samba sensor and data collection started (figure 73);

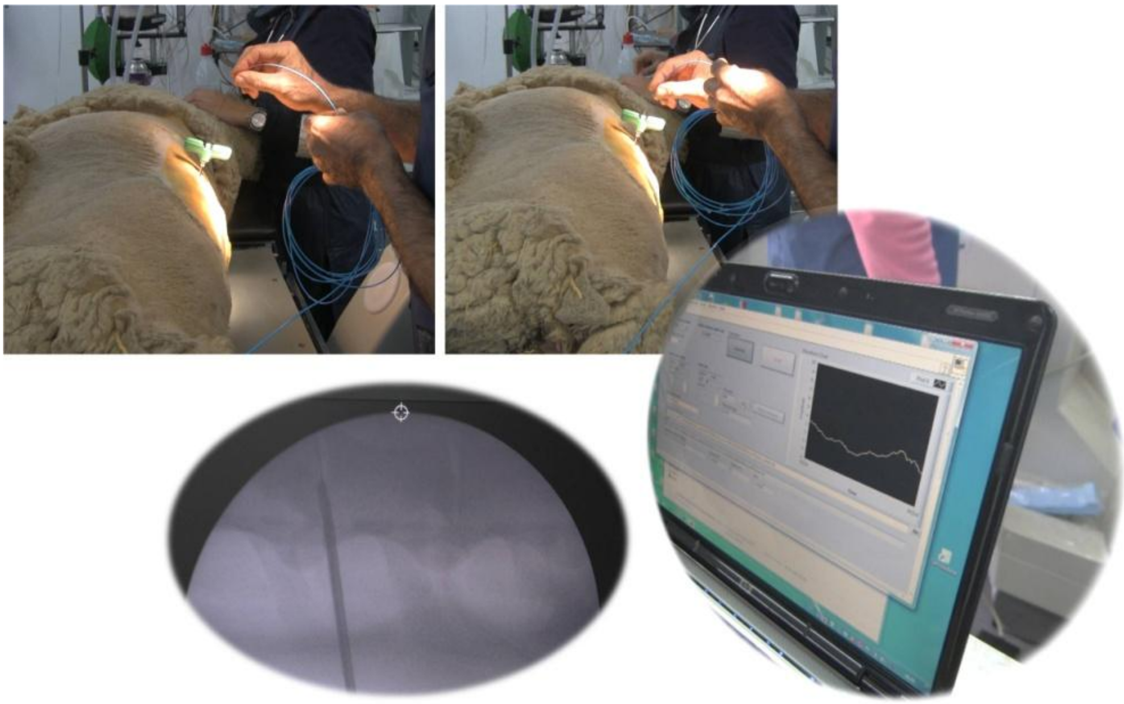

Figure 73 – Implantation of the Samba sensor into the nucleus pulposus of the intervertebral disc.

- After waking up from surgery the animal was conducted to the recovery room (figure 74);

Figure 74 – The animal going to recovery.

- The height of the disc was estimated by calculating the height of the corresponding intervertebral space using fluoroscopic images. The open source ImageJ 1.46r program (National Institutes of Health, USA) was used for calculations.

3. Results and Discussion

3.1 Calibration

The pressure interval that was used in sensor calibration varied from 0 to 14 bar (1.4 MPa) and the calibration step was of 0.5 bar (0.05 MPa). In order to detect hysteresis in the measuring system three pressure cycles were performed, each including an increasing and decreasing pressure part. As can be seen from figure 75 the average values for all increasing and all decreasing parts are similar suggesting a small but significant ($p \leq 0.05$) hysteresis effect.

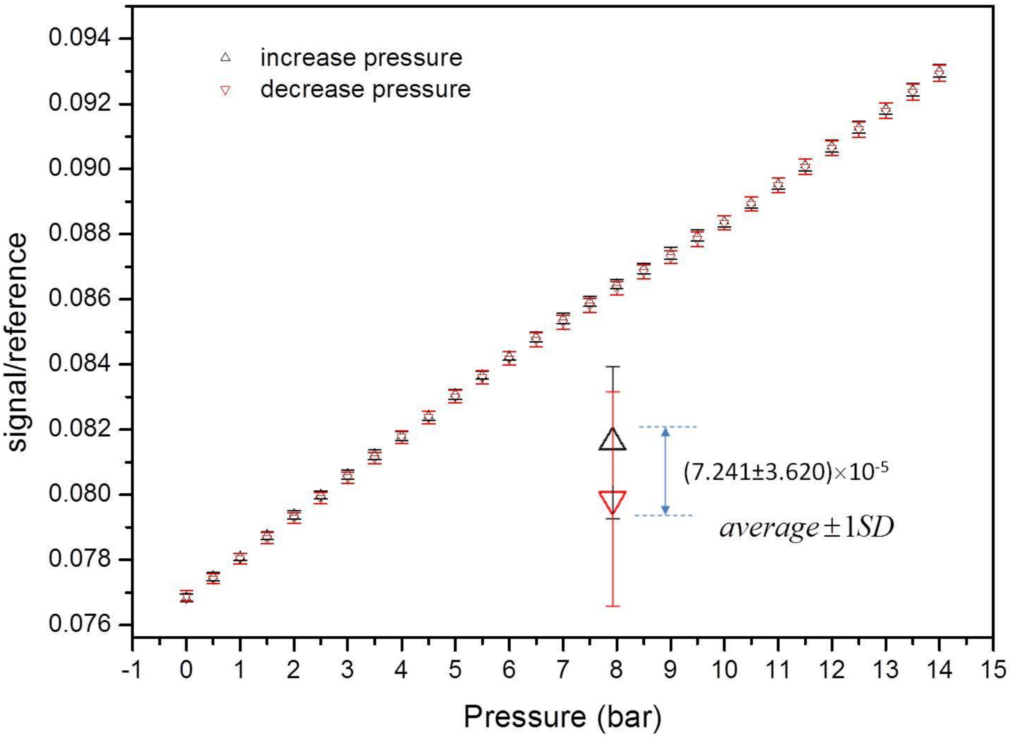

Figure 75 – Average values of increasing and decreasing parts of the three pressure cycles performed during calibration of the Samba sensor. A detail on the average of the differences between increasing and decreasing values at each step of calibration is shown. Y-error bars represent one standard deviation.

To analyze the extent of hysteresis the differences between increasing and decreasing values were calculated for each step of calibration. The average of these differences was $(7.241\pm 3.620)\times 10^{-5}$ (figure 75). With exception of the difference calculated for 0 bar the remaining differences were positive suggesting slightly lower values during pressure decreasing. Maximum hysteresis was 0.46%.

Despite the previous differences the calibration coefficients were calculated for the complete cycles. The average values of the three calibration cycles are presented in figure 76.

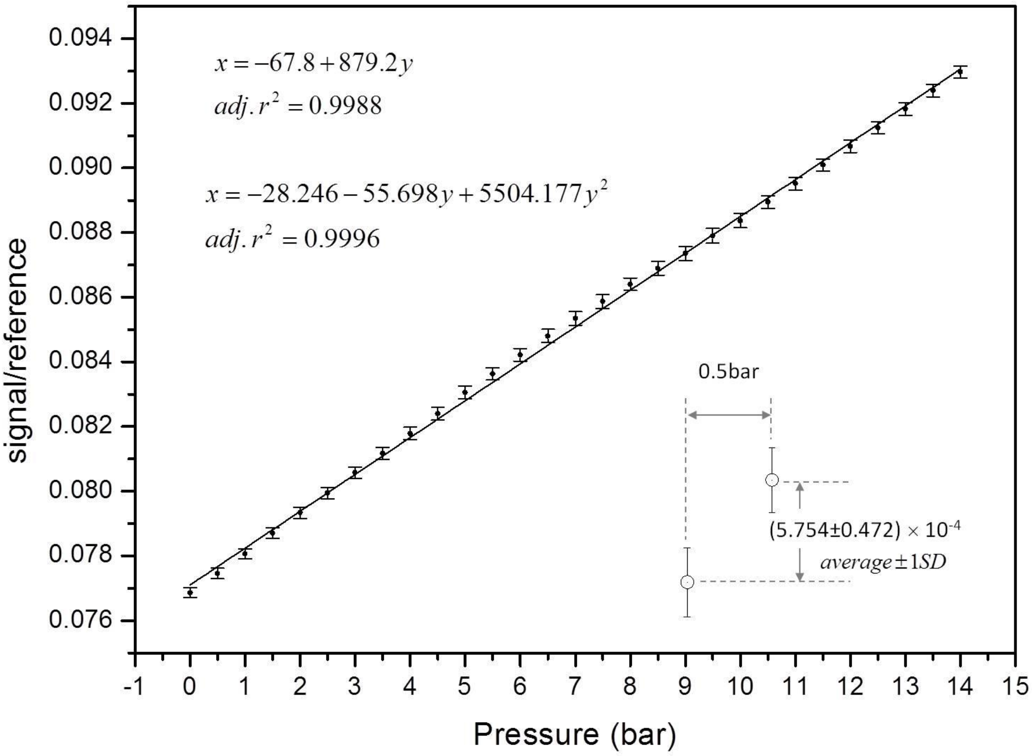

Figure 76 - Average values of the three pressure cycles performed during calibration of the Samba sensor. A detail on the average of the differences between consecutive steps of calibration was shown. Y-error bars represent one standard deviation.

The differences between consecutive steps of calibration (0.5 bar) were calculated for the above data. On average these differences were of $(5.754 \pm 0.472) \times 10^{-4}$ (figure 76). The mean standard deviation of each step of calibration was $2.022 \pm 0.262) \times 10^{-4}$ which represents about 35% of the average difference between consecutive steps of calibration.

The purpose of the calibration procedure was to convert variations in signal/reference signal into variations of pressure. For that purpose linear and quadratic fitting functions were applied to pressure *versus* signal/reference plots and the corresponding coefficients were used with a LabVIEW routine to automatically calculate pressure values during experimental measurements. In figure 76 the linear and quadratic regression models obtained are presented.

Both fitting equations can explain more than 99% of the dependent variable. Nevertheless, the adjusted coefficient of determination ($adj.r^2$) was slightly higher for quadratic fitting, justifying the use of the quadratic coefficients for experimental procedures providing the pressures were in the range of calibration pressures.

Maximum sensor drift during a measurement period of 30 minutes for pressures of 0.0 bar, 7.0 bar and 14.0 bar was of ±0.002 bar.

3.2 ***Ex Vivo* Experiments**

Ex vivo experiments were performed to decide about the most appropriate surgical approach technique, to test the whole system under more realistic conditions and to test sensor performance.

Sensor performance was evaluated on a cadaveric lumbar spine of a sheep. The sensor was inserted into the NP of an IVD using a ventrolateral approach (figure 64).

A 20-gauge hypodermic needle was used to puncture the AF and guide the sensor into the NP. An experienced veterinarian is capable of feeling the sensor *in situ*. The initial resistance posed by the denser AF to needle penetration is followed by a sensation of a decrease in resistance suggesting the needle's bevel is in the NP. Even so, sensor location in the intervertebral space was confirmed with X-ray imaging (figure 67).

It should be mentioned that before using the previous needle, some needle catheters have been tested in an attempt to guide the sensor into the NP (figure 65). Nevertheless, the majority of these attempts failed because the AF pressure acting along the catheter was enough to squeeze the lumen preventing the sensor from entering. In these cases it was decided not to force sensor entrance because it could break the sensor head. The high pressures derived of the contact of the sensor head with the catheter walls are plotted in figure 77.

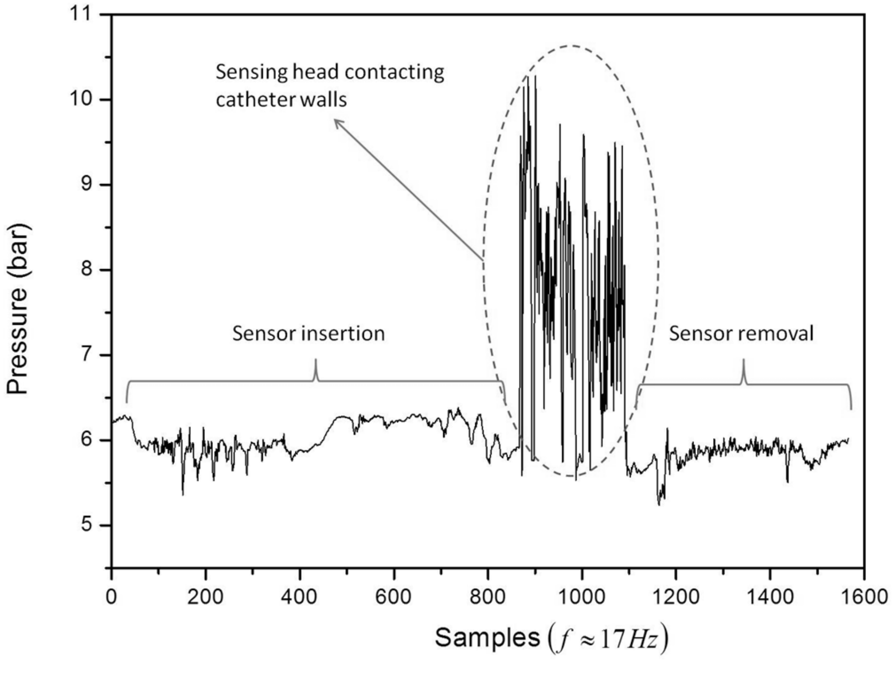

Figure 77 –Pressures measured during sensor insertion into the catheter lumen, while contacting the squeezed lumen and during its removal (raw data).

The use of needles or more rigid catheters to guide a sensor into the NP seems mandatory [20,307]. However, in the case of the Samba sensor when the needle was removed it had to remain suspended on the sensor cable during the measurements (figure 60, figure 65).

The previous observation could be an important limitation, particularly for *in vivo* measurements and requires further reflection. It was not possible to remove the needle trough the opposite extremity of the Samba sensor due to the presence of the optical connector (figure 53). Therefore, future initiatives, with commercial or purpose-built sensors, could considerer splicing the OFs of the connector and sensor only after sensor implantation and needle removal. However this procedure will probably require an *in situ* calibration, which could be a problem, and will certainly delay data acquisition.

An easier and simpler procedure could be fixing the needle to the skin using a standard medical adhesive tape. However to do it effectively requires control on the fiber optical cable length and, particularly, its diameter. For example, the diameter of the larger protective layer of the Samba sensor was about 2 mm, starting approximately 15 cm away from the sensor tip (figure 53). Therefore, imagining a needle with less than 2 mm ID and 75 mm long[14], it could not be retracted away from the site of needle puncture more than 7.5 cm. In *in vivo* studies it would not be possible removing the needle from the body completely. To accomplish it a needle with a larger bore (>2mm ID) has to be used. In fact, the previous strategy had to be followed in the present *in vivo* study. Consequently, the corresponding needle punctures will be more invasive and could develop a deleterious effect on disc properties and on its normal mechanical behavior [647-649].

Future developments should be capable to designing sensors with uniform and minimum diameters along the fiber length, preferably equal to the diameter of the sensing tip. This way a minimally invasive needle could be completely removed or kept fixed to the skin at a safer distance from the sensor tip.

Another interesting alternative is to keep the sensor within the needle during pressure measurements. This strategy would be very useful to protect the sensor head from physical damage. To maintain the procedure minimally invasive the needle should be as small as possible, preferably with an ID similar to that of the sensor head. To prevent the intradiscal fluid from escaping trough the lumen it should be sealed with a biocompatible polymer.

Ex vivo experiments were also useful to confirm that under spinal maneuvers the increase of intradiscal pressure causes the sensor tip to shift outwards. This behavior was described in a previous study using a nonoptical and larger sensor [307]. To prevent the sensor from sliding the sensor cable was sutured to the adjacent soft tissues (figure 65). Nevertheless, because the suture was far away from the AF the previous procedure was more effective preventing inadvertent movements on the cable than sliding of the sensor head. On the other hand, it was too risky to suture the bare fiber (black part of the sensor cable in figure 65) nearest the AF, because it was more fragile and could break.

---

[14] The length of typical spinal needles, used for spinal anesthesia or lumbar puncture, varies between 30 mm and 150 mm and their internal diameters between 0.35 mm and 1.27 mm.

The experiments were conducted under the previous conditions, but future alternatives, keeping in mind *in vivo* experiments, were discussed. The most effective procedure is probably bonding the sensor cable at the site of needle puncture and making it to adhere to the AF. Current topical skin closure adhesives could be tested. Furthermore, these adhesives also seem also to offer many advantages over traditional wound closure devices [650-651]. Additionally, other bonding agents, such as PMMA and isobutyl 2-cyanoacrylate monomer, which are FDA approved adhesives for bone tissue, could also be tested [592,652].

Pressure data resulting from repeated spinal maneuvers, such as flexion/extension (figure 78), lateral bending (figure 79) and axial rotation (figure 80) was plotted for analysis.

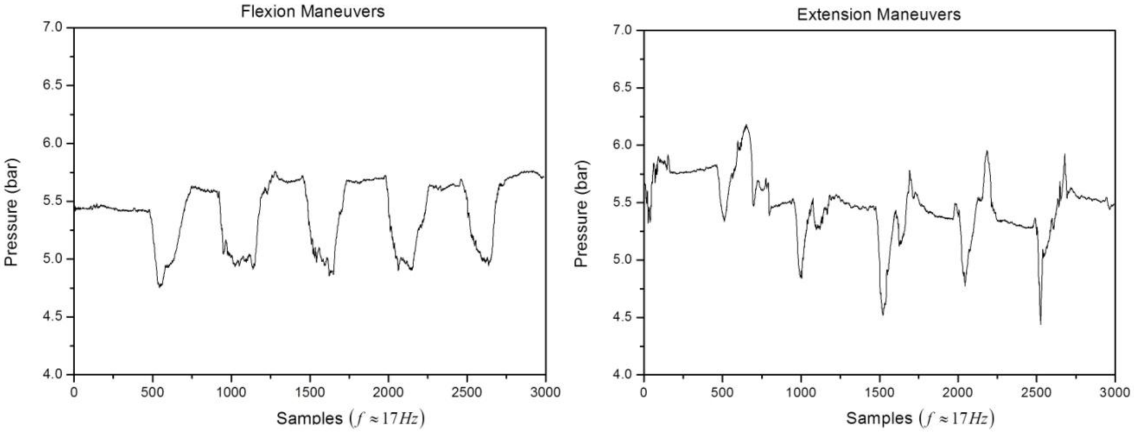

Figure 78 – Pressure raw data resulting from flexion/extension maneuvers.

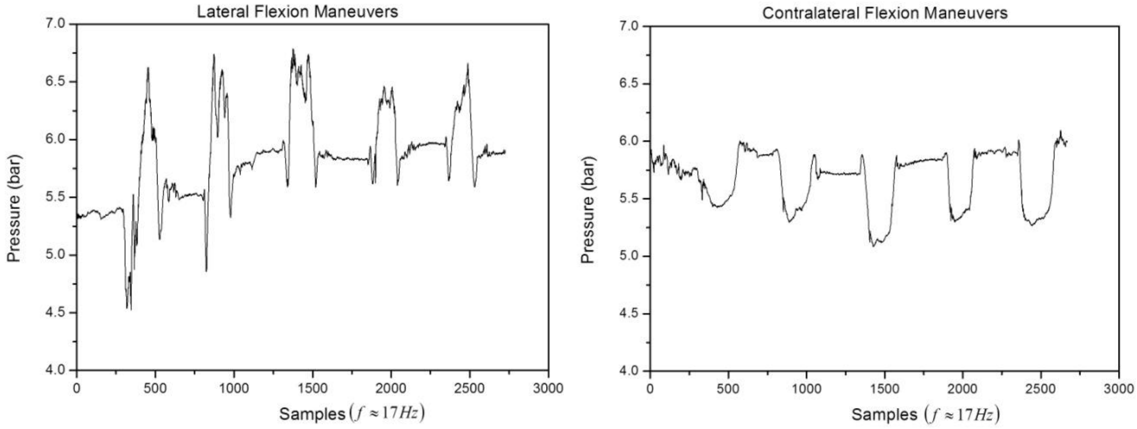

Figure 79 – Pressure raw data resulting from lateral flexion maneuvers.

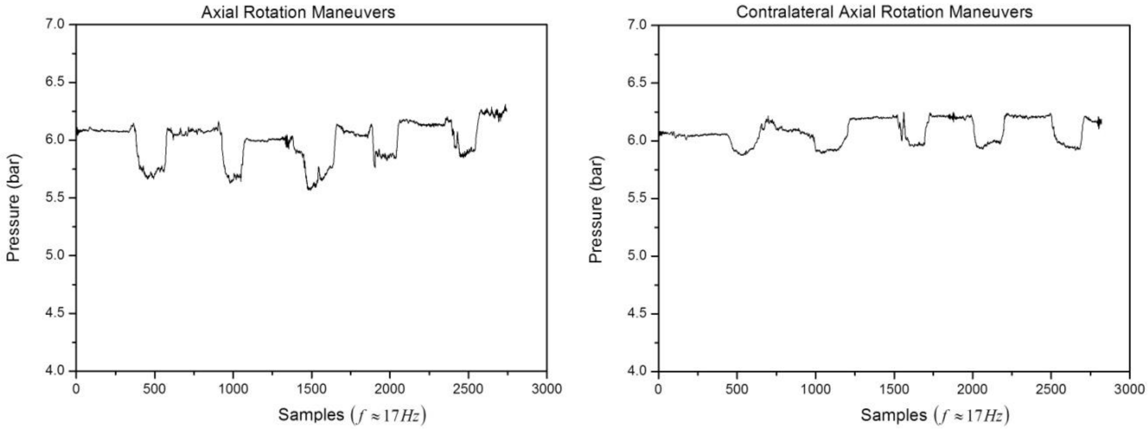

Figure 80 – Pressure raw data resulting from axial rotation maneuvers.

The previous maneuvers were performed by an experienced veterinarian aiming at measuring the pressure in the position of maximum ROM, although without controlling the magnitude of the external force applied to maintain that position and specimen angular displacement or ROM. In such conditions the Samba sensor was able to register pressure variations during repetitions of the same maneuver that are responsible for an increase in pressure [653]. Nevertheless, pressure amplitude and pressure pattern varied substantially in the same maneuver and between different maneuvers. Some possible explanations could be no control on the force produced by the veterinary, the difficulty felt by the veterinary in performing the maneuvers, changes in the position of the sensor head induced by pressure and the necessity of repositioning the sensor from one maneuver to another. Whereas the pressure in the NP is considered to be hydrostatic, changing the location of the sensor should not affect pressure readings unless it migrates to the AF. Thus, a possible migration of the sensor head to the AF could not be neglected, particularly during extension and lateral flexion maneuvers which have more irregular pressure patterns.

This type of *ex vivo* experiments demonstrates the importance of testing sensors in relatively harsh conditions capable of replicating *in vivo* scenarios. It was confirmed that sensor was capable to detect and measure pressure variations for several spinal maneuvers. Naturally, controlling force production and range of motion or using standardized protocols (*e.g.*, those associated with use of spine simulators) could provide a more comprehensive view on data.

3.3 ***In Vivo*** **Experiments**

The percutaneous approach under fluoroscopic control that was followed in the present study was similar to the approach used in human discography and percutaneous nucleotomy [307,644,654]. It seems the adequate technique for animal experiments and to ensure a transition to human *in vivo* applications. Moreover, compared to an “open” approach, where inner organs and tissues are exposed, the technique is less invasive. In fact, in the present study the animal was able to recover and released to its natural environment in less than four hours. The complete operation from the beginning to the end of anesthesia lasted for about two hours.

A standard 11-gauge biopsy Jamshidi needle ($\approx$3.0 mm OD and $\approx$2.3 mm ID) was used during percutaneous approach. The stylet of the needle was taken out and substituted by a 2.0 mm Kirschner-wire to create a passage into the NP and prepare the disc for implantation of the 360 μm OD sensing head. The previous dimensions of the needle were required because it was planned to collect the needle along the OF cable with 2 mm diameter. Nevertheless, it seems mandatory to discuss possible effects of the above procedures on disc properties.

It is well described that needle puncture can cause AF damage and alter the mechanical properties of the NP [647-649]. These effects seem to be more evident if the relative needle size (the ratio of the needle diameter to disc height) exceeds 40% [648]. In the present study disc height was estimated to be about 3.5mm. The ratio of the Jamshidi needle diameter to disc height was about 85.7% suggesting the fibers of the AF could be damaged by needle puncture. On the other hand, the ratio of the Kirschner-wire to disc height was about 57.1% suggesting a possible depressurization of the NP [648].

It is important to retain that pressure outcomes can be influenced by the previous effects and the way to minimize them is to reduce needle dimensions. However, in the present situation, it was not possible because it would require reducing the diameter of the fiber optic cable (see figure 53, p.129). Prior to *in vivo* experiments an attempt was made to acquire a modified Samba sensor, particularly with an optical cable with smaller diameter. Even so, it was not possible because the company (Samba Sensors) was acquired by FISO Technologies, Inc., a wholly owned subsidiary of Nova Metrix LLC (MA, USA) and sensors became unavailable. Moreover, to our best knowledge the market is not offering similar sensors, particularly for the same pressure range.

Solving the previous geometric constrain will result in a less invasive procedure and it will be possible to take full advantage of the micrometer dimensions of the sensor. Alternatively the same sensor could be housed within a typical spinal needle (*e.g.*, those used for anesthesia or lumbar puncture). Typical diameters of spinal needles range between 0.42 mm (27G) and 1.2 mm (18G).

Pressure results obtained in the 5th lumbar IVD with the animal in a lateral right recumbence position under general anesthesia are presented in figure 81.

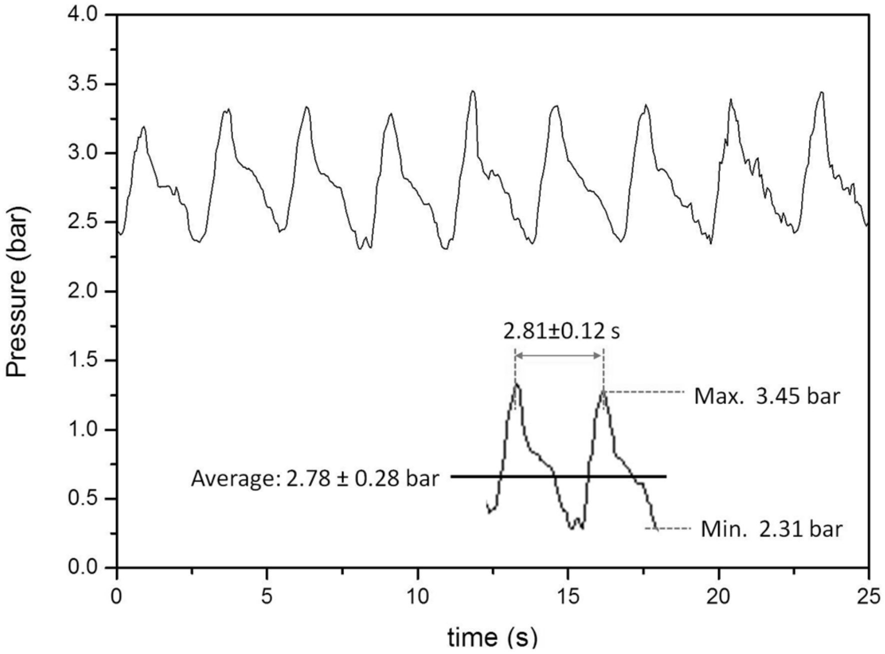

Figure 81 – Intradiscal pressure pattern in the 5th lumbar disc. Results were obtained with the animal in a lateral right recumbence position under general anesthesia. Average pressure and time were detailed as well as maximum and minimum pressures.

As can be seen in figure 81_a periodic pressure pattern was obtained during measurements. On average, the signal periodicity was 2.81 ± 0.12 s (time peak to peak), which corresponds to approximately 21.3 ± 0.12 pressure cycles per minute. The previous rate was similar to the respiratory rate under spontaneous ventilation which, on average, for the complete surgery, was ≈15.4 breaths per minute and during measurements about 20.5 breaths per minute. The hearth rate during the surgery was, on average, ≈85.5 beats per minute (bpm) and could also influence the periodicity of the observed pattern.

The effect of breathing in intradiscal pressure was also reported by Sato *et al.* [484] in lumbar discs (L4-L5) of human subjects and in lumbar discs of pigs [311-312,315]. Sato *et al.* [484], also found that the wave pattern was synchronized with the number of respirations with the subject in the prone position and existed slightly or disappeared in the standing and the sitting body positions.

The effect of breathing on the intradiscal pressure of porcine lumbar discs (L1-L2) was studied in more detail by Keller *et al.* [653,655]. The respiratory rate and breathing volume were controlled with a ventilator. Typical respiratory rates in sheep under general anesthesia could range between 12 an 27 breaths per minute [656-657]. Authors concluded that breathing had a significant effect on the intradiscal pressure, which seems to decrease with respiratory rate (breathing volume was left constant) and increase (1 to 2.5%) with breathing volume (keeping the respiratory rate constant) [653].

In the present study the anesthesia was maintained through isoflurane (2-3%) in oxygen with spontaneous ventilation. Thus it was not possible to control the respiration rate and the breathing volume in order to measure their influence on the variation of the intradiscal pressure. This could be an interesting issue for future research. In fact, it has been suggested that breathing can play an important role in the nutrition of the IVD [653,658]. The disc is the largest avascular tissue in the body and nutrients reach its cells by diffusing from blood vessels of the vertebral body through the cartilage endplate into the disc matrix under diffusion and osmotic gradients [659-660]. Therefore, the intradiscal pressure variation induced by breathing could help to pace the rate of diffusion and osmosis. On the other hand, high kinematic stresses (*e.g.*, maximum ROM) and loads rise intradiscal pressures to levels that could result in impaired nutrition of the IVD [660].

In the present study pressure fluctuations ranged between 2.31 bar and 3.45 bar, with a maximum amplitude of 1.14 bar. The average pressure was 2.78 ± 0.28 bar (figure 81).

The previous values seem to be higher than those observed in other studies. In the study of Keller *et al.* [653] the average resting intradiscal pressure in lumbar porcine specimens was found to be 0.357 ± 0.060 bar. An average value of 0.81 ± 0.05 bar was found in another study with porcine lumbar discs [315]. In the study of Höejer *et al.* [311] a similar Samba sensor (430 μm OD) was used to measure intradiscal pressures in anesthetized pigs and minimum registered resting pressures were of 0.7 bar. The amplitude of breathing pressure fluctuations was less than 0.2 bar [311]. In the study of Sato *et al.* [484] the intradiscal pressure in the prone and lateral lying positions of human subjects was of 0.91 ± 0.27 bar and 1.51 ± 0.53 bar, respectively. These values were similar to those found by Wilke *et al.* [307] for L4-L5 lumbar discs of subjects in the lying supine (1.0 bar), lying on the side (1.2 bar) and lying prone (1.1 bar) positions.

On the other hand, higher values than those observed in the present study were registered by Nachemson *et al.* [227] in human subjects. In the reclining position pressures varied from 1.4 to 8.3 bar (mean, 5.4 ± 1.8 bar) [227]. Guehring *et al.* [313] implanted a similar Samba sensor (OD not specified) in rabbits and physiologic pressures ranged between 2.2 and 4.2 bar (mean 3.6 bar).

Finally, in thoracic discs of human subjects, which have the same kyphotic curvature as the lumbar spine of a sheep, intradiscal pressure values were closer to those found in the present study, ranging between 2.0 ± 0.3 bar (T9–T10, T10–T11) and 2.9 ± 0.4 bar (T6–T7, T7–T8) for the lying prone position; and between 3.0 ± 0.3 bar (T9–T10, T10–T11) and 3.4 ± 0.5 bar (T6–T7, T7–T8) for the lying on side position [487]. More recently, a similar Samba sensor (360 μm OD) was used in the study of Hebelka *et al.* [312] and the median baseline pressures that were registered for sedated pigs were of 2.0 bar (range, 1.2 to 3.1 bar). The breathing effect on intradiscal pressure was registered but the corresponding amplitude was not reported. Even so, observing published plotted data on pressure amplitude due to breathing seems to be lower than the amplitude observed in the present study.

Previous studies suggest a marked dispersion in the intradiscal pressure values at rest. These values appear to vary with the species and within species. The sensor may have some influence on the results, given its geometry and working principle, for example. Still, the results of the present study seem to overestimate the values of intradiscal pressure and particularly the amplitude of pressure fluctuations due to breathing. These values seem also to contradict a possible depressurization of the NP due to a large needle puncture. In fact, further research using FOS to better understand these phenomena seems essential.

The major disadvantage of FOSs is perhaps their fragility. In fact, in another attempt to measure sensor repeatability it broke (figure 82).

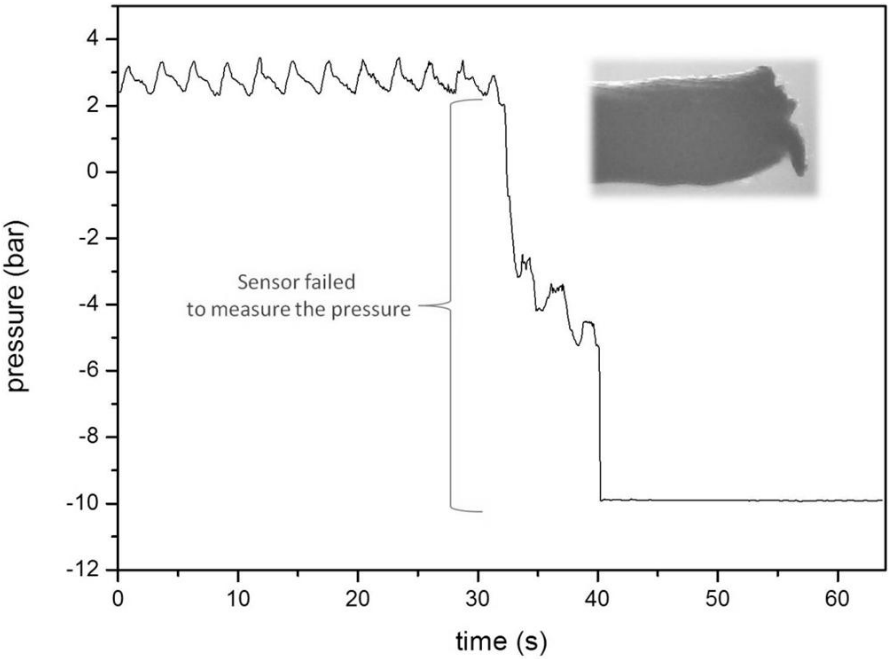

Figure 82 – Sensor failure occurred during removal of the sensor from the 5th lumbar intervertebral disc. On top a picture of the broken sensor.

A sensor of this type costs more than € 1,000 and despite the robustness demonstrated during calibration, *ex vivo* and *in vivo* experiments, the risk of failure can compromise their acquisition to carry out these experiences on a routine basis. Thus, the possibility of starting developing similar sensors for biomedical and biomechanical applications at INESC-Porto facilities represented an interesting opportunity and led us to the next study.

4. Final Remarks

In this study the possibility of using FOS to perform *in vivo* studies and measure intradiscal pressures was explored. A similar surgical protocol to the one used in humans was applied. This approach is strongly recommended if human applications are pursued [525].

Using smaller needles and/or modifying sensor geometry seem mandatory to minimize disruption of the AF and NP and preserve the minimally invasive potential of FOSs.

Studying strategies to increase FOSs robustness without compromising their micrometric dimensions also seems also a critical issue, because it will reduce the risk of adverse reactions, ensure sensor durability and diminish the cost per sensor. Probably, further improvements will require sensor encapsulation using special needles or catheters.

The interrogation unit that was developed also requires further improvement. It should be small to allow manual handling and portability. Wireless data transmission should also be considered. In such a way it could be possible to perform dynamic studies, such as locomotion studies, and collect data for longer periods without having either the human or the animal anesthetized.

Finally, further research seems mandatory to produce clinical relevant information.

Study 4 - Fiber Optic Prototypes for Pressure Measurement [15;16;17]

---

[15] Roriz P, Frazão O, Simões J, Santos J Sensores de pressão baseados em fibra ótica para aplicações biomédicas e biomecânicas. In: Física 2012: Comunicação e Informação em Ciência, Aveiro, Portugal, September, 6-8 2012.

[16] Roriz P, Frazão O, Santos JL, Simões J Fiber optic sensors for biomechanical and biomedical applications. In: Natal-Jorge R, Tavares JS, Belinha J, Parente ML, Martins PS (eds) 5th Portuguese Congress on Biomechanics, Espinho, Portugal, Feb. 8-9 2013. Sociedade Portuguesa de Biomecânica, pp 503-8.

[17] Roriz P, Frazão O, Santos JL, Simões J Fiber optic sensors for physiological pressure measurements. In: VIII RIAO/XI OPTILAS 2013, Porto, Portugal, July 22-26 2013.

1. Introduction

The main purpose of this study was to present ongoing research at INESC Porto aiming to explore FOS configurations for temperature, strain, force and pressure measurements intended for biomedical and biomechanical applications. The most common working principles applied to FOSs for biomedical and biomechanical applications are based on intensity, phase and wavelength modulation, the latter associated with the operation of FBGs.

Wavelength modulation is typically achieved through use of FBG sensors which are probably the simplest and most interesting type of FOSs, particularly for temperature and strain measurements. In fact, the majority of studies that have been conducted by Portuguese and Brazilian research groups in the field of biomedical engineering and biomechanics focused on the use of FBGs. Some major research topics included the study of dental implants and supporting tissues [140-141]; monitoring the curing process of dental resin cements [144] and of bone cements [103,146,661]; studying the possibility of osseointegration of optical fibre and FBGs [662]; and their use in orthopedic devices [147]. More recently, an FBG was used to monitor radial strain of the IVD under axial compression [138].

Intensity and phase modulation configurations are not so exploited by these research groups. Among them, interferometric based sensors, namely those based on the F-P configuration seem very attractive for biomechanical and biomedical applications. F-P interferometer sensors were introduced in the early 1980s and solved many drawbacks of intensity modulated sensors. Instead of measuring a change in light intensity, these sensors aim at phase differences in the light beams. Their most common configuration includes a small-size sensing element bonded to the tip of the fiber. This element is an optical cavity formed by two parallel reflecting surfaces where multiple reflections occur (figure 8). One of the reflecting surfaces is a diaphragm that changes the optical cavity depth (*i.e.*, the distance between mirrors) under the action of the measurand and, consequently, the characteristics of the signal that reaches the photodetector. Compared to intensity modulated schemes and FBG sensors, F-P interferometers are capable of achieving high sensitivities and resolutions, but at the expense of relatively complex interrogation/detection techniques [47].

The present study is focused on the proof of concept of two F-P based sensors that have been developed for pressure measurements of fluids. The prototypes were tested in a purpose-built pressure chamber and with further optimization they could be used to measure the pressures of specific biological fluids.

2. Material and Methods

2.1 High-pressure Fabry-Pérot sensor

Sensor 1 consisted of a high-pressure F-P sensor with an optical cavity formed by the reflecting surfaces of the tips of two single mode fibers (Corning® SMF-28™ Single-Mode Optical Fiber, NY, USA) facing each other (figure 83).

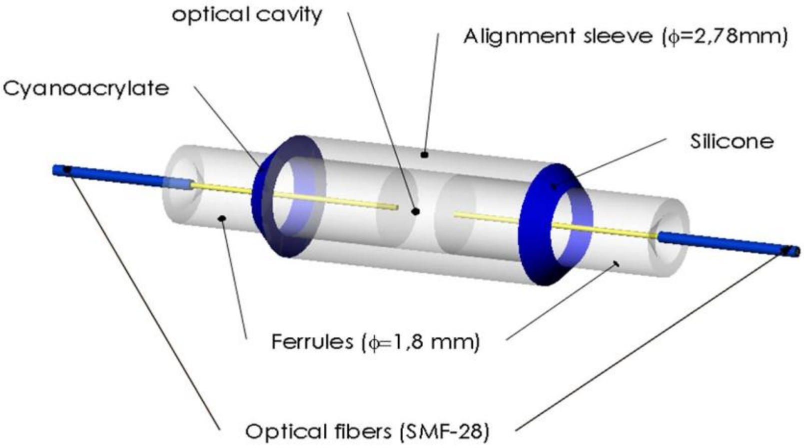

Figure 83 - Schematic drawing of a high-pressure Fabry-Pérot (F-P) prototype.

The acrylate coating of the OFs was mechanically stripped. Then, the OF was cleaved with a high precision cleaver (Sumitomo FC-6RS, Sumitomo Electric, Japan) (figure 84) in order to get a clear cross section reflecting tip surface. The quality of cleaving was inspected using an optical microscope.

Figure 84 – An image of the cleaver that was used to cleave the fiber tips.

Each OF was rigidly encapsulated (using a cyanoacrylate adhesive) inside a single bore of a borosilicate glass ferrule (ID 127±3μm, OD 1.8mm±0.005mm, unit length 5.7mm; CM Scientific LTd., Product ID: Ferrule-SB127/1.8/5.7BORO) (figure 83).

To create an optical cavity, the previous set was aligned using an alignment sleeve (ID 1815μm±10μm, OD 2780μm±30μm, length 6mm±0.1mm; CM Scientific Ltd., Product ID: TQNC18152780/6) (figure 83).

The ferrule connected to the light source was rigidly fixed to the sleeve with cyanoacrylate adhesive. After proper connections to a broadband source, an optical circulator and an optical spectrum analyzer (ADVANTEST Q8384), the output spectrum (optical power *versus* wavelength) was adjusted by controlling the distance between the reflecting surfaces of the two fibers (optical cavity length). Then, the other ferrule was glued to the sleeve with a silicone polymer (Silastic Medical Adhesive Silicone, Type A, Dow Corning) and allowed to move in order to sense the applied pressure. Under pressure, the optical cavity length changes and, consequently, the phase of the spectrum. The maximum outer diameter of the sensor was 2.78mm.

2.2 Low-pressure Fabry-Pérot Sensor

Sensor 2 consisted of low-pressure F-P sensor prototype with an optical cavity provided by a PCF (OD 125.5 μm, hollow core diameter 44.4 μm; Institute of Photonic Technology, Jena, Germany) and the reflecting surfaces of a single mode fiber (Corning® SMF-28™ Single-Mode Optical Fiber, NY, USA) at one end, and a biocompatible silicone polymer (Silastic Medical Adhesive Silicone, Type A, Dow Corning) at the other end (figure 85).

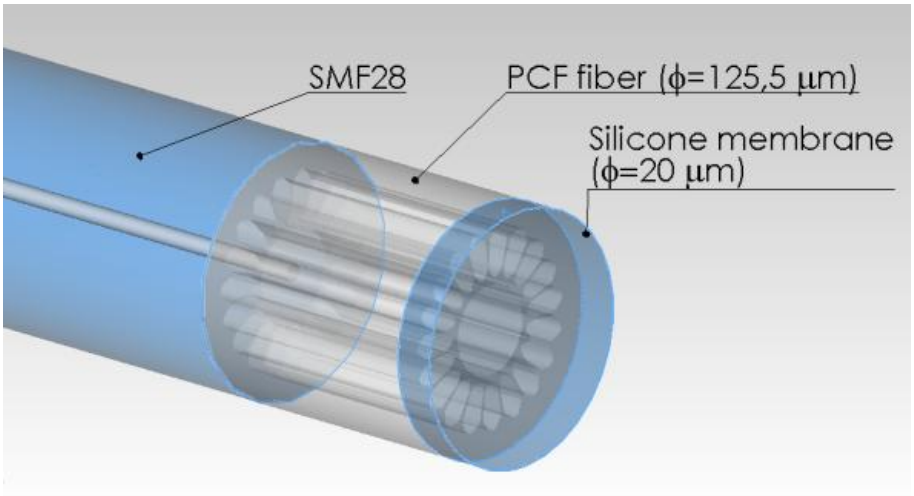

Figure 85 - Schematic drawing of a low-pressure Fabry-Pérot (F-P) prototype.

Both coatings of the OF and the PCF were mechanically stripped. Then, both tips were cleaved with a high precision cleaver (Sumitomo FC-6RS, Sumitomo Electric, Japan) (figure 84) in order to get a clear cross section. The quality of cleaving was inspected using an optical microscope.

The two tips were carefully fused using an Arc Fusion Splicer (Fujikura FSM-60S Arc Fusion Splicer) (figure 86). Manual alignment functions of the Arc Fusion Splicer program were used.

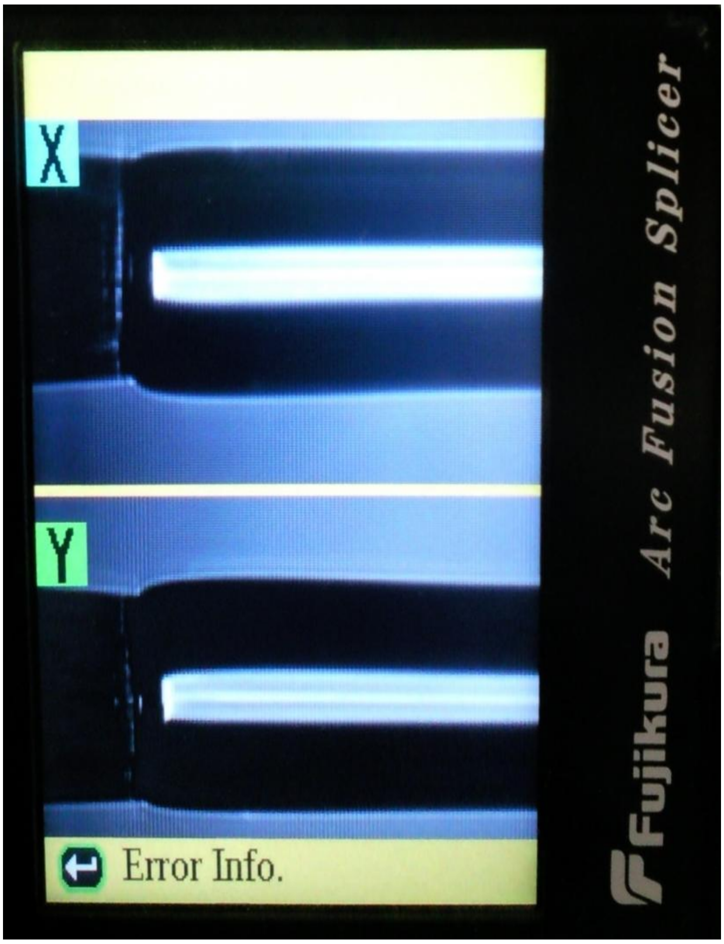

Figure 86 – An image of the result of splicing the single mode fiber to the photonic crystal fiber using the Arc Fusion Splicer.

A polymer (Silastic Medical Adhesive Silicone, Type A, Dow Corning) was applied to the cleaved tip at the opposite end of the PCF. Under pressure a silicone membrane deflection occurs varying the optical cavity length and a phase change is observed. Sensor was interrogated using a broadband source, a circulator and an optical spectrum analyzer (ADVANTEST Q8384).

2.3 Pressure Chamber

For the proof of concept pressure measurements were made in the purpose-built pressure device that has previously been described (figure 59, p.134). Sensors were tested in distilled water.

3. Results and Discussion

Average results for five consecutive pressure cycles are presented for sensor 1 and 2 in figure 87 and figure 88, respectively.

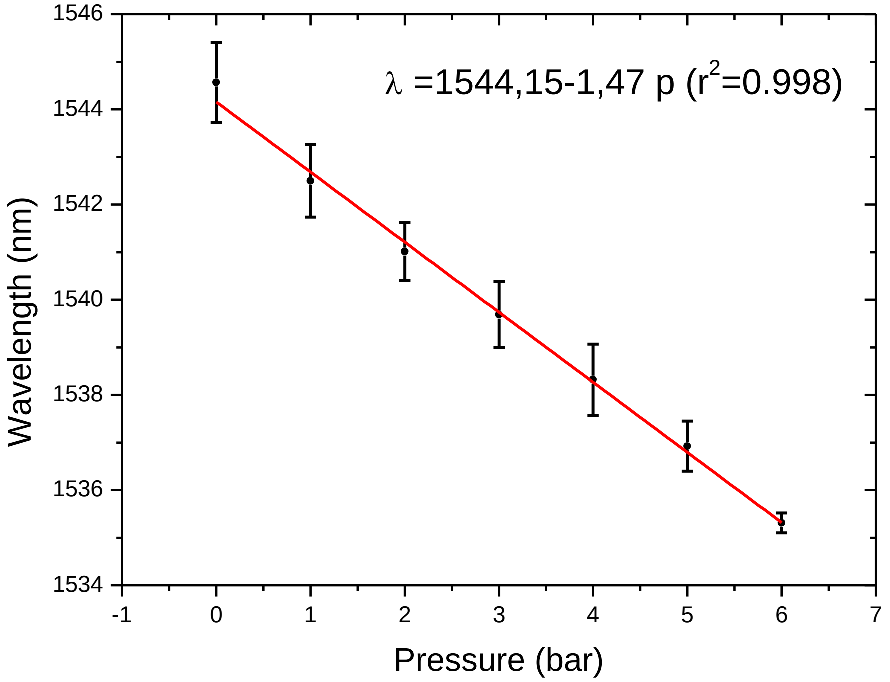

Figure 87 - Wavelength shift of sensor 1 under pressure.

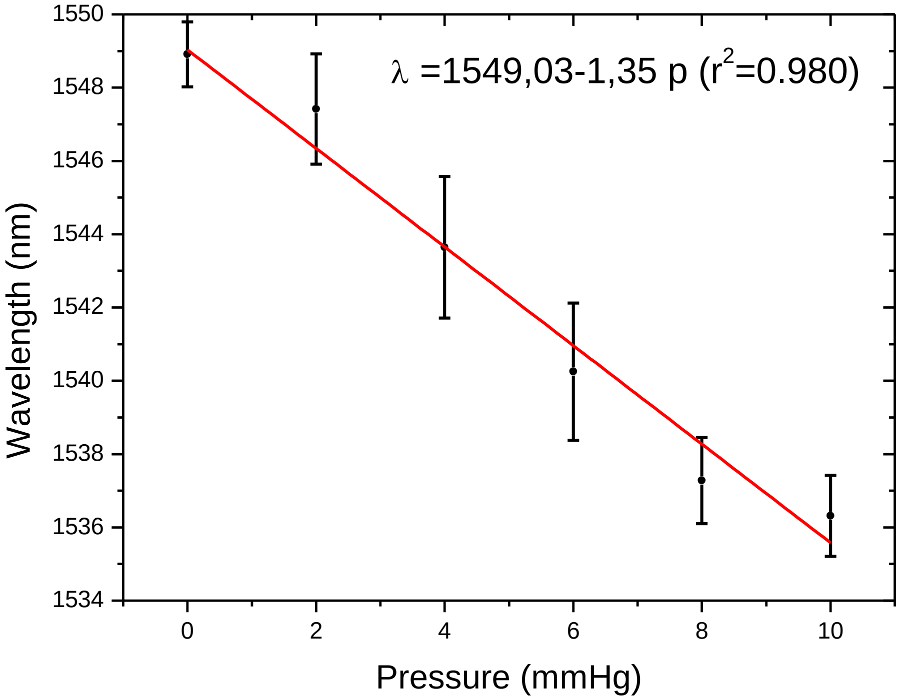

Figure 88 - Wavelength shift of sensor 2 under pressure.

Results from sensor 1 are in the range of intradiscal pressures [307]. With further miniaturization (below 1 mm is desirable), sensor encapsulation (*e.g.*, catheter or a spinal needle) and use of a biocompatible resin to fix the non movable part of the sensor, these type of sensors can be explored to sense these pressures either *ex vivo* or *in vivo*. Sensor output depended on the quality and alignment of the reflecting surfaces, the length of the optical cavity, adhesives type and their application.

Results from sensor 2 are in the range of intracranial pressures [252]. With optimization of sensor performance (namely reduction of sensor variability) and its encapsulation it can also be explored to sense these pressures either *ex vivo* or *in vivo*. Sensor output depends on the quality of splices, PCF length and silicone application.

4. Final Remarks

For the proof of concept, two possible configurations intended for pressure measurement have been presented. These sensors can be fabricated and tested in our facilities. Nevertheless to get precise and accurate measurements fabrication techniques should be optimized, especially if biomechanical and biomedical testing is pursued.

Part IV – Conclusion and Future Work

The present work represents an effort to better understand the mechanical behavior of the spine and, particularly, of the spinal motion segment and the intervening disc. Simultaneously, it also allowed to deepen the knowledge of fiber optic sensors and explore their potential beyond the bench tests, especially in cadaveric specimens and *in vivo*.

The two previous topics were explored in the review of literature. The state of the art concerning fiber optic sensors has been reviewed comprehensively looking at their major working principles and focusing on biomechanical and biomedical applications. *In vivo* applications were highlighted as well as the physical quantities of temperature, strain, force and pressure. Addressing the spinal motion segment, anatomical, histological and mechanical properties allowed a deep knowledge on the structure that would be explored in the experimental part. Moreover, the literature review launched the foundations for a systematic study in the field and offered the possibility of defining and exploring several research lines and projects in the near future.

The experimental part reflects author's efforts to perform research not only on an autonomous basis but also in partnership, benefiting from and collaborating with several research teams, from mechanics to physics and medicine. The author has no doubt that the quality of research depends on multidisciplinary teams and the path to knowledge and innovation is often drawn along border lines.

Experimental work is also an unfinished task. Thus the author expects to continue spine research depending on research projects funding, human resources and the willing to accomplish them. The main objectives for the near future are:

Creating a research group/network on spine biomechanics and the conditions to apply standards in spinal testing;

To develop a fiber optic sensor prototype for *in vivo* intradiscal pressure measurements.

Finally the author must admit that if it has not been possible to go further, all responsibility lies on him and his limitations. Still, he continues to dream about the uncertainty and the unknown, always living with the pleasure the smallest of discoveries can provide.

References

1. Mignani AG, Baldini F (1996) Biomedical sensors using optical fibres. Rep Prog Phys 59 (1):1-28.

2. Arkwright JW, Blenman NG, Underhill ID, Maunder SA, Szczesniak MM, Dinning PG, Cook IJ (2009) In-vivo demonstration of a high resolution optical fiber manometry catheter for diagnosis of gastrointestinal motility disorders. Opt Express 17 (6):4500-8.

3. Ladd ME, Quick HH (2000) Reduction of resonant RF heating in intravascular catheters using coaxial chokes. Magn Reson Med 43 (4):615-9.

4. Voskerician G, Shive MS, Shawgo RS, Recum Hv, Anderson JM, Cima MJ, Langer R (2003) Biocompatibility and biofouling of MEMS drug delivery devices. Biomaterials 24 (11):1959-67.

5. Monk DJ, Soane DS, Howe RT (1993) Determination of the etching kinetics for the hydrofluoric acid/silicon dioxide system. J Electrochem Soc 140 (8):2339-46.

6. Bühler J, Steiner FP, Baltes H (1997) Silicon dioxide sacrificial layer etching in surface micromachining. J Micromech Microeng 7 (1):R1-R13.

7. Thompson M, Vandenberg ET (1986) In vivo probes: Problems and perspectives. Clin Biochem 19 (5):255-61.

8. Biswas DR (1991) Characterization of polyimide-coated optical fibers. Opt Eng 30 (6):772-5.

9. Biswas DR (1992) Optical fiber coatings for biomedical applications. Opt Eng 31 (7):1400-3.

10. Samset E, Mala T, Ellingsen R, Gladhaug I, Soreide O, Fosse E (2001) Temperature measurement in soft tissue using a distributed fibre Bragg-grating sensor system. Minim Invasiv Ther 10 (2):89-93.

11. Chen L, Wansapura JP, Heit G, Butts K (2002) Study of laser ablation in the in vivo rabbit brain with MR thermometry. J Magn Reson Imag 16 (2):147-52.

12. Pleros N, Kanellos GT, Papaioannou G Optical fiber sensors in orthopedic biomechanics and rehabilitation. In: 9th Int Conf Information Technology Applications Biomedicine (ITAB), Larnaca, Cyprus, November 4-7 2009. IEEE, pp 1-4.

13. Wonneberger U, Schnackenburg B, Wlodarczyk W, Walter T, Streitparth F, Rump J, Teichgräber UKM (2010) Intradiscal temperature monitoring using double gradient-echo pulse sequences at 1.0T. J Magn Reson Imag 31 (6):1499-503.

14. Stolov AA, Simoff DA, Li J (2008) Thermal stability of specialty optical fibers. J Lightwave Technol 26 (20):3443-51.

15. Webb DJ, Hathaway MW, Jackson DA, Jones S, Zhang L, Bennion I (2000) First in-vivo trials of a fiber Bragg grating based temperature profiling system. J Biomed Opt 5 (1):45-50.

16. Utzinger U, Richards-Kortum RR (2003) Fiber optic probes for biomedical optical spectroscopy. J Biomed Opt 8 (1):121-47.

17. Ferreira LA, Araújo FM, Mascarenhas T, Natal-Jorge RM, Fernandes AA Dynamic assessment of women pelvic floor function by using a fiber Bragg grating sensor system. In: Proc SPIE 6083

San Jose, CA, USA, February 15 2006. Optical Fibers and Sensors for Medical Diagnostics and Treatment Applications VI. SPIE, pp H1-H10.

18. Nesson S, Yu M, Zhang X, Hsieh A, H. (2008) Miniature fiber optic pressure sensor with composite polymer-metal diaphragm for intradiscal pressure measurements. J Biomed Opt 13 (4):1-19.

19. Dennison CR, Wild PM, Wilson DR, Cripton PA (2008) A minimally invasive in-fiber Bragg grating sensor for intervertebral disc pressure measurements. Meas Sci Technol 19 (8):1-12.

20. Dennison CR, Wild PM, Dvorak MF, Wilson DR, Cripton PA (2008) Validation of a novel minimally invasive intervertebral disc pressure sensor utilizing in-fiber Bragg gratings in a porcine model: An ex vivo study. Spine 33 (17):E589-E94.

21. FISO (2011) FOP-MIV product datasheet. FISO Technologies. http://www.fiso.com/admin/useruploads/files/fop-miv.pdf. Accessed May 10 2013

22. Xu J (2005) High temperature high bandwidth fiber optic pressure sensors. Ph.D. thesis, Faculty of Virginia Polytechnic Institute and State University, Blacksburg, Virginia

23. Udd E (1991) Fiber optic sensors: An introduction for engineers and scientists John Wiley & Sons, Inc., vol Pure and Applied Optics Wiley Interscience, NY.

24. Wehrle G, Nohama P, Kalinowski HJ, Torres PI, Valente LCG (2001) A fibre optic Bragg grating strain sensor for monitoring ventilatory movements. Meas Sci Technol 12 (7):805-9.

25. Jackson DA, Jones JDC (1986) Fibre optic sensors. Opt Acta: Int J Opt 33 (12):1469-503.

26. Fresvig T, Ludvigsen P, Steen H, Reikerås O (2008) Fibre optic Bragg grating sensors: An alternative method to strain gauges for measuring deformation in bone. Med Eng Phys 30 (1):104-8.

27. Mohanty L, Tjin SC, Lie DTT, Panganiban SEC, Chow PKH (2007) Fiber grating sensor for pressure mapping during total knee arthroplasty. Sensor Actuat A-Phys 135 (2):323-8.

28. Hopkins HH, Kapany NS (1954) A flexible fibrescope using static scanning. Nature 173 (4392):39-41.

29. Polanyi ML, Hehir RM (1962) In vivo oximeter with fast dynamic response. Rev Sci Instrum 33 (10):1050-4.

30. Enson Y, Briscoe WA, Polanyi ML, Cournand A (1962) In vivo studies with an intravascular and intracardiac reflection oximeter. J Appl Physiol 17 (3):552-8.

31. Enson Y, Jameson AG, Cournand A (1964) Intracardiac oximetry in congenital heart disease. Circulation 29:499-507.

32. Clark F, Schmidt E, DeLaCroix R (1965) Fiber optic blood pressure catheter with frequency response from DC into the audio range. Paper presented at the Proc Nat Elec Conf, McCormick Place, Chicago, IL, October 25-27

33. Gamble WJ, Hugenholtz PG, Monroe RG, Polanyi ML, Nadas AS (1965) The use of fiberoptics in clinical cardiac catheterization: I. intracardiac oximetry. Circulation 31 (3):328-43.

34. Hugenholtz PG, Gamble WJ, Monroe RG, Polanyi ML (1965) The use of fiberoptics in clinical cardiac catheterization: II. In vivo dye-dilution curves. Circulation 31 (3):344-55.

35. Frommer PL, Ross Jr J, Mason DT, Gault JH, Braunwald E (1965) Clinical applications of an improved, rapidly responding fiberoptic catheter. The American Journal of Cardiology 15 (5):672-9.

36. Harrison DC, Kapany NS, Miller HA, Silbertrust N, Henry WL, Drake RP (1966) Fiber optics for continuous in vivo monitoring of oxygen saturation. American Heart Journal 71 (6):766-74.

37. McCarthy B, Hood WB, Lown B (1967) Fiberoptic monitoring of cardiac output and hepatic dye clearance in dogs. J Appl Physiol 23 (5):641-5.

38. Mook GA, Osypka P, Sturm RE, Wood EH (1968) Fibre optic reflection photometry on blood. Cardiovascular Research 2 (2):199-209.

39. Ramirez A, Hood WB, Polanyi ML, Wagner R, Yankopoulos NA, Abelmann WH (1969) Registration of intravascular pressure and sound by a fiberoptic catheter. J Appl Physiol 26 (5):679-83.

40. Lekholm A, Lindström LH (1969) Optoelectronic transducer for intravascular measurements of pressure variations. Med Biol Eng Comput 7 (3):333-5.

41. Hugenholtz PG, Wagner HR, Ellison RC (1969) Application of fiberoptic dye-dilution technic to the assessment of myocardial function. I. Description of technic and results in 100 patients with congenital or acquired heart disease. Am J Cardiol 24 (1):79-94.

42. Singh R, Ranieri AJ, Jr., Vest HR, Jr., Bowers DL, Dammann JF, Jr. (1970) Simultaneous determinations of cardiac output by thermal dilution, fiberoptic and dye-dilution methods. Am J Cardiol 25 (5):579-87.

43. Silvestri S, Schena E (2011) Optical-fiber measurement systems for medical applications. In: Predeep P (ed) Optoelectronics: Devices and Applications. InTech, Rijeka, Croatia, pp 205-24.

44. Lindström LH (1970) Miniaturized pressure transducer intended for intravascular use. IEEE T Bio-Med Eng 17 (3):207-19.

45. Fields JN, Asawa CK, Ramer OG, Barnoski MK (1980) Fiber optic pressure sensor. J Acoust Soc Am 67 (3):816-8.

46. Fabry C, Perot A (1898) Mesure de petites epaisseurs en valeur absolue. Comptes Rendus. Academie des Sciences, Paris.

47. Yu FTS, Shizhuo Y (eds) (2002) Fiber optic sensors. Marcel Dekker, Inc., New York.

48. Hill KO, Fujii Y, Johnson DC, Kawasaki BS (1978) Photosensitivity in optical fiber waveguides: Application to reflection filter fabrication. Appl Phys Lett 32 (10):647-9.

49. Hill KO, Malo B, Bilodeau F, Johnson DC (1993) Photosensitivity in optical fibers. Annu Rev Mater Sci 23 (1):125-57.

50. Meltz G, Morey WW, Glenn WH (1989) Formation of Bragg gratings in optical fibers by a transverse holographic method. Opt Lett 14 (15):823-5.

51. Keck DB (1996) Optoelectronics in Japan and the United States. Japanese Technology Evaluation Center (JTEC), Baltimore, MD, USA.

52. Othonos A (1997) Fiber Bragg gratings. Rev Sci Instrum 68 (12):4309-41.

53. Rao YJ, Jackson DA Recent progress in multiplexing techniques for in-fiber Bragg grating sensors. In: Bennett KD, Kim BY, Liao Y (eds) P SPIE 2895, 171, Beijing, China, 6 Nov 1996. Photonics China, Fiber Optic Sensors V: Strain and Pressure Sensing. SPIE, pp 171-82.

54. Rao YJ, Lobo Ribeiro AB, Jackson DA, Zhang L, Bennion I Simultaneously spatial-time and wavelength-division-multiplexed in-fiber Bragg grating sensor network. In: P SPIE 2838, 23, Denver, CO, USA, 5 Aug 1996. Fiber Bragg Grating Sensors I: Distributed and Multiplexed Fiber Optic Sensors VI. pp 23-30.

55. Arkwright JW, Doe SN, Blenman NG, Underhill ID, Maunder SA, Lim B, Szczesniak MM, Dinning PG, Cook IJ The use of wavelength division multiplexed fiber Bragg grating sensors for distributed sensing of pressure in the gastrointestinal tract. In: IEEE Photonics Global Conf (IPGC), Singapore, December 8-11 2008. IEEE, pp 1-4.

56. Tjin SC, Hao J, Lam Y-Z, Ho YC, Ng BK (2001) A pressure sensor using fiber Bragg grating. Fiber Integrated Opt 20 (1):59-69.

57. Rao YJ, Webb DJ, Jackson DA, Zhang L, Bennion I (1997) In-fiber Bragg-grating temperature sensor system for medical applications. J Lightwave Technol 15 (5):779-85.

58. James SW, Tatam RP, Twin A, Morgan M, Noonan P (2002) Strain response of fibre Bragg grating sensors at cryogenic temperatures. Meas Sci Technol 13 (10):1535-9.

59. Dennison CR, Wild PM (2008) Enhanced sensitivity of an in-fibre Bragg grating pressure sensor achieved through fibre diameter reduction. Meas Sci Technol 19 (12):1-11.

60. Mishra V, Singh N, Tiwari U, Kapur P (2011) Fiber grating sensors in medicine: Current and emerging applications. Sensor Actuat A-Phys 167 (2):279-90.

61. Xu MG, Archambault JL, Reekie L, Dakin JP (1994) Discrimination between strain and temperature effects using dual-wavelength fibre grating sensors. Electron Lett 30 (13):1085-7.

62. Polla DL, Erdman AG, Robbins WP, Markus DT, Diaz-Diaz J, Rizq R, Nam Y, Brickner HT, Wang A, Krulevitch P (2000) Microdevices in medicine. Annu Rev Biomed Eng 2 (1):551-76.

63. Voldman J, Gray ML, Schmidt MA (1999) Microfabrication in biology and medicine. Annu Rev Biomed Eng 1 (1):401-25.

64. Stendel R, Heidenreich J, Schilling A, Akhavan-Sigari R, Kurth R, Picht T, Pietilä T, Suess O, Kern C, Meisel J, Brock M (2003) Clinical evaluation of a new intracranial pressure monitoring device. Acta Neurochirurgica 145 (3):185-93.

65. Citerio G, Piper I, Cormio M, Galli D, Cazzaniga S, Enblad P, Nilsson P, Contant C, Chambers IR (2004) Bench test assessment of the new Raumedic Neurovent-P ICP sensor: A technical report by the BrainIT Group. Acta Neurochir 146 (11):1221-6.

66. Citerio G, Piper I, Chambers IR, Galli D, Enblad P, Kiening K, Ragauskas A, Sahuquillo J, Gregson B (2008) Multicenter clinical assessment of the Raumedic Neurovent-P Intracranial Pressure Sensor: A report by the BrainIt Group. Neurosurgery 63 (6):1152-8

67. Wang L, Beebe DJ Shear sensitive silicon piezoresistive tactile sensor prototype. In: Remote Sensing, Proc. SPIE 3514, 359, Santa Clara, CA, USA, 21 September 1998. Micromachined Devices and Components IV. SPIE, pp 359-67.

68. Peterson J, Vurek G (1984) Fiber-optic sensors for biomedical applications. Science 224 (4645):123-7.

69. Walt DR (1992) Fiber-optic sensors for continuous clinical monitoring. P IEEE 80 (6):903-11.

70. Mignani AG, Baldini F (1995) In-vivo biomedical monitoring by fiber-optic systems. J Lightwave Technol 13 (7):1396-406.

71. Heller A (1999) Implanted electrochemical glucose sensors for the management of diabetes. Annu Rev Biomed Eng 1 (1):153-75.

72. Wolfbeis OS (2002) Fiber-optic chemical sensors and biosensors. Anal Chem 74 (12):2663-78.

73. Bosch M, Sánchez A, Rojas F, Ojeda C (2007) Recent development in optical fiber biosensors. Sensors 7 (6):797-859.

74. Leung A, Shankar PM, Mutharasan R (2007) A review of fiber-optic biosensors. Sensor Actuat B-Chem 125 (2):688-703.

75. Stitzel SE, Aernecke MJ, Walt DR (2011) Artificial noses. Annu Rev Biomed Eng 13 (1):1-25.

76. Roemer RB (1999) Engineering aspects of hyperthermia therapy. Annu Rev Biomed Eng 1 (1):347-76.

77. Grattan K, Zhang Z (2002) Fiber optic fluorescence thermometry. In: Lakowicz JR (ed) Topics in Fluorescence Spectroscopy: Probe design and chemical sensing, vol 4. Topics in Fluorescence Spectroscopy. Kluwer Academic, London, pp 335-76.

78. Wolthuis RA, Mitchell GL, Saaski EW, Hartl JC, Afromowitz MA (1991) Development of medical pressure and temperature sensors employing optical spectrum modulation. IEEE T Bio-Med Eng 38 (10):974-81.

79. Hamel C, Pinet É Temperature and pressure fiber optic sensors applied to minimally invasive diagnostics and therapies. In: Proc. SPIE 6083, 608306, San Jose, CA, USA, 21 Jan 2006. Optical Fibers and Sensors for Medical Diagnostics and Treatment Applications VI. SPIE, pp 608306-1.

80. Sholes RR, Small JG (1980) Fluorescent decay thermometer with biological applications. Rev Sci Instrum 51 (7):882-4.

81. Wickersheim KA, Alves RV A new optical technique for the measurement of temperature in RF and microwave fields. In: IEEE MTT-S Int Microwave Symposium Digest, Los Angeles, CA, USA, 15-19 Jun 1981. pp 468-9.

82. Wickersheim KA, Alves RV (1982) Fluoroptic thermometry: A new RF-immune technology. Prog Clin Biol Res 107:547-54.

83. Wickersheim KA, Mei HS (1987) Fiberoptic thermometry and its applications. J Microwave Power EE 22 (2):85-94.

84. Seat HC, Sharp JH, Zhang ZY, Grattan KTV (2002) Single-crystal ruby fiber temperature sensor. Sensor Actuat A-Phys 101 (1-2):24-9.

85. Zhang Z, Grattan K, Palmer A Cr:LiSAF fluorescence-lifetime-based fiber optic thermometer and its applications in clinical RF heat treatment. In: Summers R, Summan R, Hughes S (eds) P SPIE 1885, 300, Los Angeles, CA, USA, 1993. Advances in Fluorescence Sensing Technology: Lifetime-based sensing. SPIE, p 300.

86. LumaSense (2011) Biomedical Lab Kit - m3300 product datasheet. LumaSense Technologies. http://www.lumasenseinc.com/uploads/Products/Fiber_Optic_Temperature_Sensors/pdf/Datasheets/OEM_Modules/m3300-OEM_datasheet.pdf. Accessed 31 Mar 2013

87. Nakagawa H, Yamanashi WS, Pitha JV, Arruda M, Wang X, Ohtomo K, Beckman KJ, McClelland JH, Lazzara R, Jackman WM (1995) Comparison of in vivo tissue temperature profile and lesion geometry for radiofrequency ablation with a saline-irrigated electrode versus temperature control in a canine thigh muscle preparation. Circulation 91 (8):2264-73.

88. Sun MH, Wickersheim KA, Kim JH Fiber optic temperature sensors in the medical setting. In: Katzir A (ed) P SPIE 1067, 15, Los Angeles, CA, USA, 18-20 Jan 1989. Conference on Optical Fibers in Medicine: Optical Fibers in Medicine IV. SPIE, pp 15-21.

89. Neoptix (2011) T1™ fiber optic temperature sensor: Product datasheet. Neoptix. http://www.neoptix.com/literature/v1002_Datasheet_t1.pdf. Accessed 31 Mar 2013

90. Thurber KR, Tycko R (2008) Biomolecular solid state NMR with magic-angle spinning at 25 K. J Magn Res 195 (2):179-86.

91. Streitparth F, Knobloch G, Balmert D, Chopra S, Rump J, Wonneberger U, Philipp C, Hamm B, Teichgräber U (2010) Laser-induced thermotherapy (LITT): Evaluation of a miniaturised applicator and implementation in a 1.0-T high-field open MRI applying a porcine liver model. Eur Radiol 20 (11):2671-8.

92. Veronesi P, Leonelli C, Moscato U, Cappi A, Figurelli O (2005) Non-incineration microwave assisted sterilization of medical waste. J Microwave Power EE 40 (4):211-8.

93. Saaski EW, Hartl JC, Mitchell GL, Wolthuis RA, Afroniowitz MA A family of fiber optic sensors using cavity resonator microshifts. In: 4th Int Conf Optical Fiber Sensors, Tokyo, Japan, January 1 1986. Optical Society of America, pp 11-4.

94. Rao YJ, Jackson DA (1994) A prototype fibre-optic-based Fizeau medical pressure and temperature sensor system using coherence reading. Meas Sci Technol 5 (6):741-6.

95. Rao YJ (1997) In-fibre Bragg grating sensors. Meas Sci Technol 8 (4):355-75.

96. Rao YJ, Webb DJ, Jackson DA, Zhang L, Bennion I (1998) Optical in-fiber Bragg grating sensor systems for medical applications. J Biomed Opt 3 (1):38-44.

97. Smith EJ, Patterson BA, Webster RJ, Krug PA, Jones SK, Sampson DD Engineering a portable quasi-distributed fibre-Bragg-grating temperature sensing system for clinical hyperthermia. In: 15th Optical Fiber Sensors Conference Technical Digest, Australia, Crawley, WA, August, 7 2002. pp 269-72.

98. Saxena IF, Hui K, Astrahan M (2010) Polymer coated fiber Bragg grating thermometry for microwave hyperthermia. Med Physics 37 (9):4615-9.

99. Gowardhan B, Thomas B, Asterling S, Sheikh N, Greene D (2007) Cryosurgery for prostate cancer: Experience with third-generation cryosurgery and novel developments in the field. Eur Urol Suppl 6 (8):516-20.

100. Gowardhan B, Greene D (2007) Cryotherapy for the prostate: An in vitro and clinical study of two new developments. Advanced cryoneedles and a temperature monitoring system. BJU Int 100 (2):295-302.

101. Spillman WB, Mayer M, Bennett J, Gong J, Meissner KE, Davis B, Claus RO, Muelenaer AA, Xu X (2004) A 'smart' bed for non-intrusive monitoring of patient physiological factors. Meas Sci Technol 15 (8):1614-20.

102. Matin M, Hussain N, Shoureshi R Fiber Bragg sensor for smart bed sheet. In: P SPIE 5907, 590706, San Diego, CA, USA, 1 Aug 2005. Optics & Photonics: Photonic Devices and Algorithms for Computing VII. pp 590706-8.

103. Ramos A, Abe I, Schiller MW, Lopes P, Nogueira R, Pinto JL, Simões JA (2006) On the use of fiber Bragg sensors to assess temperature and thermal induce strain profiles in cemented hip mantles. J Biomech 39 (Supplement 1,):S514.

104. Whitney RJ (1953) The measurement of volume changes in human limbs. J Physiol 121:1-27.

105. Ravary B, Pourcelot P, Bortolussi C, Konieczka S, Crevier-Denoix N (2004) Strain and force transducers used in human and veterinary tendon and ligament biomechanical studies. Clin Biomech 19 (5):433-47.

106. Edwards RG, Lafferty JF, Lange KD (1970) Ligament strain in the human knee. J Basic Eng-T ASME 38:131-6.

107. Kennedy JC, Hawkins RJ, Willis RB (1977) Strain gauge analysis of knee ligaments. Clin Orthop Relat Res 129:225-9.

108. Draganich LF, Vahey JW (1990) An in vitro study of anterior cruciate ligament strain induced by quadriceps and hamstrings forces. J Orthop Res 8 (1):57-63.

109. Berns GS, Hull ML, Patterson HA (1992) Strain in the anteromedial bundle of the anterior cruciate ligament under combination loading. J Orthop Res 10 (2):167-76.

110. Hull ML, Berns GS, Varma H, Patterson HA (1996) Strain in the medial collateral ligament of the human knee under single and combined loads. J Biomech 29 (2):199-206.

111. Bach JM, Hull ML, Patterson HA (1997) Direct measurement of strain in the posterolateral bundle of the anterior cruciate ligament. J Biomech 30 (3):281-3.

112. Brown TD, Sigal L, Njus GO, Njus NM, Singerman RJ, Brand RA (1986) Dynamic performance characteristics of the liquid metal strain gage. J Biomech 19 (2):165-73.

113. Keegan KG, Baker GJ, Boero MJ, Pijanowski GJ, Phillips JW (1992) Evaluation of support bandaging during measurement of proximal sesamoidean strain in horses by use of a mercury strain gauge. Am J Vet Res 53 (7):1203-8.

114. van Weeren PR, Jansen MO, van den Bogert AJ, Barneveld A (1992) A kinematic and strain gauge study of the reciprocal apparatus in the equine hind limb. J Biomech 25 (11):1291-301.

115. Jansen MO, Schamhardt HC, van den Bogert AJ, Hartman W (1998) Mechanical properties of the tendinous equine interosseus muscle are affected by in vivo transducer implantation. J Biomech 31 (5):485-90.

116. Haussler KK, Bertram JEA, Gellman K, Hermanson JW (2001) Segmental in vivo vertebral kinematics at the walk, trot and canter: A preliminary study. Equine Vet J 33 (S33):160-4.

117. Barnes GG, Pinder DN (1974) In vivo tendon tension and bone strain measurement and correlation. J Biomech 7 (1):35-42.

118. Lanyon LE, Hampson WJ, Goodship AE, Shah JS (1975) Bone deformation recorded in vivo from strain gauges attached to the human tibial shaft. Acta Orthop 46 (2):256-68.

119. Aamodt A, Lund-Larsen J, Eine J, Andersen E, Benum P, Husby OS (1997) In vivo measurements show tensile axial strain in the proximal lateral aspect of the human femur. J Orthop Res 15 (6):927-31.

120. Hoshaw SJ, Fyhrie DP, Takano Y, Burr DB, Milgrom C (1997) A method suitable for in vivo measurement of bone strain in humans. J Biomech 30 (5):521-4.

121. Arndt A, Westblad P, Ekenman I, Halvorsen K, Lundberg A (1999) An in vitro comparison of bone deformation measured with surface and staple mounted strain gauges. J Biomech 32 (12):1359-63.

122. Milgrom C, Finestone A, Simkin A, Ekenman I, Mendelson S, Millgram M, Nyska M, Larsson E, Burr D (2000) In vivo strain measurements to evaluate the strengthening potential of exercises on the tibial bone. J Bone Joint Surg Br 82-B (4):591-4.

123. Szivek JA, Roberto RF, Slack JM, Majeed BS (2002) An implantable strain measurement system designed to detect spine fusion: Preliminary results from a biomechanical in vivo study. Spine 27 (5):487-97.

124. Milgrom C, Finestone A, Hamel A, Mandes V, Burr D, Sharkey N (2004) A comparison of bone strain measurements at anatomically relevant sites using surface gauges versus strain gauged bone staples. J Biomech 37 (6):947-52.

125. Burr DB, Milgrom C, Fyhrie D, Forwood M, Nyska M, Finestone A, Hoshaw S, Saiag E, Simkin A (1996) In vivo measurement of human tibial strains during vigorous activity. Bone 18 (5):405-10.

126. Rolf C, Westblad P, Ekenman I, Lundberg A, Murphy N, Lamontagne M, Halvorsen K (1997) An experimental in vivo method for analysis of local deformation on tibia, with simultaneous measures of ground reaction forces, lower extremity muscle activity and joint motion. Scand J Med Sci Spor 7 (3):144-51.

127. Fleming BC, Beynnon BD, Tohyama H, Johnson RJ, Nichols CE, Renström P, Pope MH (1994) Determination of a zero strain reference for the anteromedial band of the anterior cruciate ligament. J Orthop Res 12 (6):789-95.

128. Markolf KL, Willems MJ, Jackson SR, Finerman GM (1998) In situ calibration of miniature sensors implanted into the anterior cruciate ligament. Part I: Strain measurements. J Orthop Res 16 (4):455-63.

129. Erickson A, Beynnon B, Werthiemer C, Fleming B, Pope MH, Johnson R, Howe J, Nichols C An in-vivo study of ACL strain in the normal knee during Lachman and Drawer tests. In: 14th Annual Northeast Bioengineering Conference, Durham, NH , USA, March 10-11 1988. pp 19-21.

130. Beynnon BD, Howe JG, Pope MH, Johnson RJ, Fleming BC (1992) The measurement of anterior cruciate ligament strain in vivo. Int Orthop 16 (1):1-12.

131. Beynnon BD, Fleming BC (1998) Anterior cruciate ligament strain in-vivo: A review of previous work. J Biomech 31 (6):519-25.

132. Fleming BC, Renstrom PA, Beynnon BD, Engstrom B, Peura GD, Badger GJ, Johnson RJ (2001) The effect of weightbearing and external loading on anterior cruciate ligament strain. J Biomech 34 (2):163-70.

133. Fleming BC, Cresswell A, Nordlun M, Peura G, Saartok T, Thorstensson A, Renstrom PA (2002) Strain in the Achilles tendon during isometric contractions of the human triceps surae. T Orthop Res Soc 27:647.

134. Fleming BC, Beynnon BD (2004) In vivo measurement of ligament/tendon strains and forces: A review. Ann Biomed Eng 32 (3):318-28.

135. Markolf KL, Gorek JF, Kabo JM, Shapiro MS (1990) Direct measurement of resultant forces in the anterior cruciate ligament. An in vitro study performed with a new experimental technique. J Bone Joint Surg Am 72 (4):557-67.

136. Erdemir A, Piazza JP, Sharkey NA (2002) Influence of loading rate and cable migration on fiberoptic measurement of tendon force. J Biomech 35:857-62.

137. Ren L, Song G, Conditt M, Noble PC, Li H (2007) Fiber Bragg grating displacement sensor for movement measurement of tendons and ligaments. Appl Opt 46 (28):6867-71.

138. Roriz P, Abe I, Schiller M, Gabriel J, Simões JA (2011) Intervertebral disc bulging measurement using a fibre Bragg grating sensor. Exp Mech 51:1573-7.

139. Butler DL, Guan Y, Kay MD, Cummings JF, Feder SM, Levy MS (1992) Location-dependent variations in the material properties of the anterior cruciate ligament. J Biomech 25 (5):511-8.

140. Carvalho L, Silva JC, Nogueira RN, Pinto JL, Kalinowski HJ, Simões JA (2006) Application of Bragg grating sensors in dental biomechanics. J Strain Anal Eng 41 (6):411-6.

141. Carvalho P, Abe I, Schiller MW, Carvalho L, Simões JA, Lopes P, Pinto JL (2006) FEA and experimental FBG sensing system for the analysis of different dental implant concepts. J Biomech 39:S568.

142. Ottevaere H, Tabak M, Bartholomees F, de Wilde W, Veretennicoff I, Thienpont H Monitoring the stress build-up in dental cements: A novel optical characterization technique. In: Brouwer P (ed) P SPIE 4156, 309, Amsterdam, Netherlands, 4 July 2001. Clinical Lasers and Diagnostics. SPIE, p 309.

143. Ottevaere H, Tabak M, Fernandez Fernandez A, Berghmans F, Thienpont H Optical fiber sensors and their application in monitoring stress build-up in dental resin cements. In: Jaroszewicz LR, Culshaw B, Mignani AG (eds) P SPIE 5952, 59520P, Warsaw, Poland, September, 1 2005. Optical Fibers: Applications. SPIE, p 59520P.

144. Milczewski MS, Silva JC, Abe I, Carvalho L, Nogueira RN, Paterno AS, Kalinowski HJ, Pinto JL (2006) Determination of setting expansion of dental materials using fibre optical sensing. Meas Sci Technol 17 (5):1152-6.

145. Alberto N, Carvalho L, Lima H, Antunes P, Nogueira R, Pinto JL (2011) Characterization of different water/powder ratios of dental gypsum using fiber Bragg grating sensors. Dent Mater J 30 (5):700-6.

146. Frias C, Frazão O, Tavares S, Vieira A, Marques AT, Simões JA (2009) Mechanical characterization of bone cement using fiber Bragg grating sensors. Mater Design 30 (5):1841-4.

147. Talaia P, Ramos A, Abe I, Schiller M, Lopes P, Nogueira R, Pinto J, Claramunt R, Simões JA (2007) Plated and intact femur strains in fracture fixation using fiber Bragg gratings and strain gauges. Exp Mech 47 (3):355-63.

148. Lin JT, Lane JM (2004) Osteoporosis: A Review. Clin Orthop Relat Res 425:126-34.

149. Mishra V, Singh N, Rai DV, Tiwari U, Poddar GC, Jain SC, Mondal SK, Kapur P (2010) Fiber Bragg grating sensor for monitoring bone decalcification. Orthopaedics & Traumatology: Surgery & Research 96 (6):646-51.

150. Davis C, Mazzolini A, Mills J, Dargaville P (1999) A new sensor for monitoring chest wall motion during high-frequency oscillatory ventilation. Med Eng Phys 21 (9):619-23.

151. Babchenko A, Khanokh B, Shomer Y, Nitzan M (1999) Fiber optic sensor for the measurement of respiratory chest circumference changes. J Biomed Opt 4 (2):224-9.

152. Augousti AT, Maletras FX, Mason J (2005) Improved fibre optic respiratory monitoring using a figure-of-eight coil. Physiol Meas 26 (5):585-90.

153. Augousti AT, Maletras FX, Mason J (2006) Evaluation of cardiac monitoring using fiber optic plethysmography. Ann Biomed Eng 34 (3):416-25.

154. Allsop T, Earthrowl-Gould T, Webb DJ, Bennion I (2003) Embedded progressive three-layered fiber long-period gratings for respiratory monitoring. J Biomed Opt 8 (3):552-8.

155. Allsop T, Carroll K, Lloyd G, Webb DJ, Miller M, Bennion I (2007) Application of long-period-grating sensors to respiratory plethysmography. J Biomed Opt 12 (6):064003.

156. Grillet A, Kinet D, Witt J, Schukar M, Krebber K, Pirotte F, Depre A (2008) Optical fiber sensors embedded into medical textiles for healthcare monitoring. IEEE Sens J 8 (7):1215-22.

157. OFSETH (2006) Optical fiber sensors embedded into technical textile for healthcare. www.ofseth.org/ Accessed 15 Nov 2011

158. Park Y-L, Elayaperumal S, Daniel BL, Kaye E, Pauly KB, Black RJ, Cutkosky MR MRI-compatible haptics: Feasibility of using optical fiber Bragg grating strain-sensors to detect deflection of needles in an MRI environment. In: 16th Scientific Meeting & Exhibition, Toronto, Canada, May 2008. Proc Int Soc Magn Reson Med (ISMRM).

159. Gurkan D, Starodubov D, Xiaojing Y Monitoring of the heartbeat sounds using an optical fiber Bragg grating sensor. In: P IEEE Sensors, Irvine, CA, USA March, 13 2005. p 4.

160. van Brakel A Blood pressure manometer using a twin Bragg grating Fabry-Perot interferometer. In: P SPIE 5634, 595, Beijing, China, 8 Nov 2005. Advanced Sensor Systems and Applications II. SPIE, p 595.

161. Tiwari U, Mishra V, Bhalla A, Singh N, Jain SC, Garg H, Raviprakash S, Grewal N, Kapur P (2011) Fiber Bragg grating sensor for measurement of impact absorption capability of mouthguards. Den Traumatol 27 (4):263-8.

162. Fleming BC, Peura GD, Beynnon BD (2000) Factors influencing the output of an implantable force transducer. J Biomech 33 (7):889-93.

163. Holden JP, Grood ES, Korvick DL, Cummings JF, Butler DL, Bylski-Austrow DI (1994) In vivo forces in the anterior cruciate ligament: Direct measurements during walking and trotting in a quadruped. J Biomech 27 (5):517-26.

164. Komi PV (1990) Relevance of in vivo force measurements to human biomechanics. J Biomech 23 (Supplement 1):23-34.

165. Holden JP, Grood ES, Cummings JF (1995) Factors affecting sensitivity of a transducer for measuring anterior cruciate ligament force. J Biomech 28 (1):99-102.

166. Ahmed AM, Hyder A, Burke DL, Chan KH (1987) In-vitro ligament tension pattern in the flexed knee in passive loading. J Orthop Res 5 (2):217-30.

167. Herzog W, Hasler EM, Leonard TR (1996) In-situ calibration of the implantable force transducer. J Biomech 29 (12):1649-52.

168. Arndt AN, Komi PV, Brüggemann GP, Lukkariniemi J (1998) Individual muscle contributions to the in vivo Achilles tendon force. Clin Biomech 13 (7):532-41.

169. Fleming BC, Good L, Peura GD, Beynnon BD (1999) Calibration and application of an intra-articular force transducer for the measurement of patellar tendon graft forces: An in situ evaluation. J Biomech Eng-T ASME 121 (4):393-8.

170. Meyer DC, Jacob HAC, Nyffeler RW, Gerber C (2004) In vivo tendon force measurement of 2-week duration in sheep. J Biomech 37 (1):135-40.

171. Salmons S Meeting Report. In: Proc 8th Int Conf Med Biol Eng, Chicago, USA, 1969. pp 467-74.

172. Herrick WC, Kingsbury HB, Lou DYS (1978) A study of the normal range of strain, strain rate, and stiffness of tendon. J Biomed Mater Res 12 (6):877-94.

173. Lewis JL, Lew WD, Schmidt J (1982) A note on the application and evaluation of the buckle transducer for the knee ligament force measurement. J Biomech Eng-T ASME 104 (2):125-8.

174. An KN, Berglund L, Cooney WP, Chao EY, Kovacevic N (1990) Direct in vivo tendon force measurement system. J Biomech 23 (12):1269-71.

175. Gregor RJ, Komi PV, Browning RC, Järvinen M (1991) A comparison of the triceps surae and residual muscle moments at the ankle during cycling. J Biomech 24 (5):287-97.

176. Miller JM, Robins D (1992) Extraocular muscle forces in alert monkey. Vision Res 32 (6):1099-113.

177. Fukashiro S, Komi PV, Järvinen M, Miyashita M (1993) Comparison between the directly measured achilles tendon force and the tendon force calculated from the ankle joint moment during vertical jumps. Clin Biomech 8 (1):25-30.

178. Collins CC, O'Meara D, Scott AB (1975) Muscle tension during unrestrained human eye movements. J Physiol 245 (2):351-69.

179. Henning CE, Lynch MA, Glick KR (1985) An in vivo strain gage study of elongation of the anterior cruciate ligament. Am J Sport Med 13 (1):22-6.

180. Walmsley B, Hodgson JA, Burke RE (1978) Forces produced by medial gastrocnemius and soleus muscles during locomotion in freely moving cats. J Neurophysiol 41:1203-16.

181. Komi PV, Salonen M, Järvinen M (1984) In vivo measurements of Achilles tendon forces in man. Med Sci Sport Exer 16 (2):165.

182. Komi PV, Salonen M, Järvinen M, Kokko O (1987) In vivo registration of Achilles tendon forces in man. I. Methodological development. Int J Sports Med 8 (Suppl 1):3-8.

183. Barry D, Ahmed AM (1986) Design and performance of a modified buckle transducer for the measurement of ligament tension. J Biomech Eng-T ASME 108 (2):149-52.

184. Schuind F, Garcia-Elias M, Cooney Iii WP, An K-N (1992) Flexor tendon forces: In vivo measurements. J Hand Surg-Am 17 (2):291-8.

185. Komi PV, Belli A, Huttunen V, Bonnefoy R, Geyssant A, Lacour J (1996) Optic fibre as a transducer of tendomuscular forces. Eur J Appl Physiol O 72 (3):278-80.

186. Kear M, Smith RN (1975) A method for recording tendon strain in sheep during locomotion. Acta Orthop Scand 46 (6):896-905.

187. Xu WS, Butler DL, Stouffer DC, Grood ES, Glos DL (1992) Theoretical analysis of an implantable force transducer for tendon and ligament structures. J Biomech Eng-T ASME 114 (2):170-7.

188. Glos DL, Butler DL, Grood ES, Levy MS (1993) In vitro evaluation of an implantable force transducer (IFT) in a patellar tendon model. J Biomech Eng-T ASME 115 (4A):335-43.

189. Korvick DL, Cummings JF, Grood ES, Holden JP, Feder SM, Butler DL (1996) The use of an implantable force transducer to measure patellar tendon forces in goats. J Biomech 29 (4):557-61.

190. Markolf KL, Willems MJ, Jackson SR, Finerman GM (1998) In situ calibration of miniature sensors implanted into the anterior cruciate ligament. Part II: Force probe measurements. J Orthop Res 16 (4):464-71.

191. Hall GW, Crandall JR, Carmines DV, Hale JE (1999) Rate-independent characteristics of an arthroscopically implantable force probe in the human achilles tendon. J Biomech 32 (2):203-7.

192. Bull AJ, Reilly P, Wallace AL, Amis AA, Emery RH (2005) A novel technique to measure active tendon forces: application to the subscapularis tendon. Knee Surg Sport Tr A 13 (2):145-50.

193. Finni T, Komi PV, Lukkariniemi J (1998) Achilles tendon loading during walking: Application of a novel optic fiber technique. Eur J Appl Physiol O 77 (3):289-91.

194. Finni T, Komi PV, Lepola V (2000) In vivo human triceps surae and quadriceps femoris muscle function in a squat jump and counter movement jump. Eur J Appl Physiol 83 (4):416-26.

195. Finni T, Ikegaw S, Lepola V, Komi PV (2001) In vivo behavior of vastus lateralis muscle during dynamic performances. Eur J Sport Sci 1 (1):1-13.

196. Ishikawa M, Komi PV, Grey MJ, Lepola V, Bruggemann G-P (2005) Muscle-tendon interaction and elastic energy usage in human walking. J Appl Physiol 99 (2):603-8.

197. Müller JH, Scheffer C, Elvin A (2008) In-vivo detection of patellar tendon creep using a fibre-optic sensor. Int J Med Eng Inform 1:155-73.

198. Erdemir A, Hamel AJ, Piazza SJ, Sharkey NA (2003) Fiberoptic measurement of tendon forces is influenced by skin movement artifact. J Biomech 36 (3):449-55.

199. Vilimek M (2008) Using a fiber Bragg grating sensor for tendon force measurements. J Biomech 41 (Supplement 1):S511-S.

200. Goh PK, Fuss FK, Yanai T, Ritchie AC, Lie DT, Tjin SC (2007) Measurement of intrameniscal forces and stresses by two different miniature transducers. J Mech Med Biol 7 (1):65-74.

201. Behrmann G, Hidler J, Mirotznik M (2012) Fiber optic micro sensor for the measurement of tendon forces. BioMed Eng OnLine 11 (1):1-16.

202. Kopola HK, Mantyla O, Makiniemi M, Mahonen K, Virtanen K Instrument for measuring human biting force. In: P SPIE 2331, 149, Lille, France, 6 Sept 1995. Medical Sensors II and Fiber Optic Sensors. SPIE, pp 149-55.

203. Tjin SC, Tan Y, Yow M, Lam Y-Z, Hao J (2001) Recording compliance of dental splint use in obstructive sleep apnoea patients by force and temperature modelling. Med Biol Eng Comput 39 (2):182-4.

204. Milczeswki MS, Silva JC, Abe I, Simões JA, Paterno AS, Kalinowski HJ (2006) Measuring orthodontic forces with HiBi FBG sensors. Paper presented at the Optical Fiber Sensors (OFS), Cancún, Mexico, October, 26

205. Milczewski MS, Kalinowski H, Martelli C, Canning J, Stevenson M, Simões JA, Talaia P Orthodontic forces using polymer PCF. In: Cutolo A, Culshaw B, López-Higuera JM (eds) P SPIE 6619, 66191M, Napoli, Italy, 24-27 June 2007. Third European Workshop on Optical Fibre Sensors Joint International Conference on Optical Internet and 32nd Australian Conference on Optical Fibre Technology (COIN-ACOFT). pp 1-3.

206. Milczewski MS, Stevenson M, Canning J, Martelli C, Kalinowski H Exploiting polymer photonic crystal fibre uniqueness: A simple high resolution pressure sensor. In: 32nd Australian Conference on Optical Fibre Technology (COIN-ACOFT), Melbourne, VIC, 24-27 June 2007 2007. Joint International Conference on Optical Internet. pp 1-3.

207. Paul J, Zhao L, Ngoi BA (2005) Fiber-optic sensor for handgrip-strength monitoring: Conception and design. Appl Opt 44 (18):3696-704.

208. Park Y-L, Ryu SC, Black RJ, Moslehi B, Cutkosky MR Fingertip force control with embedded fiber Bragg grating sensors. In: IEEE Int Conf Robotics and Automation (ICRA) 19-23 May 2008. pp 3431-6.

209. Polygerinos P, Schaeffter T, Seneviratne LD, Althoefer K A fibre-optic catheter-tip force sensor with MRI compatibility: A feasibility study. In: P IEEE Eng Medicine and Biology Conf (EMBC 2009), Minneapolis, MN, 2009.

210. Polygerinos P, Puangmali P, Schaeffter T, Razavi R, Seneviratne LD, Althoefer K Novel miniature MRI-compatible fiber-optic force sensor for cardiac catheterization procedures. In: IEEE Int Conf Robotics Automation (ICRA), Anchorage, AK, USA, May 3-7 2010. pp 2598-603.

211. Yokoyama K, Nakagawa H, Shah DC, Lambert H, Leo G, Aeby N, Ikeda A, Pitha JV, Sharma T, Lazzara R, Jackman WM (2008) Novel contact force sensor incorporated in irrigated radiofrequency ablation catheter predicts lesion size and incidence of steam pop and thrombus. Circ Arrhythm Electrophysiol 1 (5):354–62.

212. Song H, Kim K, Suh J, Lee J Development of optical FBG force measurement system for the medical application. In: Quan C, Qian K, Asundi AK, Chau FS (eds) P SPIE 7522, 752230, Singapore, Singapore, November, 18 2009. Fourth Int Conf Exp Mech. pp 752230-8.

213. Iordachita I, Sun Z, Balicki M, Kang J, Phee S, Handa J, Gehlbach P, Taylor R (2009) A sub-millimetric, 0.25 mN resolution fully integrated fiber-optic force-sensing tool for retinal microsurgery. Int J Comput Assisted Radiol Surg 4 (4):383-90.

214. Endosense (2011). www.endosense.com/professionals/clinical-trials.html. Accessed 12 Nov 2011

215. Thiagalingam A, D'Avila A, Foley L, Guerrero JL, Lambert H, Leo G, Ruskin JN, Reddy VY (2010) Importance of catheter contact force during irrigated radiofrequency ablation: Evaluation in a porcine ex vivo model using a force-sensing catheter. J Cardiovasc Electr 21 (7):806-11.

216. Shah DC, Lambert H, Nakagawa H, Langenkamp A, Aeby N, Leo G (2010) Area under the real-time contact force curve (Force-time integral) predicts radiofrequency lesion size in an in vitro contractile model. J Cardiovascular Electrophysiology 21 (9):1038-43.

217. Song H, Kim K, Lee J (2011) Development of optical fiber Bragg grating force-reflection sensor system of medical application for safe minimally invasive robotic surgery. Rev Sci Instrum 82 (7):074301-9.

218. Tada M, Sasaki S, Ogasawara T Development of an optical 2-axis force sensor usable in MRI environments. In: P IEEE Sensors, Orlando, Florida, November, 7 2002. pp 984-9.

219. Takahashi N, Tada M, Ueda J, Matsumoto Y, Ogasawara T An optical 6-axis force sensor for brain function analysis using fMRI. In: P IEEE Int Conf Sensors, Toronto, Canada, October, 22-24 2003. pp 253-8.

220. Gassert R, Moser R, Burdet E, Bleuler H (2006) MRI/fMRI-compatible robotic system with force feedback for interaction with human motion. IEEE/ASME T Mechatronics 11 (2):216-24.

221. Howe RD, Matsuoka Y (1999) Robotics for surgery. Annu Rev Biomed Eng 1 (1):211-40.

222. Adson AW, Lillie WL (1927) The relationship of intracerebral pressure, choked disc, and intraocular tension. Trans Am Acad Ophthalmol Otolaryngol 30:138-54.

223. Guillaume J, Janny P (1951) Manométrie intra-crânienne continue: Intérêt pathophysiologique et clinique de la méthode. Presse Med 59:953–5.

224. Gauer OH, Gienapp E (1950) A miniature pressure-recording device. Science 112 (2910):404-5.

225. Burch GE, Sodeman WA (1937) The estimation of the subcutaneous tissue pressure by a direct method. J Clin Invest 16 (6):845-50.

226. Lundberg N (1960) Continuous recording and control of ventricular fluid pressure in neurosurgical practice. Acta Psychiatr Scand Suppl 36 (149):1-193.

227. Nachemson A, Morris JM (1964) In vivo measurements of intradiscal pressure: Discometry, a method for the determination of pressure in the lower lumbar discs. J Bone Joint Surg Am 46 (5):1077-92.

228. Nachemson A (1965) In vivo discometry in lumbar discs with irregular nucleograms: Some differences in stress distribution between normal and moderately degenerated discs. Acta Orthop 36 (4):418 - 34.

229. Scholander PF, Hargens AR, Miiller SL (1968) Negative pressure in the interstitial fluid of animals. Science 161 (3839):321-8.

230. Weinhoffer SL, Guyer RD, Herbert M, Griffith SL (1995) Intradiscal pressure measurements above an instrumented fusion: A cadaveric study. Spine 20 (5):526–31.

231. Hansen T-E (1983) A fiberoptic micro-tip pressure transducer for medical applications. Sensor Actuator 4:545-54.

232. Crenshaw AG, Styf JR, Mubarak SJ, Hargens AR (1990) A new transducer-tipped fiber optic catheter for measuring intramuscular pressures. J Orthop Res 8 (3):464-8.

233. Mubarak SJ, Hargens AR, Owen CA, Garetto LP, Akeson WH (1976) The wick catheter technique for measurement of intramuscular pressure. A new research and clinical tool. J Bone Joint Surg Am 58 (7):1016-20.

234. Rorabeck CH, Castle GS, Hardie R, Logan J (1981) Compartmental pressure measurements: An experimental investigation using the slit catheter. J Traum 21 (6):446-9.

235. Awbrey BJ, Sienkiewicz PS, Mankin HJ (1988) Chronic exercise-induced compartment pressure elevation measured with a miniaturized fluid pressure monitor. Am J Sport Med 16 (6):610-5.

236. Kaufman KR, Waveringm T, Morrow D, Davis J, Lieber RL (2003) Performance characteristics of a pressure microsensor. J Biomech 36 (2):283-7.

237. Kaufman KR, Sutherland DH (1995) Dynamic intramuscular pressure measurement during gait. Oper Techn Sports Med 3 (4):250-5.

238. Crenshaw AG, Styf JR, Hargens AR (1992) Intramuscular pressures during exercise: An evaluation of a fiber optic transducer-tipped catheter system. Eur J Appl Physiol O 65 (2):178-82.

239. Czosnyka M, Czosnyka Z, Pickard JD (1997) Laboratory testing of the Spiegelberg brain pressure monitor: A technical report. J Neurol Neurosur Ps 63 (6):732-5.

240. Morikawa S (1972) Fiberoptic catheter-tip pressure transducer. Jpn J Med Electron Biol Eng 10 (1):36-9.

241. Kobayashi K, Okuyama H, Kato T, Yasuda T (1977) Fiberoptic catheter-tip micromanometer. Jpn J Med Electron Biol Eng 15 (7):465-72.

242. INTEGRA (2010) Directions for use: OLM Intracranial pressure monitoring kit Model 110-4B. Integra Neurosciences Camino®. http://integralife.com/products/PDFs/Camino/110-4B.pdf. Accessed 10 Dec

243. Hollingsworth-Fridlund P, Vos H, Daily EK (1988) Use of fiber-optic pressure transducer for intracranial pressure measurements: A preliminary report. Heart Lung 17 (2):111-20.

244. Crutchfield JS, Narayan RK, Robertson CS, Michael LH (1990) Evaluation of a fiberoptic intracranial pressure monitor. J Neurosurg 72 (3):482-7.

245. Yablon J, Lantner H, McCormack T, Nair S, Barker E, Black P (1993) Clinical experience with a fiberoptic intracranial pressure monitor. J Clin Monitor Comp 9 (3):171-5.

246. Bruder N, N'Zoghe P, Graziani N, Pelissier D, Grisoli F, François G (1995) A comparison of extradural and intraparenchymatous intracranial pressures in head injured patients. Intensive Care Medicine 21 (10):850-2.

247. Czosnyka M, Czosnyka Z, Pickard JD (1996) Laboratory testing of three intracranial pressure microtransducers: Technical report. Neurosurgery 38 (1):219-24.

248. Münch E, Weigel R, Schmiedek P, Schürer L (1998) The CAMINO intracranial pressure device in clinical practice: Reliability, handling characteristics and complications. Acta Neurochir 140 (11):1113-20.

249. Martinez-Manas R, Santamarta D, Campos JM, Ferrer E (2000) Camino® intracranial pressure monitor: Prospective study of accuracy and complications. J Neurol Neurosur Ps 69 (1):82-6.

250. Piper I, Barnes A, Smith D, Dunn L (2001) The Camino intracranial pressure sensor: Is it optimal technology? An internal audit with a review of current intracranial pressure monitoring technologies. Neurosurgery 49 (5):1158-65.

251. Gelabert-Gonzalez M, Ginesta-Galan V, Sernamito-Garcia R, Allut AG, Bandin-Dieguez J, Rumbo RM (2006) The Camino intracranial pressure device in clinical practice. Assessment in a 1000 cases. Acta Neurochir (Wien) 148 (4):435-41.

252. Smith M (2008) Monitoring intracranial pressure in traumatic brain injury. Anesth Analg 106 (1):240-8.

253. Eide PK (2008) Comparison of simultaneous continuous intracranial pressure (ICP) signals from ICP sensors placed within the brain parenchyma and the epidural space. Medical Engineering & Physics 30 (1):34-40.

254. Bekar A, Doğan Ş, Abaş F, Caner B, Korfalı G, Kocaeli H, Yılmazlar S, Korfalı E (2009) Risk factors and complications of intracranial pressure monitoring with a fiberoptic device. Journal of Clinical Neuroscience 16 (2):236-40.

255. Raboel PH, Bartek J, Andresen M, Bellander BM, Romner B (2012) Intracranial pressure monitoring: Invasive versus non-Invasive methods: A review. Critical Care Research and Practice 2012:1-14.

256. Cox E, Jones B Fiber optic color sensors based on Fabry-Pérot interferometry. In: 1st Int Conf Opt Fiber Sensors, London, UK, April 1983. Inspec/IEE, pp 122-6.

257. Saaski EW, Hartl JC, Mitchell GL A fiber-optic sensing system based on spectral modulation. In: P ISA/86 International Conference and Exhibition, Houston, TX, USA, October 13-16 1986. Advances in Instrumentation. The International Society of Automation, p 2803.

258. Totsu K, Haga Y, Esashi M (2005) Ultra-miniature fiber-optic pressure sensor using white light interferometry. J Micromech Microeng 15 (1):71-5.

259. Dennison CR, Wild PM, Byrnes PWG, Saari A, Itshayek E, Wilson DC, Zhu QA, Dvorak MFS, Cripton PA, Wilson DR (2008) Ex vivo measurement of lumbar intervertebral disc pressure using fibre-Bragg gratings. J Biomech 41 (1):221-5.

260. Taylor JB, Lown B, Polanyi M (1972) In vivo monitoring with a fiber optic catheter. The Journal of the American Medical Association (JAMA) 221 (7):667-73.

261. Matsumoto H, Saegusa M, Saito K, Mizoi K (1978) The development of a fibre optic catheter tip pressure transducer. J Med Eng Technol 2 (5):239-42.

262. Ozerdem U (2009) Measuring interstitial fluid pressure with fiberoptic pressure transducers. Microvasc Res 77 (2):226-9.

263. Tenerz L, Smith L, Hok B A fiberoptic silicon pressure microsensor for measurements in coronary arteries. In: IEEE Int Conf Solid-State Sensor Actuator, San Francisco, CA, USA, June 24-27 1991. IEEE, pp 1021-3.

264. Tohyama O, Kohashi M, Yamamoto K, Itoh H (1996) A fiber-optic silicon pressure sensor for ultra-thin catheters. Sensor Actuat A-Phys 54 (1-3):622-5.

265. Strandman C, Smith L, Tenerz L, Hök B (1997) A production process of silicon sensor elements for a fibre-optic pressure sensor. Sensor Actuat A-Phys 63 (1):69-74.

266. Tohyama O, Kohashi M, Sugihara M, Itoh H (1998) A fiber-optic pressure microsensor for biomedical applications. Sensor Actuat A-Phys 66 (1-3):150-4.

267. Kalvesten E, Smith L, Tenerz L, Stemme G The first surface micromachined pressure sensor for cardiovascular pressure measurements. In: Micro Electro Mechanical Systems, 1998. MEMS 98. Proceedings., The Eleventh Annual International Workshop on, Heidelberg, Germany, January 25-29 1998. IEEE, pp 574-9.

268. Pedowitz RA, Gershuni DH, Crenshaw AG, Petras SL, Danzig LA, Hargens AR (1989) Intraarticular pressure during continuous passive motion of the human knee. J Orthop Res 7 (4):530-7.

269. Inokuchi W, Olsen BS, Søjbjerg JO, Sneppen O (1997) The relation between the position of the glenohumeral joint and the intraarticular pressure: An experimental study. J Shoulder Elb Surg 6 (2):144-9.

270. Iba K, Wada T, Aoki M, Tsuji H, Oda T, Yamashita T (2006) Intraoperative measurement of pressure adjacent to the ulnar nerve in patients with cubital tunnel syndrome. J Hand Surg-Am 31 (4):553-8.

271. Iba K, Wada T, Aoki M, Oda T, Ozasa Y, Yamashita T (2008) The relationship between the pressure adjacent to the ulnar nerve and the disease causing cubital tunnel syndrome. J Shoulder Elb Surg 17 (4):585-8.

272. Ostrup RC, Luerssen TG, Marshall LF, Zornow MH (1987) Continuous monitoring of intracranial pressure with a miniaturized fiberoptic device. J Neurosurg 67 (2):206-9.

273. Dario P, Femi D, Vivaldi F (1987) Fiber-optic catheter-tip sensor based on the photoelastic effect. Sensor Actuator 12 (1):35-47.

274. Wolthuis RA, Mitchell GL, Hartl JC, Saaski EW (1992) Development of a dual function sensor system for measuring pressure and temperature at the tip of a single optical fiber. IEEE T Bio-Med Eng 40 (3):298-302.

275. Reesink KD, van der Nagel T, Bovelander J, Jansen JRC, van der Veen FH, Schreuder JJ (2002) Feasibility study of a fiber-optic system for invasive blood pressure measurements. Catheterization and Cardiovascular Interventions 57 (2):272-6.

276. Zhou M-D, Yang C, Liu Z, Cysyk J, Zheng S-Y (2012) An implantable Fabry-Pérot pressure sensor fabricated on left ventricular assist device for heart failure. Biomed Microdevices 14 (1):235-45.

277. Zhou M-D, Yang C, Liu Z, Cysyk J, Zheng S-Y (2011) An implantable Fabry-Pérot pressure sensor fabricated on left ventricular assist device for heart failure. Biomed Microdevices:1-11.

278. Pinet E, Pham A, Rioux S Miniature fiber optic pressure sensor for medical applications: An opportunity for intra-aortic balloon pumping (IABP) therapy. In: Voet M, Willsch R, Ecke W, Jones J, Culshaw B (eds) P SPIE 5855, 234, Bruges, Belgium, 23 May 2005. 17th Int Conf Optical Fibre Sensors. SPIE, pp 234-7.

279. Kolipaka A, McGee KP, Araoz PA, Manduca A, Ehman RL MR elastography as a method for the assessment of myocardial stiffness throughout the cardiac cycle. In: Proc Int Soc Mag Reson Med, Honolulu, HI, USA, April 18-24 2009. International Society for Magnetic Resonance in Medicine (ISMRM). MIRA, Digital Publishing, p 1790.

280. Chavko M, Koller WA, Prusaczyk WK, McCarron RM (2007) Measurement of blast wave by a miniature fiber optic pressure transducer in the rat brain. J Neurosci Meth 159 (2):277-81.

281. Leonardi AC, Bir CA, Ritzel DV, VandeVord PJ (2010) Intracranial pressure increases during exposure to a shock wave. J Neurotraum 28 (1):85-94.

282. Matsubara A, Nakazawa T, Husain D, Iliaki E, Connolly E, Michaud NA, Gragoudas ES, Miller JW (2006) Investigating the effect of ciliary body photodynamic therapy in a glaucoma mouse model. Invest Ophth Vis Sci 47 (6):2498-507.

283. Zhang P, Su M, Liu Y, Hsu A, Yokota H (2007) Knee loading dynamically alters intramedullary pressure in mouse femora. Bone 40 (2):538-43.

284. Takeuchi S, Tohara H, Kudo H, Otsuka K, Saito H, Uematsu H, Mitsubayashi K (2007) An optic pharyngeal manometric sensor for deglutition analysis. Biomed Microdevices 9 (6):893-9.

285. Den Uil CA, Lagrand WK, van der Ent M, Jewbali LSD, Brugts JJ, Spronk PE, Simoons ML (2009) The effects of intra-aortic balloon pump support on macrocirculation and tissue microcirculation in patients with cardiogenic shock. Cardiology 114 (1):42-6.

286. MAQUET (2011) Intra-aortic balloon catheters. http://ca.maquet.com/products/iab-catheters/. Accessed May 10 2013

287. Cottler P, Karpen W, Morrow D, Kaufman KR (2009) Performance characteristics of a new generation pressure microsensor for physiologic applications. Ann Biomed Eng 37 (8):1638-45.

288. Totsu K, Haga Y, Esashi M Vacuum sealed ultra miniatue fiber-optic pressure sensor using white light interferometry. In: 12th Int Conf Solid State Sensors, Actuators and Microsystems, Boston, MA, USA, June 8-12 2003. Transducers. IEEE, pp 931-4.

289. Donlagic D, Cibula E (2005) All-fiber high-sensitivity pressure sensor with SiO2 diaphragm. Opt Lett 30 (16):2071-3.

290. Cibula E, Donlagic D (2005) Miniature fiber-optic pressure sensor with a polymer diaphragm. Appl Opt 44 (14):2736-44.

291. Cibula E, Pevec S, Lenardič B, Pinet É, Donlagic D (2009) Miniature all-glass robust pressure sensor. Opt Express 17 (7):5098-106.

292. Pinet E (2008) Medical applications: Saving lives. Nat Photon 2 (3):150-2.

293. FISO (2011) FOP-F125 product datasheet. FISO Technologies. http://www.fiso.com/admin/useruploads/files/fop-f125.pdf. Accessed 12 Nov 2011

294. Sejersted OM, Hargens AR, Kardel KR, Blom P, Jensen O, Hermansen L (1984) Intramuscular fluid pressure during isometric contraction of human skeletal muscle. J Appl Physiol 56 (2):287-95.

295. Körner L, Parker P, Almström C, Andersson GBJ, Herberts P, Kadefors R, Palmerud G, Zetterberg C (1984) Relation of intramuscular pressure to the force output and myoelectric signal of skeletal muscle. J Orthop Res 2 (3):289-96.

296. Nakhostine M, Styf JR, van Leuven S, Hargens AR, Gershuni DH (1993) Intramuscular pressure varies with depth: The tibialis anterior muscle studied in 12 volunteers. Acta Orthop 64 (3):377-81.

297. Peters P, Baker SR, Leopold PW, Taub NA, Burnand KG (1994) Compartment syndrome following prolonged pelvic surgery. Brit J Surg 81 (8):1128-31.

298. Toft I, Lindal S, Bønaa KH, Jenssen T (2003) Quantitative measurement of muscle fiber composition in a normal population. Muscle Nerve 28 (1):101-8.

299. Murphy KA, Gunther MF, Vengsarkar AM, Claus RO (1991) Quadrature phase-shifted, extrinsic Fabry-Pérot optical fiber sensors. Opt Lett 16 (4):273-5.

300. Willy C, Gerngross H, Sterk J (1999) Measurement of intracompartmental pressure with use of a new electronic transducer-tipped catheter system. J Bone Joint Surg Am 81 (2):158-68.

301. Yang C, Zhao C, Wold L, Kaufman KR (2003) Biocompatibility of a physiological pressure sensor. Biosens Bioelectron 19 (1):51-8.

302. Chen S, Pislaru C, Kinnick RR, Morrow DA, Kaufman KR, Greenleaf JF (2005) Evaluating the dynamic performance of a fibre optic pressure microsensor. Physiol Meas 26:N13-N9.

303. Davis J, Kaufman KR, Lieber RL (2003) Correlation between active and passive isometric force and intramuscular pressure in the isolated rabbit tibialis anterior muscle. J Biomech 36 (4):505-12.

304. Winters TM, Sepulveda GS, Cottler PS, Kaufman KR, Lieber RL, Ward SR (2009) Correlation between isometric force and intramuscular pressure in rabbit tibialis anterior muscle with an intact anterior compartment. Muscle Nerve 40 (1):79-85.

305. An KN (2003) In vivo force and strain of tendon, ligament, and capsule. In: Guilak F, Butler DL, Goldstein SA, Mooney DJ (eds) Functional Tissue Engineering, vol Part II. vol Biomedical and Life Sciences. Springer, NY, USA, pp 96-105.

306. Levick JR (1983) Joint pressure-volume studies: Their importance, design and interpretation. J Rheumatol 10 (3):353-7.

307. Wilke HJ, Neef P, Caimi M, Hoogland T, Claes LE (1999) New in vivo measurements of pressures in the intervertebral disc in daily life. Spine 24 (8):755-62.

308. Cunningham BW, Kotani Y, McNulty PS, Cappuccino A, McAfee PC (1997) The effect of spinal destabilization and instrumentation on lumbar intradiscal pressure: An in vitro biomechanical analysis. Spine 22 (22):2655-63.

309. Wang J-L, Kuo Y-W, Cahng C-C, Yang B-D (2007) Interference in intradiscal pressure measurement using a needle-type pressure transducer. J Chin Inst Eng 30 (1):149-53.

310. SAMBA (2011) Samba Preclin 420 and 360 transducer (discontinued). www.sambasensors.com/products/preclinical-products/samba-preclin-420-360-transducer/. Accessed 11 Nov 2011

311. Höejer S, Krantz M, Ekstroem L, Kaigle A, Holm S A microstructure-based fiber optic pressure sensor for measurements in lumbar intervertebral discs. In: Baldini F, Croitoru NI, Frenz M et al. (eds) P SPIE 3570, 115, Stockholm, Sweden, 8 Sept 1999. Biomed Sensors, Fibers, and Optical Delivery Systems. pp 115-22.

312. Hebelka H, Gaulitz A, Nilsson A, Holm S, Hansson T (2010) The transfer of disc pressure to adjacent discs in discography: A specificity problem? Spine 35 (20):E1025-E9.

313. Guehring T, Unglaub F, Lorenz H, Omlor G, Wilke H-J, Kroeber M (2006) Intradiscal pressure measurements in normal discs, compressed discs and compressed discs treated with axial posterior disc distraction: An experimental study on the rabbit lumbar spine model. Eur Spine J 15 (5):597-604.

314. Ferrara L, Triano JJ, Sohn M-J, Song E, Lee DD (2005) A biomechanical assessment of disc pressures in the lumbosacral spine in response to external unloading forces. Spine J 5 (5):548-53.

315. Ekström L, Holm S, Holm AK, Hansson T (2004) In vivo porcine intradiscal pressure as a function of external loading. J Spinal Disord Tech 17 (4):312-6.

316. Hök B, Tenerz L, Berg S, Blückert A (1994) Pressure microsensor system using a closed-loop configuration. Sensor Actuat A-Phys 41 (1-3):78-81.

317. Hsieh AH, Ryan DA, Chen Z, Liu Y, Nesson SC, Yu M (2006) Intradiscal pressures in rat tail discs measured using a miniaturized fiber-optic sensor. J Biomech 39 (Supplement 1):S28-2490.

318. Nesson S, Yu M, Hsieh A, H. A miniature fiber optic pressure sensor for intradiscal pressure measurements of rodents. In: Vijay KV (ed) P SPIE 6528, 65280P, San Diego, CA, USA, 21 March 2007. Nanosensors, Microsensors, and Biosensors and Systems. SPIE, p 65280P.

319. Hwang D, Gabai A, Yu M, Yew A, Hsieh A (2011) Role of load history in intervertebral disc mechanics and intradiscal pressure generation. Biomech Model Mechan 11 (1-2):95-106.

320. Doyle DJ, Mark PWS (1991) Analysis of intracranial pressure. J Clin Monitor Comp 8 (1):81-90.

321. Piek J, Bock WJ (1990) Continuous monitoring of cerebral tissue pressure in neurosurgical practice: Experiences with 100 patients. Intens Care Med 16 (3):184-8.

322. Vries JK, Becker DP, Young HF (1973) A subarachnoid screw for monitoring intracranial pressure. J Neurosurg 39 (3):416-9.

323. Kosteljanetz M, Børgesen SE, Stjernholm P, Christensen L, Osgaard O, Gjerris F, Rosenørn J (1986) Clinical evaluation of a simple epidural pressure sensor. Acta Neurochir 83 (3):108-11.

324. Poca MA, Martínez-Ricarte F, Sahuquillo J, Lastra R, Torné R, Armengol MS (2008) Intracranial pressure monitoring with the Neurodur-P epidural sensor: A prospective study in patients with adult hydrocephalus or idiopathic intracranial hypertension. J Neurosurg 108 (5):934-42.

325. Wald A, Post K, Ransohoff J, Hass W, Epstein F (1977) A new technique for monitoring epidural intracranial pressure. Med Instrum 11 (6):352-4.

326. Wald A (1978) Monitoring intracranial pressure. J Clin Eng 3 (4):383-8.

327. Narayan RK, Bray RS, Robertson CS, Gokaslan L, Grossman RG Experience with a new fiberoptic device for intracranial pressure monitoring. In: 55th Annual Meeting American Association Neurological Surgeons, Dallas, Texas, May 3-7 1987. American Association Neurological Surgeons.

328. Gambardella G, D'Avella D, Tomasello F (1992) Monitoring of brain tissue pressure with a fiberoptic device. Neurosurgery 31 (5):918-22.

329. Smit TH, Odgaard A, Schneider E (1997) Structure and function of vertebral trabecular bone. Spine 22 (24):2823-33.

330. AAMI (1988 (R) 2010) Intracranial pressure monitoring devices. vol NS28. ANSI/AAMI.

331. Bratton SL, Chestnut RM, Jamshid G, Hammond FF, Harris OA, Hartl R, Manley GT, Nemecek A, Newell DW, Rosenthal G, Schouten J, Shutter L, Timmons SD, Ullman JS, Videtta W, Wilberger JE, Wright DW (2007) VII. Intracranial pressure monitoring technology. J Neurotraum 24 (Suppl 1):S45-S54.

332. Holzschuh M, Woertgen C, Metz C, Brawanski A (1998) Clinical evaluation of the InnerSpace fibreoptic intracranial pressure monitoring device. Brain Injury 12 (3):191-8.

333. OPSENS (2011). http://www.opsens.com/en/industries/products/pressure/opp-m/. Accessed 16 Nov 2011

334. Sondergaard S, Karason S, Hanson A, Nilsson K, Hojer S, Lundin S, Stenqvist O (2002) Direct measurement of intratracheal pressure in pediatric respiratory monitoring. Pediatr Res 51 (3):339-45.

335. Sondergaard S, Karason S, Lundin S, Stenqvist O (2001) Fibre-optic measurement of tracheal pressure in paediatric endotracheal tubes. Eur J Anaesth 18:24-5.

336. Arkwright JW, Blenman NG, Underhill ID, Maunder SA, Spencer NJ, Costa M, Brookes SJ, Szczesniak MM, Dinning PG (2011) A fibre optic catheter for simultaneous measurement of longitudinal and circumferential muscular activity in the gastrointestinal tract. J Biophotonics 4 (4):244-51.

337. De Blasi RA, Conti G, Antonelli M, Bufi M, Gasparetto A (1992) A fibre optics system for the evaluation of airway pressure in mechanically ventilated patients. Intens Care Med 18 (7):405-9.

338. SAMBA (2011) Samba Resp 420 catheter (discontinued). www.sambasensors.com/products/clinical-products/samba-resp-420-transducer/. Accessed 11 Nov 2011

339. Voigt S, Rothhardt M, Becker M, Lupke T, Thieroff C, Teubner A, Mehner J Homogeneous catheter for esophagus high-resolution manometry using fiber Bragg gratings. In: Gannot I (ed) P SPIE 7559, 75590B, San Francisco, CA, USA, 23 Jan 2010. Optical Fibers and Sensors for Medical Diagnostics and Treatment Applications X. pp 75590B-10.

340. Wang W-C, Ledoux WR, Huang C-Y, Huang C-S, Klute GK, Reinhall PG (2008) Development of a microfabricated optical bend loss sensor for distributive pressure measurement. IEEE T Bio-Med Eng 55 (2):614-25.

341. IASIS (2009) Intelligent adaptable surface with optical fiber sensing for pressure-tension relief. http://www.ist-world.org/ProjectDetails.aspx?ProjectId=ccaa7a17cf7b4d64a1a54702bafa64a4&SourceDatabaseId=018774364ea94468b3f4dec24aa1ee53. Accessed 10 Nov 2011

342. Papaioannou G, Mitrogiannis C, Nianios G, Fiedler G, Baradaki V Validation of a novel adaptive smart surface bed with integrated decubitus prophylaxis sensors. In: Proc 56th Annual Meeting Orthopaedic Research Society, New Orleans, LA, USA, March 6-9 2010. Orthopaedic Reseach Society.

343. Papaioannou G, Mitrogiannis C, Nianios G, Fiedler G Towards a novel "SMARTsocket" design for lower extremity amputees. In: Proc HFM Symposium Advanced Technologies New Procedures Medical Field Operations, Essen, Germany, April 19-21 2010. NATO Science and Technology Organization, pp P-17.

344. Papaioannou G, Mitrogiannis C, Fiedler G, Nianios G Assessment of vacuum-assisted trans-tibial amputee socket dynamics. In: Proc 9th Int Conf Information Technology Applications Biomedicine, Larnaca, Cyprus, November 4-7 2009. IEEE, pp 1-4.

345. Hao JZ, Jayachandran M, Kng P, Foo S, Aung P, Cai Z (2010) FBG-based smart bed system for healthcare applications. Front Optoelectronics China 3 (1):78-83.

346. Cobb JR, Claremont D (1995) Transducers for foot pressure measurement: survey of recent developments. Med Biol Eng Comput 33 (4):525-32.

347. Betts RP, Duckworth T, Austin IG, Crocker SP, Moore S (1980) Critical light reflection at a plastic/glass interface and its application to foot pressure measurements. J Med Eng Technol 4 (3):136-42.

348. Franks CI, Betts RP (1988) Selection of transducer material for use with ‘optical’ foot pressure systems. J Biomed Eng 10 (4):365-7.

349. Franks C, Betts R, Duckworth T (1983) Microprocessor-based image processing system for dynamic foot pressure studies. Med Biol Eng Comput 21 (5):566-72.

350. Hao JZ, Tan KM, Tjin SC, Liaw CY, Chaudhuri PR, Guo X, Lu C Design of a foot-pressure monitoring transducer for diabetic patients based on FBG sensors. In: 16th Annual Meeting IEEE, Tucson, AZ, USA, October 27-28 2003. Lasers and Electro-Optics Society (LEOS). IEEE, pp 23-4.

351. Wang W-C, Ledoux WR, Sangeorzan BJ, Reinhall PG (2005) A shear and plantar pressure sensor based on fiber-optic bend loss. J Rehabil Res Dev 42 (3):315-25.

352. Wang W-C, Huang C-Y, Chiang T-K, Reinhall PG Optical and mechanical characterization of microfabricated optical bend loss sensor for distributive pressure measurement. In: Kundu T (ed) Health Monitoring Structural and Biological Systems 2007, San Diego, California, USA, April 11 2007. SPIE, pp 65321K-10.

353. Wang W-C, Ho C-T, Lian Y-R, Chuang W-C (2006) Transducing mechanical force by use of a diffraction grating sensor. Appl Opt 45 (9):1893-7.

354. Soetanto W, Nguyen NT, Wang W-C Fiber optic plantar pressure/shear sensor. In: Kundu T (ed) P SPIE 7984, 79840Z, San Diego, CA, USA, March, 7 2011. Health Monitoring Structural and Biological Systems. pp 79840Z-7.

355. Pina J (1995) Anatomia humana da locomoção: Anatomia humana passiva (Osteologia e artrologia), Anatomica humana activa (Miologia), Anatomia radiológica (Human anatomy of locomotion: passive anatomy (osteology and arthrology), active anatomy (miology), radiological anatomy). Lidel, Lisboa, Portugal.

356. Gray H (1918) Anatomy of the human body. Bartleby.com, 2000 edn. Lea & Febiger, Philadelphia.

357. Snijders CJ, Vleeming A, Stoeckart R (1993) Transfer of lumbosacral load to iliac bones and legs: Part 1: Biomechanics of self-bracing of the sacroiliac joints and its significance for treatment and exercise. Clinical Biomechanics 8 (6):285-94.

358. Pel JJ, Spoor CW, Pool-Goudzwaard AL, Hoek van Dijke GA, Snijders CJ (2008) Biomechanical analysis of reducing sacroiliac joint shear load by optimization of pelvic muscle and ligament forces. Ann Biomed Eng 36 (3):415-24.

359. Winter DA (1990) Biomechanics and motor control of human movement. 2nd edn. John Wiley & Sons, Inc., NY.

360. Leatt P, Reilly T, Troup JG (1986) Spinal loading during circuit weight-training and running. British Journal of Sports Medicine 20 (3):119-24.

361. Battié MC, Videman T, Levälahti E, Gill K, Kaprio J (2008) Genetic and environmental effects on disc degeneration by phenotype and spinal level: A multivariate twin study. Spine 33 (25):2801-8 10.1097/BRS.0b013e31818043b7.

362. Bornstein PE, Peterson RR (1966) Numerical variation of the presacral vertebral column in three population groups in North America. American Journal of Physical Anthropology 25 (2):139-46.

363. Atkinson PJ (1967) Variation in trabecular structure of vertebrae with age. Calc Tis Res 1 (1):24-32.

364. O'Neill TW, Varlow J, Felsenberg D, Johnell O, Weber K, Marchant F, Delmas PD, Cooper C, Kanis J, Silman AJ (1994) Variation in vertebral height ratios in population studies. Journal of Bone and Mineral Research 9 (12):1895-907.

365. Lunt M, Felsenberg D, Reeve J, Benevolenskaya L, Cannata J, Dequeker J, Dodenhof C, Falch JA, Masaryk P, Pols HAP, Poor G, Reid DM, Scheidt-Nave C, Weber K, Varlow J, Kanis JA, O'Neill TW, Silman AJ (1997) Bone density variation and its effects on risk of vertebral deformity in men and women studied in thirteen european centers: The EVOS study. Journal of Bone and Mineral Research 12 (11):1883-94.

366. McHenry HM (1976) Early hominid body weight and encephalization. Am J Physical Anthropology 45 (1):77-83.

367. Hollinshead WH (1965) Anatomy of the spine: Points of interest to orthopaedic surgeons. J Bone Joint Surg Am 47 (1):209-15.

368. Willis TA (1923) The thoracicolumbar column in white and negro stocks. Anatomical Record 26 (1):31-40.

369. Imhof H, Halpern B, Herneth AM, Friedrich KM, Matzner M, Mueller-Mang C, Noebauer-Huhmann I-M, Prayer D, Sommer O, Wolf F (eds) (2008) Direct diagnosis in radiology: Spinal imaging. Thieme, Stuttgart.

370. Konin GP, Walz DM (2010) Lumbosacral transitional vertebrae: Classification, imaging findings, and clinical relevance. American Journal of Neuroradiology 31 (10):1778-86.

371. Kertula L (2001) Magnetic resonance imaging of the intervertebral disc: Pos-traumatic findings and the value of diffusion-weighted MR imaging. University of Oulu, Oulu

372. Eyre D, Muir H (1976) Type-1 and type-2 collagens in intervertebral-disk: Interchanging radial distributions in annulus fibrosus. Biochem J 157 (1):267-70.

373. Pooni JS, Hukins DWL, Harris PF, Hilton RC, Davies KE (1986) Comparison of the structure of human intervertebral discs in the cervical, thoracic and lumbar regions of the spine. Surg Radiol Anat 8 (3):175-82.

374. Gracovetsky S, Iacono S (1987) Energy transfer in the spinal cord. J Biomed Eng 9:99-114.

375. Farfan HF (1995) Form and function of the musculoskeletal system as revealed by mathematical analysis of the lumbar spine: An essay. Spine 20 (13):1462-73.

376. Vaz, Roussouly, Berthonnaud, Dimnet (2002) Sagittal morphology and equilibrium of pelvis and spine. Eur Spine J 11 (1):80-7.

377. Vialle R, Levassor N, Rillardon L, Templier A, Skalli W, Guigui P (2005) Radiographic analysis of the sagittal alignment and balance of the spine in asymptomatic subjects. J Bone Joint Surg Am 87 (2):260-7.

378. Berlemann U, Gries NC, Moore RJ (1998) The relationship between height, shape and histological changes in early degeneration of the lower lumbar discs. European Spine Journal 7 (3):212-7.

379. Cobb JR (1948) Outline for the study of scoliosis. Am Acad Orthop Surg Instr Course Lect 5:261-75.

380. Cobb JR (1958) Scoliosis: Quo vadis? The Journal of Bone & Joint Surgery 40 (3):507-10.

381. Greenspan A, Pugh JW, Norman A, Norman RS (1978) Scoliotic index: A comparative evaluation of methods for the measurement of scoliosis. Bull Hosp Joint Dis 39 (2):117-25.

382. Chernukha KV, Daffner RH, Reigel DH (1998) Lumbar lordosis measurement: A new method versus Cobb technique. Spine 23 (1):74-9.

383. Harrison DE, Harrison DD, Cailliet R, Troyanovich SJ, Janik TJ, Holland B (2000) Cobb method or Harrison posterior tangent method: Which to choose for lateral cervical radiographic analysis. Spine 25 (16):2072-8.

384. Silber JS, Lipetz JS, Hayes VM, Lonner BS (2004) Measurement variability in the assessment of sagittal alignment of the cervical spine: A comparison of the Gore and Cobb methods. Journal of Spinal Disorders & Techniques 17 (4):301-5.

385. Been E, Pessah H, Been L, Tawil A, Peleg S (2007) New method for predicting the lumbar lordosis angle in skeletal material. Anatomical Record: Advances in Integrative Anatomy and Evolutionary Biology 290 (12):1568-73.

386. Vrtovec T, Pernus F, Likar B (2009) A review of methods for quantitative evaluation of spinal curvature. Eur Spine J 18 (5):593-607.

387. Watkins J (1999) Structure and function of the musculoskeletal system. 2 edn. Human Kinetics, Champaign, IL.

388. Frobin W, Brinckmann P, Biggemann M, Tillotson M, Burton K (1997) Precision measurement of disc height, vertebral height and sagittal plane displacement from lateral radiographic views of the lumbar spine. Clin Biomech 12 (Supplement 1):S1-S64.

389. Ferguson A (1930) The study and treatment of scoliosis. South Med J 23:116-20.

390. Diab KM, Sevastik JA, Hedlund R, Suliman IA (1995) Accuracy and applicability of measurement of the scoliotic angle at the frontal plane by Cobb's method, by Ferguson's method and by a new method. Eur Spine J 4 (5):291-5.

391. Chen YL, Chen WJ, Chiou WK (2007) An alternative method for measuring scoliosis curvature. Orthopedics 30 (10):828-31.

392. Kane WJ (1977) Scoliosis prevalence: A call for a statement of terms. Clin Orthop Relat Res (126):43-6.

393. Aroeira RM, Leal JS, de Melo Pertence AE (2011) New method of scoliosis assessment: Preliminary results using computerized photogrammetry. Spine 36 (19):1584-91.

394. Roach JW (1999) Adolescent idiopathic scoliosis. The Orthopedic Clinics of North America 30 (3):353-65.

395. During J, Goudfrooij H, Keessen W, Beeker TW, Crowe A (1985) Toward standards for posture: Postural characteristics of the lower back system in normal and pathologic conditions. Spine 10 (1):83-7.

396. Walker ML, Rothstein JM, Finucane SD, Lamb RL (1987) Relationships between lumbar lordosis, pelvic tilt, and abdominal muscle performance. Phys Ther 67 (4):512-6.

397. Marieb EN (2004) Human Anatomy and Physiology. 6th edn. Pearson Benjamin Cummings.

398. Allbrook D (1957) Movements of the lumbar spinal column. Journal of Bone & Joint Surgery, British Volume 39-B (2):339-45.

399. Loebl WY (1967) Measurement of spinal posture and range of spinal movement. Rheumatology 9 (3):103-10.

400. Moll JM, Wright V (1971) Normal range of spinal mobility. An objective clinical study. Ann Rheum Dis 30 (4):381-6.

401. Reynolds PMG (1975) Measurement of spinal mobility: a comparison of three methods. Rheumatology 14 (3):180-5.

402. Pearcy M, Portek I, Shepherd J (1984) Three-dimensional X-ray analysis of normal movement in the lumbar spine. Spine 9 (3):294-7.

403. Dvorak J, Froehlich D, Penning L, Baumgartner H, Panjabi MM (1988) Functional radiographic diagnosis of the cervical spine: flexion/extension. Spine 13 (7):748-55.

404. Van Herp G, Rowe P, Salter P, Paul JP (2000) Three-dimensional lumbar spinal kinematics: a study of range of movement in 100 healthy subjects aged 20 to 60+ years. Rheumatology 39 (12):1337-40.

405. Tousignant M, de Bellefeuille L, O’Donoughue S, Grahovac S (2000) Criterion validity of the cervical range of motion (CROM) goniometer for cervical flexion and extension. Spine 25 (3):324-30.

406. Hamill J, Knutzen KM (1995) Biomechanics and anatomy of human movement. Lippincott Williams & Wilkins, Baltimore, Maryland, USA.

407. Nordim M, Frankel VH (eds) (1989) Basic biomechanics of the musculoskeletal system. 2nd edn. Lea & Febiger, Malvern, PA.

408. Farfan HF (1975) Muscular mechanism of the lumbar spine and the position of power and efficiency. Orthop Clin North Am 6 (1):135-44.

409. Panjabi MM, Oxland T, Takata K, Goel V, Duranceau J, Krag M (1993) Articular facets of the human spine: Quantitative three-dimensional anatomy. Spine 18 (10):1298-310.

410. Hall S (1991) Basic biomechanics. McGraw Hill, NY.

411. White AA, Panjabi MM (1978) The basic kinematics of the human spine. Spine 3:12-20.

412. Pal GP, Routal RV, Saggu SK (2001) The orientation of the articular facets of the zygapophyseal joints at the cervical and upper thoracic region. J Anat 198 (Pt 4):431-41.

413. Joplin RJ (1935) The intervertebral disc. Embryology, anatomy, physiology and pathology. Surg Gyn and Obst 61 (591).

414. Wilke HJ, Wenger KH, Claes LE (1998) Testing criteria for spinal implants: Recommendations for the standardization of in vitro stability testing of spinal implants. Eur Spine J 7 (2):148-54.

415. Shirazi-Adl SA, Shrivastava SC, Ahmed AM (1984) Stress analysis of the lumbar disc-body unit in compression: A three-dimensional nonlinear finite element study. Spine 9 (2):120-34.

416. Shirazi-Adl A, Ahmed AM, Shrivastava SC (1986) A finite element study of a lumbar motion segment subjected to pure sagittal plane moments. J Biomech 19 (4):331-50.

417. Shirazi-Adl A (1991) Finite-element evaluation of contact loads on facets of an L2-L3 lumbar segment in complex loads. Spine 16 (5):533-41.

418. Goel VK, Monroe BT, Gilbertson LG, Brinckmann P (1995) Interlaminar shear stresses and laminae separation in a disc: Finite element analysis of the L3-L4 motion segment subjected to axial compressive loads. Spine 20 (6):689-98.

419. Wilke HJ, Jungkunz B, Wenger K, Claes LE (1998) Spinal segment range of motion as a function of in vitro test conditions: Effects of exposure period, accumulated cycles, angular-deformation rate, and moisture condition. Anatomical Record 251 (1):15-9.

420. Wang J-L, Parnianpour M, Shirazi-Adl A, Engin AE (2000) Viscoelastic finite-element analysis of a lumbar motion segment in combined compression and sagittal flexion: Effect of loading rate. Spine 25 (3):310-8.

421. Lodygowski T, Kakol W, Wierszycki M (2005) Three-dimensional nonlinear finite element model of lumbar intervertebral disc. Acta Bioeng Biomech 7 (2):29-37.

422. Haiyun L, Zheng W (2006) Intervertebral disc biomechanical analysis using the finite element modeling based on medical images. Computerized medical imaging and graphics : the official journal of the Computerized Medical Imaging Society 30 (6):363-70.

423. Schmidt H, Heuer F, Drumm J, Klezl Z, Claes L, Wilke H-J (2007) Application of a calibration method provides more realistic results for a finite element model of a lumbar spinal segment. Clin Biomech 22 (4):377-84.

424. Dooris AP, Goel VK, Grosland NM, Gilbertson LG, Wilder DG (2001) Load-sharing between anterior and posterior elements in a lumbar motion segment implanted with an artificial disc. Spine 26 (6):E122-E9.

425. Noailly J, Lacroix D, Planell JA, Tanner E, Ambrosio L (2006) Interaction of a novel intervertebral disc substitute with the lumbar spine tissue biomechanics: A finite element study. J Biomech 39 (Supplement 1):S263-S173.

426. Denozière G, Ku DN (2006) Biomechanical comparison between fusion of two vertebrae and implantation of an artificial intervertebral disc. J Biomech 39 (4):766-75.

427. Fung YC (1993) Bone and cartilage. In: Biomechanics: Mech properties living tissues. 2 edn. Springer, NY, p 568.

428. Teraoka K, Ito A, Maekawa K, Onuma K, Tateishi T, Tsutsumi S (1998) Mechanical properties of hydroxyapatite and OH-carbonated hydroxyapatite single crystals. Journal of Dental Research 77 (7):1560-8.

429. Termine JD, Posner AS (1966) Infrared analysis of rat bone: Age dependency of amorphous and crystalline mineral fractions. Science 153 (3743):1523-5.

430. Smith RW, Keiper DA (1965) Dynamic measurement of viscoelastic properties of bone. Am J Med Electron 4 (4):156-60.

431. Cowin S (2001) Bone mechanics handbook. 2 edn. CRC Press, London.

432. Nigg BM, Herzog W (eds) (1999) Biomechanics of the musculo-skeletal system. 2nd edn. Wiley, Chichester, England.

433. Gilsanz V, Perez FJ, Campbell PP, Dorey FJ, Lee DC, Wren T (2009) Quantitative CT reference values for vertebral trabecular bone density in children and youn adults. Radiology 250 (1):222-7.

434. Trebacz H, Gawda H (2001) The estimation of structural anisotropy of trabecular and cortical bone tissues base on ultrasonic velocity and attenuation. Acta Bioeng Biomech 3 (2):41-8.

435. Wenger K (1995) Deformation and stress og the vertebral endplate and outer annulus fibrosus. Utah, Utah

436. Carter DR, Hayes WC (1976) Bone compressive strength: The influence of density and strain rate. Science 194 (1174).

437. Bonefield W, Li CH (1967) Anisotropy if nonelastic flow in bone. J App Physics 38:2450.

438. Frankel VH, Burstein AH (1970) Orthopaedic biomechanics. Lea & Febiger, Philadelphia.

439. Schmidt H, Kettler A, Heuer F, Simon U, Claes L, Wilke H-J (2007) Intradiscal pressure, shear strain, and fiber strain in the intervertebral disc under combined loading. Spine 32 (7):748-55.

440. Evans FG (1969) The mechanical properties of bone. Artificial limbs 13:37-48.

441. Lu YM, Hutton WC, Gharpuray VM (1996) Do bending, twisting, and diurnal fluid changes in the disc affect the propensity to prolapse? A viscoelastic finite element model. Spine 21 (22):2570-9.

442. Pitzen T, Geisler F, Matthis D, Müller-Storz H, Pedersen K, Steudel W (2001) The influence of cancellous bone density on load sharing in human lumbar spine: a comparison between an intact and a surgically altered motion segment. Eur Spine J 10((1):23-9.

443. Nagy G, Gentle C (2001) Significance of the annulus properties to finite element modeling of intervertebral discs. J Musculoskeletal Research 5 (3):159-71.

444. Baroud G, Nemes J, Heini P, Steffen T (2003) Load shift of the intervertebral disc after a vertebroplasty: A finite-element study. Eur Spine J 12 (4):421-6.

445. Lavaste F, Skalli W, Robin S, Roy-Camille R, Mazel C (1992) Three-dimensional geometrical and mechanical modelling of the lumbar spine. J Biomech 25 (10):1153-64.

446. Sharma M, Langrana NA, Rodriguez J (1995) Role of ligaments and facets in lumbar spinal stability. Spine 20 (8):887-900.

447. Goel VK, Kong WZ, Han JS, Weinstein JN, Gilbertson LG (1993) A combined finite element and optimization investigation of lumbar spine mechanics with and without muscles. Spine 18 (11):1531-41.

448. Shirazi-Adl A, Ahmed AM, Shrivastava SC (1986) Mechanical response of a lumbar motion segment in axial torque alone and combined with compression. Spine 11 (9):914-27.

449. Polikeit A, Ferguson SJ, Nolte LP, Orr TE (2003) The importance of the endplate for interbody cages in the lumbar spine. European Spine Journal 12 (6):556-61.

450. Crawford RP, Christopher EC, Tony MK (2003) Finite element models predict in vitro vertebral body compressive strength better than quantitative computed tomography. Bone 33 (4):744-50.

451. Silva MJ, Wang C, Keaveny TM, Hayes WC (1994) Direct and computed tomography thickness measurements of the human, lumbar vertebral shell and endplate. Bone 15 (4):409-14.

452. Hirsch C (1951) Studies on the mechanism of low back pain. Acta Orthop 20 (4):261-74.

453. Moore RJ (2000) The vertebral end-plate: what do we know? Eur Spine J 9 (2):92-6.

454. Hee HT, Chuah YJ, Tan BHM, Setiobudi T, Wong HK (2011) Vascularization and morphological changes of the endplate after axial compression and distraction of the intervertebral disc. Spine 36 (7):505-11.

455. Van de Graaf K (1995) Human anatomy. 4th edn. Wm. C. Brown, Iowa.

456. Saar G, Zhang B, Ling W, Regatte RR, Navon G, Jerschow A (2012) Assessment of glycosaminoglycan concentration changes in the intervertebral disc via chemical exchange saturation transfer. NMR Biomed 25 (2):255-61.

457. Coventry MB, Ghormley RK, Kernohan JW (1945) The intervertebral disc. Its microscopic anatomy and pathology: Part I. Anatomy, development, and physiology. J Bone Joint Surg Am 27 (1):105-12.

458. Virgin WJ (1951) Experimental investigations into the physical properties of the intervertebral disc. J Bone Joint Surg Br 33-B (4):607-11.

459. Gilad I, Nissan M (1986) A study of vertebra and disc geometric relations of the human cervical and lumbar spine. Spine (Phila Pa 1976) 11 (2):154-7.

460. Brown T, Hansen RJ, Yorra AJ (1957) Some mechanical tests on the lumbosacral spine with particular reference to the Intervertebral discs: A preliminary report. J Bone Joint Surg Am 39 (5):1135-64.

461. Smith LJ, Fazzalari NL (2006) Regional variations in the density and arrangement of elastic fibres in the anulus fibrosus of the human lumbar disc. J Anat 209 (3):359-67.

462. White AA, Panjabi MM (1990) Clinical biomechanics of the spine. 2nd edn. Lippincott, Philadelphia.

463. Skrzypiec D, Pollintine P, Przybyla A, Dolan P, Adams M (2007) The internal mechanical properties of cervical intervertebral discs as revealed by stress profilometry. European Spine Journal 16 (10):1701-9.

464. Adams M (2004) Biomechanics of back pain. Acupuncture in Medicine 22 (4):178-88.

465. Nachemson A (1959) Measurement of intradiscal pressure. Acta Orthop 28 (4):269 - 89.

466. Hirsch C, Paulson S, Sylven B, Snellman O (1952) Biophysical and physiological investigations on cartilage and other mesenchymal tissues IV: Characteristics of human nuclei pulposi during aging. Acta Orthop 22 (1):175 - 83.

467. Gower WE, Pedrini V (1969) Age-related variations in proteinpolysaccharides from human nucleus pulposus, annulus fibrosus, and costal cartilage. J Bone Joint Surg Am 51 (6):1154-62.

468. Yu J, Tirlapur U, Fairbank J, Handford P, Roberts S, Winlove CP, Cui Z, Urban J (2007) Microfibrils, elastin fibres and collagen fibres in the human intervertebral disc and bovine tail disc. J Anat 210 (4):460-71.

469. Gregory D (2009) The influence of the tensile material properties of single annulus fibrosus lamellae and the interlamellar matrix strength on disc herniation and progression. University of Waterloo, Ontario, Canada

470. Naylor A (1962) The biophysical and biochemical aspects of intervertebral disc herniation and degeneration. Ann R Coll Surg Engl 31 (2):91–114.

471. Lyons G, Eisenstein SM, Sweet MBE (1981) Biochemical changes in intervertebral disc degeneration. Biochimica et Biophysica Acta (BBA) - General Subjects 673:443-53.

472. Holm S, Maroudas A, Urban JPG, Selstam G, Nachemson A (1981) Nutrition of the intervertebral disc: Solute transport and metabolism. Conn Tiss Res 8 (2):101-19.

473. Kraemer J, Kolditz D, Gowin R (1985) Water and electrolyte content of human intervertebral discs under variable load. Spine 10 (1):69-71.

474. Botsford DJ, Esses SI, Ogilvie-Harris DJ (1994) In vivo diurnal variation in intervertebral disc volume and morphology. Spine 19 (8):935-40.

475. Dolan P, Adams MA (2001) Recent advances in lumbar spinal mechanics and their significance for modelling. Clin Biomech 16 (Supplement 1):S8-S16.

476. McMillan DW, Garbutt G, Adams MA (1996) Effect of sustained loading on the water content of intervertebral discs: Implications for disc metabolism. Ann Rheum Dis 55:880-7.

477. Errington R, Puustjarvi K, White I, Roberts S, Urban J (1998) Characterisation of cytoplasm-filled processes in cells of the intervertebral disc. J Anat 192:369 - 78.

478. Hayes AJ, Benjamin M, Ralphs JR (2001) Extracellular matrix in development of the intervertebral disc. Matrix Biology 20 (2):107-21.

479. Pritchard S, Erickson GR, Guilak F (2002) Hyperosmotically induced volume change and calcium signaling in intervertebral disk cells: The role of the actin cytoskeleton. Biophysical J 83 (5):2502-10.

480. Bruehlmann SB, Rattner JB, Matyas JR, Duncan NA (2002) Regional variations in the cellular matrix of the annulus fibrosus of the intervertebral disc. J Anat 201 (2):159-71.

481. White III AA, Panjabi MM (1990) Clinical biomechanics of the spine. 2nd edn. Lippincott, Philadelphia.

482. Lu YM, Hutton WC, Gharpuray VM (1996) Can variations in intervertebral disc height affect the mechanical function of the disc? Spine 21 (19):2208-16.

483. Cripton PA, Dumas GA, Nolte LP (2001) A minimally disruptive technique for measuring intervertebral disc pressure in vitro: application to the cervical spine. J Biomech 34 (4):545-9.

484. Sato K, Kikuchi S, Yonezawa T (1999) In vivo intradiscal pressure measurement in healthy individuals and in patients with ongoing back problems. Spine 24:2468 - 74.

485. McNally D, Adams M (1992) Internal intervertebral disc mechanics as revealed by stress profilometry. Spine 17:66 - 73.

486. Nachemson A (1960) Lumbar intradiscal pressure. Experimental studies on post-mortem material. Acta Orthop Scand Supplementum 43 (43):1-104.

487. Polga DJ, Beaubien BP, Kallemeier PM, Schellhas KP, Lew WD, Buttermann GR, Wood KB (2004) Measurement of in vivo intradiscal pressure in healthy thoracic intervertebral discs. Spine 29 (12):1320-4.

488. Lipson S, Muir H (1981) Proteoglycans in experimental intervertebral disc degeneration. Spine 6 (3):194-210.

489. Beadle O (1932) The intervertebral discs: Observations on their normal and morbid anatomy in relation to certain spinal deformities. J Am Med Assoc 98 (14):1212.

490. Marchand F, Ahmed A (1990) Investigation of the laminate structure of lumbar disc anulus fibrosus. Spine 15 (5):402-10.

491. Cassidy JJ, Hiltner A, Baer E (1989) Hierarchical structure of the intervertebral disc. Conn Tiss Res 23 (1):75-88.

492. Marchand F, Ahmed A (1990) Investigation of the laminate structure of lumbar disc anulus fibrosus. Spine 15:402 - 10.

493. Tsuji H, Hirano N, Ohshima H, Ishihara H, Terahata N, Motoe T (1993) Structural variation of the anterior and posterior anulus fibrosus in the development of human lumbar intervertebral-disk: A risk factor for intervertebral-disk rupture. Spine 18 (2):204-10.

494. Nandan LN, Dawn ME, Robert LM (2010) Mechanical design criteria for intervertebral disc tissue engineering. J Biomech 43 (6):1017-30.

495. Holzapfel GA, Schulze-Bauer CAJ, Feigl G, Regitnig P (2005) Single lamellar mechanics of the human lumbar anulus fibrosus. Biomech Model Mechan 3 (3):125-40.

496. Heuer F, Schmidt H, Wilke H-J (2008) The relation between intervertebral disc bulging and annular fiber associated strains for simple and complex loading. J Biomech 41 (5):1086-94.

497. Eberlein R, Holzapfel GA, Schulze-Bauer CAJ (2001) An anisotropic model for annulus tissue and enhanced finite element analyses of intact lumbar disc bodies. Computer Methods in Biomech and Biomed Eng 4 (3):209-29.

498. Skaggs DL, Weidenbaum M, Iatridis JC, Ratcliffe A, Mow VC (1994) Regional variation in tensile properties and biochemical composition of the human lumbar anulus fibrosus. Spine 19 (12):1310-9.

499. Ebara S, Iatridis JC, Setton LA, Foster RJ, Mow VC, Weidenbaum M (1996) Tensile properties of nondegenerate human lumbar anulus fibrosus. Spine 21 (4):452-61.

500. Costi JJ, Stokes IA, Gardner-Morse M, Laible JP, Scoffone HM, Iatridis JC (2007) Direct measurement of intervertebral disc maximum shear strain in six degrees of freedom: Motions that place disc tissue at risk of injury. J Biomech 40 (11):2457-66.

501. Shirazi-Adl A (1989) Strain in fibers of a lumbar disc. Analysis of the role of lifting in producing disc prolapse. Spine (Phila Pa 1976) 14 (1):96-103.

502. Green TP, Adams MA, Dolan P (1993) Tensile properties of the annulus fibrosus. Eur Spine J 2 (4):209-14.

503. Klein JA, Hukins DWL (1982) X-ray diffraction demonstrates reorientation of collagen fibres in the annulus fibrosus during compression of the intervertebral disc. Biochimica et Biophysica Acta (BBA) - General Subjects 717 (1):61-4.

504. Guerin H, Elliott D (2006) Degeneration affects the fiber reorientation of human annulus fibrosus under tensile load. J Biomech 39 (8):1410-8.

505. Pezowicz CA, Robertson PA, Broom ND (2006) The structural basis of interlamellar cohesion in the intervertebral disc wall. J Anat 208 (3):317-30.

506. Fujita Y, Wagner DR, Biviji AA, Duncan NA, Lotz JC (2000) Anisotropic shear behavior of the annulus fibrosus: Effect of harvest site and tissue prestrain. Med Eng Phys 22 (5):349-57.

507. Moore R, Vernon-Roberts B, Fraser R, Osti O, Schembri M (1996) The origin and fate of herniated lumbar intervertebral disc tissue. Spine 21:2149 - 55.

508. Iatridis JC, Kumar S, Foster RJ, Weidenbaum M, Mow VC (1999) Shear mechanical properties of human lumbar annulus fibrosus. J Orthop Res 17 (5):732-7.

509. Baroud G, Nemes J, Heini P, Steffen T (2003) Load shift of the intervertebral disc after a vertebroplasty: A finite-element study. European Spine Journal 12 (4):421-6.

510. Friberg S, Hirsch C (1949) Anatomical and clinical studies on lumbar disc degeneration. Acta Orthop Scand 19 (2):222-42.

511. Shirazi-Adl A (1994) Nonlinear stress analysis of the whole lumbar spine in torsion--Mechanics of facet articulation. J Biomech 27 (3):289-91.

512. Zander T, Rohlmann A, Klockner C, Bergmann G (2002) Effect of bone graft characteristics on the mechanical behavior of the lumbar spine. J Biomech 35 (4):491-7.

513. King AI, Prasad P, Ewing CL (1975) Mechanism of spinal injury due to caudocephalad acceleration. Orthop Clin North Am 6 (1):19-31.

514. Goel VK, Kong W, Han JS, Weinstein JN, Gilbertson LG (1993) A combined finite element and optimization investigation of lumbar spine mechanics with and without muscles. Spine 18 (11):1531-41.

515. Panjabi MM, Krag M, Summers D, Videman T (1985) Biomechanical time-tolerance of fresh cadaveric human spine specimens. J Orthop Res 3 (3):292-300.

516. Panjabi MM (1988) Biomechanical evaluation of spinal fixation devices: I. A conceptual framework. Spine 13 (10):1129-34.

517. Panjabi MM, Abumi K, Duranceau J, Crisco JJ (1988) Biomechanical evaluation of spinal fixation devices: II. Stability provided by eight internal fixation devices. Spine 13 (10):1135-40.

518. Ashman RB, Bechtold JE, Edwards WT, Johnston CEI, McAfee PC, Tencer AF (1989) In vitro spinal arthrodesis implant mechanical testing protocols. Journal of Spinal Disorders & Techniques 2 (4):274-81.

519. Adams MA (1995) Mechanical testing of the spine. An appraisal of methodology, results, and conclusions. Spine (Phila Pa 1976) 20 (19):2151-6.

520. Adams MA (1995) Spine update mechanical testing of the spine: an appraisal of methodology, results, and conclusions. Spine 20 (19):2151-6.

521. Wilke HJ, Krischak S, Claes LE (1996) Formalin fixation strongly influences biomechanical properties of the spine. J Biomech 29 (12):1629-31.

522. Wilke HJ, Krischak S, Claes L (1996) Biomechanical comparison of calf and human spines. J Orthop Res 14 (3):500-3.

523. Wilke HJ, Kettler A, Wenger KH, Claes LE (1997) Anatomy of the sheep spine and its comparison to the human spine. Anatomical Record 247 (4):542-55.

524. Wilke HJ, Kettler A, Claes LE (1997) Are sheep spines a valid biomechanical model for human spines? Spine 22 (20):2365-74.

525. Goel VK, Panjabi MM, Patwardhan AG, Dooris AP, Serhan H (2006) Test protocols for evaluation of spinal implants. J Bone Joint Surg Am 88 (suppl_2):103-9.

526. Hirsch C, Nachemson A (1954) New observations on the mechanical behavior of lumbar discs. Acta Orthop 23 (4):254 - 83.

527. Hirsch C (1955) The reaction of intervertebral discs to compression forces. J Bone Joint Surg Am 37 (6):1188-96.

528. Rouleau L, Tremblay D, Cartier R, Mongrain R, Leask RL (2012) Regional variations in canine descending aortic tissue mechanical properties change with formalin fixation. Cardiovasc Pathol 21 (5):390-7.

529. Burkhart KJ, Nowak TE, Blum J, Kuhn S, Welker M, Sternstein W, Mueller LP, Rommens PM (2010) Influence of formalin fixation on the biomechanical properties of human diaphyseal bone. Biomed Tech (Berl) 55 (6):361-5.

530. Coe JD, Warden KE, Engr M, Herzig MA, McAfee PC (1990) Influence of bone mineral density on the fixation of thoracolumbar implants A comparative study of transpedicular screws, laminar hooks, and spinous process wires. Spine 15 (9):902-7.

531. Halvorson TL, Kelley LA, Thomas KA, Whitecloud TSI, Cook SD (1994) Effects of bone mineral density on pedicle screw fixation. Spine 19 (21):2415-20.

532. Park SB, Chung CK (2011) Strategies of spinal fusion on osteoporotic spine. J Korean Neurosurg Soc 49 (6):317-22.

533. Lang TF, Guglielmi G, van Kuijk C, De Serio A, Cammisa M, Genant HK (2002) Measurement of bone mineral density at the spine and proximal femur by volumetric quantitative computed tomography and dual-energy X-ray absorptiometry in elderly women with and without vertebral fractures. Bone 30 (1):247-50.

534. Hui SL, Slemenda CW, Johnston CC, Appledorn CR (1987) Effects of age and menopause on vertebral bone density. Bone and mineral 2 (2):141-6.

535. Gilsanz V, Gibbens DT, Roe TF, Carlson M, Senac MO, Boechat MI, Huang HK, Schulz EE, Libanati CR, Cann CC (1988) Vertebral bone density in children: effect of puberty. Radiology 166 (3):847-50.

536. Luckey MM, Meier DE, Mandeli JP, DaCosta MC, Hubbard ML, Goldsmith SJ (1989) Radial and vertebral bone density in white and black women: Evidence for racial differences in premenopausal bone homeostasis. Journal of Clinical Endocrinology & Metabolism 69 (4):762-70.

537. Kalender WA, Felsenberg D, Louis O, Lopez P, Klotz E, Osteaux M, Fraga J (1989) Reference values for trabecular and cortical vertebral bone density in single and dual-energy quantitative computed tomography. Eur J Radiol 9 (2):75-80.

538. Ruiz JC, Mandel C, Garabedian M (1995) Influence of spontaneous calcium intake and physical exercise on the vertebral and femoral bone mineral density of children and adolescents. Journal of Bone and Mineral Research 10 (5):675-82.

539. Nachemson A (1963) The influence of spinal movements on the lumbar intradiscal pressure and on the tensile stresses in the annulus fibrosus. Acta Orthop 33 (1):183 - 207.

540. Shah J, Hampson W, Jayson M (1978) The distribution of surface strain in the cadaveric lumbar spine. J Bone Joint Surg Br 60-B (2):246-51.

541. Linde F, Sørensen HCF (1993) The effect of different storage methods on the mechanical properties of trabecular bone. Journal of Biomechanics 26 (10):1249-52.

542. Gleizes V, Viguier E, Féron JM, Canivet S, Lavaste F (1998) Effects of freezing on the biomechanics of the intervertebral disc. Surg Radiol Anat 20 (6):403-7.

543. Hongo M, Gay RE, Hsu J-T, Zhao KD, Ilharreborde B, Berglund LJ, An K-N (2008) Effect of multiple freeze–thaw cycles on intervertebral dynamic motion characteristics in the porcine lumbar spine. Journal of Biomechanics 41 (4):916-20.

544. Callaghan JP, McGill SM (1995) Frozen storage increases the ultimate compressive load of porcine vertebrae. Journal of Orthopaedic Research 13 (5):809-12.

545. Bass EC, Duncan NA, Hariharan JS, Dusick J, Bueff UH, Lotz JC (1997) Frozen storage affects the compressive creep behavior of the porcine intervertebral disc. Spine 22 (24):2867-76.

546. Virgin W (1951) Experimental investigations into the physical properties of the intervertebral disc. J Bone Joint Surg Br 33-B:607 - 11.

547. Urban JPG, Maroudas A (1981) Swelling of the intervertebral disc in vitro. Connective Tissue Research 9 (1):1-10.

548. Pflaster DS, Krag MH, Johnson CC, Haugh LD, Pope MH (1997) Effect of test environment on intervertebral disc hydration. Spine 22 (2):133-9.

549. Wagner DR, Lotz JC (2004) Theoretical model and experimental results for the nonlinear elastic behavior of human annulus fibrosus. Journal of Orthopaedic Research 22 (4):901-9.

550. Wilke HJ, Krischak ST, Wenger KH, Claes LE (1997) Load-displacement properties of the thoracolumbar calf spine: Experimental results and comparison to known human data. Eur Spine J 6 (2):129-37.

551. Gay RE, Ilharreborde B, Zhao KD, Berglund LJ, Bronfort G, An K-N (2008) Stress in lumbar intervertebral discs during distraction: a cadaveric study. The Spine Journal 8 (6):982-90.

552. Costi JJ, Hearn TC, Fazzalari NL (2002) The effect of hydration on the stiffness of intervertebral discs in an ovine model. Clin Biomech 17 (6):446-55.

553. Kettler A, Liakos L, Haegele B, Wilke HJ (2007) Are the spines of calf, pig and sheep suitable models for pre-clinical implant tests? Eur Spine J 16 (12):2186-92.

554. Kandziora F, Pflugmacher R, Scholz M, Schnake K, Lucke M, Schröder R, Mittlmeier T (2001) Comparison between sheep and human cervical spines: An anatomic, radiographic, bone mineral density, and biomechanical study. Spine 26 (9):1028-37.

555. Holm S, Nachemson A (1982) Nutritional changes in the canine intervertebral disc after spinal fusion. Clin Orthop 169:243 - 58.

556. Cunningham BW, Dmitriev AE, Hu N, McAfee PC (2003) General principles of total disc replacement arthroplasty: Seventeen cases in a nonhuman primate model. Spine 28 (20S):S118-S24.

557. Wilke H, Claes L, Schmitt H, Wolf S (1994) A universal spine tester for in vitro experiments with muscle force simulation. Eur Spine J 3 (2):91-7.

558. Persson C, Berg S (2013) Strategies towards injectable, load-bearing materials for the intervertebral disc: a review and outlook. Journal of Materials Science: Materials in Medicine 24 (1):1-10.

559. Bhattacharya S (2011) Predictive finite element modeling of artificial cervical discs in a ligamentous functional spinal unit. University of Toledo, Toleto

560. Goertzen DJ, Lane C, Oxland TR (2004) Neutral zone and range of motion in the spine are greater with stepwise loading than with a continuous loading protocol. An in vitro porcine investigation. Journal of Biomechanics 37 (2):257-61.

561. Brodke DS, Gollogly S, Alexander Mohr R, Nguyen B-K, Dailey AT, Bachus KN (2001) Dynamic cervical plates: biomechanical evaluation of load sharing and stiffness. Spine 26 (12):1324-9.

562. SimulationSolutions (2013) Hip & Spine Implant Wear Simulator. www.prosim.co.uk/pdf/uk/HIP&Spine_ENG.pdf. Accessed Mar, 31 2013

563. MTS (2013) Bionix® Spine Wear Simulator. http://www.mts.com/ucm/groups/public/documents/library/dev_002173.pdf. Accessed Mar, 31 2013

564. EndoLabMechanicalEngineering (2013) EndoLab® Spine Simulator. http://www.endolab.org/downloads/endolab_spine_simulator.pdf. Accessed Mar, 31 2013

565. AdvancedMechanicalTechnology IA (2013) ADL Hip Simulator. http://www.amti.biz/AMTI-Hip-Simulator.pdf. Accessed Mar, 31 2013

566. Instron (2013) BioPulsTM multi-axial spine testing system. http://www.inteszt.hu/PDF/01/BiomedicalBrochure.pdf. Accessed Mar, 31 2013

567. BoseElectroForce (2013) ElectroForce® 5900 BioDynamic® Test Instrument. http://worldwide.bose.com/electroforce/assets/pdf/Products/sellsheet_5900TriAxial_022009_low.pdf. Accessed March, 2013

568. AdvancedMechanicalTechnology IA (2013) ADL Force 5. http://www.amti.biz/AMTI-Force-5.pdf. Accessed Mar, 31 2013

569. AdvancedMechanicalTechnology IA (2013) VIVO™. http://www.amti.biz/vivo.aspx. Accessed Mar, 31 2013

570. Richards L, Brown C, Stone MH, Fisher J, Ingham E, Tipper JL (2008) Identification of nanometre-sized ultra-high molecular weight polyethylene wear particles in samples retrieved in vivo. Journal of Bone & Joint Surgery, British Volume 90-B (8):1106-13.

571. Vicars R, Hall R, Fisher J (2011) 6.614 - Wear: total intervertebral disc prostheses. In: Editor-in-Chief: Paul D (ed) Comprehensive Biomaterials. Elsevier, Oxford, pp 191-205.

572. Hussain A, Kamali A, Li C, Pamu J (2012) In vitro metal-on-metal subluxation test. Journal of Bone & Joint Surgery, British Volume 94-B (SUPP XL):71.

573. Shikinami Y, Kotani Y, Cunningham BW, Abumi K, Kaneda K (2004) A biomimetic artificial disc with improved mechanical properties compared to biological intervertebral discs. Advanced Functional Materials 14 (11):1039-46.

574. Akesen B, Wu C, Mehbod AA, Transfeldt EE (2008) Biomechanical evaluation of paracoccygeal transsacral fixation. Journal of Spinal Disorders & Techniques 21 (1):39-44.

575. Cho W, Wu C, Mehbod AA, Transfeldt EE (2008) Comparison of cage designs for transforaminal lumbar interbody fusion: a biomechanical study. Clinical Biomechanics 23 (8):979-85.

576. Paré PE, Chan FW, Bhattacharya S, Goel VK (2009) Surface slide track mapping of implants for total disc arthroplasty. Journal of Biomechanics 42 (2):131-9.

577. Bhattacharya S, Nayak A, Goel VK, Warren C, Schlaegle S, Ferrara L (2010) Gravimetric wear analysis and particulate characterization of bilateral facet-augmentation system – PercuDyn™. Bio-Medical Materials and Engineering 20 (6):329-38.

578. Grupp T, Yue J, Garcia R, Jr., Basson J, Schwiesau J, Fritz B, Blömer W (2009) Biotribological evaluation of artificial disc arthroplasty devices: influence of loading and kinematic patterns during in vitro wear simulation. European Spine Journal 18 (1):98-108.

579. Grupp TM, Meisel H-J, Cotton JA, Schwiesau J, Fritz B, Blömer W, Jansson V (2010) Alternative bearing materials for intervertebral disc arthroplasty. Biomaterials 31 (3):523-31.

580. Kraft M (2012) Wear performance of a peek-on-peek bearing under cervical loading conditions and at different test frequencies. Global Spine J 2012; 02 - P129 02:129.

581. Kraft M, Koch DK, Bushelow M (2012) An investigation into PEEK-on-PEEK as a bearing surface candidate for cervical total disc replacement. The Spine Journal 12 (7):603-11.

582. Mejia L, Lusk J, Nickel T (2005) Design Considerations for a Multi-DOF Kinematic Spine Simulator. European Cells and Materials 10 (3):65.

583. Panjabi MM, Krag MH, White AA (1977) Effects of preload on load displacement curves of the lumbar spine. Orthop Clin North Am 8 (1):181-92.

584. Janevic J, Ashton-Miller JA, Schultz AB (1991) Large compressive preloads decrease lumbar motion segment flexibility. J Orthop Res 9 (2):228-36.

585. Patwardhan AG, Havey RM, Carandang G, Simonds J, Voronov LI, Ghanayem AJ, Meade KP, Gavin TM, Paxinos O (2003) Effect of compressive follower preload on the flexion-extension response of the human lumbar spine. J Orthop Res 21 (3):540-6.

586. Patwardhan AG, Carandang G, Ghanayem AJ, Havey RM, Cunningham B, Voronov LI, Phillips FM (2003) Compressive preload improves the stability of anterior lumbar interbody fusion cage constructs. J Bone Joint Surg Am 85 (9):1749-56.

587. ISO (1997) ISO TC 108/SC 4 Mechanical vibration and shock - Evaluation of human exposure to whole-body vibration - Part 1: General requirements. vol 2631-1. ISO.

588. Goel VK, Grauer JN, Patel TC, Biyani A, Sairyo K, Vishnubhotla S, Matyas A, Cowgill I, Shaw M, Long R, Dick D, Panjabi MM, Serhan H (2005) Effects of Charité artificial disc on the implanted and adjacent spinal segments mechanics using a hybrid testing protocol. Spine 30 (24):2755-64.

589. Grauer JN, Biyani A, Faizan A, Kiapour A, Sairyo K, Ivanov A, Ebraheim NA, Patel TC, Goel VK (2006) Biomechanics of two-level Charité artificial disc placement in comparison to fusion plus single-level disc placement combination. Spine J 6 (6):659-66.

590. Simões JA, Vaz MA, Blatcher S, Taylor M (2000) Influence of head constraint and muscle forces on the strain distribution within the intact femur. Med Eng Phys 22 (7):453-9.

591. Completo A, Fonseca F, Simões JA (2008) Strain shielding in proximal tibia of stemmed knee prosthesis: Experimental study. J Biomech 41 (3):560-6.

592. Yang PF, Bruggemann GP, Rittweger J (2011) What do we currently know from in vivo bone strain measurements in humans? J Musculoskelet Neuronal Interact 11 (1):8-20.

593. Shrive NG (1996) Soft tissue strain measurement. In: Orr JF, Shelton JC (eds) Optical Measurement Methods in Biomechanics. Chemistry and Materials Science. Springer, NY, pp 154-72.

594. Kulak RF, Belytschko TB, Schultz AB, Galante JO (1976) Nonlinear behavior of the human intervertebral disc under axial load. J Biomech 9 (6):377-86.

595. Fujita Y, Duncan NA, Lotz JC (1997) Radial tensile properties of the lumbar annulus fibrosus are site and degeneration dependent. Journal of Orthopaedic Research 15 (6):814-9.

596. Martinez JB, Oloyede VOA, Broom ND (1997) Biomechanics of load-bearing of the intervertebral disc: an experimental and finite element model. Med Eng Physics 19 (2):145-56.

597. Ambard D, Cherblanc F (2009) Mechanical behavior of annulus fibrosus: A microstructural model of fibers reorientation. Ann Biomed Eng 37 (11):2256-65.

598. Markolf KL, Morris JM (1974) The structural components of the intervertebral disc: A study of their contributions to the ability of the disc to withstand compressive forces. J Bone Joint Surg Am 56 (4):675-87.

599. McNally DS, Adams MA, Goodship AE (1992) Development and validation of a new transducer for intradiscal pressure measurement. J Biomed Eng 14 (6):495-8.

600. Adams M, Roughley P (2006) What is intervertebral disc degeneration, and what causes it? Spine 31 (18):2151-61.

601. Santos M, Ferreira J, Simões JA Position control of a servo-pneumatic system - Hybrid fuzzy P+I controller of a servo-pneumatic fatigue simulator. In: ICINCO - 6th Int C on Informatics in Control, Automation and Robotics, Milan, Italy, 2009. pp 234-9.

602. Santos M (2009) Controlo de um sistema servopneumático para ensaios de fadiga (Development of a distributed control platform for real-time operation of a servo-pneumatic fatigue test machine in order to perform tests involving the control of the force and position). MSc, University of Aveiro, Aveiro

603. Winter DA (1991) The biomechanics and motor control of human gait: Normal, elderly and pathological. 2nd edn. University of Waterloo Press, Waterloo, Ontario, Canada.

604. Kasra M, Goel V, Martin J, Wang S-T, Choi W, Buckwalter J (2003) Effect of dynamic hydrostatic pressure on rabbit intervertebral disc cells. Journal of Orthopaedic Research 21 (4):597-603.

605. Webster DJ, Morley PL, van Lenthe GH, Müller R (2008) A novel in vivo mouse model for mechanically stimulated bone adaptation: A combined experimental and computational validation study. Computer Methods in Biomechanics and Biomedical Engineering 11 (5):435-41.

606. Lai A, Chow DHK, Siu SW, Leung SS, Lau EFL, Tang FH, Pope MH (2008) Effects of static compression with different loading magnitudes and durations on the intervertebral disc: An in vivo rat-tail study. Spine 33 (25):2721-7.

607. Sarver JJ, Elliott DM (2005) Mechanical differences between lumbar and tail discs in the mouse. J Orthop Res 23 (1):150-5.

608. Heiss C, Kraus R, Schluckebier D, Stiller A-C, Wenisch S, Schnettler R (2006) Bone adhesives in trauma and orthopedic surgery. Eur J Trauma 32 (2):141-8.

609. Teixeira HM, Do Nascimento AB, Hebling J, De Souza Costa CA (2006) In vivo evaluation of the biocompatibility of three current bonding agents. J Oral Rehabil 33 (7):542-50.

610. Belytschko T, Kulak RF, Schultz AB, Galante JO (1974) Finite element stress analysis of an intervertebral disc. J Biomech 7 (3):277-85.

611. Eberlein R, Holzapfel GA, Fröhlich M (2004) Multi-segment FEA of the human lumbar spine including the heterogeneity of the annulus fibrosus. Computational Mechanics 34 (2):147-63.

612. Li H, Wang Z (2006) Intervertebral disc biomechanical analysis using the finite element modeling based on medical images. Computerized Med Imaging and Graphics 30 (6-7):363-70.

613. Heuer F, Schmidt H, Claes L, Wilke H-J (2008) A new laser scanning technique for imaging intervertebral disc displacement and its application to modeling nucleotomy. Clin Biomech 23 (3):260-9.

614. O'Connell GD, Johannessen W, Vresilovic EJ, Elliott DM (2007) Human internal disc strains in axial compression measured noninvasively using magnetic resonance imaging. Spine 32 (25):2860-8.

615. Heuer F, Wolfram U, Schmidt H, Wilke H-J (2008) A method to obtain surface strains of soft tissues using a laser scanning device. J Biomech 41 (11):2402-10.

616. Stokes IAF, Iatridis JC (2004) Mechanical conditions that accelerate intervertebral disc degeneration: Overload versus immobilization. Spine 29 (23):2724-32.

617. Nachemson A (1965) The effect of forward leaning on lumbar intradiscal pressure. Acta Orthop 35 (1):314 - 28.

618. Nachemson A, Elfstrom G (1970) Intravital dynamic pressure measurements in lumbar discs. A study of common movements,maneuvers and exercises. Scand J Rehabil Med 1 (Suppl 1):1-40.

619. Pospiech J, Stolke D, Wilke HJ, Claes LE (1999) Intradiscal pressure recordings in the cervical spine. Neurosurgery 44 (2):379-84.

620. Sato K, Kikichi S, Yonezawa T (1999) In vivo intradiscal pressure measurement in healthy individuals and in patients with ongoing back problems. Spine 24 (23):2468.

621. Steffen T, Baramki HG, Rubin R, Antoniou J, Aebi M (1998) Lumbar intradiscal pressure measured in the anterior and posterolateral annular regions during asymmetrical loading. Clin Biomech 13 (7):495-505.

622. Polga D, Beaubien B, Kallemeier P, Schellhas K, Lew W, Buttermann G, Wood K (2003) In vivo measurement of intradiscal pressure in healthy thoracic intervertebral discs. Spine J 3 (5, Supplement 1):83-4.

623. Seo K-S, Derby R, Date ES, Lee S-H, Kim B-J, Lee C-H (2007) In vitro measurement of pressure differences using manometry at various injection speeds during discography. Spine J 7 (1):68-73.

624. Mastro SA (2000) The effect of transverse load on fiber bragg grating measurements. master's thesis, Drexel University, Philadelphia, PA

625. Nogueira R, Abe I, Kalinowski HJ, Pinto JL, Rocha JRF (2002) Sistema interferométrico automatizado para gravação de redes de Bragg [Interferometric automtic system for FBG writing]. Paper presented at the 13ª Conferência Nacional de Física, Évora,

626. Videman T, Sarna S, Battié MC, Koskinen S, Gill K, Paananen H, Gibbons L (1995) The long-term effects of physical loading and exercise lifestyles on back-related symptoms, disability, and spinal pathology among men. Spine 20:699-709.

627. Bono CM (2004) Low-back pain in athletes. J Bone Joint Surg Am 86 (2):382-96.

628. Videman T, Battie M (1999) The influence of occupation on lumbar degeneration. Spine 24:1164 - 8.

629. Adams M (2005) Mechanical Influences in disc degeneration. Eur Cells and Materials 10 (3):18.

630. Battié MC, Videman T (2006) Lumbar disc degeneration: Epidemiology and genetics. J Bone Joint Surg Am 88 (suppl_2):3-9.

631. Adams M, Hutton W (1982) Prolapsed intervertebral disc. A hyperflexion injury 1981 Volvo Award in Basic Science. Spine 7:184-91.

632. Gordon SJ, Yang KH, Mayer PJ, Mace AHJ, Kish VL, Radin EL (1991) Mechanism of disc rupture: A preliminary report. Spine 16 (4):450-6.

633. Adams M, Freeman B, Morrison H, Nelson I, Dolan P (2000) Mechanical initiation of intervertebral disc degeneration. Spine 25 (13):1625-36.

634. Lencean SM (2000) Lumbar intervertebral disc herniation following experimental intradiscal pressure increase. Acta Neurochirurgica 142 (6):669-76.

635. Wilke HJ, Neef P, Hinz B, Seidel H, Claes LE (2001) Intradiscal pressure together with anthropometric data: A data set for the validation of models. Clin Biomech 16 (Supplement 1):S111-S26.

636. Sato K, Nagata K, Hirohashi T (2002) Intradiscal pressure after repeat intradiscal injection of hypertonic saline: an experimental study. Eur Spine J 11 (1):52-6.

637. Cao KD, Grimm MJ, Yang K-H (2001) Load sharing within a human lumbar vertebral body using the finite element method. Spine 26 (12):e253-e60.

638. Natarajan RN, Williams JR, Andersson GBJ (2006) Modeling changes in intervertebral disc mechanics with degeneration. J Bone Joint Surg Am 88 (suppl_2):36-40.

639. Cooke PM, Lutz GE (2000) Internal disc disruption and axial back pain in the athlete. Phys Med Rehabil Clin N Am 11 (4):837-65.

640. McNally DS, Shackleford IM, Goodship AE, Mulholland RC (1996) In vivo stress measurement can predict pain on discography. Spine 21 (22):2580-7.

641. Kwan-Sik S, Richard D, Elaine SD, Sang-Heon L, Byung-Jo K, Chang-Hyung L (2007) In vitro measurement of pressure differences using manometry at various injection speeds during discography. Spine J 7 (1):68-73.

642. Wang J-L, Panjabi MM, Kato Y, Nguyen C (2002) Radiography cannot examine disc injuries secondary to burst fracture: Quantitative discomanometry validation. Spine 27 (3):235-40.

643. SAMBA (2011) Samba Preclin quick handling and cleaning guide. www.sambasensors.com. Accessed May 07 2011

644. Fye MA, Southern EP, Panjabi MM, Cholewicki J (1998) Quantitative discomanometry: Technique and reproducibility in vitro. J Spinal Disord Tech 11 (4):335-40.

645. Rehbinder C, Alenius S, Bures J, de las Heras M, Greko C, Kroon PS, Gutzwille A (2000) FELASA recommendations for the health monitoring of experimental units of calves, sheep and goats: Report of the Federation of European Laboratory Animal Science Associations (FELASA) Working Group on Animal Health. Laboratory Animals 34 (4):329-50.

646. Voipio H-M, Baneux P, de Segura IAG, Hau J, Wolfensohn S (2008) Guidelines for the veterinary care of laboratory animals: report of the FELASA/ECLAM/ESLAV Joint Working Group on Veterinary Care. Laboratory Animals 42 (1):1-11.

647. Wang J-L, Tsai Y-C, Wang Y-H (2007) The leakage pathway and effect of needle gauge on degree of disc injury post anular puncture: A comparative study using aged human and adolescent porcine discs. Spine 32 (17):1809-15.

648. Elliott DM, Yerramalli CS, Beckstein JC, Boxberger JI, Johannessen W, Vresilovic EJ (2008) The effect of relative needle diameter in puncture and sham injection animal models of degeneration. Spine 33 (6):588-96.

649. Korecki CL, Costi JJ, Iatridis JC (2008) Needle puncture injury affects intervertebral disc mechanics and biology in an organ culture model. Spine 33 (3):235-41.

650. Singer AJ, Quinn JV, Hollander JE (2008) The cyanoacrylate topical skin adhesives. The American journal of emergency medicine 26 (4):490-6.

651. Taravella MJ, Chang CD (2001) 2-Octyl cyanoacrylate medical adhesive in treatment of a corneal perforation. Cornea 20 (2):220-1.

652. Harper MC, Ralston M (1983) Isobutyl 2-cyanoacrylate as an osseous adhesive in the repair of osteochondral fractures. Journal of Biomedical Materials Research 17 (1):167-77.

653. Keller TS, Holm SH, Hansson TH, Spengler DM (1990) 1990 Volvo Award in Experimental Studies: The dependence of intervertebral disc mechanical properties on physiologic conditions. Spine 15 (8):751-61.

654. Derby R, Lee S-H, Kim B-J, Chen Y, Aprill C, Bogduk N (2005) Pressure-controlled lumbar discography in volunteers without low back symptoms. Pain Medicine 6 (3):213-21.

655. Keller TS, Hansson TH, Holm SH, Pope MM, Spengler DM (1988) In vivo creep behavior of the normal and degenerated porcine intervertebral disk: a preliminary report. Journal of spinal disorders 1 (4):267-78.

656. Natalini C, Möllerke R, Motta U, Teixeira A, Endler J, Jobim GB, Jobim GO (1993) Anestesia geral em ovinos submetidos a cirurgia fetal experimental. Acta Cirúrgica Brasileira 8 (2):63-7.

657. Kohn DF, Wixson SK, White WJ, Benson GJ (eds) (1997) Anesthesia and analgesia in laboratory animals American College of Laboratory Animal Medicine Series. Academic Press, San Diego, California, USA.

658. Urban M, Fairbank J, Etherington P, Loh F, Winlove C, Urban J (2001) Electrochemical measurement of transport into scoliotic intervertebral discs in vivo using nitrous oxide as a tracer. Spine 26:984 - 90.

659. Urban JPG, Smith S, Fairbank JCT (2004) Nutrition of the intervertebral disc. Spine 29 (23):2700-9.

660. Dmitriev AE, Cunningham BW, Hu N, Sell G, Vigna F, McAfee PC (2005) Adjacent level intradiscal pressure and segmental kinematics following a cervical total disc arthroplasty: an in vitro human cadaveric model. Spine (Phila Pa 1976) 30 (10):1165-72.

661. Ramos A, Schiller MW, Abe I, Lopes PA, Simões JA (2012) Experimental measurement and numerical validation of bone cement mantle strains of an in vitro hip replacement using optical FBG sensors. Experimental Mechanics 52 (9):1267-74.

662. Carvalho L, Alberto NJ, Gomes PS, Nogueira RN, Pinto JL, Fernandes MH (2011) In the trail of a new bio-sensor for measuring strain in bone: osteoblastic biocompatibility. Biosens Bioelectron 26 (10):4046-52.